

**KERNFORSCHUNGSZENTRUM
KARLSRUHE**

Oktober 1977

KFK 2538

Institut für Angewandte Kernphysik

**PROGRESS REPORT
of the
Teilinstitut Nukleare Festkörperphysik
1.6.1976 - 31.5.1977**

Editors: J. Geerk, G. Linker



**GESELLSCHAFT
FÜR
KERNFORSCHUNG M.B.H.**

KARLSRUHE

Als Manuskript vervielfältigt

Für diesen Bericht behalten wir uns alle Rechte vor

GESELLSCHAFT FÜR KERNFORSCHUNG M. B. H.
KARLSRUHE

KERNFORSCHUNGSZENTRUM KARLSRUHE

KFK 2538

Institut für Angewandte Kernphysik

P R O G R E S S R E P O R T

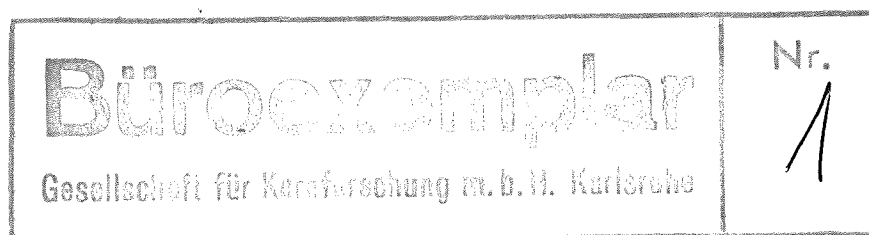
of the

Teilinstitut Nukleare Festkörperphysik

1.6.1976 - 31.5.1977

Editors:

J. Geerk and G. Linker



Gesellschaft für Kernforschung mbH., Karlsruhe

Wir danken Frau J. Steigleder für die umfangreichen Schreibarbeiten zu diesem Report.

This progress report of the Teilinstitut Nukleare Festkörperphysik covers the period from June 1st, 1976 - May 31st, 1977. The arrangement has been chosen to emphasize the main research areas the institute is presently involved.

These areas are the Dynamics of Solids and Liquids, the Electronic Structure and Magnetism of Solids, and the Development and Investigation of New Materials. Some of the technical developments relevant to these topics are also included.

Dieser Progress Report des Teilinstituts Nukleare Festkörperphysik erfaßt den Zeitraum vom 1. Juni 1976 - 31. Mai 1977. Die Darstellung betont die Hauptforschungsgebiete, auf denen das Institut zur Zeit tätig ist. Diese sind: Dynamik von Festkörpern und Flüssigkeiten, Elektronenstruktur und Magnetismus von Festkörpern und die Entwicklung und Untersuchung neuartiger Materialien. Einige technische Entwicklungen, die für diese Forschungsarbeiten wichtig sind, wurden ebenfalls in den Bericht aufgenommen.

In dem vorliegenden Bericht gibt das Teilinstitut IAK I "Nukleare Festkörperphysik" einen Überblick über die wissenschaftlichen Arbeiten in dem Zeitraum vom 1. Juni 1976 bis 31. Mai 1977. Das Forschungsprogramm des Instituts hat derzeit folgende drei Hauptrichtungen:

- Untersuchungen zur Struktur und Dynamik von kondensierter Materie
- Untersuchungen der elektronischen und magnetischen Eigenschaften von Festkörpern
- Herstellung neuer Materialien mittels Ionenimplantation, Kathodenzerstäubung und simultanen Aufdampfens.

Mit den Methoden der Neutronenspektroskopie werden am Forschungsreaktor FR2 in Karlsruhe und am Hochflußreaktor in Grenoble Experimente zur Bestimmung der Phononendispersion und Phononenzustandsdichten von Festkörpern sowie der Streugesetze von Flüssigkeiten durchgeführt. Zur Zeit stehen Untersuchungen an supraleitenden Materialien im Vordergrund. Hierdurch soll ein Beitrag zum besseren Verständnis der Wechselwirkung zwischen gitterdynamischen und supraleitenden Eigenschaften von Festkörpern geleistet werden. Von besonderem Interesse ist ferner das Studium der Dynamik von eindimensionalen metallischen Systemen.

Bei den Untersuchungen von elektronischen und magnetischen Eigenschaften von Festkörpern werden die Methoden der Mößbauerspektroskopie (^{61}Ni , ^{155}Gd) und der Neutronenstreuung eingesetzt, um Information über Hyperfeinfelder, Spindichteverteilungen und magnetische Anregungen zu erhalten. Es wird hier die Möglichkeit genutzt, die sehr kurzlebigen ^{61}Ni -Quellen am Zyklotron des Kernforschungszentrum herzustellen. Zur Zeit werden vorwiegend metallische Verbindungen und Legierungen des Nickels und des Gadoliniums untersucht.

Die Methoden der Ionenimplantation, der Kathodenzerstäubung und des simultanen Aufdampfens werden derzeit ausschließlich zur Herstellung von Supraleitern und zur gezielten Veränderung ihrer supraleitenden Eigen-

schaften eingesetzt. Im Rahmen dieses Programms werden auch Fragen der Strahlenschädigung untersucht. Als wichtige Hilfsmittel für die Charakterisierung der hergestellten Materialien dienen Rückstreu- und Channellingmessungen, Kernreaktionen, Tunnelspektroskopie und Röntgenbeugung.

Die experimentellen Arbeiten des IAK I werden durch eine kleine Theoriegruppe unterstützt, die sich zur Zeit vorwiegend mit Fragen der Elektron-Phonon Wechselwirkung sowie der Dynamik von Festkörpern und Flüssigkeiten beschäftigt.

Das IAK I hat zur Zeit 22 wissenschaftlich-technische Mitarbeiter. Das Institut betrachtet es als eine wesentliche Aufgabe, auswärtige Forschungsgruppen bei der Nutzung der Experimentiereinrichtungen am Reaktor FR2 zu unterstützen. Zwei Mitarbeiter sind nahezu ausschließlich für die Betreuung von Gastgruppen bei der Durchführung von Experimenten an drei Strukturspektrometern des FR2 eingesetzt. Experimente zur unelastischen Neutronenstreuung erfolgen häufig auf der Basis einer Zusammenarbeit. Insbesondere werden Experimente vorbereitet, die anschließend am Hochflußreaktor in Grenoble weitergeführt werden.

Der größte Teil der von Gastgruppen durchgeführten Arbeiten zur elastischen Neutronenstreuung erfolgt außerhalb des Forschungsprogramms des IAK I und wird daher in dem vorliegenden Bericht nicht berücksichtigt.

Von den Arbeiten, die bereits veröffentlicht bzw. zur Veröffentlichung eingereicht sind, werden nur Kurzfassungen oder Literaturhinweise angegeben. Erste Ergebnisse von laufenden Arbeiten werden dagegen ausführlicher beschrieben.

C O N T E N T S

1.	I N V E S T I G A T I O N S O N T H E D Y N A - M I C S O F S O L I D S A N D L I Q U I D S	
		page
1.1	Comparison of the Phonon Densities of States of the Non-Superconductor TiC and the Superconductor TiN with Model Calculations <i>F. Gompf and W. Reichardt</i>	1
1.2	Phonon Dispersion of Vanadium Carbide <i>L. Pintschovius, W. Reichardt, and B. Scheerer</i>	4
1.3	Phonon Density of States of Vanadium Carbide <i>F. Gompf and W. Reichardt</i>	6
1.4	Phonon Dispersion of Vanadium Nitride <i>L. Pintschovius, P. Roedhammer and A.N. Christensen</i>	8
1.5	Acoustic Phonon Density of States of Vanadium Nitride <i>W. Reichardt and F. Gompf</i>	10
1.6	Studies on the Partial Debye Waller Factors of VN and NbN <i>W. Reichardt, B. Scheerer and A.N. Christensen</i>	11
1.7	Phonon Anomalies in Yttrium Sulfide <i>P. Roedhammer, W. Reichardt and F. Holtzberg</i>	15
1.8	Investigations on the Phonon Density of States of Yttrium Sulfide <i>P. Roedhammer and W. Reichardt</i>	17
1.9	Phonon Softening of Nb ₃ Sn Between Room Temperature and 673 K <i>N. Nücker and E. Schneider</i>	18
1.10	Untersuchung der Partiellen Debye-Waller- Faktoren von Nb ₃ Sn <i>Ch. Geibel</i>	19

	page
1.11 Investigation of High Field Superconducting Molybdenum Chalcogenides <i>P. Schweiß, B. Renker, and J.-B. Suck</i>	23
1.12 Phonon Density of States of Lanthanum in the fcc and dhcp Phases <i>N. Nücker</i>	28
1.13 Comparison of Phonon Densities of States $F(\hbar\omega)$ and Tunneling Densities of States $\alpha^2(\hbar\omega) \cdot F(\hbar\omega)$ for Niobium <i>F. Gompf</i>	30
1.14 Investigations of the Polymeric Metal $(\text{SN})_x$ Part I: Lattice Dynamics <i>L. Pintschovius, H. Wendel, H.J. Stolz, A. Otto, H. Kahlert, and R. Currat</i> Part II: Optical Studies of the Electronic Transport Properties <i>H.P. Geseirich, W. Möller, G. Scheiber, and L. Pintschovius</i> Part III: Neutron Diffraction Study of the Crystal Structure of $(\text{SN})_x$ <i>G. Heger, S. Klein, L. Pintschovius, and H. Kahlert</i>	32
1.15 Inelastic Neutron Scattering from Diacetylene Polymers <i>B. Renker, P. Schweiß, and G. Wegner</i>	36
1.16 The Phonon Densities of States of Trigonal and Vitreous Selenium <i>F. Gompf</i>	38
1.17 The Frequency Distribution of KCN and NaCN from Inelastic Neutron Scattering of Powders <i>N. Nücker, J. Daubert, H. Jex, K. Knorr, M. Müllner, and J.-B. Suck</i>	44
1.18 Structure Factor of Expanded Liquid Rubidium up to 1400 K and 200 bar <i>R. Block, J.-B. Suck, W. Freyland, F. Hensel, and W. Gläser</i>	45

	page
2. ELECTRONIC STRUCTURE AND MAGNETISM OF SOLIDS	
2.1 Local Susceptibilities in Dilute <u>PdNi</u> Alloys <i>J. Fink, G. Czjzek, H. Schmidt, K. Tomala, and F.E. Obenshain</i>	47
2.2 Hyperfine Interactions in Intermetallic Compounds of Gd with 3d-Transition Metals <i>G. Czjzek, J. Fink, H. Schmidt, and K. Tomala</i>	50
2.3 Hyperfine Interactions at ¹⁵⁵ Gd Nuclei in Pseudo- binary Alloys Gd(Fe _{1-x} Co _x) ₂ and Gd(Fe _{1-x} Al _x) ₂ <i>G. Czjzek, J. Fink, H. Schmidt, G. Wiesinger, and M.J. Besnus</i>	51
2.4 Crystal Electric Fields in Rare-Earth-M ₃ Compounds <i>W. Groß, K. Knorr, P.v. Blanckenhagen, and A.P. Murani</i>	54
2.5 Crystal Field Transition in La _{0.85} Tb _{0.15} Sn ₃ Investigated by Inelastic Neutron Scattering <i>P.v. Blanckenhagen and H.E. Hoenig</i>	55
2.6 A Single Crystal Neutron Diffraction Study of Cs ₂ PbCu(NO ₂) ₆ at 313 K and the α → β Phase Transition <i>S. Klein</i>	56
2.7 Magnon Dispersion of the Quasi Two-Dimensional Heisenberg Antiferromagnet (CD ₃ ND ₃) ₂ MnCl ₄ <i>N. Lehner, V. Wagner, G. Heger, and R. Geick</i>	59
2.8 Neutron Diffraction Studies on Simple Molecular Crystals for the Determination of Electron Density Distributions <i>G. Heger, D. Mullen, and W. Treutmann</i>	64
2.9 Combined X-Ray and Neutron Diffraction Study of K ₂ [Pt(CN) ₄] _x O _{0.3} · 3H ₂ O with X = Br, Cl (KCP) be- tween 31 K and Room Temperature <i>G. Heger, H.J. Deiseroth, and Heinz Schulz</i>	66

	page
2.10 Untersuchung der Wasserstoffbrückenbindungen im Schlipfeschen Salz ($\text{Na}_3\text{SbS}_4 \cdot 9\text{D}_2\text{O}$) <i>H. Guth and G. Heger</i>	67
2.11 Hyperfine Interactions of Neutron Activated ^{28}Al in Sapphire <i>H.-J. Stöckmann, H. Ackermann, D. Dubbers, F. Fujara, M. Grupp, P. Heitjans, and A. Körblein</i>	70

3. THEORY

3.1 Energy Dependence of the Coupling Function $\alpha^2(\omega)$ for Compounds <i>H. Rietschel</i>	74
3.2 Neutron Scattering Law $S(k, \omega)$ for a Peierls System <i>K. Käfer</i>	77
3.3 Comment on "Fokker-Planck Equations for Simple Non-Markovian Systems" <i>W. Schommers and T. Geszti</i>	81
3.4 Theoretical Investigation of the Liquid-Solid Transition. A Study for Gallium <i>W. Schommers</i>	81
3.5 Extended Born-Green Equation: A New Approach for Determining Pair Potentials in Disordered Systems <i>W. Abel, R. Block, and W. Schommers</i>	82
3.6 Correlations in the Motion of Particles in α -Silver Iodide: A Molecular Dynamics Study <i>W. Schommers</i>	82
3.7 Liquid Argon: The Influence of Three-Body Interactions on Atomic Correlations <i>W. Schommers</i>	83

4. MATERIALS RESEARCH

- 4.1 Low Temperature Self-Ion Irradiation and Superconductivity in Al Thin Films 84
P. Ziemann and M. Kraatz
- 4.2 Thickness Determination and Matthiessen's Rule in Granular Aluminium Thin Films 86
P. Ziemann
- 4.3 Production of Metastable Lead-Bismuth Alloys 90
Chr. Gauss
- 4.4 Proximity Effect in Ion Implanted Molybdenum Films 91
O. Meyer
- 4.5 Preparation of Superconducting Vanadium Layers 94
G. Linker and R. Smithey
- 4.6 Influence of Impurities on the Superconducting Transition Temperature of Ion Bombarded Vanadium Layers 96
G. Linker and M. Kraatz
- 4.7 Energy Dependent Channelling Analysis of Disorder in Ion Bombarded Metal Crystals 98
G. Linker
- 4.8 The Dynamic Conductivity of Nb-I-Ag and Ta-I-Ag Tunneling Diodes at Low Energies 100
J. Geerk and K. Gärtner
- 4.9 Superconducting Partial Isotope Effect for $VN^{14/15}$ 103
B. Hofmann-Kraeft and H. Rietschel
- 4.10 Structural and Superconducting Properties of Sputtered Vanadium-Nitride Layers 105
H.J. Klein

	page
4.11 Channeling Studies in C-Implanted NbC _{0.89} Single Crystals <i>J.M. Lombaard and O. Meyer</i>	107
4.12 Computer Simulation of Channeling in V ₃ Si with a Modified Binary Collision Model <i>R. Kaufmann</i>	110
4.13 Channeling Effect Studies in V ₃ Si Single Crystals <i>O. Meyer and R. Kaufmann</i>	114
4.14 Heavy Ion Radiation Damage in V ₃ Si-Single Crystals <i>O. Meyer, J. Geerk, and G. Linker</i>	118
4.15 Proximity Effect in Irradiated V ₃ Si Single Crystals <i>O. Meyer</i>	121
4.16 Channeling Effect Measurements of ⁴ He-Induced Damage in V ₃ Si Single Crystals <i>O. Meyer</i>	124
4.17 Determination of Oxygen Profiles in Layers and Bulk Material <i>E.L. Haase and M. Conrad</i>	126
4.18 The Influence of Oxygen Content on the Superconducting Properties of Nb ₃ Ge Films <i>M. Conrad and E.L. Haase</i>	128
4.19 Determination of Inert Gas Concentrations in Metals with Rutherford Backscattering and X-Ray Photoelectronspectroscopy <i>H.J. Schmidt, E. Henrich, and G. Linker</i>	132
4.20 Single Crystal Growth <i>B. Scheerer</i>	134

5. DATA PROCESSING

- 5.1 The Improvement of our Structure Calculation Programs, Adaption of the XRAY76 to an IBM Computer 135
R. Kuhn
- 5.2 Zeichnungserstellung von Printer-Card-Layouts 136
R. Moser
- 5.3 Mega - Channel - Kicksorter ASSTRO 138
G. Ehret and H. Hanak
- 5.4 A Lightpen for the TC-Display of the NOVA-Computer 139
G. Ehret, H. Hanak, and H. Sobiesiak

6. DEVELOPMENT OF MEASURING DEVICES AND TECHNIQUES

- 6.1 Automatic Data Collection in Tunneling Experiments 140
J. Geerk
- 6.2 Some Experiences with the "Cold Crucible" 142
B. Scheerer
- 6.3 The Time-of-Flight Spectrometer TOF3 143
N. Nücker
- 6.4 Wechsel- und Justiereinheit für Monochromator-einkristalle 145
K. Weber

7.	PUBLICATIONS, CONFERENCE CONTRIBUTIONS, AND SEMINARS	
7.1	PUBLICATIONS	149
7.2	CONFERENCE CONTRIBUTIONS AND SEMINARS	153
8.	LIST OF THE NEUTRON SPECTROMETERS AT THE FR2 AT KARLSRUHE OPERATED BY THE IAK I	157
9.	STAFF MEMBERS	158

1. INVESTIGATIONS ON THE DYNAMICS OF SOLIDS AND LIQUIDS

1.1 Comparison of the Phonon Densities of States of the Non-Superconductor TiC and the Superconductor TiN with Model Calculations.

F. Gompf and W. Reichardt

In /1/ we compared the generalized phonon densities of states $G(\hbar\omega)$ of TiC and TiN. The measurements were performed at TOF II (cold source with $E_0 = 5$ meV). Due to insufficient resolution the results were not transformed into the true $F(\hbar\omega)$ and compared with model calculations - they were however used to demonstrate the strong shift to smaller frequencies of $G(\hbar\omega)$ for TiN in comparison to TiC. As later justified by /2/ we assumed these high intensities at low frequencies to be mainly caused by contributions of pronounced anomalies in some of the dispersion curves, which were known to exist for transition metal carbides with high T_c . As these model calculations can now be carried out for both substances we investigated the frequency distributions of TiC_{.98} and TiN_{.92} in more detail by performing neutron scattering experiments with an incident energy of 64.3 meV which improved our resolution considerably.

In Fig. 1a) we compare the true $F(\hbar\omega)$ of TiC which has been corrected for the difference in mass and scattering power of the two different atoms with a shell model calculation fitted to the phonon dispersion curves measured by /3/. The acoustic part of the spectrum is a combination of energy loss and energy gain data and the overall agreement with the model calculation is good. The sharp peaks are smeared out due to resolution effects. The optical part of $F(\hbar\omega)$ can of course only be determined from the energy gain data where the resolution is not good enough to reveal a possibly detailed structure.

The θ_D versus T curve deduced from this $F(\hbar\omega)$ of TiC is shown in Fig. 2 and compared with experimental results obtained from specific heat data /4/ and with the curve resulting from the model calculation.

The acoustic part of the true $F(\hbar\omega)$ of TiN is shown in Fig. 1b) and compared with a double shell model (DSM) calculation fitted to the dispersion curves measured by /2/. For TiN the DSM calculations agree rather well with

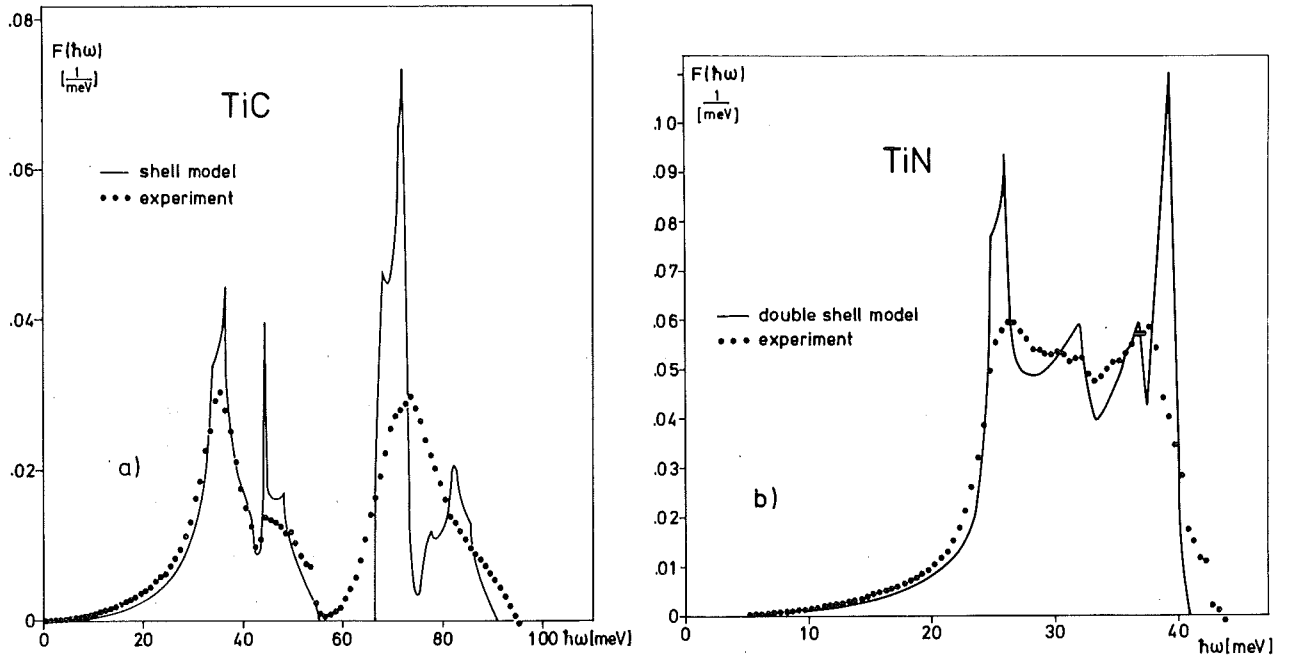


Fig. 1 Comparison of the directly determined phonon density of states with model calculations:

- a) TiC - shell model calculations of Ref. /3/
- b) TiN - double shell model calculations of Ref. /2/.

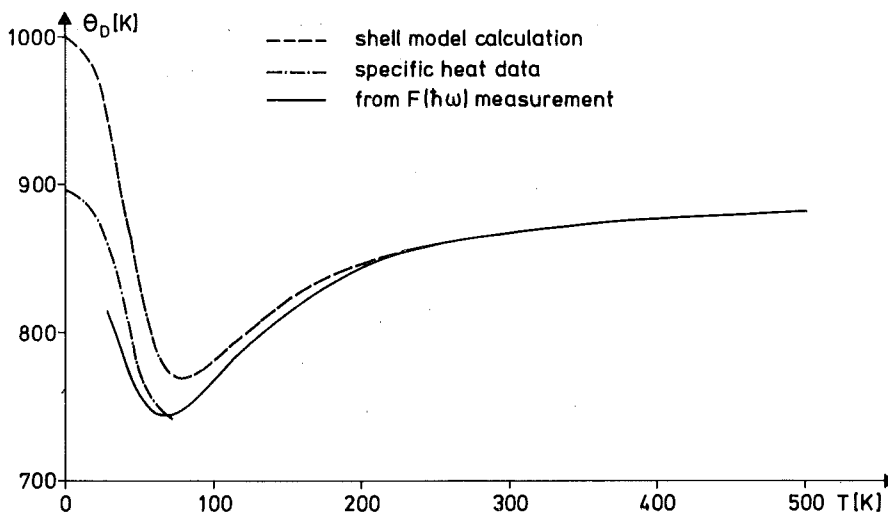


Fig. 2 Different θ_D versus T curves for TiC.

the directly determined $F(\hbar\omega)$. In fact the agreement is better than the result the DSM-calculations gave for the superconductor $\text{NbC}_{.96}$ /5/ which also has 9 valence electrons and which is expected to be quite similar. In Fig. 3 we compare $F(\hbar\omega)$ for both materials.

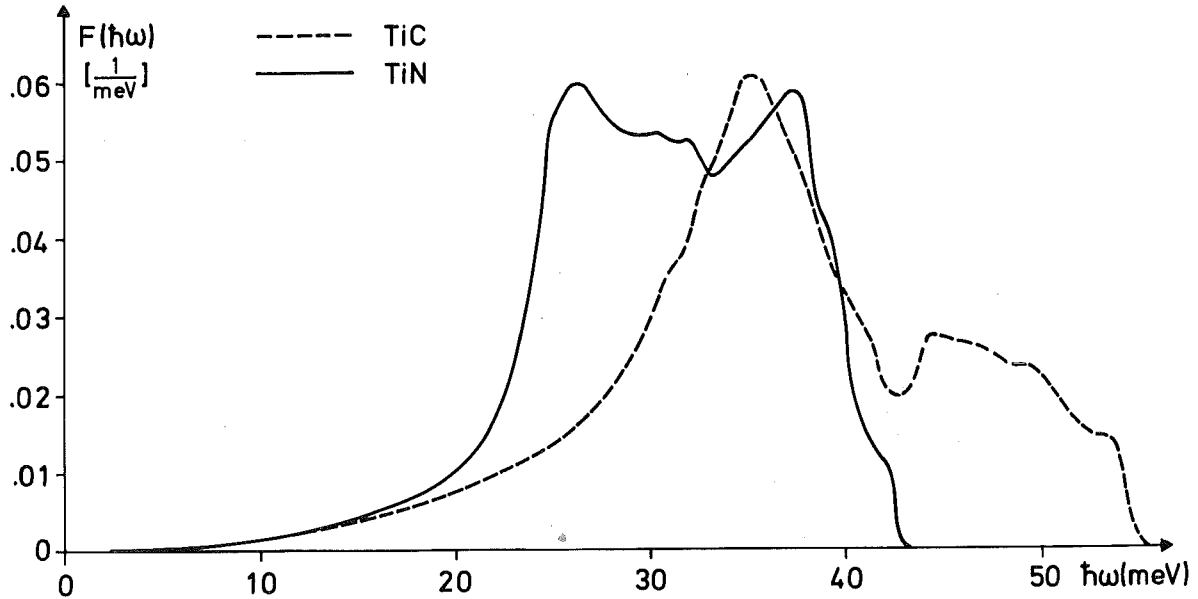


Fig. 3 Comparison of the acoustic phonon densities of states for TiC and TiN.

REFERENCES

- /1/ F. Gompf, in Progress Report of the Teilinstitut Nukleare Festkörperphysik, Gesellschaft für Kernforschung Karlsruhe (KFK 2183), 29 (1975)
- /2/ P. Roedhammer, W. Kress, private communication
- /3/ L. Pintschovius and W. Reichardt, in Progress Report of the Teilinstitut Nukleare Festkörperphysik, Gesellschaft für Kernforschung Karlsruhe (KFK 2183), 1 (1975)
- /4/ P. Roedhammer, W. Weber, E. Gmelin, and K.H. Rieder, J. Chem. Phys. 64, 581 (1976)
- /5/ J. Geerk, F. Gompf, W. Reichardt, and E. Schneider, in Progress Report of the Teilinstitut Nukleare Festkörperphysik, Gesellschaft für Kernforschung Karlsruhe (KFK 2183), 31 (1975)

1.2 Phonon Dispersion of Vanadium Carbide

L. Pintschovius, W. Reichardt, and B. Scheerer

Our investigations on the phonon dispersion of VC_{.87} /1/ have been continued by measurements on the triple axis spectrometers IN8 and IN1 at the HFR in Grenoble and on TAS1 at the FR2 in Karlsruhe. The main effort was directed towards the determination of the optic branches. Little progress only was achieved in the acoustic region because these measurements turned out to be very difficult even at the HFR.

The results are plotted in Fig. 1. The zone boundary phonons at the L-point and the maximum of the LA-branch in $[110]$ -direction were taken from a $g(\nu)$ - measurement /2/. A fit based on a normal shell model with free electron screening is included in that figure. The parameters are listed in Tab. 1.

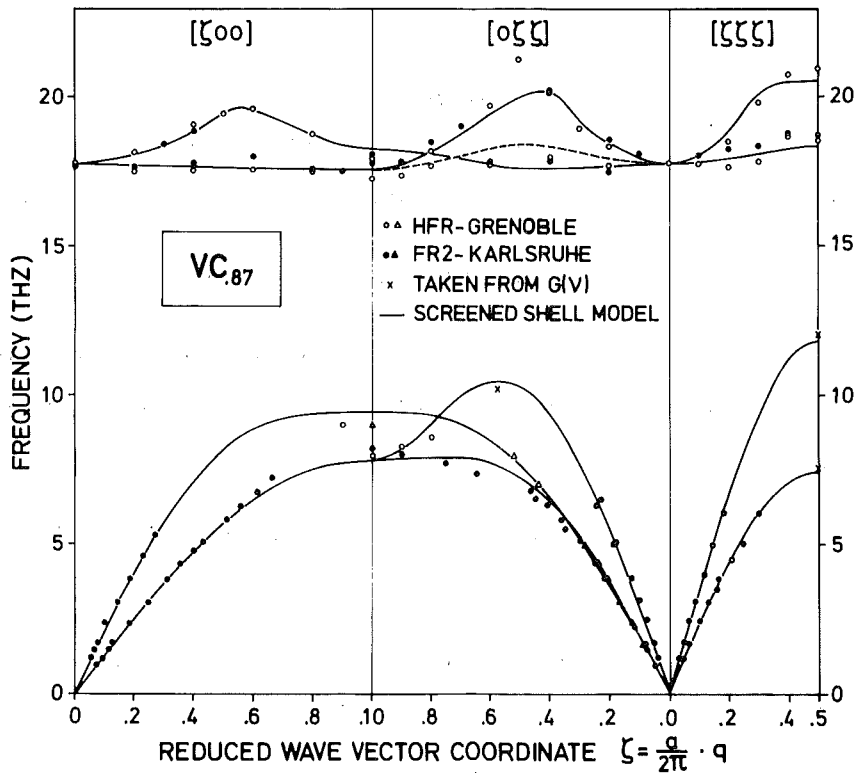


Fig. 1 Phonon dispersion of VC_{.87}. The lines are the result of a fit on the basis of a shell model with free electron screening.

Small but systematic deviations for the TA-branch in $[110]$ -direction with polarization $[001]$ indicate that the use of a double shell model is presumably appropriate in this case. However, the data so far available are not sufficient for a determination of the model parameters.

It is intended to complete these investigations at the end of this year.

Table 1

Parameters of the screened shell model for VC₈₆ (force constants in units of $e^2/2r_0^3$, charges in units of e , k_S and k_F in units of $2\pi/a$). The density and the effective mass of the screening electrons calculated on the basis of a free electron model are included in that table (n in units $1/2r_0^3$, m_{eff} in units of n_{el}).

A (12)	17.73	k_1	500
B (12)	2.92	k_2	137
A' (22)	3.01	k_S	.234
B' (22)	-3.06	k_F	.585
C' (22)	1.21	n_{el}	.027
Z	-.73	m_{eff}	.607
Y_1	0		
Y_2	-1.36		

REFERENCES

- /1/ L. Pintschovius, W. Reichardt, and B. Scheerer, in Progress Report of the Teilinstitut Nukleare Festkörperphysik, Gesellschaft für Kernforschung Karlsruhe (KFk 2183), 3 (1975)
- /2/ F. Gompf and W. Reichardt, this report, p. 6

1.3 Phonon Density of States of Vanadium Carbide

F. Gompf and W. Reichardt

Measurements of the acoustic phonon dispersion curves of VC are extremely difficult for large wave vectors where the carbon atoms are essentially at rest and consequently the coherent one phonon cross section is very small. As the phonon density of states is sensitive to phonons with wave vectors close to the boundary of the Brillouin zone it is hoped that the combined information obtained from single crystal measurements and a scattering experiment on a powder sample will eventually lead to a reliable knowledge of the lattice dynamics of this material.

The sample was prepared by zone refining a hot pressed cylindrical rod (delivered by CERAC) which was crashed to small pieces. From both chemical analysis and a measurement of the lattice constant the carbon concentration was determined to be 87 %. The oxygen concentration was negligibly small. The experiment was performed on TOF1 with a primary neutron energy of 64.3 meV in energy loss.

The acoustic phonon density of states obtained from this measurement is shown in Fig. 1. The arrows mark the frequencies of some zone boundary phonons as estimated from this distribution.

As expected the phonon density of states of VC_{.87} is very similar to that of nonstoichiometric NbC_{.76} (both materials are not superconducting). This can be seen by comparing the experimental points with the dashed curve in Fig. 1, which represents the phonon density of states of NbC_{.76} /1/ after rescaling the frequencies with a factor $\sqrt{\frac{M_{Nb}}{M_V}}$, where M_{Nb} and M_V are the masses of Nb and V respectively. However, the distribution for VC_{.87} shows a shoulder at 26 meV which is absent in NbC_{.76}. Measurements on a different VC sample (powder delivered by VENTRON CORP) confirm the existence of this shoulder. A comparison with the phonon density of states of nearly stoichiometric NbC_{.96} /1/ suggests that this shoulder may be a relict of the phonon anomalies which we expect in stoichiometric VC. The differences between the results of VC_{.87} and NbC_{.76} may be explained by the ordering of the C-vacancies in VC_{.875} (= V₈C₇) which has been observed by Froidevaux and Rossier /2/. Therefore in V₈C₇ there is a regular arrangement of V-atoms

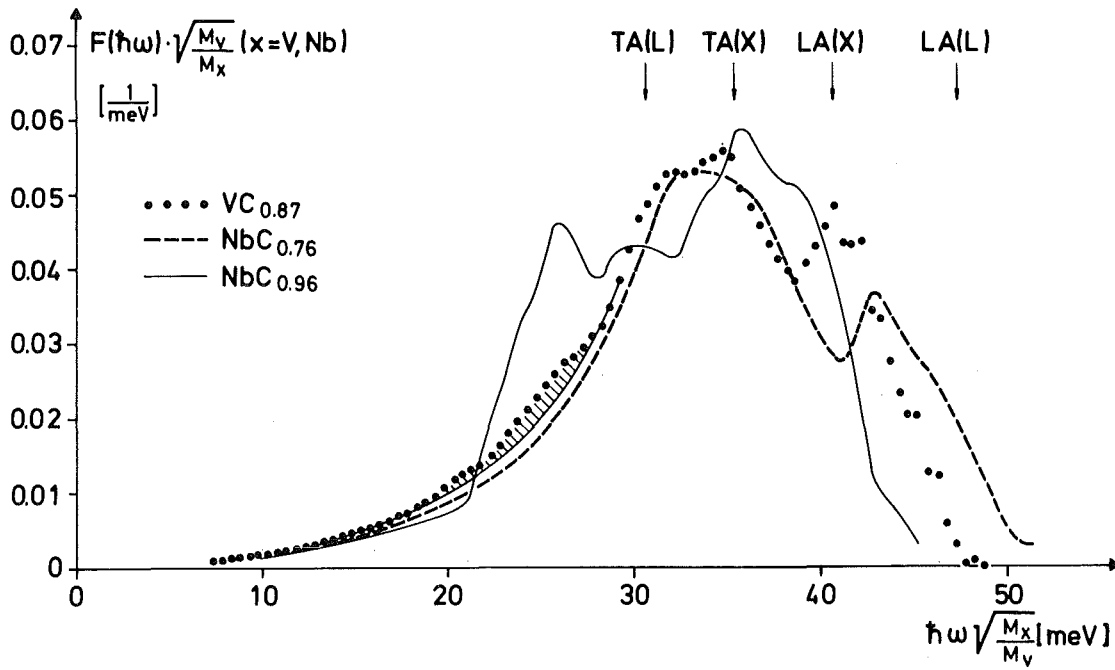


Fig. 1 Comparison of the acoustic phonon density of states of $VC_{.87}$ with those of $NbC_{.96}$ and $NbC_{.76}$.

whose carbon environment is intact which seems to be essential for the occurrence of the resonance-like interaction causing the dips in the dispersion curves of the refractory carbides and nitrides /3/. The superstructure in V_8C_7 may cause that some of the phonon branches of stoichiometric VC split into several branches, some of them remaining essentially unchanged while in the others the anomalies disappear.

REFERENCES

- /1/ F. Gompf, in Progress Report of the Teilinstitut Nukleare Festkörperphysik, Gesellschaft für Kernforschung Karlsruhe (KFK 2357), 46 (1976)
- /2/ Froidevaux and Rossier, J. Phys. Chem. Solids 28, 1167 (1967)
- /3/ W. Hanke, J. Hafner, and H. Bilz, Phys. Rev. Lett. 37, 1560 (1976)

1.4 Phonon Dispersion of Vanadium Nitride

L. Pintschovius, P. Roedhammer^a, and A.N. Christensen^b

^a*Fachbereich Physik, Universität Konstanz, D-7750 Konstanz*

^b*Institute of Inorganic Chemistry, University of Aarhus, Denmark*

The phonon dispersion curves of all transition metal compounds (TMC's) with 9 valence electrons (VE) per primitive unit cell investigated to this date exhibit pronounced anomalies in some of the acoustic branches. At the same time, they are strong-coupling superconductors with high superconducting transition temperatures (T_C 's) around 10 K. The TMC's with nominally 10 VE per unit cell have even higher T_C 's (up to 18 K). From measurements of the specific heat and of the phonon density of states on polycrystalline samples we know that the phonon frequencies decrease strongly when going from TMC's with 9 VE to TMC's with 10 VE /1, 2, 3/. However, attempts to explain this shift by an enhancement of the anomalies found in TMC's with 9 VE were not successful.

Recently, one of us (A.N. Christensen) was able to grow two large (.35 and 1 cm³) single crystals of VN_x using a floating - zone technique. By annealing in nitrogen atmosphere at 200 bar for about 90 hours the nitrogen content was increased to $x \sim 0.85$.

Measurements of the phonon dispersion curves are currently made on TAS1 at the FR2 in Karlsruhe. For most of the scans the two crystals have been co-aligned. In spite of the rather large sample volume the measurements of the acoustic branches towards higher q-values are extremely difficult due to the following reasons:

- (i) The scattering from the vanadium atoms is almost completely incoherent and the amplitudes of the nitrogen atoms are small for these modes.
- (ii) The background due to incoherent scattering shows a peak at about 4.5 THz. Therefore in this energy region it is very difficult to distinguish between neutron groups originating from coherent and from incoherent scattering, respectively.

Our preliminary results are shown in Fig. 1. The following features are most remarkable:

- (i) The elastic constants are not much smaller than in VC (9 VE). Therefore the strong increase of the phonon density of states between 2 and 5 THz cannot be attributed only to phonons with small q -values.
- (ii) The maximum of the TA-branch in $[100]$ -direction is located at $q \approx 0.6$. The decrease of the phonon frequencies when going to the zone boundary is unexpected. It indicates that the lattice dynamics of the TMC's with 10 VE are quite different from those of the TMC's with 9 VE.

The investigations will be completed at the HFR Grenoble in July 1977.

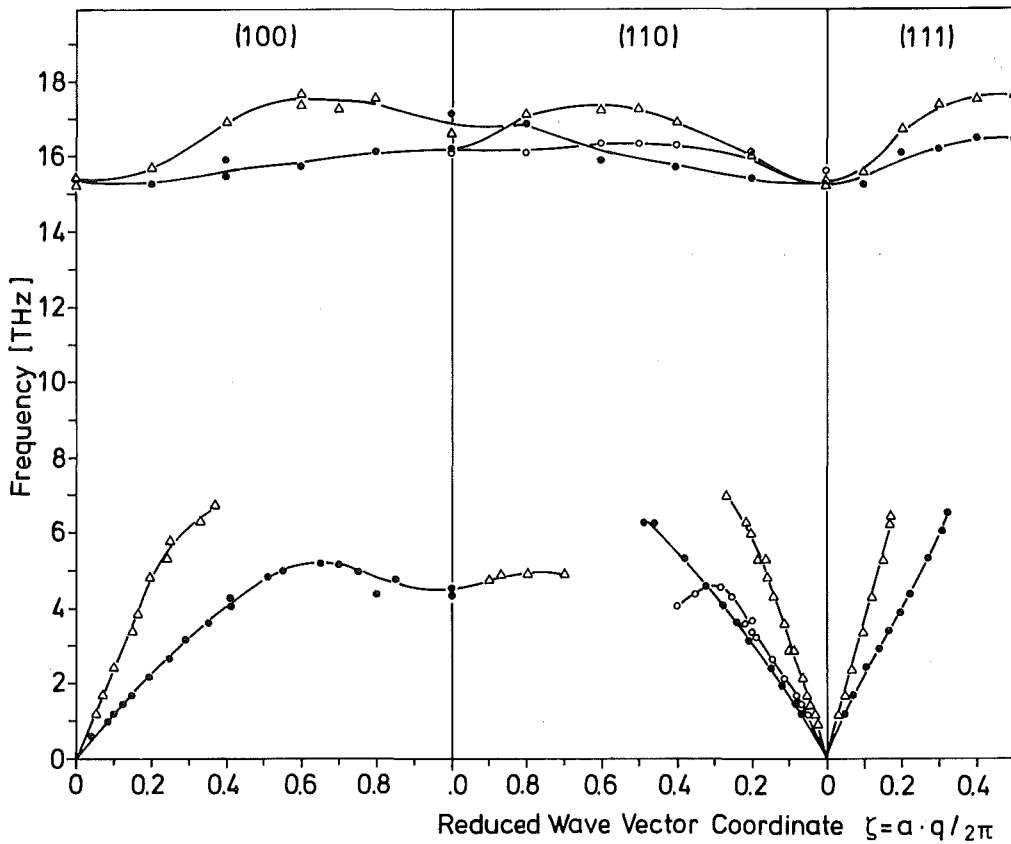


Fig. 1 Phonon dispersion of VN_{0.85}.

REFERENCES

- /1/ P. Roedhammer, E. Gmelin, W. Weber, J.P. Remeika, Phys. Rev. B15, 711 (1977)
- /2/ F. Gompf, L. Pintschovius, W. Reichardt, and B. Scheerer, in Proc. of Conf. Neutron Scattering Gatlinburg (USA), June 1976, p. 129
- /3/ F. Gompf and W. Reichardt, this report, p. 10

1.5 Acoustic Phonon Density of States of Vanadium Nitride

W. Reichardt and F. Gompf

As a supplement of the present investigations of the phonon dispersion curves of vanadium nitride we performed measurements on powder samples in order to obtain information on the phonon density of states. Two different samples were used which were characterized by measurements of the superconducting transition temperatures T_C and the lattice constants a_0 and by chemical analysis. The results are given in Table 1, where the two values for each T_C represent the width of the transition.

Table 1

Some physical properties of the two VN samples.

	T_C [K]	a_{0AV} [Å]	Δa_0 [Å]	N-concentration at. %	O-concentration at. %
SAMPLE 1	6.4 - 8.2	4.119	.012	46.8	2.9
SAMPLE 2	8.3 - 8.9	4.138	not observable	47.5	2.6

The acoustic parts of the generalized phonon densities of states determined from scattering experiments on TOF1 at the FR2 are shown in Fig. 1. There is a considerable dependence on T_C . The sample with the higher T_C has a much softer phonon spectrum. We observe that the general shape of the spectra is similar to that of the closely related compound $NbN_{.95}$ /1/ which is also shown in the figure after scaling the frequencies by a factor $\sqrt{\frac{M_{Nb}}{M_V}}$, where M_{Nb} and M_V are the atomic masses of Nb and V, respectively. This comparison shows that the frequency moment of VN ($M\langle\omega^2\rangle_{VN}$) is much smaller than that of NbN ($M\langle\omega^2\rangle_{NbN}$) while the T_C of NbN is much higher (17 K) than that of VN.

The dashed curve in the figure has been calculated using a model that gives a good description of the measured phonon data at small wave vectors. The extreme deviation of this curve from the experimentally determined distributions clearly demonstrates, that some of the acoustic branches in VN have

to bend down below 10 meV in regions of the Brillouin zone far away from the Γ -point.

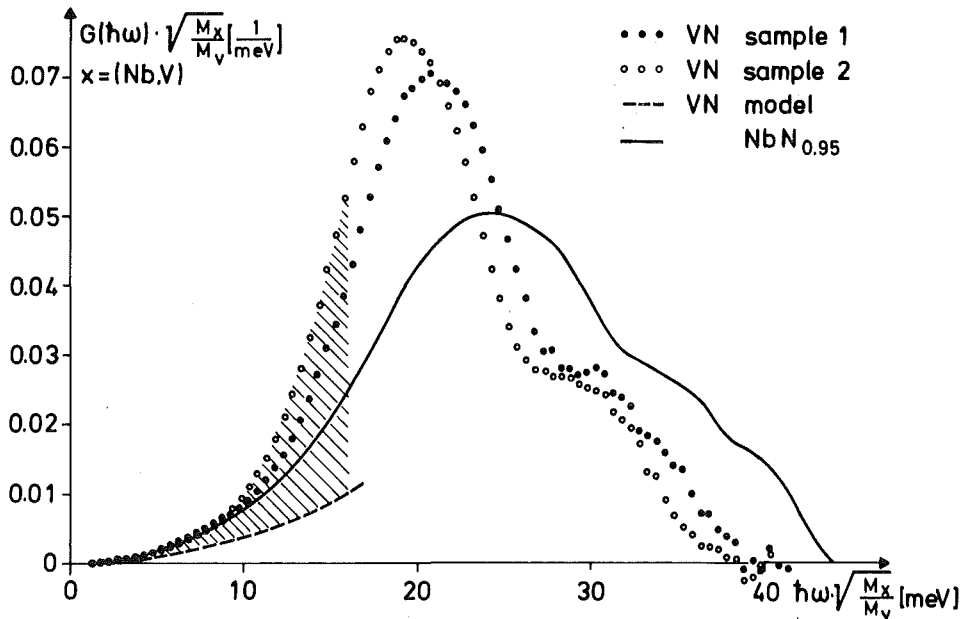


Fig. 1 Comparison of $G(\hbar\omega)$ of two VN-samples with that of $\text{NbN}_{.95}$.

REFERENCES

/1/ F. Gompf, W. Reichardt, and A.N. Christensen, in Progress Report of the Teilinstitut Nukleare Festkörperphysik, Ges. f. Kernforschung Karlsruhe (KFK 2357), 11 (1976)

1.6 Studies on the Partial Debye Waller Factors of VN and NbN

W. Reichardt, B. Scheerer, and A.N. Christensen^a

^aInstitute of Inorganic Chemistry, University of Aarhus, Denmark

From diffraction experiments on simple compounds the partial Debye Waller coefficients $2W_i(Q)$ of the individual components i can be determined. For cubic crystals without defects and for temperatures T of the order of the Debye temperatures $2W_i(Q)$ is given by

$$2W_i(Q) = \frac{1}{3} \langle u^2 \rangle_i Q^2 = \frac{\hbar^2 Q^2}{M_i} k_B T \left[\langle (\hbar\omega)^{-2} \rangle_i + \frac{1}{12(k_B T)^2} - O\left(\frac{1}{T^4}\right) \right], \quad (1)$$

where $\langle u^2 \rangle_i$ is the mean square displacement of the atomic species i due to the thermally excited lattice vibrations and M_i is the mass of the i -th scatterer.

Hence from such an experiment the inverse second frequency moments $\langle \omega^{-2} \rangle_i$ of the amplitude weighted phonon density of states of the individual components can be determined.

We present here preliminary results of neutron diffraction experiments on two samples of VN and NbN which have also been used in the measurements of the phonon density of states (see preceding contribution to this report).

In order to avoid contamination of the Bragg-intensities by higher order reflections and inelastically scattered neutrons the measurements were performed on a high resolution diffractometer using Cu(420) as monochromator ($2\theta_M = 90^\circ$, $\lambda = 1.1426 \text{ \AA}$, $\Delta(2\theta) \leq .6^\circ$ for $0 \leq 2\theta \leq 110^\circ$). The contribution of higher order reflections was completely negligible and the sharp Bragg-peaks could well be discriminated against the broad distributions of inelastically scattered neutrons. The intensities I_{hkl} obtained from the diffraction patterns after corrections for the Lorentz factor and the multiplicities of the reflections are plotted in Fig. 1.

The curves fitted to the experimental data of NbN_x were calculated with the following parameters: $\langle u^2 \rangle_{Nb} = .030 \text{ \AA}^2$, $\langle u^2 \rangle_N = .023 \text{ \AA}^2$, $x = .945$. The intensities of the odd reflections could not be determined very precisely as they are about 50 times smaller than those of the even reflections.

Writing

$$I_{hkl}^{\text{even}} = 4b_{Nb} b_N \exp \left[\frac{1}{2} (2W_{Nb}(Q) + 2W_N(Q)) \right] + \left[b_{Nb} \exp(-W_{Nb}(Q)) - b_N \exp(-W_N(Q)) \right]^2 \quad (2)$$

where b_{Nb} and b_N are the scattering amplitudes of Nb and N, respectively, it is seen that the even reflections are determined by the first term of

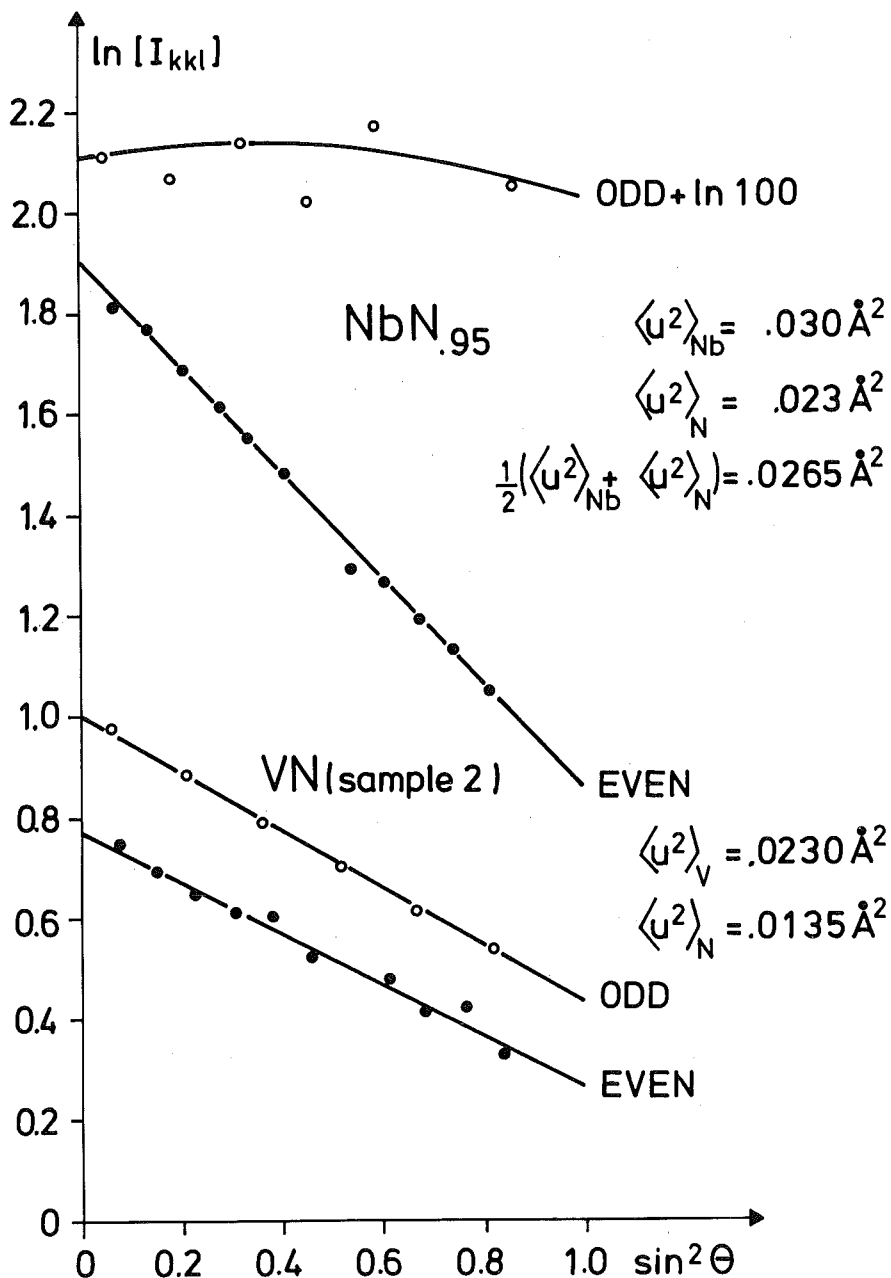


Fig. 1 Bragg intensities of NbN and VN

(2) within about 2 %. Thus the average $\frac{1}{2}(\langle u^2 \rangle_{\text{Nb}} + \langle u^2 \rangle_{\text{N}}) = .0265 \text{ \AA}^2$ can be determined with much better accuracy than the individual values for Nb and N.

Due to the small coherent cross section of V the VN results are mainly sensitive to $\langle u^2 \rangle_{\text{N}}$. Therefore, in the analysis of the experimental data, $\langle u^2 \rangle_{\text{V}}$ was calculated from the acoustic phonon density of states which was shown in the preceding article. From the model discussed in the same article a value $\langle u^2 \rangle_{\text{N}} = 0.0104 \text{ \AA}^2$ is obtained which is about 30 % lower than the ex-

perimental value of 0.0135 \AA^2 . This difference appears to be reasonable, as the model yields a much harder acoustic spectrum than has been determined in the experiment.

From measurements of the phonon densities of states we know that the optic frequencies of NbN and VN are not very different. Therefore we expect $\langle u^2 \rangle_N$ for NbN to be about 0.0135 as in VN. Furthermore from the acoustic phonon density of states an approximate value $\langle u^2 \rangle_{Nb} = .018 \text{ \AA}^2$ is obtained. Both values are considerably smaller than the experimental values quoted above. We interpret this difference ($\Delta \langle u^2 \rangle_{Nb} = .012 \text{ \AA}^2$, $\Delta \langle u^2 \rangle_N = .0095 \text{ \AA}^2$) to be due to a static distortion of the lattice caused by both Nb and N vacancies. According to Ref. /1/ NbN_{.95} contains about 3 % Nb vacancies and 8 % N vacancies. As a N vacancy distorts mainly the Nb sublattice, we expect $\Delta \langle u^2 \rangle_{Nb}$ to be larger than $\Delta \langle u^2 \rangle_N$ in accordance with our experimental result.

It cannot be completely excluded that also the VN results are slightly affected by a static distortion of the lattice, as by chemical analysis the N concentration was determined to be 47.5 at. %. As the total nonmetal concentration (N + O) is near 50 at. % and the lattice constant is close to that of stoichiometric VN /2/ we have to assume that the concentration of nonmetal vacancies is small.

It is intended to perform further measurements as a function of temperature in order to obtain a more reliable separation of the Debye Waller coefficients into static and dynamic contributions.

REFERENCES

/1/ G. Brauer and H. Kirner, Z. Anorg. Allg. Chem. 328, 34 (1964)

/2/ F.A. Shunk, Constitution of Binary Alloys, Second Supplement, McGraw-Hill Book Company (1969)

1.7 Phonon Anomalies in Yttrium Sulfide

P. Roedhammer^a, W. Reichardt, and F. Holtzberg^b

^aFachbereich Physik, Universität Konstanz, D-7750 Konstanz

^bIBM Thomas J. Watson Research Center, Yorktown Heights, New York 10598
U.S.A.

Yttrium monosulfide (YS) is a transition metal chalcogenide with physical properties that in many respects correspond to those of the group IVb mononitrides and the group Vb monocarbides. Similar to these compounds, YS crystallizes in the B1 structure and has 9 valence electrons. It is metallic and becomes superconducting at $T_c = 2.8$ K. These similarities suggest that the phonon dispersion relation of YS might exhibit a soft mode behavior similar to that observed in the IVb-nitrides and Vb-carbides.

We have measured the phonon dispersion curves of a single crystal of YS (volume ~ 0.6 ccm) at room temperature. Measurements were performed at the triple-axis-spectrometer TAS1 at the FR2 Karlsruhe.

Fig. 1 shows the experimentally determined phonon dispersion curves of YS in the three main symmetry directions. The slopes of the dispersion curves at $q = 0$ are calculated from measured elastic constants /1/. They agree well with our data.

A striking feature in the phonon dispersion relation of YS is the softening of the LA phonons in certain parts of the Brillouin zone. In the $[110]$ - and $[111]$ -directions, the longitudinal branches resemble those observed in NbC and TiN whereas in the $[100]$ -direction the dip seems to be masked by the overall depression of the branch towards the zone boundary. In contrast to NbC and TiN none of the TA branches of YS exhibits a softmode region.

For an analysis of the data we have fitted the double shell model (DSM) of Weber /2/ to the experimental data. The curves in Fig. 1 were obtained from an 11-parameter fit, with 5 parameters for the normal shell model and 6 parameters for the supershells. All charges were put equal to zero.

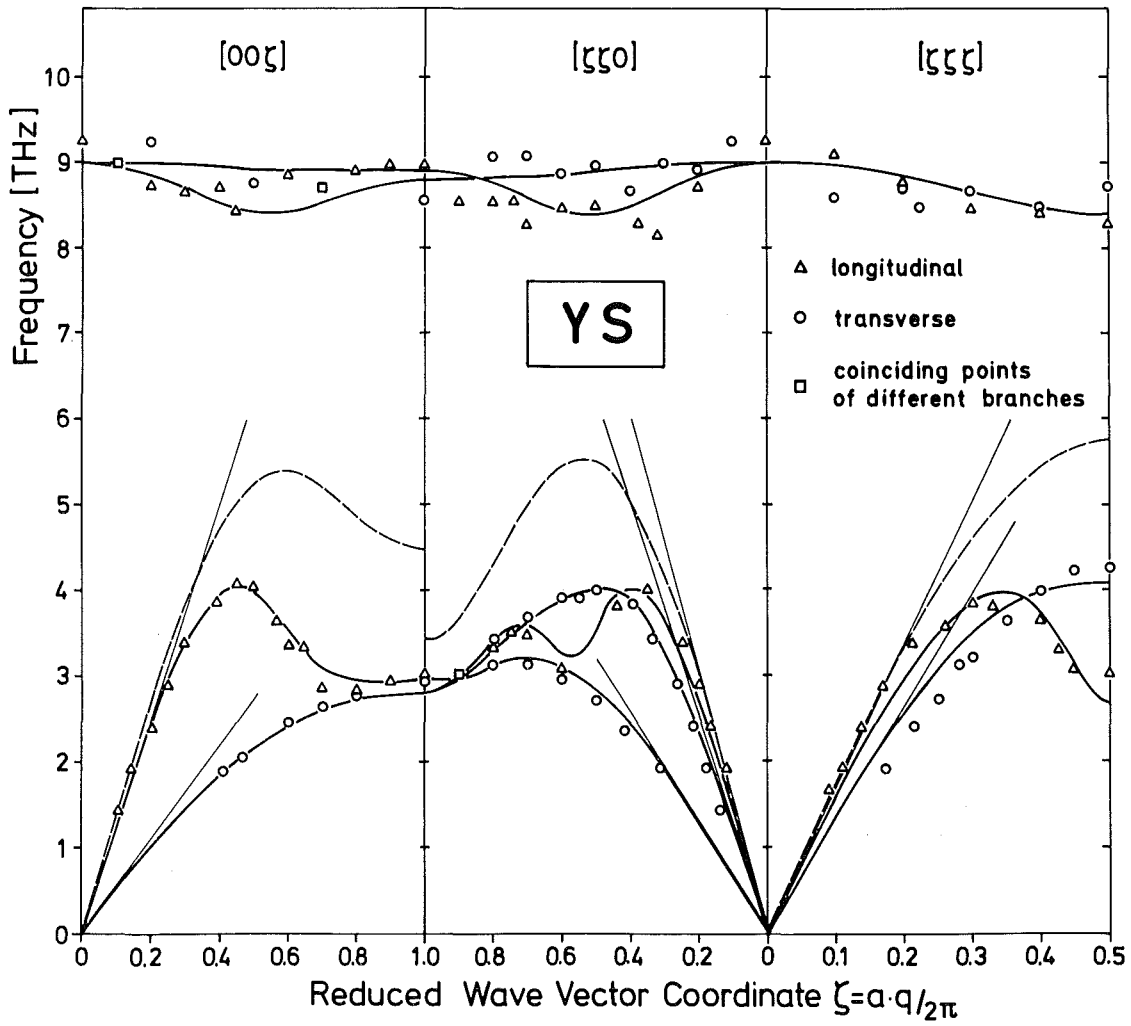


Fig. 1 The phonon dispersion of yttrium sulfide.

REFERENCES

- /1/ R. Melcher, G. Güntherodt, T. Penny, and F. Holtzberg, IEEE Symposium on Ultrasonics, Los Angeles (1975)
- /2/ W. Weber, Phys. Rev. B8, 5082 (1973)

1.8 Investigations on the Phonon Density of States of Yttrium Sulfide

P. Roedhammer^a and W. Reichardt

^aFachbereich Physik, Universität Konstanz, D-7750 Konstanz

In order to support the unusual results obtained in the measurements of the phonon dispersion curves of YS (see previous article) we have performed a scattering experiment on a powder sample for a determination of the phonon density of states. Unfortunately the sample contained a considerable amount of other phases besides the rocksalt structure of the mono-sulfide. From neutron and X-ray diffraction measurements this contamination was estimated to be about 10 %.

Fig. 1 shows the generalized phonon density of states obtained from a scattering experiment on TOF2 with a primary neutron energy of 5.05 meV. The arrows mark some zone boundary frequencies determined by the phonon measurements while the full line represents the acoustic phonon density of states calculated with the double shell model of Weber fitted to the experimental dispersion curves.

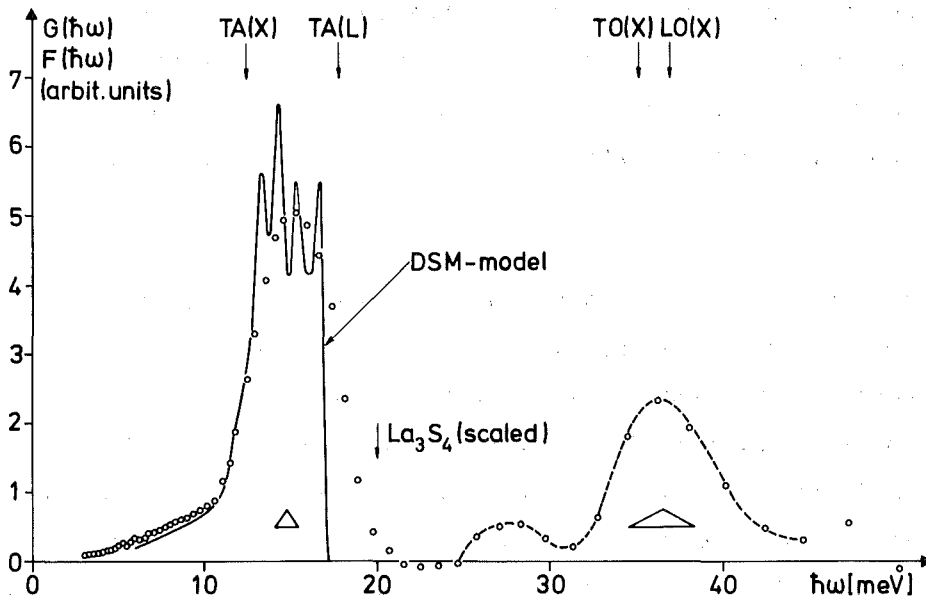


Fig. 1 Generalized phonon density of states of yttrium sulfide containing 90 % B1-phase.

Although a quantitative comparison is hampered by the presence of parasitic phases in the sample a satisfactory correspondence between the experimental distribution and the results of the phonon measurements is observed. The intensity in the acoustic region above 18 meV and the peak at about 28 meV are believed to be due to the parasitic phases. This assumption is supported by a present measurement on La_3S_4 . The frequency distribution of La_3S_4 shows a pronounced peak between 20 and 30 meV and the acoustic region extends up to 20 meV when scaled by the ratio $\sqrt{\frac{M_{\text{La}}}{M_{\text{Y}}}}$, where M_{La} and M_{Y} are the atomic masses of La and Y respectively.

1.9 Phonon Softening of Nb_3Sn Between Room Temperature and 673 K

N. Nücker and E. Schneider^a

^a*Physikdepartment der TU München*

In /1/ we presented measurements of the phonon frequency distribution of Nb_3Sn . A considerable softening of the phonon frequencies of Nb_3Sn on cooling from room temperature to 77 K and to 5.5 K was observed. To investigate if this trend continues we extended our measurements to elevated temperatures up to 673 K.

The experiment was performed on the TOF1 spectrometer of the FR2 Karlsruhe using 64.5 meV neutrons. Our results are shown in Fig. 1. It is obvious that phonon softening continues to higher temperatures. The change in the phonon density of states between 673 K and room temperature - the frequencies below 18 meV are shifted by about 0.5 meV - however is less drastic compared to shifts of about 2 meV between room temperature and 5.5 K. Considering the Debye temperature of Nb_3Sn $\Theta_{\text{D}} = 290 \text{ K}$ /2/ however a phonon softening with increasing temperatures should be expected in the temperature range of our experiment. Thus the observed inverse effect is exceptional.

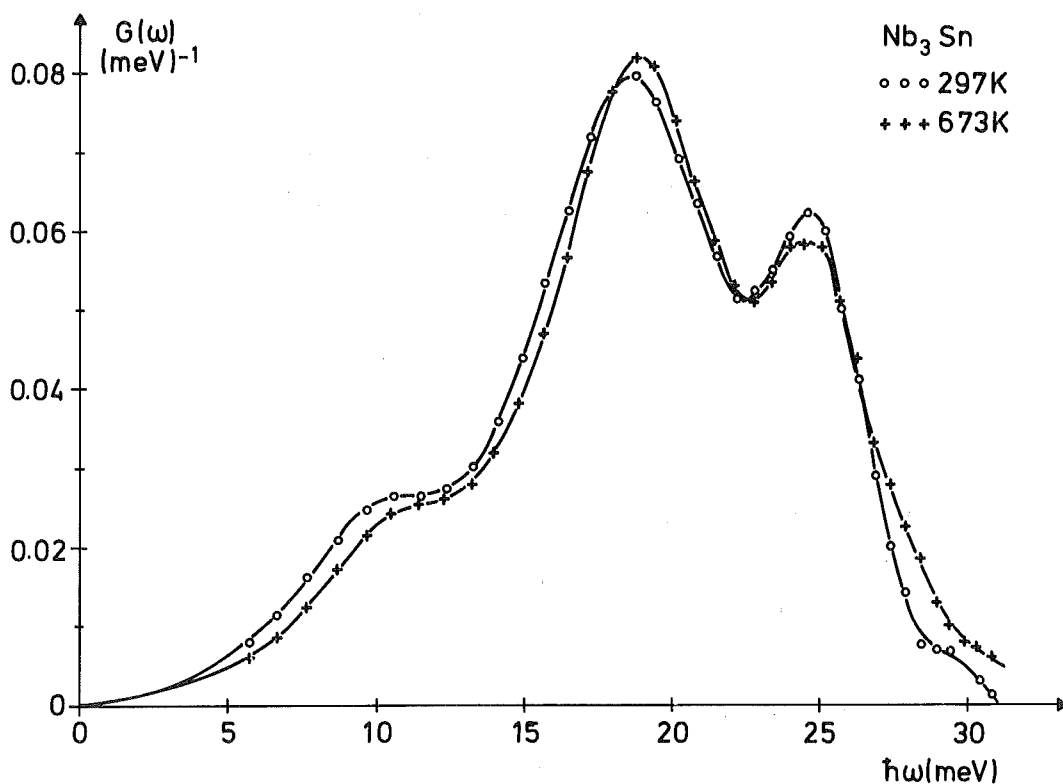


Fig. 1 Temperature dependence of the phonon density of states of Nb₃Sn.

REFERENCES

- /1/ E. Schneider, N. Nücker, W. Reichardt, in Progress Report of the Teilinstitut Nukleare Festkörperphysik, Ges. f. Kernforschung Karlsruhe (KFK 2183), 25 (1975)
- /2/ F. Morin, J. Maita, Phys. Rev. 129, 1115 (1963)

1.10 Untersuchung der Partiellen Debye-Waller-Faktoren von Nb₃Sn

Ch. Geibel

Mehrere A15 (A₃B)-Verbindungen sind mittels unelastischer Neutronenstreuung untersucht worden /1/. In solchen Experimenten kann nur die verallgemeinerte Zustandsdichte $G(\omega)$ bestimmt werden.

Für ein besseres Verständnis des Zusammenhangs zwischen Gitterdynamik und supraleitenden Eigenschaften dieser Substanzen ist es wünschenswert, Informationen über die amplitudengewichteten Phononenzustandsdichten $F_1(\omega)$ der einzelnen Komponenten zu bekommen.

Wir haben an einem hochauflösenden Spektrometer am R1-Kanal ($\lambda = 1.1426 \text{ \AA}$, maximaler Streuwinkel $2\theta = 146.5^\circ$) die partiellen Debye-Waller-Faktoren von Nb_3Sn bei Raumtemperatur bestimmt.

Nb_3Sn hat eine A15 Struktur und es treten 4 Arten von Reflexen auf. Wir haben ausgemessen:

$$4 \text{ Reflexe mit } S_N = 6 b_{\text{Nb}} e^{-W_{\text{Nb}}} + 2 b_{\text{Sn}} e^{-W_{\text{Sn}}} \quad \text{A)}$$

$$3 \text{ Reflexe mit } S_N = 6 b_{\text{Nb}} e^{-W_{\text{Nb}}} - 2 b_{\text{Sn}} e^{-W_{\text{Sn}}} \quad \text{B)}$$

$$10 \text{ Reflexe mit } S_N = 4 b_{\text{Nb}} e^{-W_{\text{Nb}}} \quad \text{C)}$$

$$15 \text{ Reflexe mit } S_N = 2 b_{\text{Nb}} e^{-W_{\text{Nb}}} + 2 b_{\text{Sn}} e^{-W_{\text{Sn}}} \quad \text{D)}$$

Die Differenz-Reflexe, bei denen $S_N = 2 b_{\text{Nb}} e^{-W_{\text{Nb}}} - 2 b_{\text{Sn}} e^{-W_{\text{Sn}}}$, sind zu schwach, um beobachtet zu werden.

Zusätzlich zu den Nb_3Sn -Reflexen treten Reflexe von freiem Niob $\sim 1.3 \%$ und sehr schwache Reflexe einer anderen Substanz auf, die noch nicht identifiziert werden konnte. Im Bereich großer Winkel $2\theta > 110^\circ$ waren die Meßergebnisse nicht sehr gut reproduzierbar. Der Unterschied betrug maximal 6% . Wir haben keine Korrektur für thermisch-diffuse Streuung durchgeführt.

$$I' = \frac{I \cdot \sin\theta \cdot \sin 2\theta}{N S_N} \quad \text{ist in Abb. 1 logarithmisch dargestellt.}$$

N = Anzahl äquivalenter Netzebenen

Wenn der Unterschied zwischen den Debye-Waller-Koeffizienten von Nb und Sn klein ist, liegen die Punkte auf Geraden.

Für kubische Gitter und bei $T > 0.5 \theta_D$ gibt es einen einfachen Zusammenhang zwischen dem partiellen Debye-Waller-Faktor und der amplitudengewichteten Phononenzustandsdichte.

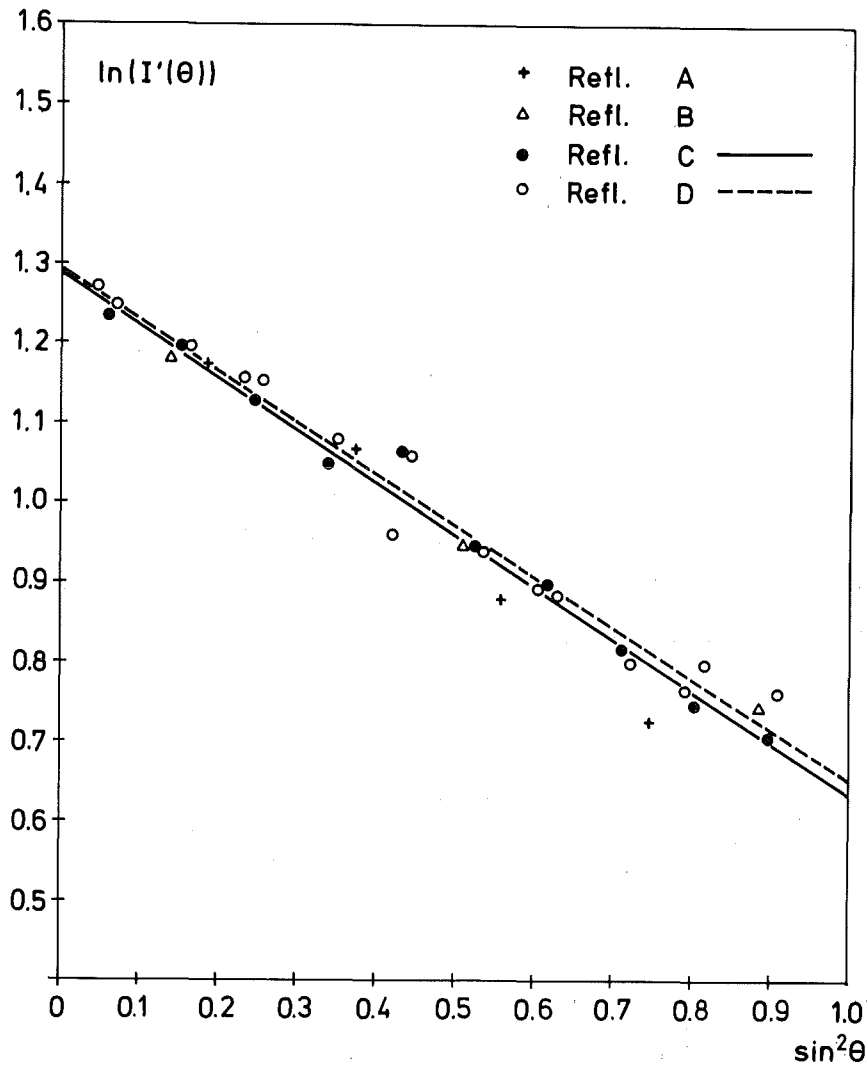


Abb. 1 Bragg Intensitäten von Nb₃Sn

$$W_i(Q) = \frac{\hbar Q^2}{2M} k_B T \left[\langle (\hbar\omega)^{-2} \rangle_i + \frac{1}{12 k_B^2 T^2} - \frac{\langle (\hbar\omega)^2 \rangle}{720 k_B^4 T^4} + \right] \quad (1)$$

$W_i(Q)$ ist proportional zu $\langle (\hbar\omega)^{-2} \rangle_i$. Damit können wir aus $W_i(Q)$ die Debye-Abschneidefrequenzen θ_{-2} der einzelnen amplitudengewichteten Phononenzustandsdichten bestimmen.

$$\theta_{-2,i}^{-2} = \frac{1}{3} \langle (\hbar\omega)^{-2} \rangle_i$$

Wir bekommen:

$$\theta_{-2Nb} = 296 \pm 8 \text{ K}^\circ$$

$$\theta_{-2Sn} = 265 \pm 20 \text{ K}^\circ,$$

Daraus ergibt sich

$$\frac{M_{Nb} \theta_{-2 Nb}^{+2}}{M_{Sn} \theta_{-2 Sn}^{+2}} = 0.976$$

Dieses Ergebnis unterstützt die Folgerungen von Ref. /1/, daß in A15-Verbindungen das Produkt $M_i \langle \omega^2 \rangle_i$ für beide Komponenten annähernd gleich ist. Mit diesen Werten können wir die Debye-Abschneidefrequenzen der verallgemeinerten Phononenzustandsdichte ausrechnen.

$$\theta_{-2 Nb_3 Sn}^2 = \frac{3 \left(\frac{\sigma}{M}\right)_{Nb} \theta_{-2 Nb}^2 + \left(\frac{\sigma}{M}\right)_{Sn} \theta_{-2 Sn}^2}{3 \left(\frac{\sigma}{M}\right)_{Nb} + \left(\frac{\sigma}{M}\right)_{Sn}}$$

Wir bekommen $\theta_{-2 Nb_3 Sn} = 292 \text{ K} \pm 12 \text{ K}$ in guter Übereinstimmung mit dem Wert $\theta_{-2} = 287 \text{ K}$, der direkt aus $G(\omega)$ bestimmt wurde.

REFERENCE

- /1/ B.P. Schweiss, B. Renker, E. Schneider and W. Reichardt, in Superconductivity in d- and f-Band Metals, edited by D.H. Douglass AIP, New York, 189 (1976)

1.11 Investigation of High Field Superconducting Molybdenum Chalcogenides

P. Schweiss, B. Renker, and J.-B. Suck^a

^a*Institute Laue Langevin, F-38042 Grenoble*

Compounds of the series $Y Mo_6X_8$ ($X = S, Se, Te, Y = Pb, Sn, Cu, \dots$) have a rhombohedral structure with units of Mo_6X_8 "molecules" which are stabilized by a nearly cubic lattice of metal atoms Y /1/. For $PbMo_6S_8$ the critical temperatures and critical fields reach up to values of 15 K and 700 kG, respectively /2/.

We have measured the phonon density of states $G(\hbar\omega)$ for $PbMo_6S_8, Mo_6S_8, PbMo_6Se_8, Mo_6Se_8, SnMo_6S_8,$ and $Cu_2Mo_6S_8$. For the latter compound phonon dispersion measurements on a single crystal have been started. Most of the $G(\hbar\omega)$ measurements were performed at 297 K and 5 K.

In view of the different superconducting properties of these compounds our aim was to study vibrational spectra of the individual components by comparison of the different $G(\hbar\omega)$ functions and to search for an anomalous temperature behavior. Indications for a phonon softening on cooling were observed in prior measurements /3, 4/ and were comparable to the temperature effect found in A-15 compounds before /4/.

Our samples were prepared in a furnace at $1050^\circ C$ by direct synthesis of components with exception of Mo_6S_8 which was produced indirectly by dissolving the Ni atoms of $Ni_2Mo_6S_8$ in hydrochloric acid. The transition temperatures were determined for the different compounds in the sequence mentioned above to be ~ 14.6 K, 1.6 K, 3.9 K, 6.5 K, 13 K, 11 K (values below 4 K were taken from literature).

As has been described in detail previously /3, 5/ the $G(\hbar\omega)$ spectra can be divided into two parts. Contributions above 18 meV mainly consist of internal vibrations of the Mo_6X_8 cages whereas the lower part contains the acoustical vibrations, rocking modes of the Mo_6X_8 units and an Einstein like mode attributed to vibrations of the metal atoms in the open "channels". This model which has already been discussed in the preceding Progress Report /5/ is supported by further measurements: The comparison of spectra for $Y Mo_6X_8$

with $X = S$ and Se shows a shift in the highest energy peak approximately of $\sqrt{m_S/m_{Se}}$ whereas the remaining part is mainly unchanged (Fig. 1). From comparison

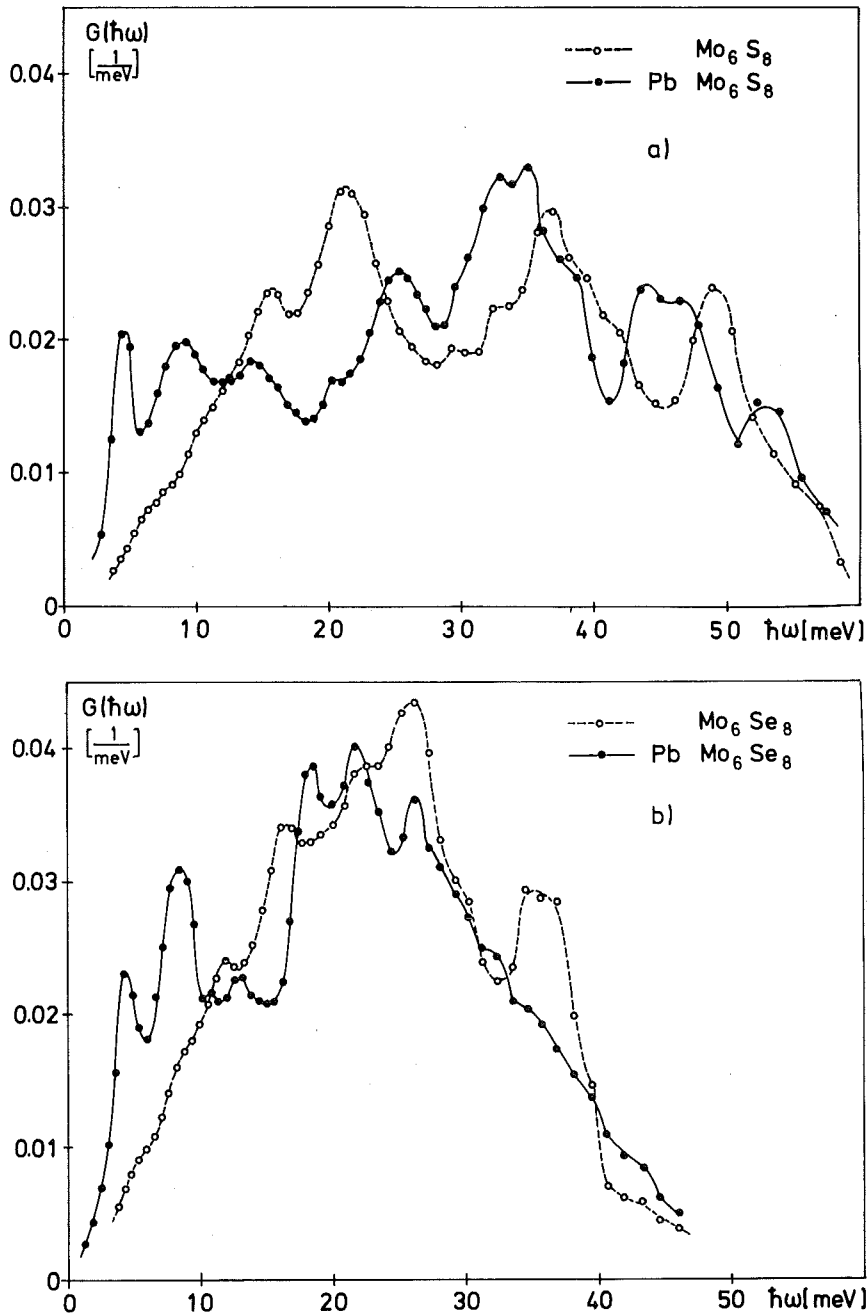


Fig. 1 Comparison of the room temperature generalized phonon density of states $G(\hbar\omega)$ for $PbMo_6S_8$ and Mo_6S_8 (a) and $PbMo_6Se_8$ and Mo_6Se_8 (b) showing a connection between vibrational frequencies and predominant motion of a specific particle: $Pb \leftrightarrow 4.3 \text{ meV}$, acoustical modes + rocking modes of Mo_6X_8 units $\leftrightarrow 9 < \hbar\omega < 18 \text{ meV}$, $Mo \leftrightarrow$ middle of the optical region, S resp. $Se \leftrightarrow$ highest frequency peak. For the low frequency region with $\hbar\omega < 9 \text{ meV}$ which contains predominantly vibrations of the lead atoms a Debye Waller coefficient of about twice the average value had to be assumed in order to give a proper description of the experimental scattering law.

of the spectra of PbMo_6X_8 and Mo_6X_8 the Einstein like mode at about 4 meV is ascribed to a vibration of the metal atom. A shift of the 4 meV excitation is observed by comparing spectra with $Y = \text{Pb}, \text{Sn}, \text{Cu}$. As far as results for the single crystal measurements have been obtained the extrapolated zone boundary frequencies for acoustical branches correspond to the singularities in the phonon density of states in agreement with the simple model.

According to the theory of McMillan high values of T_c correspond to a large electron phonon coupling parameter λ which again is correlated with large values of $G(\hbar\omega)$ at low frequencies. Strong electron phonon coupling can lead to an anomalous temperature behavior of phonon frequencies and may therefore show up in our experiments. Comparing the 5 K and 297 K spectra (Fig. 2) a phonon softening indeed is observed. The increase in the low frequency part of $G(\hbar\omega)$ caused by this mode softening is roughly correlated to the superconducting transition temperature. Mo_6S_8 ($T_c \sim 1$ K) does not show a remarkable effect in contrast to Mo_6Se_8 ($T_c = 6.3$ K), PbMo_6Se_8 ($T_c = 3.9$) and PbMo_6S_8 ($T_c = 14.6$). The bump in the low temperature spectrum of Mo_6Se_8 at about 2 meV showed up in different evaluation procedures and does not seem to be an artefact.

In the data reduction the low frequency region of $G(\hbar\omega)$ with the prominent peak around 4 meV was treated with special accuracy. For energy transfers less than 9 meV the scattering law data from measurements with 5 meV incident neutron energy and high resolution at small energy transfers were included in the data evaluation. It turned out that for compounds with metal atoms in the channels the experimental results at energy transfers less than 9 meV could only be reproduced using a Debye Waller coefficient nearly twice as large as the average value. In agreement with the structural and Mössbauer data, this points to extremely large thermal amplitudes of the metal atom.

An attribution of the mode softening to the movements of certain atoms is difficult in the present analysis. But as Mo_6Se_8 and Mo_6S_8 show a large number of low frequency lattice modes, one has to assume also in the ternary compounds a comparable high density of translational and librational states of the Mo-chalcogenide cages underlying the prominent low frequency peak caused by vibrations of the heavy metal atom. Therefore it is probable that also in the ternary compounds the increase of the phonon density of low frequencies on cooling has its origin predominantly in the softening of cage oscillations. This would also agree with the fact that the conduction

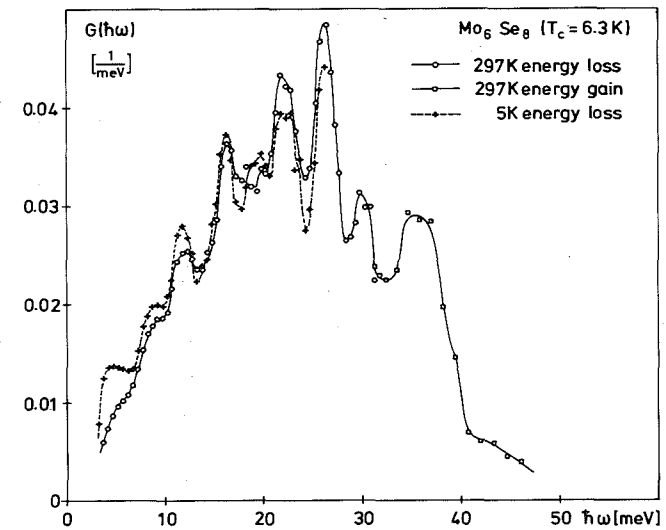
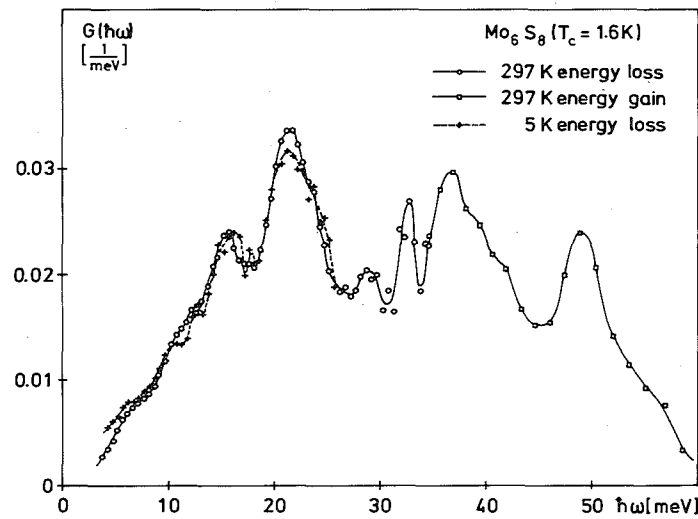
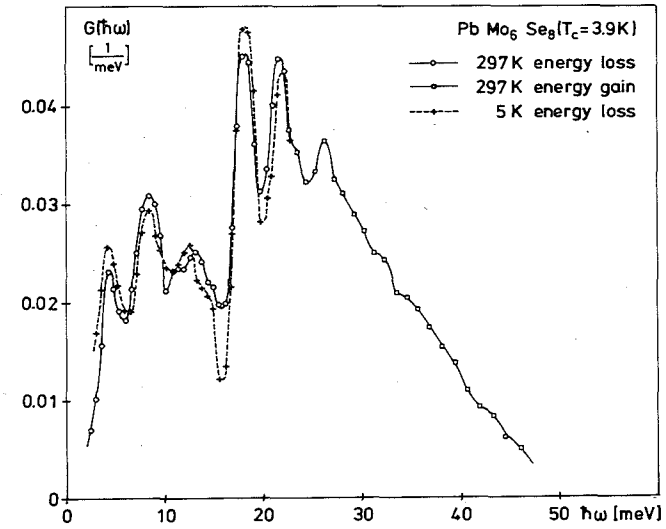
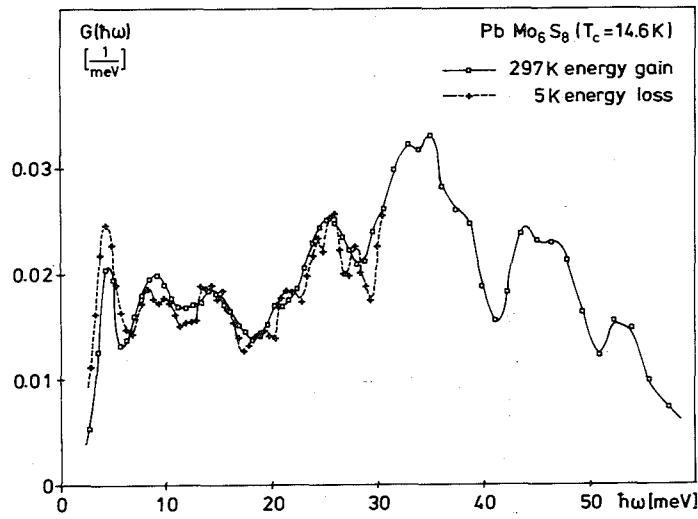


Fig. 2 Comparison of room temperature and 5 K spectra of $G(h\nu)$ for PbMo_6S_8 , PbMo_6Se_8 , Mo_6S_8 , and Mo_6Se_8 showing an anomalous temperature effect qualitatively correlated to the transition temperatures. Results derived by neutron down- and upscattering are shown for room temperature. The low frequency part of the spectrum was treated as described in Fig. 1.

electrons are believed to be predominantly d-like states from Mo. Therefore in extension to the already known fact that a proper Mo-Mo spacing between neighbouring Mo_6X_8 units is essential for the transition temperatures we find evidence for a strong electron phonon coupling. This result can be understood on the basis of bandstructure calculations for PbMo_6S_8 of Anderson, Klose and Nohl /6/ which show that the molecular levels of the Mo_6S_8 units are composed of narrow d-bands near the Fermi surface. Actually the bandstructure may be different for the Se-compounds as considered by Sergent et al. /7/ but according to our investigations all compounds behave similar concerning their lattice dynamics.

Acknowledgement

We like to acknowledge the collaboration with Ø. Fischer and the members of his research group at the Physics Department of Condensed Matter of the University of Geneva. Especially we thank S. Flükiger for supplying a single crystal of $\text{Cu}_2\text{Mo}_6\text{S}_8$.

REFERENCES

- /1/ R. Chevrel, M. Sergent, and J. Prigent, J. Sol. State Chem. 3, 515 (1971)
- /2/ Ø. Fischer, M. Decroux, S. Roth, R. Chevrel, and M. Sergent, J. Phys. C: Sol. State Phys. 8, L474 (1975)
- /3/ S.D. Bader, G.S. Knapp, S.K. Sinha, P. Schweiß, and B. Renker, Phys. Rev. Lett. 37, 6, 344 (1976)
- /4/ P. Schweiß, B. Renker, E. Schneider, and W. Reichardt, 2. Conf. on Superconductivity in d- and f-Band Metals, Rochester, April 30 (1976)
- /5/ P. Schweiß and B. Renker, in Progress Report of the Teilinstitut Nukleare Festkörperphysik, Ges. f. Kernforschung (KFK 2357), 16 (1976)
- /6/ O.K. Anderson, W. Klose, and H. Nohl, to appear in Phys. Rev. (1977)
- /7/ M. Sergent, Ø. Fischer, M. Decroux, C. Perrin, and R. Chevrel, to be published.

1.12 Phonon Density of States of Lanthanum in the fcc and dhcp Phases

N. Nücker

In extension of our investigations on dhcp lanthanum /1/ we determined the phonon density of states of lanthanum in the metastable fcc phase.

The fcc sample was prepared by rf melting of small pieces of lanthanum (99.999 % purity) in a vacuum better than 10^{-5} mbar. In this way about 400 small spheres 2 - 5 mm in diameter were formed. The structure was analysed with a neutron powder diffractometer and yielded 80 % content of fcc-phase.

The phonon densities of states were measured at 4.7 K, 37 K, 140 K and room temperature using the time-of-flight instrument IN4 at the HFR Grenoble. Similar to the results of the dhcp lanthanum the temperature dependence of the phonon density of states was negligible as shown in Fig. 1. Considering the low Debye temperature of fcc lanthanum, i.e. 120 K, a phonon softening with increasing temperature should be expected. The absence of this effect

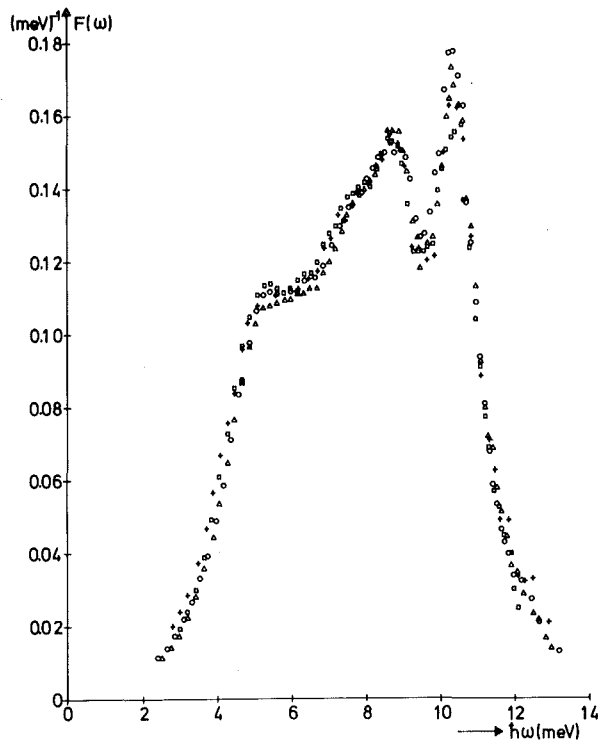


Fig. 1 Phonon density of states of 80 % fcc lanthanum
 □□□ 295 K ΔΔΔ 140 K +++ 37 K
 ooo 4.7 K

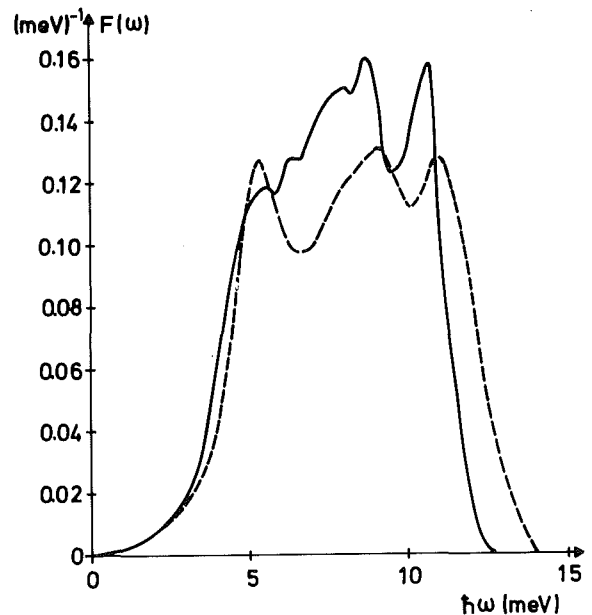


Fig. 2 Phonon density of states of lanthanum (T = 295 K)
 — fcc ---- dhcp

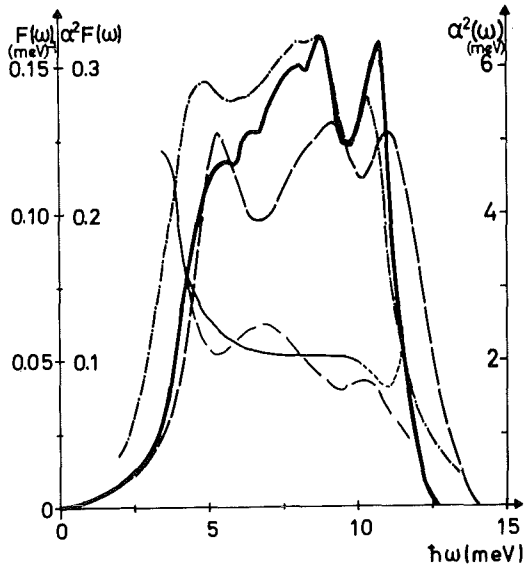


Fig. 3
Phonon density of states $F(\omega)$ of
dhcp (---) and fcc (—) La,
Eliashberg function (—•—) $\alpha^2 F(\omega)$
from Ref. 3
Electron phonon coupling $\alpha^2(\omega)$
(--- and —)

and the negative coefficient of heat expansion below 37 K reported by Andres /2/ may be a hint for a lattice instability.

Using the results of our measurements on 95 % dhcp lanthanum and on 80 % fcc lanthanum the phonon density of states of pure fcc and dhcp lanthanum was calculated. Comparing the density of states in both structures (Fig. 2) it is evident that the average phonon frequency $\langle\omega\rangle$ of lanthanum in the fcc phase is lower than in the dhcp phase. We made a crude check to see whether this difference in $\langle\omega\rangle$ may be responsible for the difference in the superconducting T_c 's by inserting the measured mean phonon frequencies to McMillan's T_c -formula. Assuming the electron-phonon-coupling to be the same in both phases and inserting the $T_c = 4.9$ K value of the dhcp lanthanum we derived a $T_c = 5.7$ K for the fcc phase instead of the measured value 6 K. Thus about 75 % of the difference in the T_c 's may be understood by differences in the phonon spectra.

Comparing our results of $F(\omega)$ with the Eliashberg function $\alpha^2 F(\omega)$ (Fig. 3) determined by tunneling experiment /3,4/ we find best conformity with our results of a mixture containing 55 % dhcp with 45 % fcc lanthanum. Thus we argue that the tunneling diodes prepared by vapor deposition on cooled targets contained a mixture of both phases.

$\alpha^2(\omega)$ is nearly constant in the energy region with main intensities in phonon frequency distribution. At lower energies an increase in $\alpha^2(\omega)$ is observed.

REFERENCES

- /1/ N. Nücker, in Progress Report of the Teilinstitut Nukleare Festkörperphysik, Ges. f. Kernforschung Karlsruhe (KFK 2357), p. 23 (1976)
- /2/ K. Andres, Phys. Rev. 168, 708 (1968)
- /3/ L.F. Lou and W.J. Tomasch, Phys. Rev. Lett. 29, 858 (1972)
- /4/ H. Wühl, A. Eichler, and J. Wittig, Phys. Rev. Lett. 31, 1393 (1973)

1.13 Comparison of Phonon Densities of States $F(\hbar\omega)$ and Tunneling Densities of States $\alpha^2(\hbar\omega) \cdot F(\hbar\omega)$ for Niobium

F. Gompf

The dispersion relations of the superconducting transition metal niobium have been measured in symmetry directions by Nakagawa et al. /1/. They analyzed their data on the basis of the Born-von-Kármán theory including interaction forces out to the eighth neighbor in order to fit the unusual features of the phonon dispersions. Using the interpolation formalism they deduced the phonon density of states.

We have directly determined the frequency distribution for niobium with good resolution using TOF I with an incident energy of 37.15 meV.

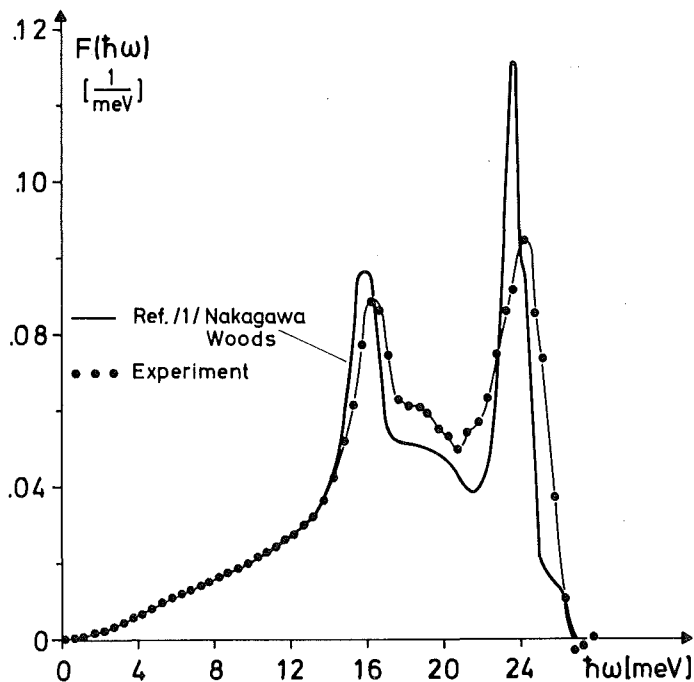


Fig. 1 Comparison of the directly determined phonon density of states for niobium with the model calculation of ref. /1/.

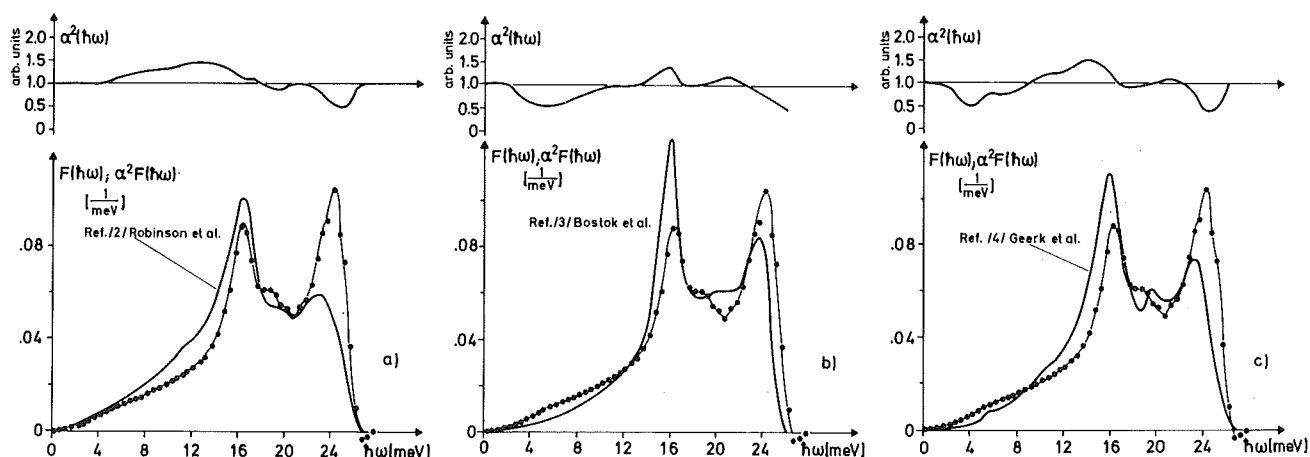


Fig. 2 Comparison of the phonon density of states for niobium with tunneling data.

a) Ref. /2/, $\lambda = .81$, $\mu^* = .051$, $\Delta_0 = 1.46$ meV, $T_c = 10.1$ K

b) Ref. /3/, $\lambda = .58$, $\mu^* = -.05$, $\Delta_0 = 1.56$ meV, $T_c = 9.2$ K

c) Ref. /4/, $\lambda = .58$, $\mu^* = -.02$, $\Delta_0 = 1.54$ meV, $T_c = 9.5$ K.

Both results are compared in Fig. 1. Except for the peaks around 16 and 24 meV which differ by about 0.5 meV the agreement is rather good considering the inadequacy of the Born-von-Kármán model to give a perfect fit to the data of /1/. Up to 15 meV both results are identical. This also underlines their findings that for niobium at small frequencies there exists an unusual deviation from the Debye spectrum.

In order to get some information on the electron-phonon coupling function $\alpha^2(\hbar\omega)$, the tunneling densities of states $\alpha^2(\hbar\omega) \cdot F(\hbar\omega)$ from Ref. /2/, /3/, and /4/ are compared with $F(\hbar\omega)$ in Fig. 2, a), b), and c) respectively. In this representation the Eliashberg functions $\alpha^2(\hbar\omega) \cdot F(\hbar\omega)$ and $F(\hbar\omega)$ were normalized to unity. Whilst the overall shape and the positions of the peaks in the tunneling data agree with the neutron data (especially Ref. /3/ and /4/) all three lack intensity for the longitudinal peak. Ref. /3/ states that this disagreement is the main reason that the microscopic parameters λ and μ^* differ so strongly from the values predicted by the strong coupling theory of superconductivity. In fact best agreement for α^2F with F was found for a negative $\mu^* \sim -.05$ and $\lambda \sim .58$ in comparison with the theoretical expectations of $\mu^* = +.13$ and $\lambda = .82$. The data from Ref. /2/ seem to verify this: a positive $\mu^* \approx +.051$ and a high value for $\lambda = .81$ lead to a worse agreement with the phonon density of states. For a more detailed

representation and explanation of the Eliashberg function in Fig. 2c see Ref. /4/ in this report.

The frequency dependence of the electron-phonon coupling function $\alpha^2(\omega)$ cannot accurately be determined, as long as the tunneling data differ amongst each other as they do. If the longitudinal peak gains intensity as tunneling techniques improve, only a small shift in the energy scale is necessary to get a rather constant $\alpha^2(\omega)$.

REFERENCES

- /1/ Y. Nakagawa and A.D.B. Woods, Phys. Rev. Lett. 11, 271 (1963)
- /2/ B. Robinson, R.H. Geballe, and J.M. Rowell, Superconductivity in d- and f-Band Metals, Proceedings of the Second Rochester Conference, Plenum Press, N.Y. (1976), p. 381
- /3/ J. Bostock, K.H. Lo, W.N. Cheung, V. Diadiak, and M.L.A. MacVicar, Superconductivity in d- and f-Band Metals, Proceedings of the Second Rochester Conference, Plenum Press, N.Y. (1976), p. 381
- /4/ J. Geerk and K. Gärtner, this report, p. 100

1.14 Investigations of the Polymeric Metal. (SN)_x

Part I: Lattice Dynamics

*L. Pintschovius, H. Wendel^a, H.J. Stolz^b, A. Otto^b, H. Kahlert^c,
and R. Currat^d*

^a*Xerox Research Center, Palo, Alto, U.S.A.*

^b*Max-Planck-Institut für Festkörperforschung, Stuttgart*

^c*Ludwig-Boltzmann-Institut für Festkörperforschung, Vienna, Austria*

^d*Institut Laue Langevin, Grenoble, France*

The results of our Raman and IR studies and of the first inelastic neutron scattering experiments on (SN)_x have been collected in the following publication:

Acoustic and Optical Phonons in $(\text{SN})_x$

H.J. Stolz, H. Wendel, A. Otto, L. Pintschovius, and H. Kahlert,
Phys. Stat. Sol. (b) 78, 277 (1976)

Abstract

Measurements are made of both polarized and unpolarized Raman spectra and IR reflection and transmission spectra of epitaxial films of polysulfur nitride $(\text{SN})_x$ on mylar substrates as well as of single crystals. The dispersion of acoustic phonons of $(\text{SN})_x$ is measured for small wave vectors parallel and in two directions perpendicular to the chain axis by means of inelastic neutron scattering. Force constants are estimated from a simple model.

The inelastic neutron scattering investigations have been continued at the ILL Grenoble. The LA-branch in chain direction and a low lying optic mode have been measured up to the zone boundary. The first results suggested the occurrence of a pronounced anomaly in the LA-branch in the vicinity of the zone boundary (see Fig. 1). However, later investigations at other reciprocal lattice points indicated that the observed intensity distribution was presumably caused by a crossing of several branches (Fig. 2). This interpretation is backed by preliminary results of a calculation based on a valence force model.

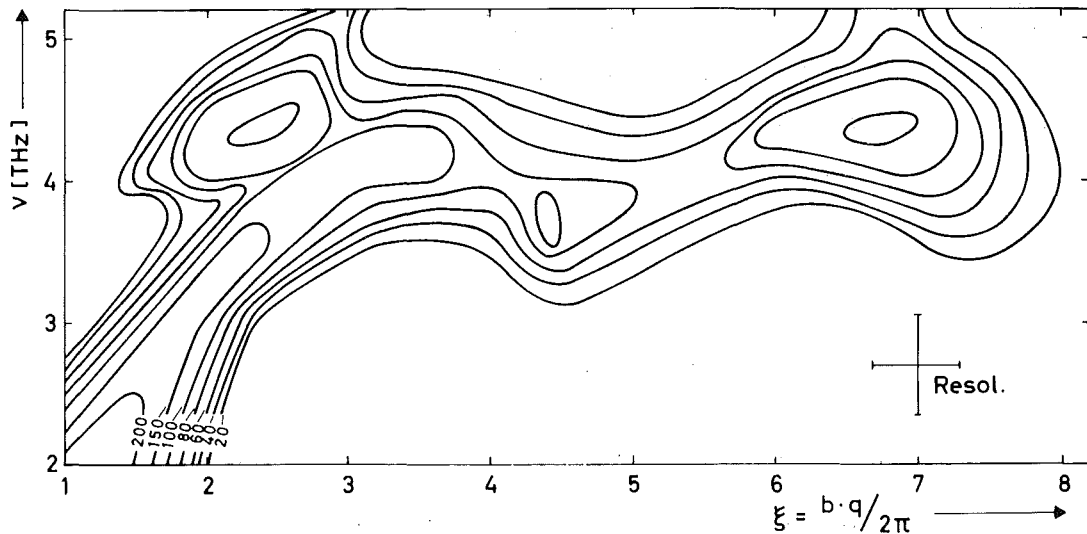


Fig. 1 Intensity contours of longitudinal phonons in chain direction, measured at reciprocal lattice points $(1 \ 3 + \xi \ 0)$. Background and incoherent scattering have been subtracted.

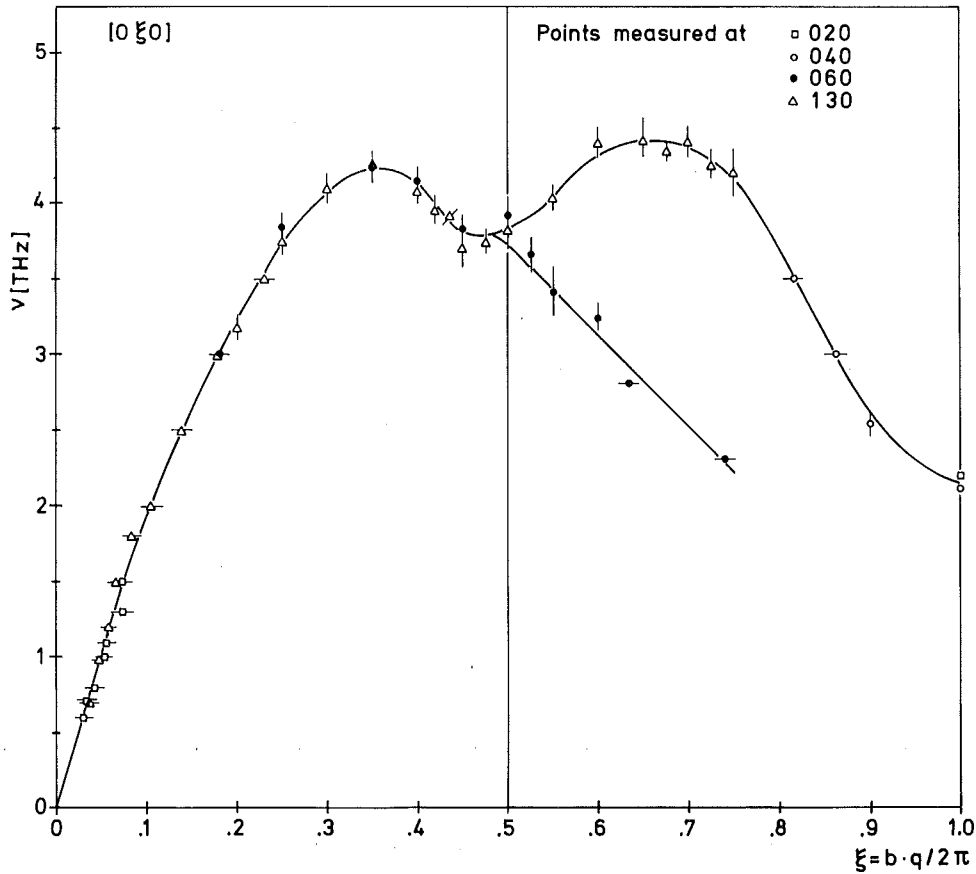


Fig. 2 Dispersion relation of longitudinal phonons traveling in chain direction (extended zone scheme). The different symbols refer to measurements at different reciprocal lattice points.

Due to the loss of our sample the investigations have not yet been completed. Meanwhile we were able to grow several crystals with volumes between 20 and 50 mm³. Co-alignment of 14 crystals will yield a sample about twice as large as the first one (12 crystals with a total volume of 0.2 cm³). Using this sample we will extend our investigations to low temperatures in June 1977 at the ILL Grenoble.

Part II : Optical Studies of the Electronic Transport Properties

H.P. Geserich^a, W. Möller^b, G. Scheiber^a, and L. Pintschovius

^aInstitut für Angewandte Physik der Universität Karlsruhe

^bInstitut für Didaktik der Physik der Universität Karlsruhe

Our investigations of the optical reflectance in (SN)_x single crystals have been continued. The results are reported in the following publication:

Optical Investigation of the Electrical Anisotropy of $(\text{SN})_x$ Single Crystals

H.P. Geserich, W. Möller, G. Scheiber, and L. Pintschovius

Phys. Stat. Sol. (b) 80, 119 (1977)

Abstract

Polarized reflectance spectra of $(\text{SN})_x$ single crystals are investigated in the range from 0.15 to 4 eV. For light polarized parallel to the polymeric chains the Drude behaviour found previously is confirmed. The optical properties perpendicular to the chains, however, are explained by a modified Maxwell-Garnett model. This model takes into account the fibrous structure of $(\text{SN})_x$ crystals and allows to separate the intrinsic and extrinsic transverse transport properties.

Part III : Neutron Diffraction Study of the Crystal Structure of $(\text{SN})_x$

G. Heger, S. Klein^a, L. Pintschovius, and H. Kahlert^b

^aSonderforschungsbereich 127, Fachbereich Geowissenschaften der Universität Marburg

^bLudwig-Boltzmann Institut für Festkörperphysik, Vienna, Austria

The analysis of the data of our neutron diffraction study has been completed. The results are published in a paper the abstract of which is given below:

Determination of the Crystal Structure of $(\text{SN})_x$ by Neutron Diffraction

G. Heger, S. Klein, L. Pintschovius, and H. Kahlert

to be published in Journal of Sol. State Chem.

Abstract

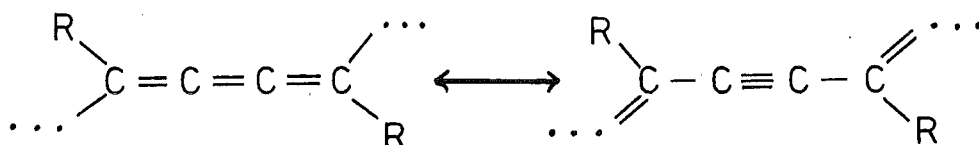
The structure of the $(\text{SN})_x$ polymer metal has been redetermined at room temperature by using neutron diffraction on single crystals. It is characterized by endless strands of N and S atoms with equal intrachain distances of $d(\text{S-N})_{\text{intra}} = 1.585 \text{ \AA}$. The interchain bond angles at S and N atoms are 107.0° and 120.3° , respectively. The shortest interchain distances, $(d(\text{S-N})_{\text{inter}} = 3.26 \text{ \AA}$, $d(\text{N-N})_{\text{inter}} = 3.34 \text{ \AA}$ and $d(\text{S-S})_{\text{inter}} = 3.47 \text{ \AA}$), are in the range of the sum of the van der Waals radii. Besides the N and S sites of the ordinary strands additional defect sites were found.

1.15 Inelastic Neutron Scattering from Diacetylene Polymers

B. Renker, P. Schweiß, and G. Wegner^a

^aInstitut für Makromolekulare Chemie, Universität Freiburg

Diacetylene polymers are linear chain compounds which are obtained by solid state polymerisation and whereof large and perfect single crystals have been grown /1/. The polymer backbone exists in two resonance forms



whereby the latter one is largely preferred. Conductivity measurements show an anisotropy $\sigma_{||}/\sigma_{\perp} \geq 10^3$. Since the electronic gap is about 2 eV these compounds have only a low dark conductivity $\sigma \sim 10^{-13} \Omega^{-1} \text{ cm}^{-1}$. The mechanism of solid state polymerisation as well as the outlook that a new class of linear conductors may be obtained by an oxidation or reduction process make these compounds attractive for detailed investigations.

For first investigations the phonon density of states $G(\hbar\omega)$ was measured for the monomer and polymer forms of $\text{C}_{20}\text{H}_{18}\text{O}_6\text{S}_2$. Phonon measurements on a single crystal of the polymer proved to be extremely difficult for the non deuterated compound and therefore the present results are limited to some few acoustical phonons.

In general the vibrational spectrum of the compound is rather complex. The aim of our experiments was to obtain information of the interesting modes by a comparison of spectra for the monomer and polymer compound. For the monomer, rocking modes of the whole molecule within the plane of the main chains are of interest since the corresponding elongations may be important for the onset of polymerisation. For the polymer, modes which involve elongations of backbone atoms are of interest since primarily these modes might be influenced by the one-dimensional electronic structure of the compound.

Fig. 1 shows first results for $G(\hbar\omega)$ for the monomer and polymer compound. All conditions for the experiment and the data reduction were exactly the same in both cases thus any difference reflects the different morphology of

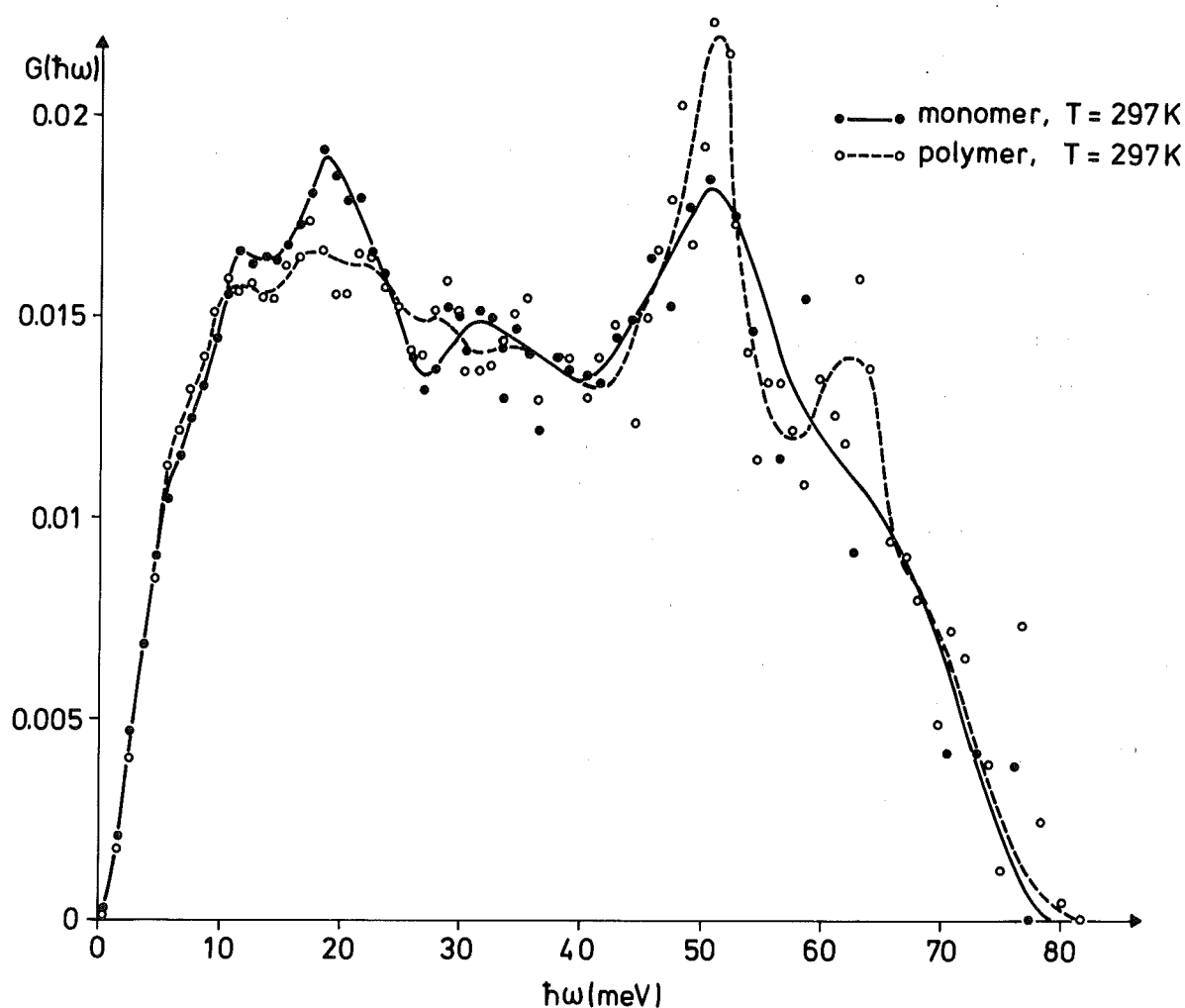


Fig. 1 Comparison of the generalized phonon density of states for the linear chain compound polydiacetylene ($C_{20}H_{18}O_6S_2$)_n and its monomer

the samples. Generally both spectra show little structure which we attribute to the dominant number of side chain modes which additionally get more weight by the large nuclear cross-section of hydrogen. The $G(\hbar\omega)$ spectrum for the monomer shows a higher weight and a more pronounced structure in the region between 10 and 20 meV. Additional excitations in this frequency region might be caused by rocking modes of the monomer molecules as discussed before. A connection of these excitations with the process of polymerisation appears possible since it is well known that polymerisation starts already at room temperature ($300\text{ K} \approx 25\text{ meV}$).

Remarkably both spectra show a close agreement in the higher frequency region where two maxima at 50.5 and about 63 meV are more pronounced for the polymer. Due to the experimental technique (time-of-flight measurements and neutron upscattering) the experimental error increases with increasing energy transfer. Any specific modes which correspond to transverse and longitudinal excitations of the main backbone chain do not show up in the polymer spectrum. Possibly a weak line which appears at about 65 meV in the Raman spectrum /2/ and which involves small displacements of backbone atoms caused by side group normal modes corresponds to the shoulder at about 63 meV.

Better results in view of the questions discussed before appear possible if deuterated compounds are available.

REFERENCES

- /1/ D. Kobelt and E.F. Paulus, *Acta Cryst.* B30, 232 (1974)
/2/ D. Bloor, F.H. Preston, D.J. Ando, and D.N. Batchelder, Department of Physics, Queen Mary College, Mile End Rd., London E1 4NS, to be published

1.16 The Phonon Densities of States of Trigonal and Vitreous Selenium

F. Gompf

The structure of trigonal Se consists of covalently bonded helical chains which wind around the triad screw axis of the crystal. The helices contain three atoms per turn which form the unit cell. Selenium may be considered to be molecular in character, with molecules of infinite chains. The closest distance between atoms in adjacent chains is 3.46 \AA as compared to the intra-chain length of 2.32 \AA (3.69 \AA to the second neighbor).

The structure of amorphous Se is lattice-like and as H. Richter reports in /1/ exists in 3 forms Se(I), Se(II) and Se(III) depending on various ways of preparation. We have investigated Se(II) (vitreous Se) which exists in the form of plane zigzag chains. For Se(II) the distance between atoms

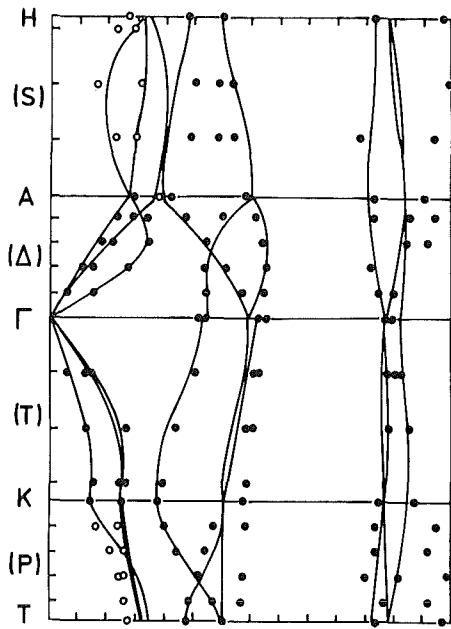


Fig. 1 Comparison of the phonon density of states for trigonal selenium with the experimentally determined dispersion relations and a shell model calculation of Teuchert /4/.

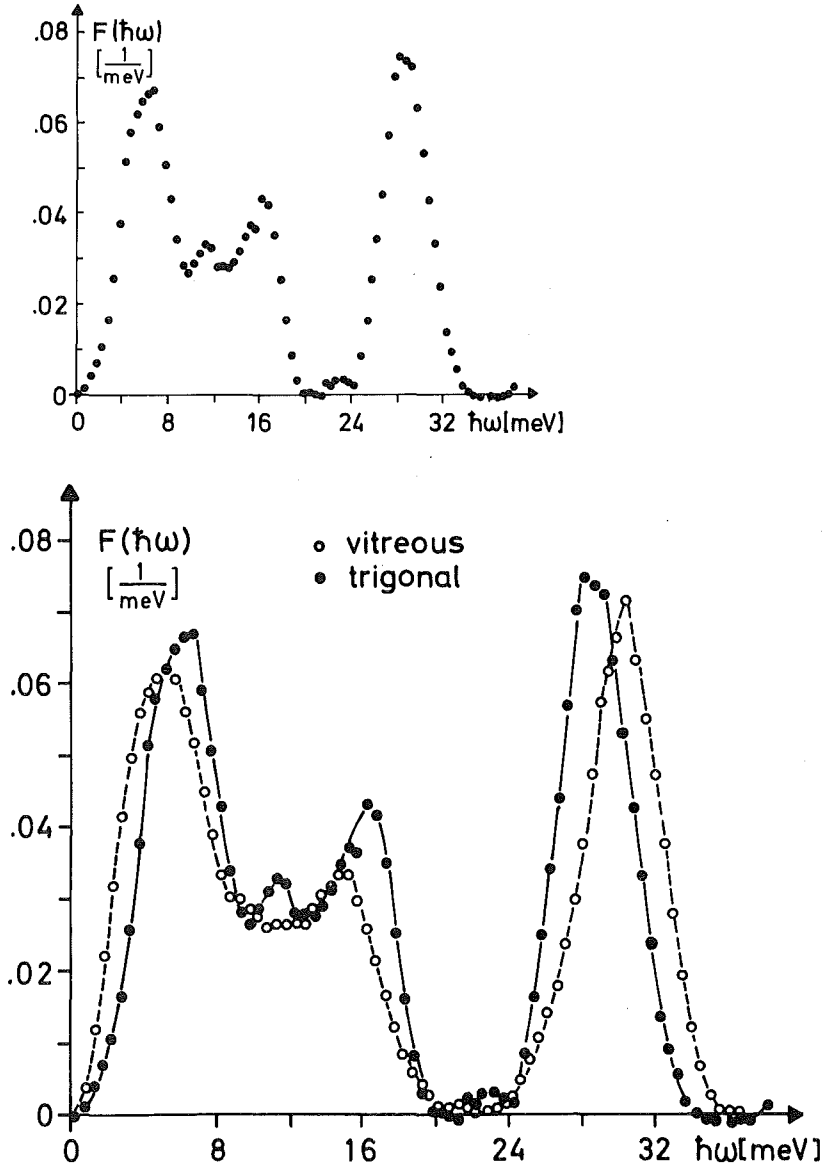


Fig. 2 Comparison of the phonon density of states for trigonal selenium with that of vitreous selenium.

in adjacent chains increases to 3.86 Å while the intrachain distances remain the same. This modification can be prepared by heating crystalline Se up to 450°C and quenching it in ice-water. In order to check for remaining Se₈-rings one can use the method of Popov /2/ who showed that CH₂J₂ dissolves the monomeric ring-shaped molecules only. Our starting material was purchased from Kochlight (99.9997 purity). The structure of both modifications was checked with X-ray diffraction as well as with neutron diffraction.

With the help of inelastic neutron scattering at TOF II with an incident neutron energy of 5.0 meV we have determined their phonon densities of states $F(\hbar\omega)$. This seemed of interest since:

- a) For trigonal Se the phonon dispersion relations have been measured /3/, /4/ but no physically meaningful model has yet been able to give a good fit to those data and subsequently $F(\hbar\omega)$ has not been calculated.
- b) Comparing $F(\hbar\omega)$ of both modifications should help to interpret and understand the vibrations in vitreous Se.
- c) The increase of the interchain distance and the plane largely enmeshed zigzag chains of the vitreous state make Se(II) a suitable candidate to test models which have been developed for isolated chains in high polymers.

In Fig. 1 we show the phonon density of states of trigonal Se. The measurement has partially been corrected for resolution. The strongly structured spectrum agrees well with the measured dispersion relations of Teuchert /4/. In Fig. 2 we compare the $F(\hbar\omega)$ for both modifications. At first sight the similarity seems striking considering that we are going from the crystalline to the vitreous state. A closer look however reveals that in some details these two modifications are quite different. In Fig. 3a we give a more detailed view of the lower acoustic part of $F(\hbar\omega)$ where each dot represents a truly measured point.

Stockmayer and Hecht /5/ developed a model with a monoatomic tetragonal lattice for chain polymeric crystals in which the masses within the linear chain are bound by strong valence forces and the interchain forces are of a weak van der Waals type. Such assumptions lead to two typical types of modes:

- a) stretching modes where the chain members are elongated in the direction of the chain axis and
- b) bending modes where the chain members are elongated perpendicular to the chain axis.

The stretching modes show a "normal" behaviour by means of their phonon dispersion relations (see Bauer /6/). The bending modes however display the $\omega \sim |\vec{k}|$ behaviour for very small ω 's only and then curve in a convex manner in relation to the $|\vec{k}|$ -axis for $|\vec{k}| \leq K_{BZ}/2$ which gives rise to strong intensity contributions for this ω -region. The curvature depends on the relation of the elastic constants κ/α (κ = stiffness of the valence angles, α = strength of binding between interchain next neighbors) and the relation of the distances c/a (c = intrachain n.n. distance, a = interchain n.n. distance) and will be largest for polymers with isolated chains. According to this behaviour /5/ and later in a more sophisticated approach Genensky and Newell /7/ show that for strongly uncoupled chains the frequency range over which $F(\hbar\omega) \sim \omega^2$ holds is unusually short, followed by a range where $F(\hbar\omega)$ is proportional to $\omega^{3/2}$. In the model of /5/ this dependence extends from about 5 % to 13 % of ω_{\max} the cutoff frequency of the spectrum.

Kirkwood /8/ has shown that going from linear chains to zigzag chains additionally introduces optical modes and torsional modes but this does not principally alter the statements of /5/ for the lower acoustic part of the spectrum.

As seen in Fig. 3b for trigonal Se the ω^2 -dependence seems to go up to 3 meV only. Then going towards the first peak in $F(\hbar\omega)$ the power of ω increases and $F(\hbar\omega)$ remains approximately proportional to $\omega^{2.7}$ between 3 and 4.5 meV. For vitreous Se however this lower acoustic part of the spectrum

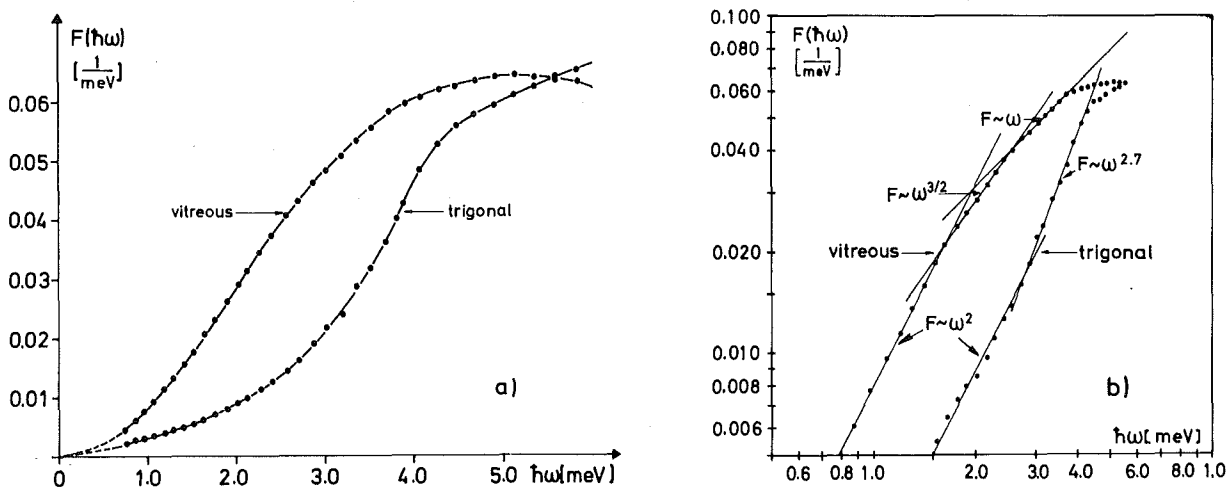


Fig. 3a and 3b Enlarged view of the lower acoustic part of the selenium spectra

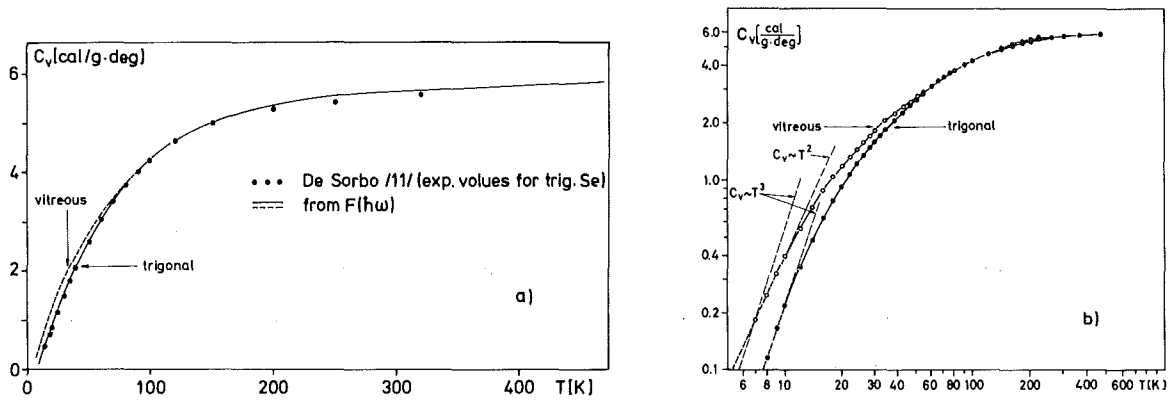


Fig. 4a and 4b The specific heat c_v for both modifications of selenium as deduced from their phonon densities of states

differs strikingly and can be divided into three parts: a) a rather small range (only up to 1.6 meV) where $F(\hbar\omega) \sim \omega^2$ holds. b) From 1.6 meV to 2.7 meV where $F(\hbar\omega)$ is proportional to $\omega^{3/2}$. c) From 2.7 to about 4 meV where $F(\hbar\omega)$ seems to display a linear proportionality to ω . a) and b) are in good accordance with the theoretical predictions of /5/ and /7/. $F(\hbar\omega) \sim \omega$ can be interpreted with the model of Weik and Tsobanis /9/ who have proposed such a law for the lower frequencies of the polyethylene spectrum, stating that the overwhelming part of lattice vibrations in polyethylene are elongations perpendicular to the chain axis, giving these bending modes a two dimensional character within an isolated zigzag chain.

As seen in Fig. 2 around 12 and 16 meV, where strong contributions to $F(\hbar\omega)$ for trigonal Se seem to be caused by torsional modes (see Fig. 1 and /4/), a pronounced decrease of intensity can be registered for the vitreous modification. This could be explained with Kirkwood's /8/ model for high polymers with zigzag chains who shows that for a three dimensional polymer there exists a low (close to the gap) and flat optical torsional mode which comes down and degenerates into an acoustic mode ($\omega \rightarrow 0$, $|\vec{k}| \rightarrow 0$) for the isolated zigzag chain.

Newell /10/ and /7/ show that for stretching modes $F'(\hbar\omega)$ tries to become infinite for ω_{\max} as one-dimensionality is approached. If higher dimensionality exists for polymeric chains the high frequency end of the spectrum becomes finite and the center of the broadend peak is moved towards smaller frequencies. This trend can be seen in Fig. 2 where the high well separated optical modes of

Se(II) lie about 2 meV higher than those of trigonal Se, which again demonstrates the decrease of dimensionality of the vitreous modification.

The specific heat c_v which can be deduced from the phonon spectra is shown as a function of temperature in Fig.4a and compared with the experimental points of DeSorbo /10/ for trigonal Se. In Fig. 4b c_v versus T is shown in a log-log-scale. For trigonal Se the Debye law $c_v \sim T^3$ is only valid up to 10 K. Down to 7 K such a proportionality could not be found for the vitreous modification, however we do see, that up to 10 K $c_v \sim T^2$ holds. This again is in good accordance with the model of /5/ who show that adherence of the heat capacity to a T^2 law does not necessarily imply a layer lattice structure but over a short range of low temperatures should also exist for high polymeric chains.

REFERENCES

- /1/ H. Richter, J. Non-Crystalline Solids 8 - 10, 388 (1972)
- /2/ A.J. Popov, J. Phys. C: Solid State Phys. 9, 675 (1976)
- /3/ W.C. Hamilton, B. Lassier, and M.J. May, J. Phys. Chem. Solids 35, 1089 (1974)
- /4/ W. Teuchert, Phonons in Trigonal Selenium, Dissertation, University of Würzburg (1975)
- /5/ W.H. Stockmayer and C.E. Hecht, J. Chem. Phys. 21, 1954 (1953)
- /6/ H. Bauer, Kolloid-Z. und Z. Polymere 250, 1000 (1972)
- /7/ S.M. Genensky and G.F. Newell, J. Chem. Phys. 26, 486 (1965)
- /8/ J.G. Kirkwood, J. Chem. Phys. 7, 506 (1939)
- /9/ D. Weik and D. Tsobanis, Kolloid-Z. und Z. Polymere 247, 774 (1971)
- /10/ W. DeSorbo, J. Chem. Phys. 21, 1144 (1953)

1.17 The Frequency Distribution of KCN and NaCN from Inelastic Neutron Scattering of Powders

N. Nücker, J. Daubert^a, H. Jex^b, K. Knorr^c, M. Müllner^b, and J.-B. Suck^d

^aTU München, Reaktorstation, 8046 Garching

^bIKF der J.W. Goethe Universität, 6000 Frankfurt am Main

^cJ. Gutenberg Universität, 6500 Mainz

^dInstitut Laue Langevin, F-38042 Grenoble, France

In KCN and NaCN a determination of the complete phonon dispersion relation applying inelastic neutron scattering from single crystals turned out to be very difficult [1,2]. At room temperature one phonon signals with energies above about 15 meV could not be well resolved due to large anharmonicity and phonon-libron interaction. Cooling of the crystals is not possible because of their destructive phase transitions.

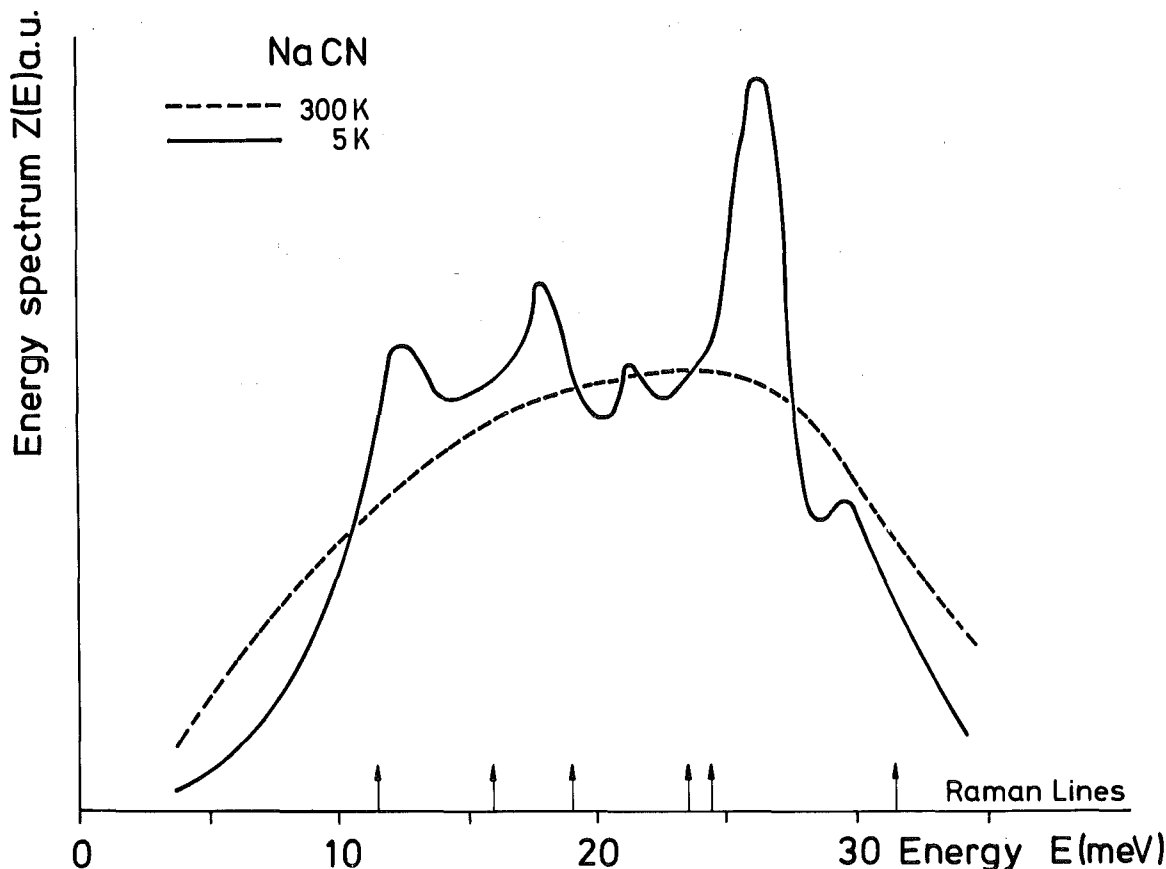


Fig. 1 Phonon density of states of NaCN at 5 K and 300 K

Therefore we determined the density of states using inelastic neutron scattering with time-of-flight technique from powdered samples. The measurements at different temperatures (KCN $T = 5, 50, 77, 95, 145, 180, 295$ K and NaCN $T = 5, 100, 140, 200, 295$ K) were performed on IN4/HFR Grenoble and on TOF2/FR2 Karlsruhe. The available data cover all three phases of the crystals; the energy ranges up to 40 meV. Fig. 1 presents the data from NaCN at two temperatures. At room temperature the spectrum is almost smeared out while the low temperature data at 5 K show well resolved peaks coinciding with the Raman data by Dultz /3/. Considering all our data and comparing with theoretical calculations we conclude that the two phase transitions have little effect on the spectrum. The dominant effect is anharmonicity which is due to the large amplitudes of the librational motion of the CN-molecules and - in the higher temperature phases - due to the statistical orientation of the molecules.

REFERENCES

- /1/ J. Daubert, K. Knorr, W. Dultz, H. Jex, and R. Currat, J. Phys. C9, L389 (1976)
- /2/ J.M. Rowe, J.J. Rush, N. Vagelatos, D.L. Price, D.G. Hinks, and S. Susman, J. Chem. Phys. 62, 4551 (1975)
- /3/ W. Dultz, Habilitationsschrift, Universität Regensburg (1976)

1.18 Structure Factor of Expanded Liquid Rubidium up to 1400 K and 200 bar

R. Block, J.-B. Suck^a, W. Freyland^b, F. Hensel^b, and W. Gläser^c

^aInstitut Laue Langevin, F-38042 Grenoble, France

^bInstitut für Physikalische Chemie der Universität Mainz

^cPhysik Department der Technischen Universität München

Inst. Phys. Conf. Ser. Nr. 30, Chapter 1, Part 1 (1977), p. 126

Abstract

The structure factor of liquid rubidium has been measured for densities between 1.42 and 0.98 g cm⁻³ and temperatures up to 1400 K in a region of momentum transfer between 0.2 and 2.5 Å⁻¹. The first maximum of the structure

factor is shifted to lower momentum transfers and broadened with decreasing densities. The comparison of the results with a hard-core model shows that a temperature-dependent hard-core radius is needed to fit the data. Using the measured structure factors the conductivity of the liquid was calculated within the NFE model. The results agree satisfactorily with those of a recent measurement.

2. ELECTRONIC STRUCTURE AND MAGNETISM OF SOLIDS

2.1 Local Susceptibilities in Dilute PdNi Alloys

J. Fink, G. Czjzek, H. Schmidt, K. Tomala^a, and F.E. Obenshain^b

^a*Guest scientist from Jagiellonian University, Cracow, Poland, under IAEA-fellowship*

^b*Oak Ridge National Laboratory, Oak Ridge, Tenn. 37830, U.S.A.*

The properties associated with local spin fluctuations in nearly magnetic dilute alloys and their variation with the approach to the magnetically ordered state have found considerable interest. The Pd-Ni system, in particular, has been studied extensively by measurements of bulk properties such as magnetic susceptibility and electrical resistivity. Complementary information on local properties of the nearly magnetic centers as for example Ni in PdNi alloys which may be derived from measurements of hyperfine interactions is important for testing theoretical models proposed for these alloys.

We have investigated the local susceptibility of Ni atoms in dilute PdNi alloys in the concentration range 0.5 to 3 at % by measurements of the magnetic hyperfine fields at ⁶¹Ni nuclei in external magnetic fields up to 50 kOe and in the temperature range from 1.1 to 140 K. In addition, we have measured the bulk susceptibility of the absorber samples in the same temperature range and in magnetic fields up to 60 kOe by Faraday's method.

For all concentrations the individual lines of the hyperfine spectrum are broadened due to a distribution of hyperfine fields. The width of the distribution increases with increasing nickel concentration. For $c_{Ni} \gtrsim 1$ at % the observed spectra are well described by a superposition of two components for which the hyperfine fields differ strongly. For $c_{Ni} = 1$ to 1.5 at % the relative intensities of the two components correspond to the concentration of isolated Ni atoms and of Ni pairs respectively. For given external field H_{ext} the ratio of the hyperfine field and thus of the local susceptibility

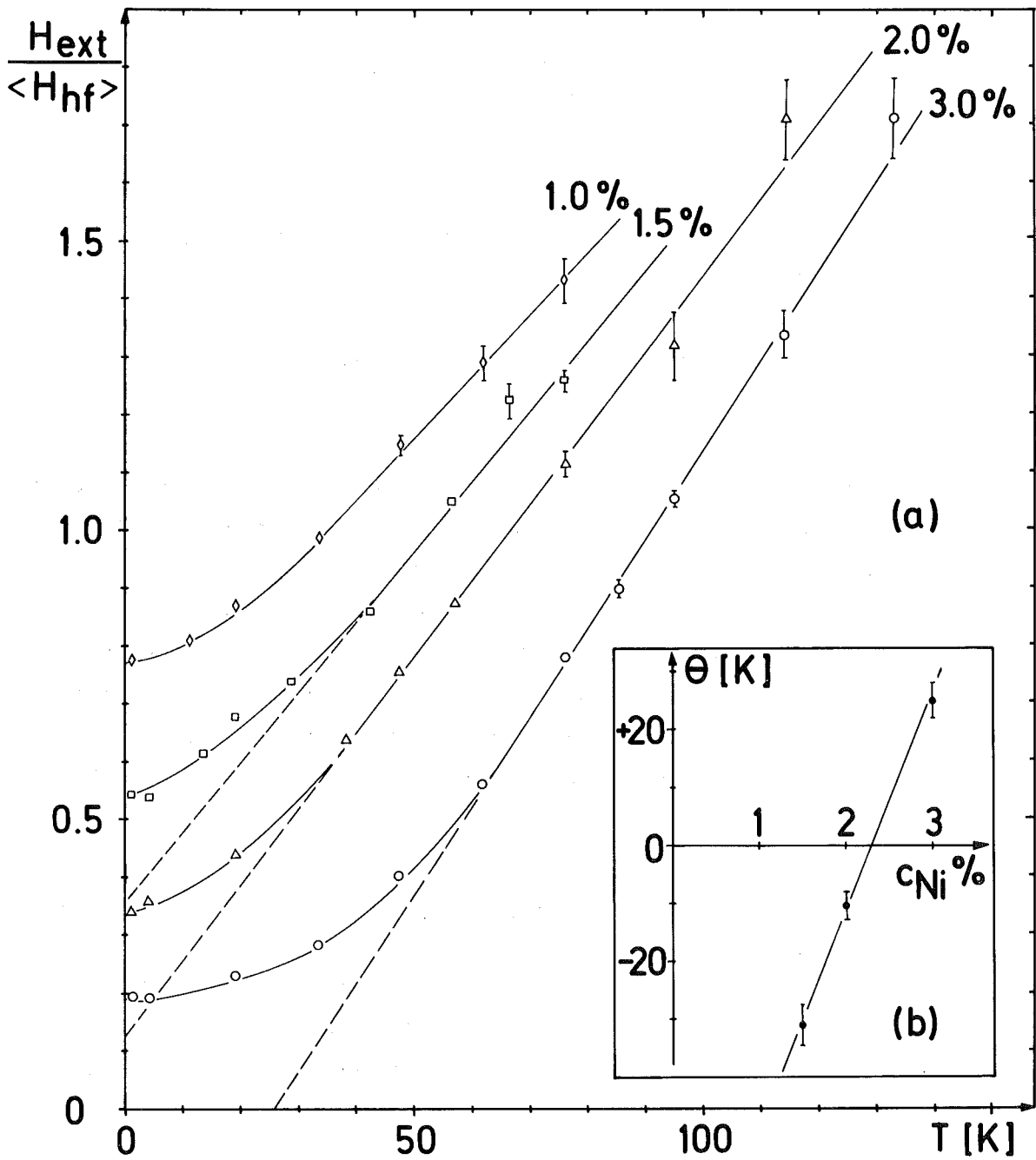


Fig. 1 (a) Temperature dependence of $\chi_{Ni,loc}^{-1} = H_{ext} / \langle H_{hf} \rangle$ for $H_{ext} = 20$ kOe of dilute PdNi alloys with $c_{Ni} = 1, 1.5, 2,$ and 3 at %.

(b) Concentration dependence of the Curie-Weiss temperature θ derived from the high-temperature slopes of the curves shown in Fig. 1a.

of paired to that of isolated Ni atoms is 1.8. At low temperatures ($T \lesssim 50$ K) the variation of the hyperfine field of both components with temperature and with H_{ext} does not show the behaviour characteristic for local magnetic moments.

As in bulk measurements the contributions from different components are not separated, we have to use averages of our data for comparison with bulk results. The mean value of the magnetic hyperfine field, $\langle H_{\text{hf}} \rangle$, is proportional to H_{ext} for $c_{\text{Ni}} \leq 1$ at %. For higher nickel concentrations, the slope $d\langle H_{\text{hf}} \rangle/dH_{\text{ext}}$ decreases with increasing H_{ext} at low temperatures ($T \lesssim 50$ K). In zero external field we find no magnetic hyperfine splitting down to 1.1 K in all samples with $c_{\text{Ni}} \leq 2$ at %.

The temperature dependence of the inverse local susceptibility, $\chi_{\text{Ni,loc}}^{-1} = H_{\text{ext}}/\langle H_{\text{hf}} \rangle$ for $H_{\text{ext}} = 20$ kOe is shown in Fig. 1a. The gradual transition from nonmagnetic behaviour at low temperatures to a temperature dependence characteristic for local moments at higher temperatures is consistent with the predictions of the spin fluctuation model of Ref. /1/. For $T \gtrsim 50$ K the data are well described by a Curie-Weiß law, $\chi_{\text{Ni,loc}}^{-1} \sim (T - \theta)$. The concentration dependence of θ derived from the lines shown in Fig. 1a is presented in Fig. 1b. The concentration $c_{\text{crit}} \sim 2.4$ at % at which $\theta = 0$ agrees well with the critical concentration for magnetic ordering determined by Murani et al. /2/.

The additional magnetization per nickel impurity $\Delta M_{\text{Ni}} = (M_{\text{Alloy}} - M_{\text{Pd}})/N_{\text{Ni}}$ = $M_{\text{Ni,loc}} + \delta M_{\text{Pd}}$ (where δM_{Pd} is the additional magnetization induced by a Ni impurity in the Pd matrix) derived from bulk magnetization measurements for $H_{\text{ext}} = 20$ kOe shows a qualitatively similar temperature dependence as $\chi_{\text{Ni,loc}}$. However, the ratio $R = \Delta M_{\text{Ni}}/\langle H_{\text{hf}} \rangle \sim 1 + \delta M_{\text{Pd}}/M_{\text{Ni}}$ decreases with increasing temperature for $c_{\text{Ni}} \leq 2$ at %. This result indicates a substantial magnetization δM_{Pd} of the Pd matrix around a Ni impurity at low temperatures. For high temperatures R tends towards the value $\mu_{\text{Ni}}/\langle H_{\text{hf}} \rangle$ found in ferromagnetic alloys for $c_{\text{Ni}} \sim 10$ at %.

REFERENCES

- /1/ N. Rivier and M.J. Zuckermann, Phys. Rev. Lett. 21, 904 (1968)
- /2/ A.P. Murani, A. Tari, and B.R. Coles, J. Phys. F: Metal Phys. 4, 1769 (1974)

2.2 Hyperfine Interactions in Intermetallic Compounds of Gd with 3d-Transition Metals

G. Czjzek, J. Fink, H. Schmidt, and K. Tomala^a

^aGuest scientist from Jagiellonian University, Cracow, Poland, under IAEA-fellowship

Intermetallic rare earth-transition metal compounds have received considerable interest because of the variety of their magnetic properties and their importance for technical applications. Using $^{155}\text{EuPd}$ as source we have observed the nuclear resonance absorption of ^{155}Gd in GdT_2 , $T = \text{Mn, Fe, Co, Ni}$; GdT_3 , $T = \text{Fe, Co, Ni}$; GdT_5 , $T = \text{Co, Ni}$; $\text{Gd}_2\text{Co}_{17}$, and $\text{Gd}_6\text{Mn}_{23}$. The results reported here are obtained for absorber temperatures of 4.2 K. By measurements in an external magnetic field of 50 kOe, the sign of the magnetic hyperfine field has been determined unambiguously in several cases.

A linear relationship between the values of the magnetic hyperfine fields at Gd-nuclei (H_{Gd}) and those at Dy-nuclei (H_{Dy}) in corresponding compounds has been established from our results and Dy-data taken from the literature /1/. This relation appears to hold irrespective of the symmetry of the rare earth sites. From this fact we infer that crystal field induced variations of the Dy-moment are negligible in these compounds. Thus, changes of the hyperfine fields have to be ascribed to varying conduction electron polarizations. The linear relationship between H_{Dy} and H_{Gd} implies that the conduction electron polarisation induced by the 4f moments is directly related to that caused by the 3d moments.

The experimentally determined electric field gradients $V_{\text{ZZ}}^{\text{exp}}$ are remarkably constant at sites of given symmetry with the exception of GdNi_3 . From a comparison of the experimental results with point charge calculations of the lattice contribution $V_{\text{ZZ}}^{\text{lat}}$ it follows that the effective charges of Fe, Co and Ni in a given type of compound are almost the same, only the Ni charge in GdNi_3 may be somewhat smaller than that of Fe and Co in GdFe_3 and GdCo_3 , respectively. In the compounds GdT_3 the ratios $V_{\text{ZZ}}^{\text{exp}}/V_{\text{ZZ}}^{\text{lat}}$ are quite different at sites of different symmetry for any reasonable choice of the effective charges. We conclude that the conduction electron contributions differ considerably at different sites.

Differences between the electron densities at ^{155}Gd -nuclei in these compounds and that in Gd-metal have been derived from isomer shifts measured with respect to our source. The hypothesis of a near-complete d-electron transfer from Gd to Fe in GdFe_2 proposed in Ref. /2/ is not supported by our data. It would lead to a significant increase of the electron density at the Gd-nuclei in GdFe_2 compared to that in metallic Gd - in clear contradiction to our experimental results - if it is not accompanied by a comparable s-electron transfer. The latter appears unlikely in view of the lower s-electron density of states near the Fermi energy. The electron density at Gd-nuclei in sites of trigonal and hexagonal symmetry is significantly lower than that in cubic and nearly cubic sites indicating a loss of 6s-character of the conduction electrons at sites of axial symmetry. This may be explained by a stronger admixture of the 5d- and/or 6p-states in the conduction electron wave function caused by the axial crystal field.

REFERENCES

- /1/ I. Nowik, S. Ofer, and J.H. Wernick, *Phys. Lett.* 20, 232 (1966)
G.J. Bowden, R.K. Day, and M. Sarwar, *Proc. Int. Conf. Magnetism, Moscow*, 475 (1973)
- /2/ D.M. Eagles, *Phys. kondens. Materie* 16, 181 (1973);
A.A. Comès and A.D. Guimarães, *J. Phys.* F4, 1454 (1974)

2.3 Hyperfine Interactions at ^{155}Gd Nuclei in Pseudobinary Alloys $\text{Gd}(\text{Fe}_{1-x}\text{Co}_x)_2$ and $\text{Gd}(\text{Fe}_{1-x}\text{Al}_x)_2$

G. Czjzek, J. Fink, H. Schmidt, G. Wiesinger^a, and M.J. Besnus^b

^a*Institut für Experimentalphysik, Technische Universität Wien*

^b*Laboratoire Pierre-Weiss, Université Strasbourg*

In continuation of our studies of intermetallic compounds between Gd and transition metals we have started investigations of pseudobinary alloys $\text{Gd}(\text{Fe}_{1-x}\text{M}_x)_2$ with $\text{M} = \text{Co}, \text{Al}$. The cubic C15 structure is stable for all concentrations for Co-alloys whereas in alloys with Al in the concentration

range $0.4 \lesssim x \lesssim 0.7$ phase mixtures of cubic C15 and hexagonal C14 structure are obtained.

Here we report on results derived from ^{155}Gd -Mössbauer spectra of samples with C15 structure. They are shown in Fig. 1 as function of the concentration x : (a) average magnetic hyperfine fields $\langle H_{\text{hf}} \rangle$ in $\text{Gd}(\text{Fe},\text{Co})_2$ and $\text{Gd}(\text{Fe},\text{Al})_2$; and for $\text{Gd}(\text{Fe},\text{Co})_2$: (b) width of the field distribution expressed in terms of the second moment $M_2(H) = \langle H^2 \rangle - \langle H \rangle^2$, (c) isomer shift and (d) recoilless fraction.

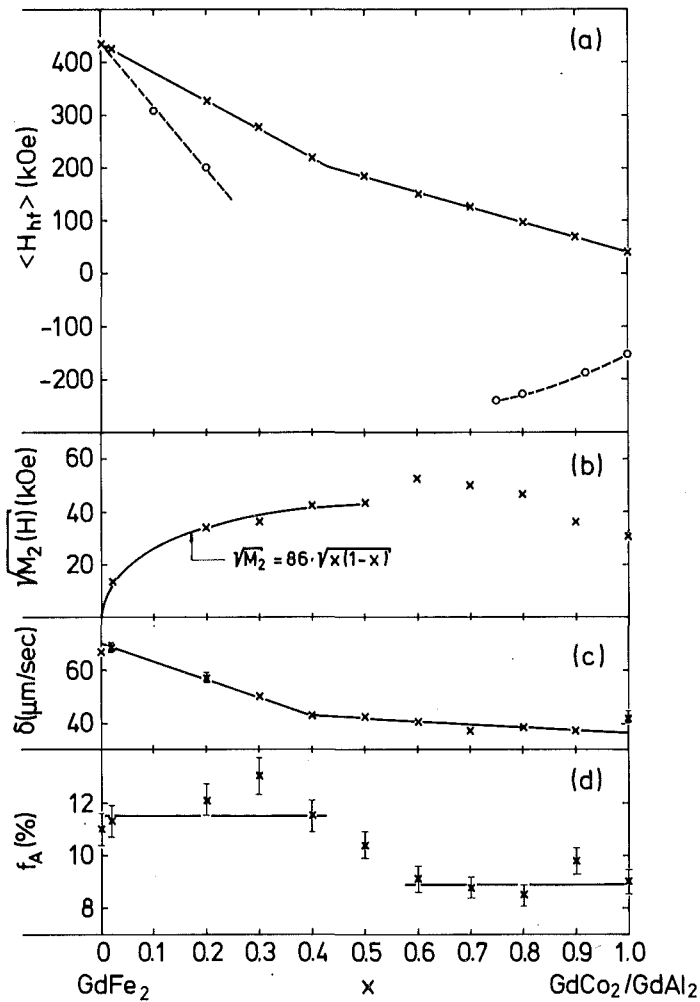


Fig. 1 Concentration dependence of hyperfine interactions at ^{155}Gd nuclei in pseudobinary alloys $\text{Gd}(\text{Fe}_{1-x}\text{M})_2$.

(a) Average hyperfine field in $\text{Gd}(\text{Fe}_{1-x}\text{Co})_2$:
 (—x—) and in $\text{Gd}(\text{Fe}_{1-x}\text{Al})_2$ (---o---)

(b) Width of the field distribution expressed in terms of the second moment $M_2(H) = \langle H^2 \rangle - \langle H \rangle^2$ in $\text{Gd}(\text{Fe}_{1-x}\text{Co})_2$

(c) Isomer shift in $\text{Gd}(\text{Fe}_{1-x}\text{Co})_2$

(d) Recoilless fraction in $\text{Gd}(\text{Fe}_{1-x}\text{Co})_2$

The absorption spectra of ^{155}Gd in $\text{Gd}(\text{Fe},\text{Al})_2$ alloys are not well described by a field distribution centered about one average value $\langle H_{\text{hf}} \rangle$. Good fits are obtained only if we assume a superposition of two components centered about two different fields (in Fig. 1 the weighted averages over both components are shown). By measurements in an external field of 50 kOe we have determined both fields in Fe-rich alloys to be positive, whereas in Al-rich alloys the hyperfine field of both components is negative. The bulk magnetization was found to vary linearly with x between 0 and 1. This result indicates that the Fe atoms have the same moment as in GdFe_2 , coupled antiferromagnetically to the Gd moments, at all concentrations. Thus, the transferred hyperfine field at Gd sites due to Fe moments which is strongly positive in GdFe_2 obviously is negative for Fe atoms replacing Al in GdAl_2 for Fe concentrations up to $\sim 25\%$. The cause for this different behaviour may be associated either with the larger lattice parameter of GdAl_2 compared to that of GdFe_2 or else with a different response of the conduction electrons to the Fe moments in the two compounds.

In the alloys $\text{Gd}(\text{Fe}_{1-x}\text{Co}_x)_2$ the average magnetic hyperfine field (Fig. 1a) and the isomer shift (Fig. 1c) vary linearly with x in the range $0 \leq x \leq 0.4$ and again for $0.5 \leq x \leq 1$, but with different slopes in these two regions of concentration. Near $x = 0.4$ to 0.5 also significant changes of the Debye-Waller factor (Fig. 1d) and of the width of the hyperfine field distribution (Fig. 1b) are observed.

For $x \leq 0.5$ the second moment $M_2(H)$ of the field distribution is proportional to $x \cdot (1 - x)$ as expected when the hyperfine field at a Gd nucleus is determined by the number of iron and cobalt atoms within a finite region around it. From the slope of $\langle H_{\text{hf}} \rangle$ vs. x and the variation of $M_2(H)$ with x we derive a range of approximately 6 \AA embracing about 40 3d atoms (1^{st} to 3^{rd} coordination shell on the 3d sublattice).

The increased values of $M_2(H)$ for $x > 0.5$ indicate a shorter range of influence for Co-rich alloys. However, a similar analysis is not possible in this region as the observed line broadening does not tend to zero for pure GdCo_2 .

An interpretation of the results obtained in $\text{Gd}(\text{Fe},\text{Co})_2$ alloys may be based on the assumption of weak ferromagnetism (that is, holes both in the majority- and minority-spin subbands) for the d-bands in GdFe_2 and strong ferromagnetism (holes in the minority-spin subband only) for the d-bands in GdCo_2 . A break in

the concentration dependence of Gd hyperfine interactions in mixtures may then be expected at that concentration where the majority-spin subband is just filled. At this point the part of the Fermi surface associated with majority-spin electrons disappears and the ensuing rather sudden change of the total density of states at the Fermi energy may lead to a change of the binding forces and thus of the Debye-Waller factor.

2.4 Crystal Electric Fields in Rare-Earth-M₃ Compounds

W. Groß^a, K. Knorr^b, P. v. Blanckenhagen, and A.P. Murani^c

^a*Physikalisches Institut der Universität Frankfurt*

^b*Institut für Physik der Universität Mainz*

^c*Institut Laue-Langevin, Grenoble, France*

The temperature dependence of the magnetic susceptibility and the specific heat of many RE-M₃ compounds have been used to determine the crystal field parameters /1 - 3/. As the results could not be interpreted unambiguously so far it seemed interesting, to investigate the crystal field transitions directly by the method of inelastic neutron scattering. These measurements have been started on the Pr-M₃ compounds (M = In, Tl, Pb, Sn) /4/. They have been extended to compounds containing heavy rare earth ions (RE = Er, Ho; M = In, Tl, Pb).

The inelastic neutron scattering experiments on polycrystalline samples in the paramagnetic state were mainly carried out on the spectrometer IN7 at the ILL Grenoble. In addition we have been able to resolve two low lying crystal field transitions in ErTl₃ at 2.0 and 2.7 meV, on the cold neutron spectrometer (MAG2) at the FR2. The present neutron spectra show at least two well resolved crystal field transitions for the Er-compounds and for HoPb₃, but less information is available for HoIn₃ and HoTl₃.

On the spectrometer MAG1 at the FR2 we checked the crystal structure of the samples and determined the magnetic ordering temperature for those

compounds, for which it was not known before (HoTl_3 : $T_N = 17 \pm 1$ K;
 ErTl_3 : $T_N = 6 \pm 1$ K).

The final analyses of the data including the determination of the crystal field parameters is still in work.

REFERENCES

- /1/ E. Bucher, K. Andres, J.P. Maita, and G.W. Hull, Jr., *Helv. Phys. Acta* 41, 723 (1968)
- /2/ K.H.J. Buschow, H.W. de Wijn, and A.M. van Diepen, *J. Chem. Phys.* 50, 137 (1969)
- /3/ P. Lethuillier, J. Pierre, and D.K. Ray, *J. Phys. F: Metal Phys.* 7, 175 (1977)
- /4/ W. Groß, K. Knorr, A.P. Murani, and K.H. Buschow, in *Crystal Field Effects in Metals and Alloys*, ed. by A. Furrer, Plenum Publ. Corp., N.Y., (1977)

2.5 Crystal Field Transition in $\text{La}_{0.85}\text{Tb}_{0.15}\text{Sn}_3$ Investigated by Inelastic Neutron Scattering

P.v.Blanckenhagen and H.E. Hoenig^a

^a*Physikalisches Institut der Universität Frankfurt*

In $\text{La}_{0.85}\text{Tb}_{0.15}\text{Sn}_3$ the crystal field is responsible for the coexistence of superconductivity and van Vleck antiferromagnetism of short range /1/. With the present investigation we successfully applied inelastic neutron scattering to a direct spectroscopy of the low lying crystal field states of Tb^{3+} in superconducting $\text{La}_{0.85}\text{Tb}_{0.15}\text{Sn}_3$. The measurements were performed on the spectrometers MAG1 and MAG2 /2/ in the time-of-flight mode of operation with $E_0 = 3.07$ meV at 1.7, 4.5, 11, 25 and 77 K and with $E_0 = 13.6$ meV at 6, 50 and 300 K.

The spectra for 1.7 and 4.5 K show a crystal field transition at 0.6 meV with a line width large compared with the instrumental resolution. No dispersion was observed for this transition in the range of momentum transfer from 0.3 to 1.5 \AA^{-1} . At higher temperatures the quasi-elastic line and the

inelastic peak are increasingly broadened. No significant peaks have been observed in the energy-loss-spectra for $E_0 = 13.6$ meV at 6 and 50 K, whereas the spectra measured at 300 K show some peaks which are obviously due to maxima of the phonon density of states.

The observed crystal field transition at 0.6 meV is compatible with our data for the temperature dependence of the magnetic susceptibility and the specific heat.

REFERENCES

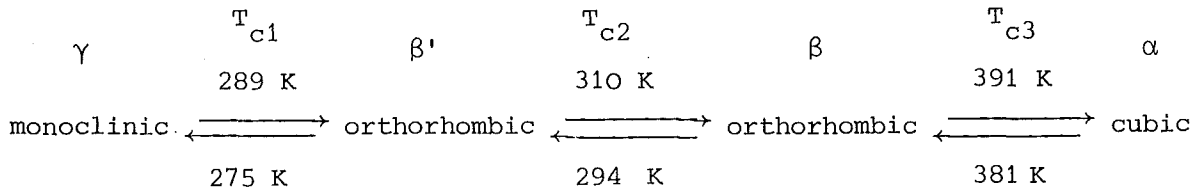
- /1/ H.E. Hoenig and P.v.Blanckenhagen, in Crystal Field Effects in Metals and Alloys (1977) ed. by A. Furrer, Plenum Publ. Corp., N.Y., and in Progress Report of the Teilinstitut Nukleare Festkörperphysik, Ges. f. Kernforschung Karlsruhe, (KFK 2357), 73 (1976)
- /2/ P.v.Blanckenhagen et al. in Progress Report of the Teilinstitut Nukleare Festkörperphysik, Ges. f. Kernforschung Karlsruhe, (KFK 2357), 124 (1976)

2.6 A Single Crystal Neutron Diffraction Study of $Cs_2PbCu(NO_2)_6$ at 313 K and the $\alpha \rightarrow \beta$ Phase Transition

S. Klein^a

^aSFB 127, Fachbereich Geowissenschaften der Universität Marburg

Nitrocomplexes $A_2^I PbCu(NO_2)_6$ (A : Cs, Rb, Tl, K) exhibit strong Jahn-Teller effects leading to distortions of the cubic symmetry in several structural modifications /1/. For $Cs_2PbCu(NO_2)_6$ the sequence of structural phase transitions has been investigated by means of EPR - /2/ and IR-spectroscopy /3/, polarising microscope studies /3/, and neutron diffraction on single crystals /4/:



Below T_{c1} a static Jahn-Teller distortion should occur. The suggested monoclinic γ -phase is probably characterized by an antiferrodistortive order of tetragonally elongated CuN_6 -octahedra /5/. The growth of untwinned $Cs_2PbCu(NO_2)_6$

crystals at room temperature is very difficult. Therefore neutron diffraction measurements had to be carried out with a sample containing two additional smaller twins besides the dominant orientation. All efforts to grow single crystals in the monoclinic γ -phase failed until now. To analyse the static Jahn-Teller distorted γ -modification powder measurements of very high resolution at 260 K and 77 K at the instrument D1A in Grenoble are in preparation.

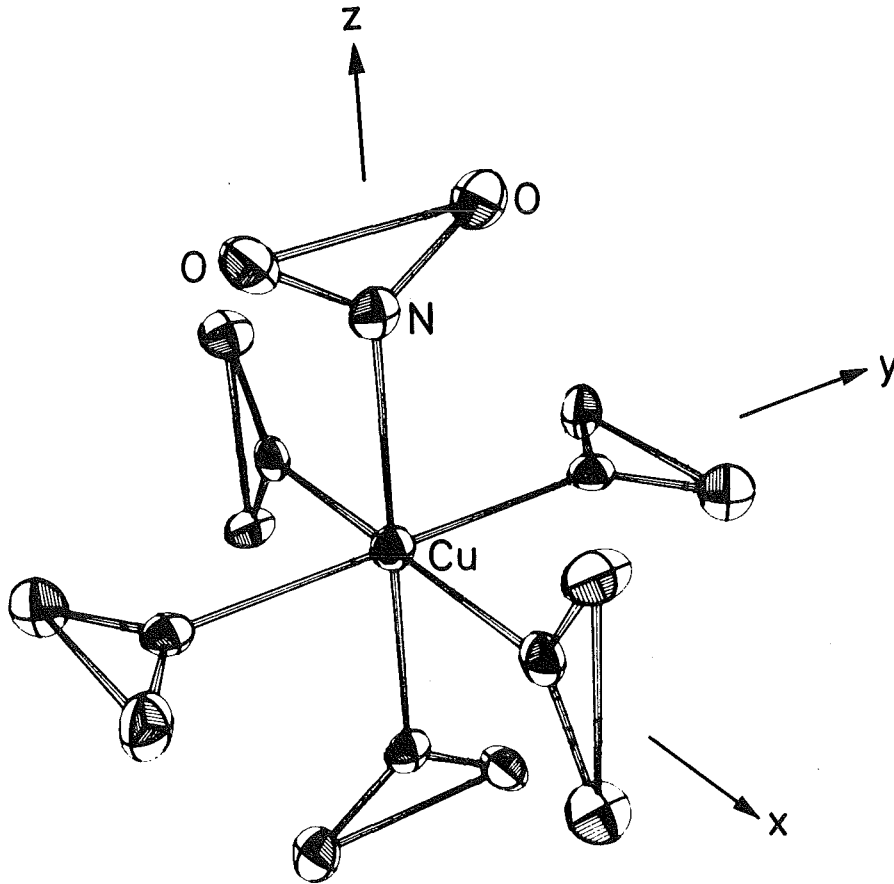


Fig. 1 CuN_6 octahedra with O-atoms of the $\text{Cs}_2\text{PbCu}(\text{NO}_2)_6$ in the cubic α -phase.

Neutron diffraction investigations at 293 K and 323 K were not able to clarify structural differences indicated by the phase transition at T_{c2} /3/ proposed by /2/.

The discontinuous phase transition at T_{c3} leads from a two dimensionally dynamic Jahn-Teller phase (β, β') with $c/a < 1$ ($a \approx b$) to the cubic α -phase. In the α -phase there is a fully dynamic Jahn-Teller effect causing undistorted CuN_6 octahedra in time average (Fig. 1). The lattice constant amounts to $a = 10.97(2) \text{ \AA}$. The root-mean-square-displacements of the Cs^+ -, Pb^+ - and Cu^{2+} -ions lie with $0.15(1) \text{ \AA}$, $0.11(1) \text{ \AA}$ and $0.16(1) \text{ \AA}$ in the usual range

/4/, /6/, /7/. The values of the N- and O-atoms (in average $0.17(1) \text{ \AA}$ and $0.20(1) \text{ \AA}$) indicate a three dimensionally Jahn-Teller effect, because these values normally amount to 0.13 \AA and 0.16 \AA . In the orthorhombic β -phase we find that next to a dominant orientation we have two additional smaller twins, whose reflections disappear at the phase transition into the cubic α -phase (Fig. 2).

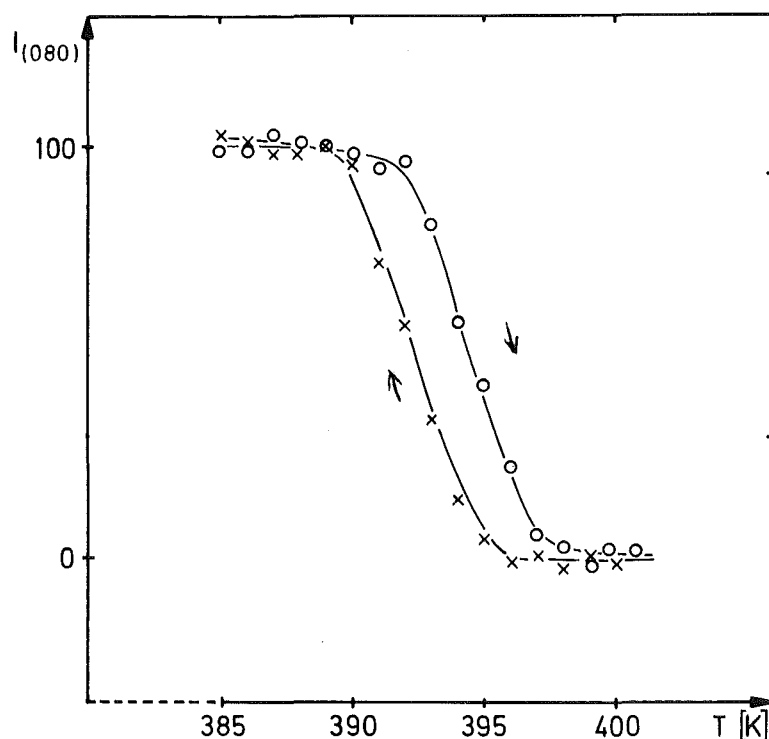


Fig. 2 The integral intensity of the (080)-reflex of the domain II at the phase transition from the orthorhombic β -phase to the cubic α -phase and reverse.

REFERENCES

- /1/ D. Reinen, D. Friebel, and K.P. Reetz, *Solid State Commun.* 4, 103 (1972)
- /2/ C. Friebel, *Z. anorg. Chem.* 417, 197 (1975)
- /3/ R. Helmbold, D. Mullen, H. Ahsbahs, A. Klopsch, E. Hellner, and G. Heger, *Z. Krist.* 143, 220 (1976)
- /4/ D. Mullen, G. Heger, and D. Reinen, *Solid State Commun.* 17, 1249 (1975)
- /5/ D. Reinen, *Solid State Commun.* 20, 137 (1977)
- /6/ N.W. Isaacs and C.H.L. Kennard, *J. Chem. Soc. A.* 386 (1969)
- /7/ D.L. Cullen and E.C. Lingafelter, *Inorg. Chem.* 10, 1264 (1971)

2.7 Magnon Dispersion of the Quasi Two-Dimensional Heisenberg Antiferromagnet $(\text{CD}_3\text{ND}_3)_2\text{MnCl}_4$

N. Lehner, V. Wagner^a, G. Heger, and R. Geick^b

^aInstitute Laue - Langevin, F-38042 Grenoble

^bPhysikalisches Institut der Universität Würzburg

$(\text{CD}_3\text{ND}_3)_2\text{MnCl}_4$, abbreviated as MAMC-D, is an example of a quasi two-dimensional Heisenberg antiferromagnet with small anisotropy /1/. Its crystal structure is basically similar to that of Rb_2MnCl_4 (shown in Fig. 1). For MAMC-D the Rb^+ -ions are replaced by (CD_3ND_3) -molecules, whose orientation and reorientation lead to a sequence of structural phase transitions/2/. As the axes of these dumb-bell molecules are almost aligned along \underline{c} , there results a large separation of the MnCl_2 -layers one from the other ($\underline{c}_{\text{MAMC}} \approx 19.5 \text{ \AA}$).

While the crystal structure of MAMC-D is very complicated, the arrangement of the magnetic Mn^{2+} ions and thus the magnetic structure at low temperatures is rather simple. In Fig. 1 the ordering of the magnetic moment vectors of the Mn^{2+} along the \underline{c} -axis is indicated by arrows. Inside the MnCl_2 -layers neighbored moments are strictly antiparallel due to a strong antiferromagnetic superexchange-interaction. By reasons of symmetry the magnetic interactions between adjacent MnCl_2 layers are excluded. The remaining magnetic interactions between largely separated next-nearest layers are extremely small.

We studied the magnetic behaviour of MAMC-D by neutron scattering on single crystals, which were grown for the first time by E. Neumann of Konstanz University. The experiments were performed at the IN3 triple axis spectrometer of the HFR in Grenoble. The sublattice magnetization has been investigated by intensity measurements of the magnetic superstructure reflections at several temperatures. In Fig. 2 the intensity of the magnetic (102)-peak is shown as a function of temperature. As the intensity of these superstructure reflections is proportional to the square of the sublattice magnetization, it may be described by a power-law:

$$I(T)/I(0) = B^2 \cdot \left(1 - \frac{T}{T_N}\right)^{2\beta}.$$

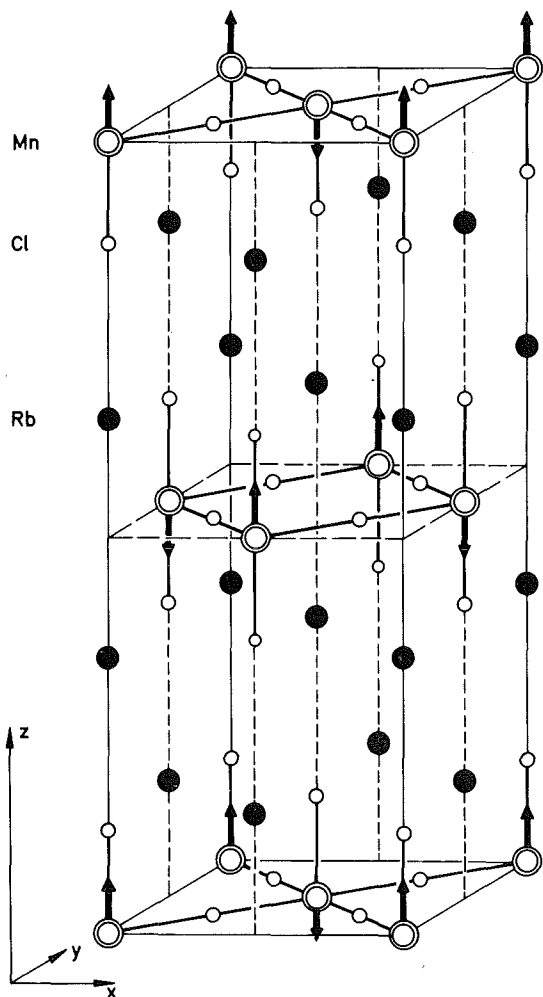


Fig. 1 The crystal structure and the magnetic structure of Rb_2MnCl_4 . The lattice parameters are $\underline{a} = 7.2 \text{ \AA}$ and $\underline{c} = 16.2 \text{ \AA}$. For MAMC-D the Rb^+ -ions are replaced by (CD_3ND_3) -molecules with their axes basically parallel to the z-direction. The lattice constant \underline{c} changes to $\underline{c} = 19.5 \text{ \AA}$. The magnetic structure is indicated by arrows.

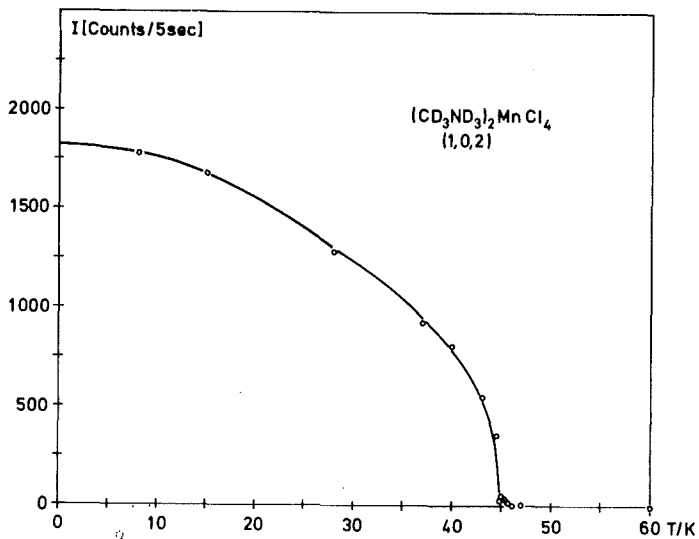


Fig. 2 Temperature dependence of the Bragg-intensity of the magnetic (102)-reflex of MAMC-D. The solid curve is the result of a fit with a power-law yielding the critical exponent $\beta = 0.21$.

Herein β is the critical exponent describing the temperature dependence of the order parameter, i.e. sublattice magnetization. The results from a least-squares fit are listed in Table I together with the corresponding values for related substances. It is remarkable that we could fit our data in the whole temperature region, i.e. between 8 K and the Néel temperature $T_N \approx 45$ K.

The magnon dispersion relation of MAMC-D was measured at 8 K in $[\xi 00]$ - and $[00\xi]$ -direction, i.e. parallel and perpendicular to the magnetic MnCl_2 -layers (see Fig. 3). While parallel to the layers there is a pronounced dispersion, perpendicular to them no dispersion could be detected within our experimental resolution ($\Delta E = 0.15$ THz). We tried to describe the dispersion in $[\xi 00]$ -direction using the model of a quasi Heisenberg antiferromagnet with weak anisotropy and magnetic interactions to the four nearest Mn^{2+} neighbours within a layer:

$$\omega(q_\xi) = \gamma \left[(H_E + H_A)^2 - H_E^2 \cdot \cos^2 \left(\frac{q_\xi \cdot \xi}{2} \right) \right]^{\frac{1}{2}}$$

where $\gamma = \frac{g \cdot \mu_B}{h}$, H_A the anisotropy field and H_E the exchange field. From our fit we found

$$\gamma H_E = 1.998 \pm 0.040 \text{ ThZ}$$

$$\gamma H_A = 0.015 \pm 0.005 \text{ THz}$$

Assuming that $g = 2.0$ and $H_E = -2J \cdot Z \cdot S$ with $Z = 4$ and $S = \frac{5}{2}$ we calculated the values given in Table I.

For a comparison of our results with the data of de Jongh and Miedema /1/ (nondeuterated MAMC) and related measurements on K_2MnF_4 and Rb_2MnF_4 /3/, in Table 1 the experimental data are listed together with the theoretical predictions of the two-dimensional Ising and the three-dimensional Heisenberg model. The overall agreement between the experimental data is satisfactory. The Néel temperature for MAMC-D $T_N = 45.3$ K is slightly lower than that given by de Jongh and Miedema /1/. Heger /4/ found $T_N = 44.5$ in close correspondence to our value.

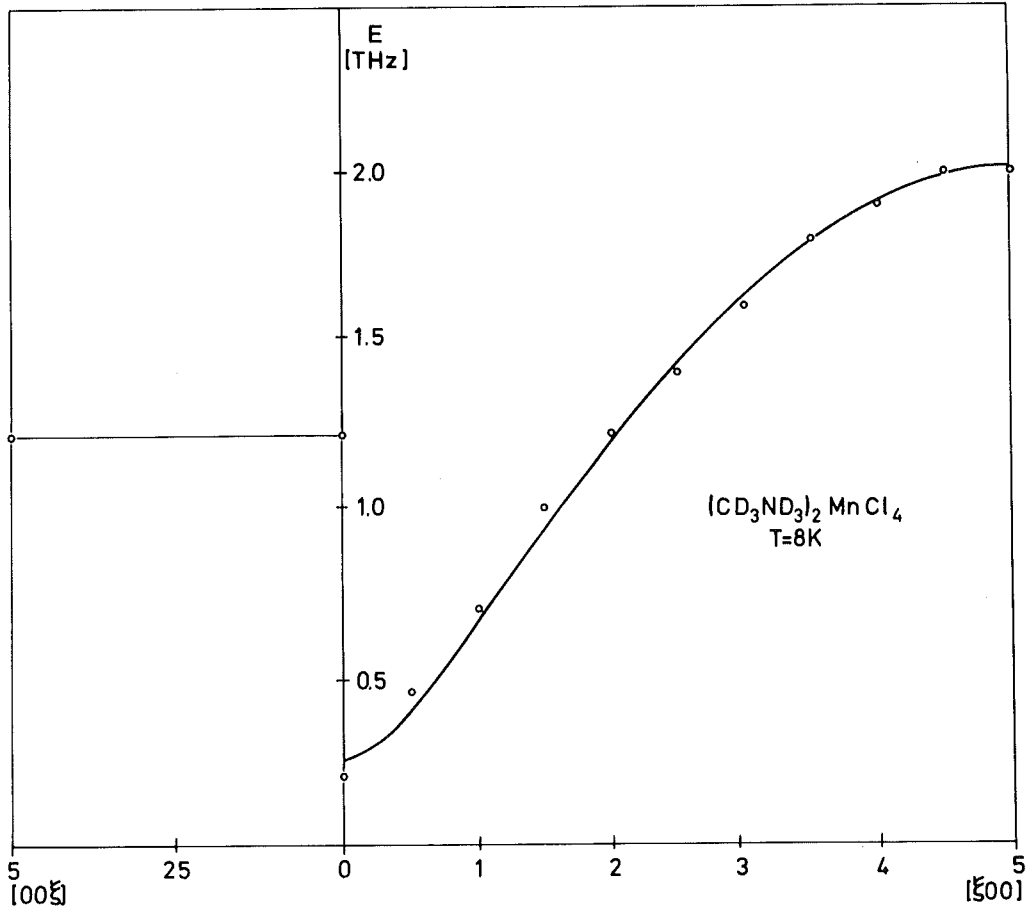


Fig. 3 Magnon dispersion of MAMC-D at 8 K. In $[00\xi]$ -direction no dispersion could be found. For the $[\xi 00]$ -direction the solid line is the result of the fit described in text.

Table 1: Comparison of experimental data from quasi two-dimensional systems with spin $\frac{5}{2}$ and theoretical predictions.

	β	T_N [K]	J/k [K]	$\alpha = H_A/H_E$
K_2MnF_4 /1/, /3/	0.15 ± 0.01	42.3	- 4.2	$3.9 \cdot 10^{-3}$
Rb_2MnF_4 /1/, /3/	0.16 ± 0.02	38.4 ± 0.07	- 3.7	$4.7 \cdot 10^{-3}$
Rb_2MnCl_4 /1/		57	- 6.2	$1.5 \cdot 10^{-3}$
MAMC /1/		47	- 5.0	$1.1 \cdot 10^{-3}$
MAMC-D (this work)	0.21 ± 0.02	45.3 ± 0.2	-4.80 ± 0.10	$7(?) \cdot 10^{-3}$
Rb_2MnCl_4 (own results)	0.19 ± 0.02	55.0 ± 0.2	1.00 ± 0.02	$4(?) \cdot 10^{-3}$
2d-Ising model /1/	0.125			
3d-Heisenberg model /1/	~ 0.36			

Our measurement yields three indications for the dominant two-dimensional behaviour of MAMC-D:

1. the power-law to describe the sublattice magnetization holds in a large temperature region ($\sim .15 T_N \leq T < T_N$)
2. within the energy resolution of our magnon measurements we were not able to detect any dispersion in direction perpendicular to the magnetic layers.
3. the magnons are well defined up to T_N and visible up to about $1.3 T_N$.

Corresponding measurements have been performed on the related Rb_2MnCl_4 . The results are also given in Table 1.

REFERENCES

- /1/ L.J. de Jongh and A.R. Miedema, *Adv. Phys.* 23, 1 (1974)
- /2/ G. Heger, D. Mullen, and K. Knorr, *phys. stat. sol. (a)* 35, 627 (1976)
- /3/ R.J. Birgeneau, H.J. Guggenheim, and G. Shirane, *Phys. Rev.* B8, 304 (1973)
- /4/ G. Heger, E. Henrich, and B. Kanellakopoulos, *Solid State Commun.* 12, 1157 (1973)

2.8 Neutron Diffraction Studies on Simple Molecular Crystals
for the Determination of Electron Density Distributions

G. Heger, D. Mullen^a, and W. Treutmann^a

^aSFB 127, Fachbereich Geowissenschaften der Universität Marburg

In order to study the electron density distribution of simple molecular crystals we have completed X-ray and neutron diffraction measurements on thiourea ($S = C(NH_2)_2$), urea ($O = C(NH_2)_2$) and tetracyanoethylene ($(NC)_2C = C(CN)_2$) at several temperatures. For thiourea the structure data obtained by neutron diffraction at room temperature are to be published (abstract below).

For urea neutron diffraction measurements were performed at low temperatures in addition to earlier room temperature work /1/. Using a Displex Split-Cycle Refrigerator (Air Products & Chemicals) on the four-circle diffractometer P32/FR2 ($\lambda_n = 1.0327 \text{ \AA}$) 320 reflection intensities were measured up to $2\theta = 90^\circ$ at $95 \pm 10 \text{ K}$. The lattice parameters of the tetragonal unit cell of urea at this temperature were determined to $a = 5.572(5) \text{ \AA}$ and $c = 4.573(5) \text{ \AA}$. Because of the large incoherent neutron scattering cross-section of hydrogen, an absorption correction /2/ was applied to the measured data using an experimentally determined effective linear absorption coefficient $\mu_{(NH_2)_2CO} = 2.3 \text{ cm}^{-1}$. For the structure refinement in the space group $P\bar{4}2_1m$, the corrected intensities were averaged over all symmetry equivalent reflections yielding a data set of 124 independent reflection intensities. With anisotropic temperature factors for all atoms we obtained a final R_F -factor of 0.30. ($R_F = \sum | |F_O| - |F_C| | / \sum |F_O|$, with F_O and F_C for the observed and calculated structure factors, respectively). The $O = C(NH_2)_2$ molecules (Fig. 1) are nearly planar.

In contrast to thiourea, urea shows no structural phase transitions. This might be explained from the different intermolecular hydrogen bonding strengths (Table 1): While the N-H...O hydrogen bonds are rather strong, characterized by short H - O distances (1.909 \AA and 1.998 \AA) and N - H - O angles close to linearity (168.1° and 147.0°), the corresponding N - H...S bridges at room temperature differ between one strong (N - H(2) ... S) and two weak (N - H(1)...S) bonds.

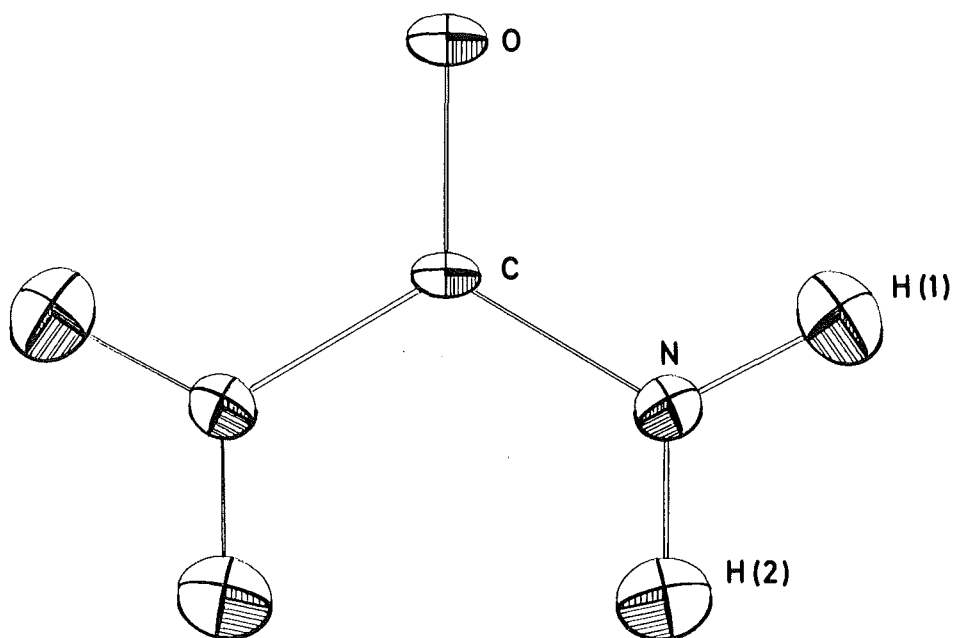


Fig. 1 The urea molecule with the thermal ellipsoids

Table 1 Comparison of the hydrogen bondings of urea (95 K) and thiourea (295 K)

$\text{O}=\text{C}(\text{NH})_2$ 95 K	$\text{N}-\text{H} \left[\overset{\text{O}}{\text{A}} \right]$	$\text{H}-\text{O} \left[\overset{\text{O}}{\text{A}} \right]$	$\text{N}-\text{O} \left[\overset{\text{O}}{\text{A}} \right]$	Angle $\left(\text{N}-\overset{\text{H}}{\text{O}} \right)$
$\text{N}-\text{H}(1) \dots \text{O}$	0.994(11)	1.998(11)	2.982(4)	$168.1(4)^\circ$
$\text{N}-\text{H}(2) \dots \text{O}$	0.990(11)	1.909(11)	2.899(4)	$147.0(5)^\circ$
$\text{S}=\text{C}(\text{NH}_2)_2$ 295 K	$\text{N}-\text{H} \left[\overset{\text{O}}{\text{A}} \right]$	$\text{H}-\text{S} \left[\overset{\text{O}}{\text{A}} \right]$	$\text{N}-\text{S} \left[\overset{\text{O}}{\text{A}} \right]$	Angle $\left(\text{N}-\overset{\text{H}}{\text{S}} \right)$
$\text{N}-\text{H}(2) \dots \text{S}$	1.009(6)	2.403(6)	3.398(3)	$168.6(4)^\circ$
$\text{N}-\text{H}(1) \dots \text{S}$	0.993(7)	2.738(11)	3.523(8)	$136.2(6)^\circ$
$\text{N}-\text{H}(1) \dots \text{S}$	0.993(7)	3.092(9)	3.677(6)	$119.0(6)^\circ$

REFERENCES

- /1/ A.W. Pryor and P.L. Sanger, Acta Cryst. A26, 543 (1970)
 /2/ C.T. Prewitt, Z. Kristallogr. 122, 24 (1965)

Refinement of the Structure of Thiourea: A Neutron Diffraction Study at 293 K.

D. Mullen, G. Heger and W. Treutmann

to be published in Zeitschrift für Kristallographie

Abstract

The room temperature structure of thiourea was refined on the basis of new neutron diffraction intensities. An improved R-factor of 0.057 was obtained.

Thiourea has the orthorhombic space group Pnma (No. 62) at room temperature. The molecule is found to be planar, with one hydrogen atom about 0.08 Å out of plane. This out-of-plane H atom is associated with the strongest hydrogen bond, linking molecules in continuous chains.

The more accurate data obtained from this study are being used in an investigation of bonding electron density in thiourea.

2.9 Combined X-Ray and Neutron Diffraction Study of $K_2 [Pt(CN)_4]_{x_{0.3}} \cdot 3H_2O$ with X = Br, Cl (KCP) between 31 K and Room Temperature

G. Heger, H.J. Deiseroth^a, and Heinz Schulz^a

^aMax-Planck-Institut für Festkörperforschung, D-7000 Stuttgart

The results of six crystal structure refinements of $K_2 [Pt(CN)_4]_{x_{0.3}} \cdot 3H_2O$ with X = Br, Cl (KCP) from X-ray and neutron diffraction measurements between 31 K and room temperature are presented and compared. Particular subjects of the discussion are the parameters of the $[Pt(CN)_4]$ groups, the distribution of the water molecules, and the temperature dependence of the temperature factors. The Pt-Pt distances deviate from each other by less than 0.007 Å. The $[Pt(CN)_4]$ groups are not planar. X-ray data show a correlation between the z-parameters of the K atoms and (CN) groups. Zero point vibrations and the magnitude of the positional disorder of the various atoms are derived from their temperature factors at different temperatures.

to be published in Acta Cryst. A

2.10 Untersuchung der Wasserstoffbrückenbindungen im Schlippeschen Salz ($\text{Na}_3\text{SbS}_4 \cdot 9\text{D}_2\text{O}$)

H. Guth and G. Heger

Das in der Photographie als Negativverstärker und Tönungsmittel verwendete Schlippesche Salz ($\text{Na}_3\text{SbS}_4 \cdot 9\text{H}_2\text{O}$) verdankt seine Eigenschaften insbesondere verschiedenen Wasserstoffbrückenbindungen. Ergänzend zu Röntgenbeugungsuntersuchungen von Mereiter und Preisinger /1/ wurden Neutronenbeugungsuntersuchungen an einem volldeutერიerten $\text{Na}_3\text{SbS}_4 \cdot 9\text{D}_2\text{O}$ -Kristall durchgeführt, um die Wassermoleküle mit ihren Brückenbindungen zu S^{2-} -Ionen genauer zu studieren. Der verwendete volldeutერიerte Kristall wurde von S. Haussühl an der Universität Köln hergestellt.

Für die Messung wurde ein Würfel mit einer Kantenlänge von 4 mm geschliffen (Flächen: {1 0 0}). Dieser Probenkristall wurde in flüssigem Stickstoff abgeschreckt, um seine Mosaikstruktur zu vergrößern und so Extinktionseffekte bei der Messung auszuschalten. Mit dem automatischen Vierkreisdiffraktometer P110 im FR2 wurden die Intensitäten von etwa 2400 Reflexen im Winkelbereich $8^\circ \leq 2\theta \leq 80^\circ$ aufgenommen. Die Neutronenwellenlänge betrug $\lambda_N = 0.926 \text{ \AA}$. Die Gitterkonstante von $\text{Na}_3\text{SbS}_4 \cdot 9\text{D}_2\text{O}$ wurde mit Hilfe einer Least-Squares-Verfeinerung von 5 zentrierten Reflexen bestimmt: $a = 11.97(1) \text{ \AA}$.

Zur Verfeinerung der Kristallstruktur wurde über symmetrisch gleichwertige Reflexe gemittelt. In der kubischen Raumgruppe $P2_13$ ergab sich somit ein Datensatz von 912 unabhängigen Reflexintensitäten. Für die Rechnungen wurde das Programmsystem X-RAY'76 benutzt. Als Startparameter dienten die Atomkoordinaten aus der Röntgenstrukturbestimmung. Mit anisotropen Temperaturfaktoren wurde ein R_F -Wert ($R_F = \frac{\sum |F_O| - |F_C|}{\sum |F_O|}$) von 5.4 % erreicht.

Dabei wurde festgestellt, daß die Temperaturfaktoren von Atom D(6) außergewöhnlich stark anisotrope Werte annehmen. Da D(6) gleichzeitig an zwei schwachen Wasserstoffbrückenbindungen (O(3)-D(6)...S(1) und O(3) - D(6)...S(2)) beteiligt ist, wurde versucht mit einem Splitmodell (D(6) wird ersetzt durch die Splitlagen D(61) und D(62)) eine bessere Beschreibung zu erreichen (Abb. 1). Bei der Weiterverfeinerung der Struktur festigten sich diese Splitpositionen mit einem Abstand D(61) - D(62) von $0.56(2) \text{ \AA}$; die Besetzungen beider Lagen waren innerhalb der Fehlergrenzen jeweils 50 %. Obwohl sich an den Parametern

der restlichen Atome keine signifikanten Änderungen ergaben, wurde mit dem Splitmodell ein leicht verbesserter R_F -Wert von 5.2 % erreicht.

Für die Wassermoleküle und ihre Wasserstoffbrückenbindungen sind die Abstände und Winkel in Tabelle I zusammengestellt. Es zeigt sich, daß für die D_2O -Moleküle die Abstände und Winkel gut übereinstimmen: die O-D-Abstände streuen zwischen 0.949 Å und 0.968 Å, die D-O-D-Winkel zwischen 106.7° und 107.8° . Eine Ausnahme bildet $D_2O(3)$ mit einem Abstand O(3) - D(6) von 0.928 Å im ungesplitteten Fall.

Tabelle I

Wasser I:	vor Spaltung	Wasser I:	nach Spaltung
O(1)-D(1): 0.968(4) Å	∠ D(1)-O(1)-D(2): 107.8(4)°	O(1)-D(1): 0.966(4) Å	∠ D(1)-O(1)-D(2): 107.8(4)°
O(1)-D(2): 0.949(4) Å		O(1)-D(2): 0.950(4) Å	
O(1)-S(2): 3.348(6) Å	∠ O(1)-D(1)-S(2): 175.4(4)°	O(1)-S(2): 3.350(6) Å	∠ O(1)-D(1)-S(2): 175.4(3)°
D(1)-S(2): 2.382(6) Å		D(1)-S(2): 2.386(6) Å	
O(1)-O(3): 2.811(4) Å	∠ O(1)-D(2)-O(3): 167.7(3)°	O(1)-O(3): 2.812(4) Å	∠ O(1)-D(2)-O(3): 167.7(3)°
O(2)-O(3): 1.877(5) Å		D(2)-O(3): 1.877(5) Å	
<hr/>			
Wasser II:		Wasser II:	
O(2)-D(3): 0.960(5) Å	∠ D(3)-O(2)-D(4): 106.7(4)°	O(2)-D(3): 0.960(5) Å	∠ D(3)-O(2)-D(4): 106.6(4)°
O(2)-D(4): 0.962(4) Å		O(2)-D(4): 0.963(4) Å	
O(2)-S(1): 3.362(6) Å	∠ O(2)-O(3)-S(1): 173.9(4)°	O(2)-S(1): 3.364(6) Å	∠ O(2)-D(3)-S(1): 173.8(3)°
D(3)-S(1): 2.406(7) Å		D(3)-S(1): 2.408(7) Å	
O(2)-S(2): 3.323(6) Å	∠ O(2)-D(4)-S(2): 173.2(4)°	O(2)-S(2): 3.322(6) Å	∠ O(2)-D(4)-S(2): 173.2(4)°
D(4)-S(2): 2.366(6) Å		D(4)-S(2): 2.364(6) Å	
<hr/>			
Wasser III:		Wasser III:	
O(3)-D(5): 0.959(5) Å	∠ D(5)-O(3)-D(6): 106.8(5)°	O(3)-D(5): 0.960(6) Å	∠ D(5)-O(3)-D(6): 120.9(9)°
O(3)-D(6): 0.928(6) Å		O(3)-D(6): 0.98(1) Å	
O(3)-S(2): 3.298(6) Å	∠ O(3)-D(5)-S(2): 175.9(4)°	O(3)-S(2): 3.301(6) Å	∠ O(3)-D(5)-S(2): 176.1(4)°
D(5)-S(2): 2.341(7) Å		D(5)-S(2): 2.343(7) Å	
O(3)-S(1): 3.593(3) Å	∠ O(3)-D(6)-S(1): 139.8(5)°	O(3)-S(1): 3.593(4) Å	∠ O(3)-D(6)-S(1): 159(1)°
D(6)-S(1): 2.834(6) Å		D(6)-S(1): 2.66(1) Å	
O(3)-S(2): 3.599(6) Å	∠ O(3)-D(6)-S(2): 137.0(5)°	O(3)-S(2): 3.596(6) Å	∠ O(3)-D(6)-S(2): 159(1)°
D(6)-S(2): 2.865(8) Å		D(6)-S(2): 2.69(2) Å	

$D_2O(1)$ besitzt je eine Wasserstoffbrücke zum Schwefel (O(1) - D(1)...S(2)) und zum Sauerstoff des dritten Wassermoleküls (O(1) - D(2)...O(3)). $D_2O(2)$ hat zwei gleichwertige Wasserstoffbrücken O(2) - D(3)...S(1) und O(2) - D(4)...S(2) zu Schwefelatomen. $D_2O(3)$ hat auch eine normale Wasserstoffbrückenbindung O(3) - D(5)...S(2) zum Schwefel. Für die üblichen O-D...S-Brückenbindungen findet man D-S-Abstände zwischen 2.34 Å und 2.41 Å und O-D-S-Winkel von 173.8° bis 176.1° . Die Wasserstoffbrücke von O(1) zu O(3) ist ebenfalls fast linear (\angle O(1) - D(2) - O(3) = 167.7°) mit einem O(1) - O(3) - Abstand von 2.81 Å.

Eine Ausnahme bilden die Wasserstoffbrückenbindungen O(3) - D(6)...S (Abb. 1). Es gibt hier zwei praktisch gleichwertige Möglichkeiten O(3) - D(6) ...S(1) und O(3) - D(6)...S(2) mit D-S-Abständen von 2.83 Å bzw. 2.87 Å und Winkeln O-D-S von 139.8° bzw. 137.0° (im ungesplitteten Modell). Diese Bindungen sind offensichtlich bedeutend schwächer ausgeprägt. Im Splitmodell (D(6) → D(61), D(62)) sind die Unterschiede in den Bindungslängen und -winkeln weniger deutlich. Man findet D-S-Abstände von 2.66 Å bzw. 2.69 Å und O-D-S-Winkel von 159°. Während die O(3) - D(61,62)-Abstände mit den üblichen Werten übereinstimmen (0.96 Å bzw. 0.98 Å), ergeben sich bei der Splitmodellverfeinerung gravierende Unterschiede für D(5) - O(3) - D(61,62)-Winkel (120.9° bzw. 90°). Möglicherweise wird durch die zusätzliche Wasserstoffbrücke O(1) - D(2)...O(3) eine Schwächung der innermolekularen Kräfte des D₂O(3) erreicht, was eine starke Winkeldeformation des dritten Wassermoleküls erklären könnte.

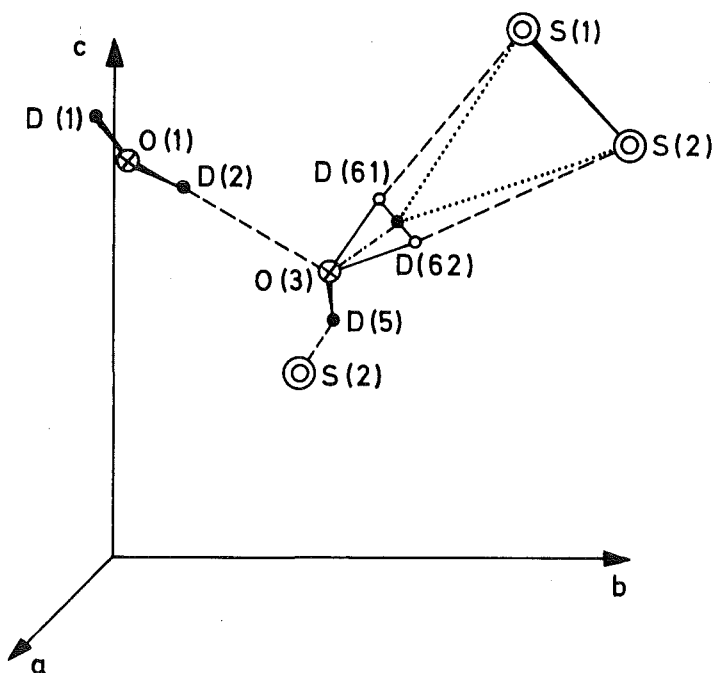


Abb. 1 Wasser III mit Umgebung

Bei Beugungsuntersuchungen erhält man nur ein gemittelttes Bild der Struktur; man kann dabei nicht direkt zwischen statischer Fehlordnung und dynamischen Effekten unterscheiden. Deshalb könnten erst Neutronenbeugungsuntersuchungen bei tiefen Temperaturen entscheiden, ob eine statische Fehlordnung entsprechend dem Splitmodell für das dritte Wassermolekül vorliegt.

REFERENCE

/1/ K. Mereiter and A. Preisinger, Private Mitteilung (1977)

2.11 Hyperfine Interactions of Neutron Activated ^{28}Al in Sapphire

H.-J. Stöckmann, H. Ackermann, D. Dubbers, F. Fujara, M. Grupp, P. Heitjans, and A. Körblein

Physikalisches Institut der Universität Heidelberg, Germany and

Institute Laue - Langevin, F-38042 Grenoble

Hyperfine interactions of the β emitter ^{28}Al have been studied in Al_2O_3 by in-beam nuclear magnetic resonance. The transition frequencies yield the ^{28}Al magnetic moment $|\mu| = 3.24(2)\mu_N$ and the quadrupole coupling constant $|e^2qQ/h| = 2.8(2)$ MHz.

Polarized ^{28}Al nuclei ($\tau = 3.26$ min, $I = 3$) are produced by capture of polarized neutrons in a Al_2O_3 single crystal. The ^{28}Al β -decay to ^{28}Si shows an asymmetry proportional to the polarization of the ^{28}Al ground state. ^{28}Si decays to the ^{28}Si ground state (Fig. 1). Because of the short lifetime of the excited ^{28}Si state an alignment of the ^{28}Al ground state can be detected by a γ -ray anisotropy. An alignment may be produced by reorientation of the originally purely dipolar polarization (created by the neutron capture process) due to internal or external fields /2/.

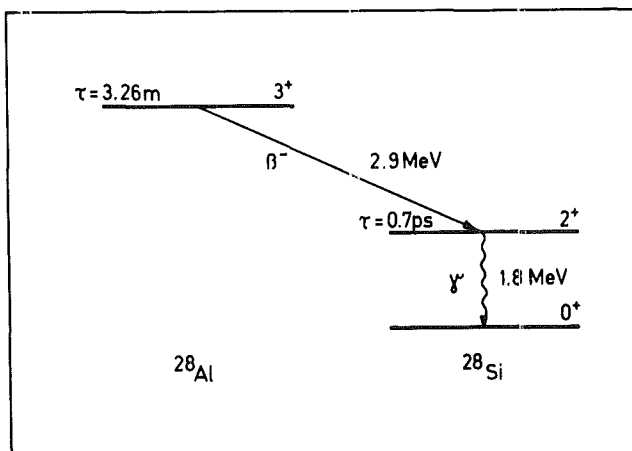


Fig. 1

Part of the decay scheme of ^{28}Al (data taken from /1/).

Al_2O_3 is a rhombohedral crystal (space group D_{3d}^6) with an axially symmetric electric field gradient (efg) tensor at the Al site. The crystal was oriented in a cryostat at 77 K with the principal axis of the efg tensor parallel to the external magnetic field $\dot{B} = 0.5$ T. Because of $I = 3$ one expects a quadrupolar split NMR spectrum consisting of six lines at the frequencies

$$\nu_m = (E_m - E_{m-1})/h = \nu_L + (m - \frac{1}{2})\nu_Q \quad (m = -2, \dots +3),$$

where $\nu_L = \mu/3h$, $\nu_Q = e^2qQ/10h$.

μ is the magnetic moment of the ^{28}Al ground state and e^2qQ the quadrupole coupling constant at the Al site.

In order to measure the quadrupole splitting with a minimum amount of time, the following modulation technique was applied (for details see /3/): a broad band modulated rf field is swept over the six NMR transitions from low to high frequencies. Each time the rf band reaches a transition it saturates it, and a step occurs in the β -decay asymmetry. As soon as all transitions are saturated, the β -decay asymmetry is reduced to zero. If the band is swept to still higher frequencies, the transitions leave the band one by one, until the maximum polarization is obtained again. The resulting step curve is shown in Fig. 2. The position of the most pronounced steps in Fig. 2 was localized by further measurements with improved precision.

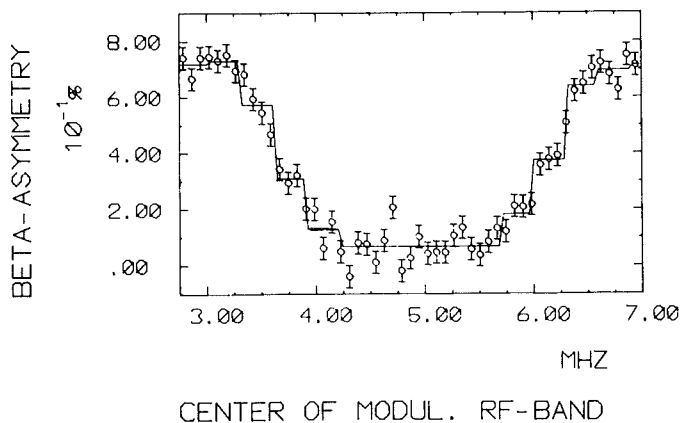


Fig. 2 NMR-step curve of ^{28}Al in Al_2O_3 . A broad band modulated rf field (depth of modulation 3 MHz) is swept over the six NMR transitions. Whenever a transition enters or leaves the band, a step in the β -decay asymmetry occurs. The solid line results from a least-squares fit yielding μ and e^2qQ .

Since the induction of rf transitions converts the initial polarization partly to an alignment, a corresponding step curve can also be observed in the anisotropy of the γ decay of ^{28}Si /2, 4/. The relative sign of β -decay asymmetry and γ -decay anisotropy yielded a positive sign for e^2qQ of ^{28}Al in Al_2O_3 .

As the statistics of the measured asymmetry is rather poor, a least-squares fit was applied varying both μ and e^2qQ . Fig. 3 shows the χ^2 -contour lines in dependence of the two parameters. A definite χ^2 minimum is obtained, yielding the following results

$$|\mu| = 3.24(2) \mu_N, \quad |e^2qQ/h| = 2.8(2) \text{ MHz}.$$

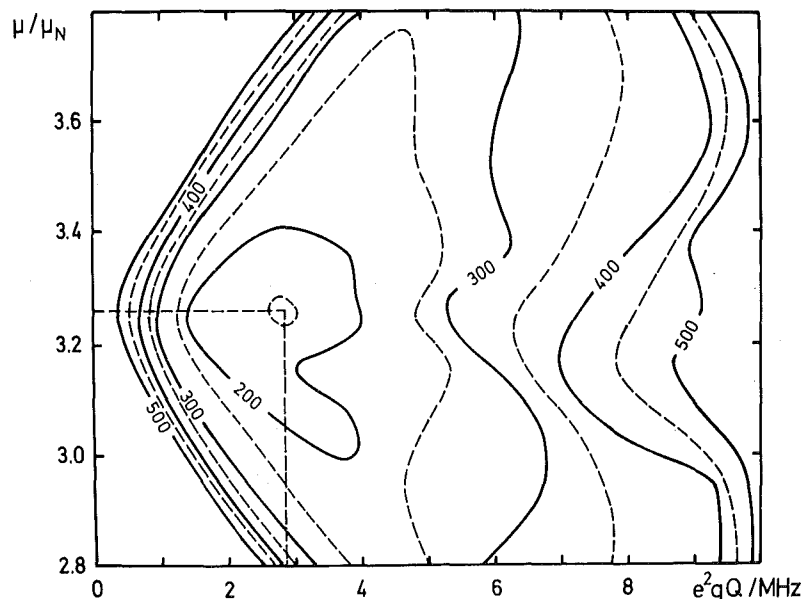


Fig. 3 χ^2 -contour lines in dependence of the fit parameters μ and e^2qQ . The fit yields a distinct χ^2 minimum.

Using $|e^2qQ/h| = 2.393(6)$ MHz of ^{27}Al in Al_2O_3 /5/ one gets for the ratio of the quadrupole moments

$$\left| Q(^{28}\text{Al}) / Q(^{27}\text{Al}) \right| = 1.17(8).$$

Inserting $Q(^{27}\text{Al}) = 0.15 \cdot 10^{-24} \text{ cm}^2$ /6/ one gets

$$\left| Q(^{28}\text{Al}) \right| = 0.17(1) \cdot 10^{-24} \text{ cm}^2.$$

The theoretical predictions for the magnetic dipole and the electric quadrupole moment of ^{28}Al /7/ are

$$\mu_{\text{calc}} = 3.13 \mu_N, \quad Q_{\text{calc}} = 0.165 \cdot 10^{-24} \text{ cm}^2,$$

and agree with the experimental values.

The efg at the Al site in Al_2O_3 has been calculated to be positive /8, 9/. Since the sign of the calculated $Q(^{28}\text{Al})$ is positive, one expects a positive sign for e^2qQ , again in agreement with the experiment.

It should be mentioned that a magnetic moment value of ^{28}Al is reported, $|\mu| = 2.789(1) \mu_N$ /10/, which deviates significantly from our one. The applied method was also β -detected NMR, the used compound was a powder sample of AlP. The cause for this discrepancy is not known, and it is intended to repeat the experiment on AlP.

This work was sponsored by the Bundesministerium für Forschung und Technologie.

REFERENCES

- /1/ P.M. Endt and C. van der Leun, Nucl. Phys. A214, 1 (1973)
- /2/ D. Dubbers, H. Ackermann, M. Grupp, P. Heitjans, and H.-J. Stöckmann, Z. Phys. B25, 363 (1976)
- /3/ H.-J. Stöckmann, H. Ackermann, D. Dubbers, M. Grupp, and P. Heitjans, Z. Phys. 269, 47 (1974)
- /4/ D. Dubbers, H. Ackermann, F. Fujara, M. Grupp, H. Grupp, P. Heitjans, A. Körblein, and H.-J. Stöckmann, Hyperfine Interactions (1977)
- /5/ R.V. Pound, Phys. Rev. 79, 685 (1950)
- /6/ G.H. Fuller, Journ. Phys. and Chem. Ref. Data 5, 835 (1976)
- /7/ M.J.A de Voigt and B.H. Wildenthal, Nucl. Phys. A206, 305 (1973)
- /8/ S. Hafner and M. Raymond, Journ. Chem. Phys. 49, 3570 (1968)
- /9/ R.R. Sharma, Phys. Rev. Lett. 25, 1622 (1970)
- /10/ H. Lades, Z. Phys. 252, 242 (1972)

3. THEORY

3.1 Energy Dependence of the Coupling Function $\alpha^2(\omega)$ for Compounds

H. Rietschel

The transition temperature T_c of a superconductor is essentially determined by the strength of the electron-phonon coupling, a suitable measure of which is given by the electron mass enhancement factor λ . For compounds, λ may be written as

$$\lambda \sim \sum_{\vec{k}, \vec{k}'} \sum_{\vec{q}, \nu} \frac{1}{\omega_{\vec{q}, \nu}^2} \sum_{\substack{1, \alpha \\ 1', \alpha'}} \frac{1}{(M_\alpha M_{\alpha'})^{1/2}} e^{i\vec{q}(\vec{R}_{1, \alpha} - \vec{R}_{1', \alpha'})} \quad (1)$$

$$\cdot \left[(\vec{\epsilon}_{\vec{q}, \nu}(\alpha) \langle \vec{k}' | \nabla U_{1, \alpha} | \vec{k} \rangle) (\vec{\epsilon}_{\vec{q}, \nu}^*(\alpha') \langle \vec{k} | \nabla U_{1', \alpha'} | \vec{k}' \rangle) \right] \delta(\epsilon_f - \epsilon_{\vec{k}}) \delta(\epsilon_f - \epsilon_{\vec{k}'}) .$$

Here $\vec{R}_{1, \alpha}$ is the position vector of the α -th atom in the 1-th unit cell, M_α the corresponding atomic mass and $\omega_{\vec{q}, \nu}$ and $\vec{\epsilon}_{\vec{q}, \nu}(\alpha)$ frequency and amplitude of a phonon of branch ν with wave vector \vec{q} . $\langle \vec{k}' | \nabla U_{1, \alpha} | \vec{k} \rangle$ is the matrix element of the gradient of the electron-ion potential between Bloch states and ϵ_f the Fermi energy, $\epsilon_f = \epsilon_{k_f}$.

Alternatively, one may write (1) as

$$\lambda = 2 \int_0^\infty d\omega \alpha^2(\omega) F(\omega) / \omega \quad (2)$$

where $F(\omega)$ is the phonon density of states and $\alpha^2(\omega)$ an energy dependent electron-phonon coupling function. The product $\alpha^2(\omega) \cdot F(\omega)$ is the well-known Eliashberg function which can directly be measured by tunneling experiments.

An evaluation of (1) in terms of band structure quantities has been given in /1/, /2/. For λ these authors arrived at the expression

$$\lambda = \frac{2m \epsilon_f}{h^2 \pi^2 n(\epsilon_f)} \sum_{\alpha} \frac{1}{M_\alpha \langle \omega^2 \rangle} \sum_1 2(1+1) \frac{n_1^\alpha n_{1+1}^\alpha + 1}{n_1^\alpha n_{1+1}^\alpha} \sin^2 (\delta_{1+1}^\alpha - \delta_1^\alpha) \quad (3)$$

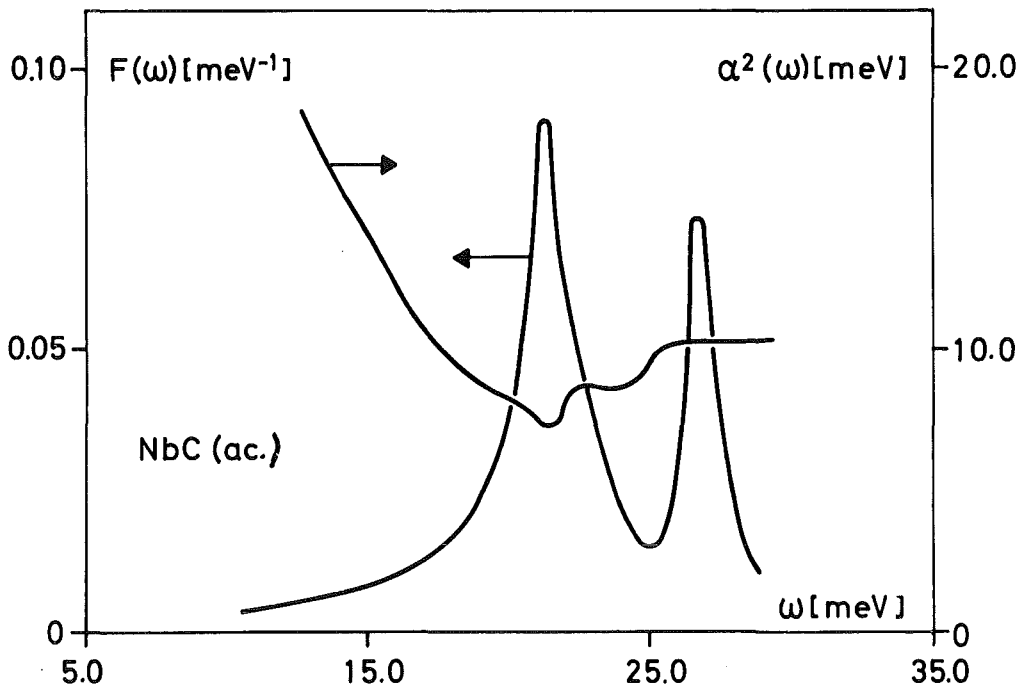


Fig. 1 Phonon density of states and coupling function $\alpha^2(\omega)$ in NbC for acoustical phonons.

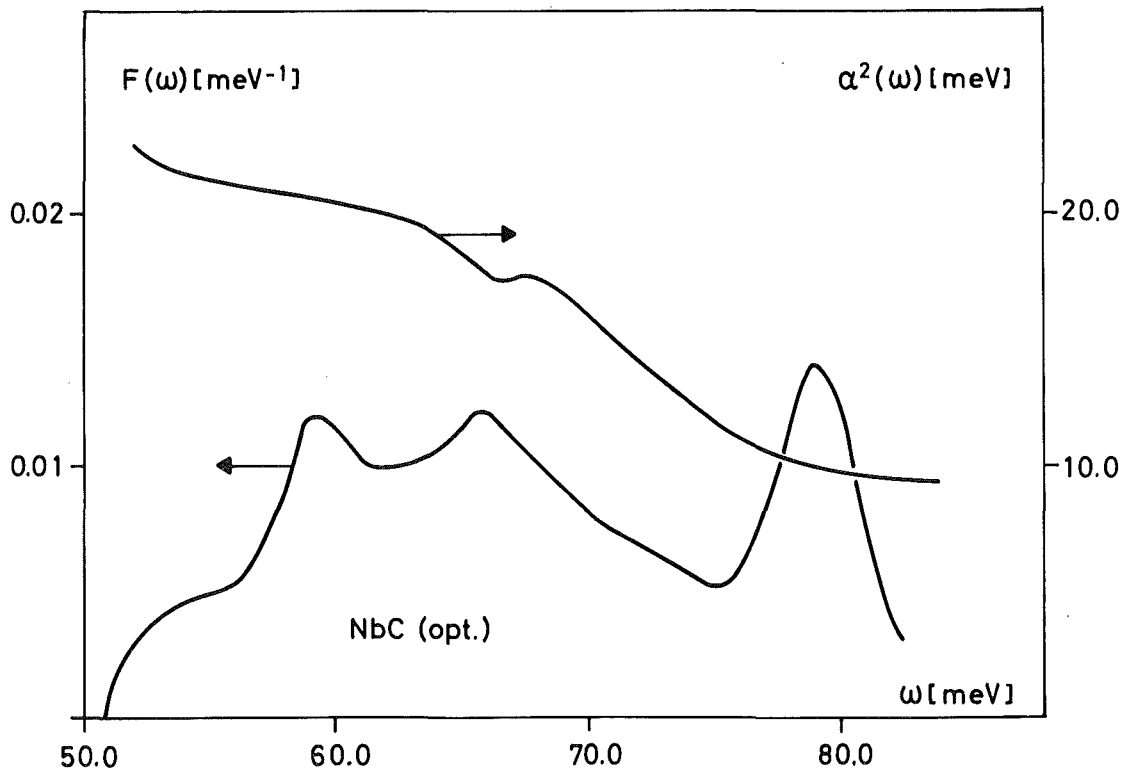


Fig. 2 Phonon density of states and coupling function $\alpha^2(\omega)$ for optical phonons.

where $n(\varepsilon_f)$ is the total electronic density of states at the Fermi level, while the n_1^α are the corresponding partial components and δ_1^α the phase shifts for the α -th atom and for angular momentum l . In deriving (3) three essential approximations were made:

- a) The electron-phonon coupling was calculated within the rigid muffin tin approximation.
- b) The Fermi surface integrals in (1) were spherically approximated.
- c) Only diagonal terms $\alpha = \alpha'$, $l = l'$ were retained in the sum $\sum_{l, l', \alpha, \alpha'}$ in (1) ("local approximation").

Using only approximately a) and b) one may evaluate the matrix elements in (1) on the Fermi surface to be

$$\langle \vec{k} | \nabla U_{1, \alpha} | \vec{k}' \rangle_{k, k' = k_f} = (\vec{k} - \vec{k}') \cdot \tilde{V}_\alpha(|\vec{k} - \vec{k}'|), \quad (4)$$

$$\tilde{V}_\alpha(Q) = \frac{2\pi\hbar^2}{m k_f} \sum_l \left[\frac{n_1^\alpha n_{l+1}^\alpha}{n_1 (1)^\alpha n_{l+1} (1)^\alpha} \right]^{\frac{1}{2}} \sin(\delta_1^\alpha - \delta_{l+1}^\alpha) \sum_{l'=0}^l (2l'+1) P_{l'}\left(1 - \frac{Q^2}{2k_f^2}\right).$$

Thus, these matrix elements turn out to be formally identical with those of the pseudopotential theory for free electron metals, a fact which allows to calculate $\alpha^2(\omega)F(\omega)$ and λ in \vec{q} -space without the local approximation c). We performed such calculations for a binary model compound with NaCl-structure, the nearest and next-nearest neighbour spring constants of which were chosen so as to reproduce as well as possible the phonon density of states of NbC. The band structure data for NbC necessary to calculate the $\tilde{V}_\alpha(Q)$ were taken from /3/.

In Figure 1 and 2, respectively, the coupling function $\alpha^2(\omega)$ is shown together with the resulting phonon density of states for the acoustical and optical phonons, respectively. Whereas for the optical phonons $\alpha^2(\omega)$ behaves roughly as $1/\omega$, it deviates largely from a $1/\omega$ -shape for the acoustical phonons, particularly in the region of a high density of states.

In calculating λ it turned out that in our example the local approximation leads to an increase of about 7%. Generally, this error increases with decreasing k_f and in addition depends strongly on $\tilde{V}_\alpha(Q)$.

We finally emphasize that our calculations do not take into account phonon anomalies which possibly may play an important role for λ and $\alpha^2(\omega)$. However, we think that apart from such anomalies the overall shape of $\alpha^2(\omega)$ for NbC is well represented by our results.

REFERENCES

- /1/ R. Evans, G.D. Gaspari, and B.L. Gyorffy, J. Phys. F.: Metal Phys. 3, 39 (1973)
- /2/ I.R. Gommersall and B.L. Gyorffy, J. Phys. F: Metal Phys. 3, L138 (1973)
- /3/ B.M. Klein, D.A. Papaconstantopoulos, and L.L. Boyer, NRL Memorandum Report 3323 (1976)
- B.M. Klein, private communication

3.2 Neutron Scattering Law $S(k, \omega)$ for a Peierls System

K. Käfer

Qualitative considerations indicate /1/ that the measured phonon anomaly in KCP /2/ might be interpreted in terms of amplitude- and phase-modes of the Peierls-CDW /3/. We therefore developed a model for a system of Peierls-distorted chains and calculated the neutron scattering law.

Our Hamiltonian consists of 4 parts:

$$H = H^{el} + H^{ph} + H^{el-ph} + H^{el-el}.$$

H^{el} describes the Peierls-electrons, i.e. nearly-free electrons with a gap Δ at $\pm k_F$ in their dispersion. H^{ph} contains the unrenormalized phonons with ion-plasma frequency Ω . For the electron-phonon coupling in H^{el-ph} we chose for simplicity an Ashcroft potential with radius R_C . The electron-electron interaction is represented in H^{el-el} by a Coulomb-matrix element $\frac{4\pi e^2}{q} \alpha^2$, where α is a measure for the localisation of the electrons on the chains (compare /4/, q will always be near the chain axis). We used the RPA.

Since the Peierls-electrons are represented by nearly free electrons, anomalous diagrams appear (Fig. 1) and cause coupling between phonons with k and $k - 4 k_F$ sign k .

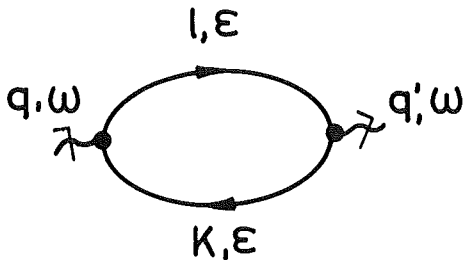


Fig. 1

Anomalous pair bubble. q' can take the values $q, q - 2 k_F, q - 4 k_F$ ($q > 0$).

Taking this into account by a Nambu-formalism and finally diagonalizing the phonon-matrix propagator, we get the renormalized phonon frequencies and the now uncoupled new phonon field-amplitudes. The result is shown in Fig. 2. (Coulomb interaction is taken into account). Due to the electron-mediated phonon-phonon coupling we get for every q -value two frequencies, i.e. now we have two branches. Their contribution to $S(k, \omega)$ is determined by the expansion coefficients of the new field amplitudes ϕ with respect to the bare amplitudes ϕ . At $2 k_F$ the ϕ 's are given by $\phi_{\pm}(2 k_F) = \frac{1}{\sqrt{2}} (\phi_{2 k_F} \pm \phi_{-2 k_F})$, i.e. correspond to the phase (-) and amplitude (+) mode /3/ which at this q -value contribute with equal weight. In a very small neighbourhood of $2 k_F$, however, virtually the whole weight is shifted to one branch only. In Fig. 2 this is symbolized by the strength of the drawing line.

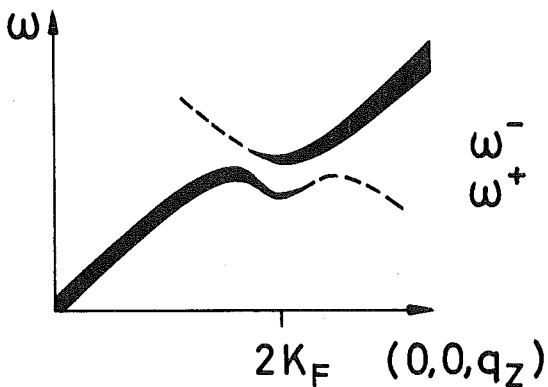


Fig. 2

$4 k_F$ -phonon-phonon coupling splits the acoustic branch into two branches, whose relative weight is symbolized by the strength of the drawing line.

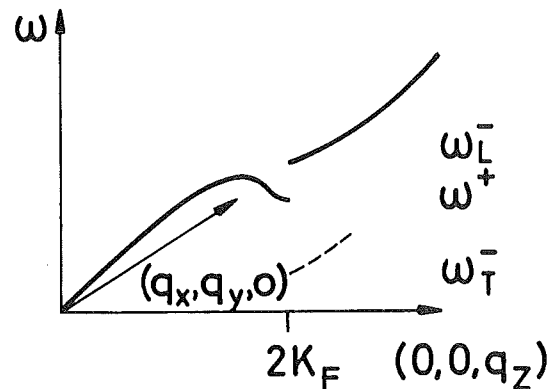


Fig. 3

Phonon dispersion along the q_z -axis together with ending points of $\omega^-(q_x, q_y, 2 k_F)$.

To complete our picture we have to take into account that for $\underline{q} = (\epsilon, \epsilon, 2 k_F)$, i.e. \underline{q} slightly off the chain direction, the corresponding phase mode frequency ω_T^- is significantly lower than the frequency ω_L^- with $\underline{q} = (0, 0, 2 k_F + \epsilon)$, ϵ infinitesimal, /1/. In fact, for a model with no Coulomb-interaction and no U-processes ω_T^- would be zero /3/. This is sketched in Fig. 3, where for clarity we have drawn only the dominant branch of the $(0, 0, q)$ -phonon dispersion together with the ending points of $\omega^-(\epsilon, \epsilon, 2 k_F)$. The amplitude mode shows no such spectacular behaviour.

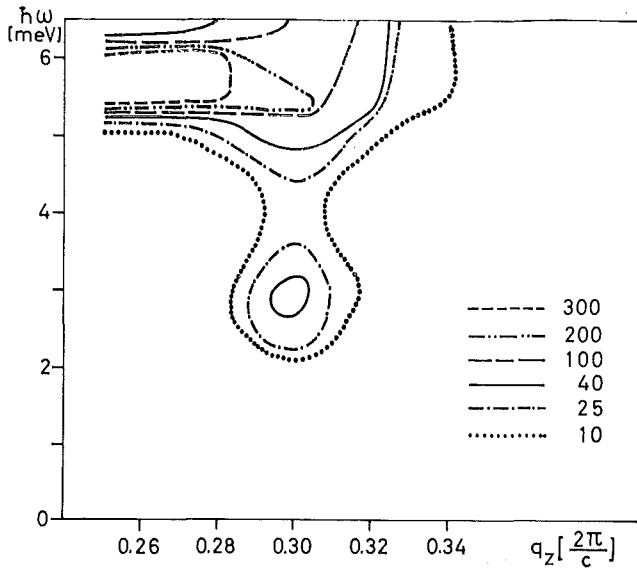


Fig. 4a

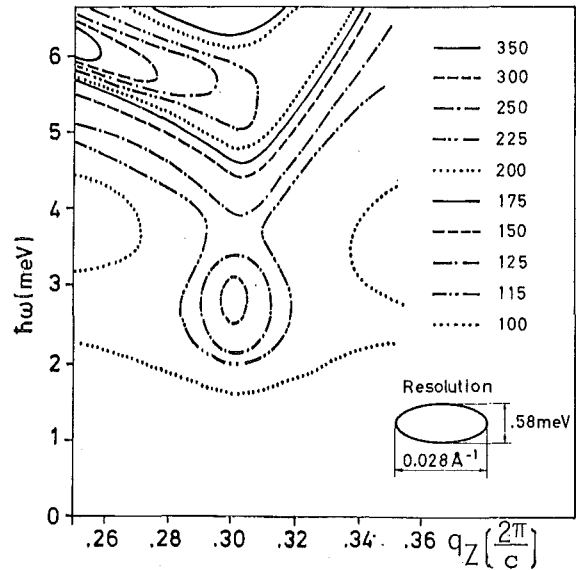


Fig. 4b

Fig. 4 Contour diagrams of inelastic neutron scattering intensity

a) Contour diagram near $\underline{q} = (0, 0, 2 k_F)$, obtained by folding calculated $S(k, \omega)$ with instrumental resolution given in Fig. b), $T = 60$ K, other parameters see text. All chains are assumed in phase.

b) Contour diagram of KCP, measured by Renker & Comès at $T = 60$ K near $\underline{q} = (1/2, 1/2, 2 k_F)$. (Measured intensities at $(0, 0, 2 k_F)$ look more complicated due to another phonon branch, but the part due to the phonon anomaly investigated here shows no qualitative difference to $\underline{q} = (1/2, 1/2, 2 k_F)$).

Using the so found frequencies and relative weights we calculated the neutron scattering law $S(k, \omega)$ and simulated an inelastic neutron scattering experiment by folding $S(k, \omega)$ with a Gaussian-shaped instrumental resolution. For k_F , ϵ_F , Δ etc. we used the experimental data of KCP and tried to reproduce the inelastic neutron data by adjusting the parameters Ω , α , R_C . With the fit-values $\Omega = 30$ meV, $\alpha = 2.05$, $R_C = 0.32 \text{ \AA}$ we obtained $\omega_T^- = 2.5$ meV, $\omega_L^- = 6.7$ meV, $\omega^+ = 5.8$ meV, and finally the contour diagram shown in Fig. 4a. In view of the simplicity of our model the agreement with the experimental data (Fig. 4b) seems to us rather satisfactory.

In order to further improve our understanding of the neutron data of KCP, we ought to take into account the phase relations of the CDWs of the different chains. (So far we assumed that the chains have mutual relative phases 0.) This will alter the contribution of the ω_L^- -mode to the neutron scattering law /5/. In conclusion, however, we think that such a mean-field theory is well suited to explain the low temperature inelastic neutron scattering data of KCP.

REFERENCES

- /1/ K. Käfer, in Progress Report of the Teilinstitut Nukleare Festkörperphysik, Ges. f. Kernforschung Karlsruhe (KFK 2357), 39 (1976)
- /2/ R. Comès, B. Renker, L. Pintschovius, R. Currat, W. Gläser, and G. Scheiber, phys. stat. sol. (b) 71, 171 (1975)
K. Carneiro, G. Shirane, S.A. Werner, and S. Kaiser, Phys. Rev. B13, 4258 (1976)
- /3/ P.A. Lee, T.M. Rice, and R.W. Anderson, Solid State Comm. 14, 703 (1974)
- /4/ P.F. Williams and A.N. Bloch, Phys. Rev. B10, 1097 (1974)
- /5/ P.A. Lee, private communication

3.3 Comment on "Fokker-Planck Equations for Simple Non-Markovian Systems"

W. Schommers and T. Geszti^a

^a*Research Institute for Technical Physics of the Hungarian Academy of Sciences, H-1325 Budapest POB 76, Hungary*

J. Chem. Phys. 66, 2767 (1977)

Abstract

Recently Adelman /1/ derived generalized Fokker-Planck equations for simple non-Markovian systems. The basic assumption in his theory is that the velocities of the particles of the system can be represented by stationary Gaussian random variables (Gaussian approximation). In this note we want to check by molecular dynamics whether the Gaussian approximation is a reasonable approximation in the case of an unbound Brownian particle. As an example we have chosen liquid rubidium. The results for the velocity autocorrelation function (VAF) are satisfactory only for small times t (up to 10^{-13} sec). For $t > 0.8 \cdot 10^{-12}$ sec the VAF becomes imaginary and which is in contrast to the fact in classical systems the VAF must always be real.

REFERENCES

/1/ S.A. Adelman, J. Chem. Phys. 64, 124 (1976)

3.4 Theoretical Investigation of the Liquid-Solid Transition.
A Study for Gallium

W. Schommers

Sol. State Comm. 21, 65 (1977)

Abstract

Schneider et al. developed a theory of the liquid state which relates the stability of the liquid to the dynamics of its collective modes. In this

development the liquid-solid transition temperature T_L is given in the classical approximation $T_{L,cl}$. In this paper we show that in the case of gallium a classical treatment of the problem is too imprecise. Taking into account quantummechanical corrections up to \hbar^2 in the determination of the stability limit the correction to the experimental value of Page et al. ($T_{L,cl} = 27 \pm 20$ K) is about 90 K.

3.5 Extended Born-Green Equation: A New Approach for
Determining Pair Potentials in Disordered Systems

W. Abel, R. Block, and W. Schommers

Phys. Letters, 58A, 367 (1976)

Abstract

The Born-Green equation was tested using molecular dynamics data for liquid rubidium at 319 K. The unsatisfactory results of this equation for the pair potential are caused by the insufficient precision of the Kirkwood approximation for describing the triplet correlation function $g_3(r,s,t)$. A more realistic ansatz for $g_3(r,s,t)$ was employed in the formulation of an extended Born-Green equation. This new approach gives much better results for the potential than the simple Born-Green equation.

3.6 Correlations in the Motion of Particles in α -Silver
Iodide: A Molecular Dynamics Study

W. Schommers

Phys. Rev. Letters, 38, 1526 (1977)

Abstract

For α -AgI at 563 K molecular dynamics calculations have been performed using a realistic pair potential and a model system of 256 particles. The influence is investigated of I^- ions on single-particle motion in the Ag^+ subsystem. Furthermore, it is shown that correlations between different ions must be distinctly reflected in frequency-dependent conductivity.

3.7 Liquid Argon: The Influence of Three-Body Interactions
on Atomic Correlations

W. Schommers

Phys. Rev. A16, 327 (1977)

Abstract

Molecular dynamics calculations on a two-dimensional argon liquid at 96 °K have been performed taking into account three-body interactions. The three-body forces were assumed to have the Axilrod-Teller-form. For the pair interaction the Lennard-Jones potential was chosen. The differences between structural and dynamical correlations which arise from calculations with and without the presence of three-body interactions have been studied. Whereas the differences between distribution functions (pair correlation function and triplet correlation function) due to the three-body forces are not significant, time correlation functions (velocity autocorrelation function and intermediate scattering function) show systematic deviations. For example, in the case of the velocity autocorrelation function, deviations up to 25 % have been observed. Furthermore, the fourth moment of the scattering law is calculated for wave numbers $0.234 \leq k \leq 2.34 \text{ \AA}^{-1}$. Here, also, the deviations (up to 12 %) from the pair-theory values are systematic. The results indicate that the determination of pair potentials from the fourth moment (a recent method by Rahman) does not give unique pair potentials for argon and argonlike systems since three-body forces are clearly reflected in the fourth moment.

4. MATERIALS RESEARCH

4.1 Low Temperature Self-Ion Irradiation and Superconductivity in Al Thin Films

P. Ziemann and M. Kraatz

In a low temperature irradiation experiment the interesting question arises, to what extent changes of the transition temperature to superconductivity (T_c) can be attributed to a certain kind of defects, e.g. Frenkel pairs (F.P.). To answer this question for aluminium we irradiated films, which were prepared by evaporation at room temperature, with small fluences (up to 10^{14} cm^{-2}) of self-ions (Al^{++}) of 500 keV at 4.2 K. To this energy corresponds a mean projected range being about 3 times larger than the film thicknesses (1500 \AA). To estimate the homogeneity of the damage introduced into the layers, the projected nuclear energy loss of the ions was calculated as a function of depth using a procedure given by /1/. This calculation showed that up to about 1500 \AA quite homogeneous damage profiles can be expected. The films having a resistance ratio of about 11, were also

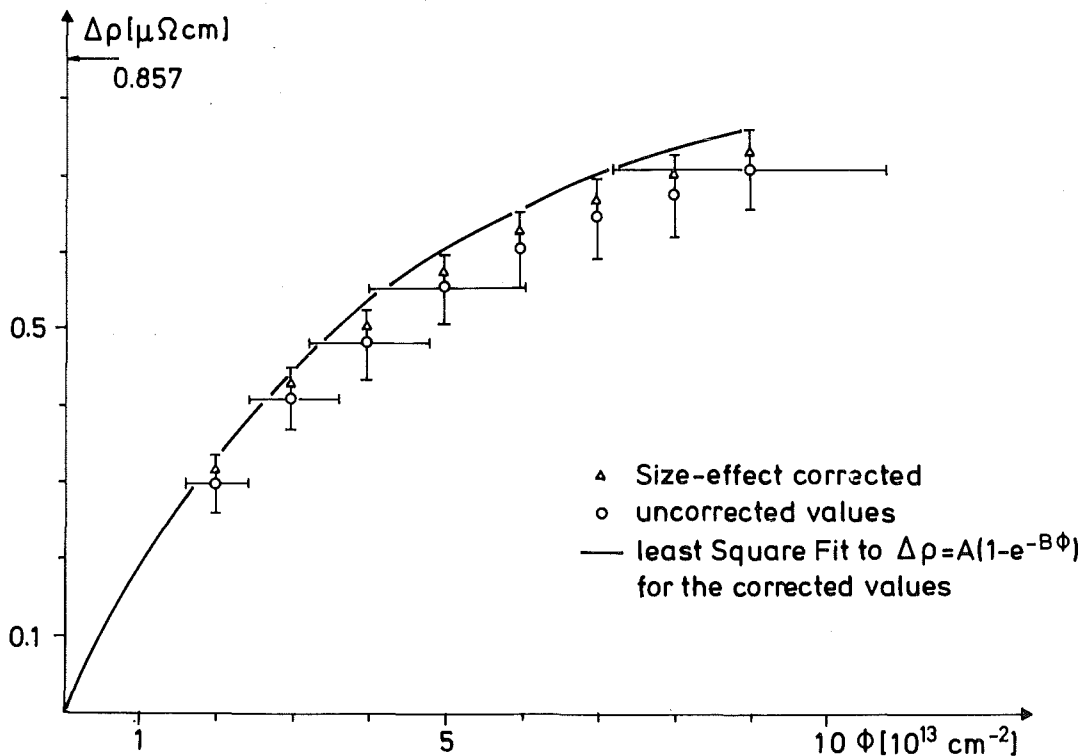


Fig. 1 Resistivity change vs. ion fluence in Al films irradiated with 500 keV Al^{++} ions.

analysed by backscattering of 2 MeV α -particles and no impurities could be detected within the limits of this method.

In Fig. 1 the resistivity increase $\Delta\rho$ caused by radiation damage is plotted as a function of the fluence ϕ . The triangles represent the data corrected for the size effect in a procedure described in /2/. Also shown is a least square fit of $\Delta\rho = A(1 - e^{-B \cdot \phi})$ to these data with fitting parameters A and B, which gives a saturation value of 0.857 $\mu\Omega\text{cm}$. This value agrees well with those found by 2 MeV α -particle irradiation of epitaxially grown Al-films /3/ (0.88 $\mu\Omega\text{cm}$) or by neutron irradiation of bulk samples /4/ (0.86 $\mu\Omega\text{cm}$). It is therefore assumed, that as in these experiments the disorder is mainly due to Frenkel pairs.

To the saturation value corresponds a change of the transition temperature ΔT_c of 0.1 K, as measured resistively by a standard four point technique, which also seems to saturate in this fluence range. The T_c before irradiation was 1.28 K. With a value of 3.4 $\mu\Omega\text{cm}$ per 1 % F.P. for the resistivity change /5/, a saturation concentration of about 0.25 % F.P. is obtained. Together with ΔT_c , this leads to the answer of the introducing question, that point defects lead to an increase of the transition temperature in Al with a rate of 0.4 K per 1 % F.P..

REFERENCES

- /1/ C.R. Fritzsche, Appl. Phys. 12, 347 (1977)
- /2/ A.M. Toxen, M.J. Quinn, Phys. Rev. 138, 1145 (1965)
- /3/ K.L. Merkle, L.R. Singer, Appl. Phys. Lett. 11, 35 (1967)
- /4/ G. Burger, H. Meissner, W. Schilling, phys. stat. sol. 4, 281 (1964)
- /5/ P.G. Lucasson, R.M. Walker, Phys. Rev. 127, 485 (1962)

4.2 Thickness Determination and Matthiessen's Rule in Granular Aluminium Thin Films

P. Ziemann

The main difficulty in measuring resistivities of thin films results from the uncertainty of thickness determinations. Therefore in this contribution two methods have been compared.

The first method (I) has been described in detail by v. Bassewitz et al. /1/ and is based on the validity of Matthiessen's rule also when size effect corrections are necessary. The geometry factor $G = \frac{L}{B \cdot D}$ (L length of the film, B width and D thickness) from this method is given by $G = (\Delta R / \Delta T) / (\Delta \rho / \Delta T)$, with $(\Delta R / \Delta T)$, and $(\Delta \rho / \Delta T)$ being the temperature dependence of resistance and resistivity measured in the linear part respectively. The value of $(\Delta \rho / \Delta T)$ for Al is taken from /1/.

In the second method (II) the thickness is measured by Rutherford backscattering of 2 MeV α -particles as described in e.g. /5/.

Granular aluminium films, whose preparation and superconducting properties have been described in /2/ were used for a comparison of the two methods. The films had oxygen contents, also determined by backscattering, between less than 0.5 at. % and 7 at. %. The results are shown in Fig. 1, where the different thicknesses are plotted.

It is seen that, through the points of samples with an oxygen content of less than 3.6 at. % a linear fit parallel to the diagonal can be drawn giving an extrapolation value for D_{II} of 350 \AA when D_I is zero. Backscattering spectra of the films on carbon substrates show two oxide peaks, the one arises from the surface oxide, the other from an oxide layer at the interface between film and substrate. From the area of these peaks it is possible to estimate the total oxide thickness to be 270 \AA , which agrees with the extrapolated value within the error bars. This means that the difference in the thicknesses is due to oxide layers, which carry no current and can therefore not be measured with method I.

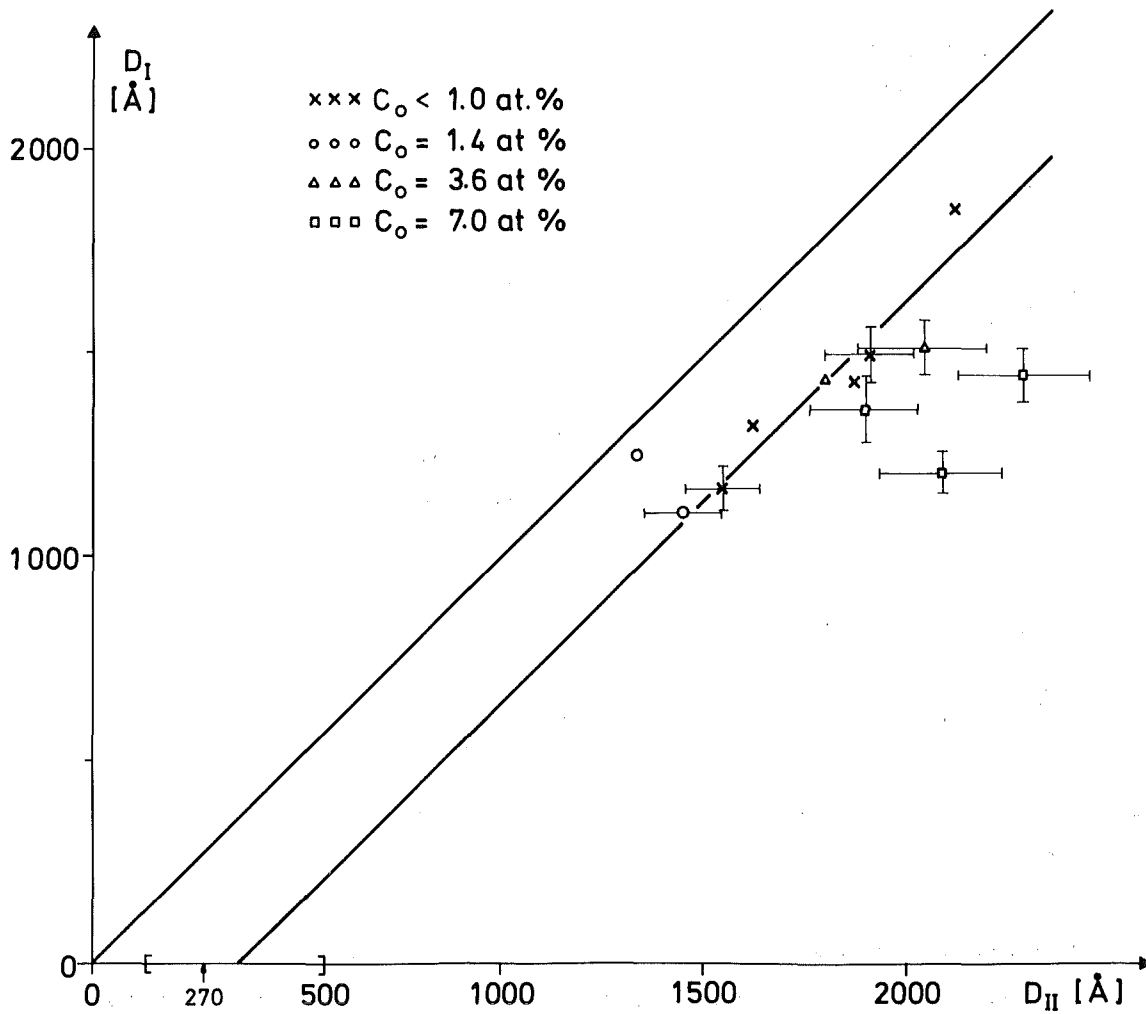


Fig. 1 Thickness of granular aluminium films

(D_I thickness given by method I, D_{II} by method II, C_O oxygen content of the films).

But figure 1 also shows that the films with 7 at. % oxygen lie significantly outside the linear fit (typical relative errors of D_{II} for these films are 7 %, for D_I errors are 4.5 % mainly due to the uncertainty of $(\Delta\rho/\Delta T)$, which was taken as the difference between the values of /1/ and /3/). There are two possible explanations for this fact:

- The oxygen content of 7 at. % leads to a strong deviation of Matthiessen's rule and method I can only be applied with a new $(\Delta\rho/\Delta T)$ - value
- The films are still in the percolation region, where the resistivity mainly results from the increase of conduction path length due to intervening insulating oxide particles. This oxide diminishes the effective current carrying thickness measured by method I, but within the conduction paths Matthiessen rule is still valid.

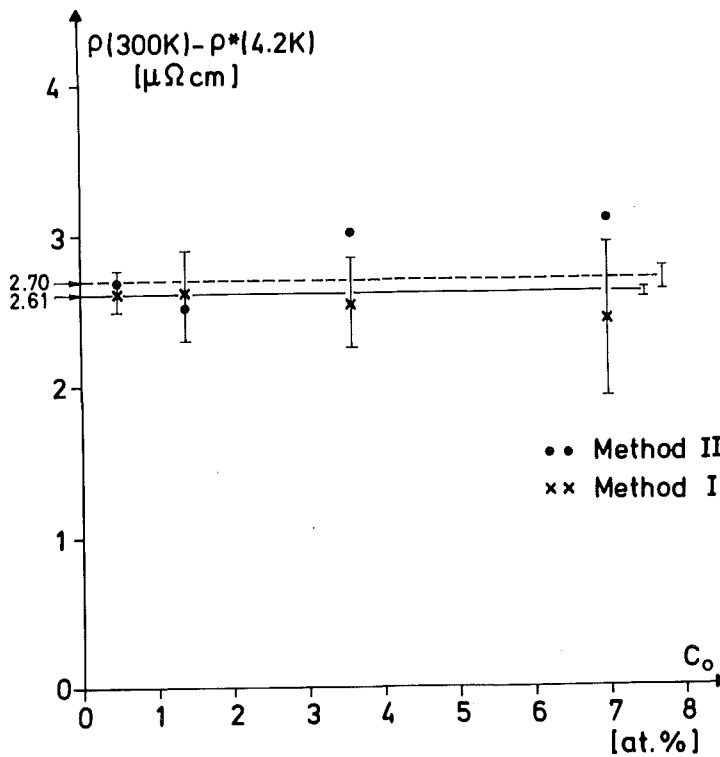


Fig. 2 Resistivity difference ρ (300 K) - ρ^* (4.2 K) as a function of oxygen content C_o .

To test these two assumptions the resistivity difference ρ (300 K) - ρ^* (4.2 K) was measured as a function of the oxygen content C_o , the results are shown in figure 2. ρ^* is the size-effect corrected value /4/ for the liquid helium temperature resistivity. The error bars, shown for method I in Fig. 2 are calculated from detailed error analysis. The errors for method II are even larger due to the uncertainty of the oxide thickness corrections. Also shown are the weighted average values for the two methods and their mean average deviations. One finds $2.61 \pm 0.03 \mu\Omega\text{cm}$ for method II and $2.70 \pm 0.08 \mu\Omega\text{cm}$ for method I, that means the two values overlap within their errors and are very close to the bulk-value at 20°C of $2.6548 \mu\Omega\text{cm}$ /3/.

In figure 3 as a further test of the above considerations the resistivities at 300 K, 93 K and 4.2 K are plotted as a function of the oxygen content C_o . Again the curves are parallel within the error bars.

From the results of the last two figures follows that the second assumption holds. For practical purposes then it can be concluded that for oxygen contents lower than 3.6 at. % method I may be applied, for higher oxygen contents method II together with corrections for the oxide thickness should

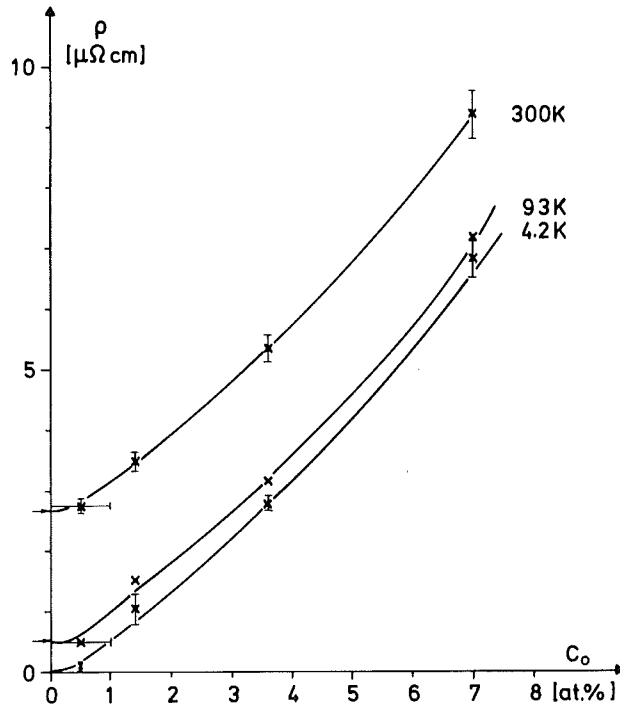


Fig. 3 Resistivity at 300 K, 93 K and 4.2 K as a function of oxygen content C_O .

be used. Since the oxygen content is correlated with the transition temperature to superconductivity (T_C) in these aluminium films /2/ the above statement reads, for films with a T_C lower than 1.4 K method I can be applied, for films with a higher T_C method II with oxide corrections must be used.

REFERENCES

- /1/ A.v. Bassewitz, G.v. Minnigerode, Z. Physik 181, 368 (1964)
- /2/ P. Ziemann, in Progress Report of the Teilinstitut Nukleare Festkörperphysik, Ges. f. Kernforschung Karlsruhe (KFK 2357), p. 88 (1976)
- /3/ Handbook of Chemistry and Physics, Ed. R.C. Weast, 50th edition
- /4/ A.M. Toxen, M.J. Burns, D.J. Quinn, Phys. Rev. 138, 1145 (1965)
- /5/ Catania Working Data, U.S.-Italy Seminar, Catania, Italy (1974)

4.3 Production of Metastable Lead-Bismuth Alloys

Chr. Gauss

The system Tl-Pb-Bi has been of great interest for the superconductivity, because in this system the electron-per-atom ratio can be varied from 3.0 to 4.3 and the electron-phonon coupling parameter λ from 0.8 to 2.0, respectively. A higher value than $\lambda = 2.0$ which corresponds to an alloy with the composition $\text{Pb}_{0.7}\text{Bi}_{0.3}$ in the crystalline state was never measured. This is due to the limited solubility of Bi in Pb which prevents a higher enrichment of Bi in Pb in the solid state.

The method of ion implantation is one possibility to raise the solubility beyond the thermal limit. However, the direct implantation of Bi^+ -ions into a saturated Pb-Bi film was not successful due to the high sputtering coefficient of about 65 in this ion-target system. A crude estimate indicated that only an enrichment of about 1.5 at. % Bi would be possible by direct implantation.

Therefore, we chose the method of recoil implantation to increase the Bi content in this system. Layers consisting of an eutectic mixture of Pb-Bi with precipitated Bi and a thickness of 200 nm have been prepared by codeposition. These layers were then bombarded with Ar^{++} -ions of 600 KeV. On their way through the film the Ar particles transfer energy to the target atoms by nuclear collisions, such that Bi atoms from the precipitates can be introduced into the saturated Pb-Bi phase by recoil implantation.

The Bi enrichment of the saturated Pb-Bi layers has been measured via the superconducting transition temperature. A maximum T_c -increase of 0.25 K could be measured, corresponding to an enrichment of 6 at. % Bi, which was calculated from the T_c -dependence on Bi concentration $T_c = 7.2 + 0.0423 \text{ K/at. \% Bi} / 1/$. These supersaturated alloys are not stable at room temperature and perform an eutectic phase-transition which is completed after 90 hours. From the analysis of this transformation it was found that the process is determined by Fick's 1. diffusion law and a diffusion constant of $D \approx 10^{-15} \text{ cm}^2 \text{ sec}^{-1}$ at 20°C has been evaluated.

REFERENCES

/1/ E. Nembach, J. Phys. Chem. Solids 29, 1205 (1968)

4.4 Proximity Effect in Ion Implanted Molybdenum Films

O. Meyer

In our previous work /1/,/2/ we have shown that ions having a larger electronegativity value than that of Mo will enhance the superconducting transition temperature T_C after implantation in pure Mo-layers. In Mo-layers with an oxygen content above 1 at. % T_C could be enhanced by implanting any kind of ion. The maximum T_C -value of 9.2 K was obtained for impurity concentrations between 14 and 30 at. %, depending on the kind of ion, and was attributed to a disordered Mo-phase stabilized by impurity atoms /2/,/3/. In the following we assume that the proximity effect is responsible for the observed increase of T_C with fluence ϕt and we hope to gain more insight on the formation mechanism and structure of this disordered phase. The calculation is based on the BCS theory using an effective $(N(o)V_{\text{eff}})$ -value as derived by DeGennes /4/ for layered structures ($N(o)$ is the electronic density of states at the Fermi level and V is the electron-electron interaction parameter):

$$T_C = T_{CO} \exp - (Q_O + Q_1 \frac{\langle d \rangle_s}{r})^{-1}$$

with $Q_O = RN_N V_N$, $Q_1 = RN_S V_S (N_S/N_N)$ and $R = N_S V_S / (N_S V_S - N_N V_N)$ where the index S refers to the matrix and N to the disordered regions. N_S/N_N is equal to 0.5 as has been measured with UPS for amorphous Mo films /5/. $\langle d \rangle$ is the average mean free distance between spherical disordered regions of radius r . Bansal and Ardell /6/ calculated the dependence of $\langle d \rangle_r$ on F , the disordered volume fraction. This function has to be extrapolated to F equal to 0.64 (random dense packing of spheres) for $\langle d \rangle_r$ - values smaller than 0.3.

i) Mo films contaminated with oxygen:

For Mo-layers having an oxygen concentration N_O of 15 at. % and a residual resistance ratio, r of 1.2, T_C increases steeply with Xe ion fluence (Fig. 1). In this case the reaction velocity of Mo being transferred into the disordered phase is proportional to the particle flux ϕ and independent of the impurity concentration: $dN_d/dt = K_1 \phi$ and $N_d = K_1 (\phi t)$ where N_d is the number of disordered regions/cm³ and ϕt is the fluence. The maximum T_C -value is reached when the

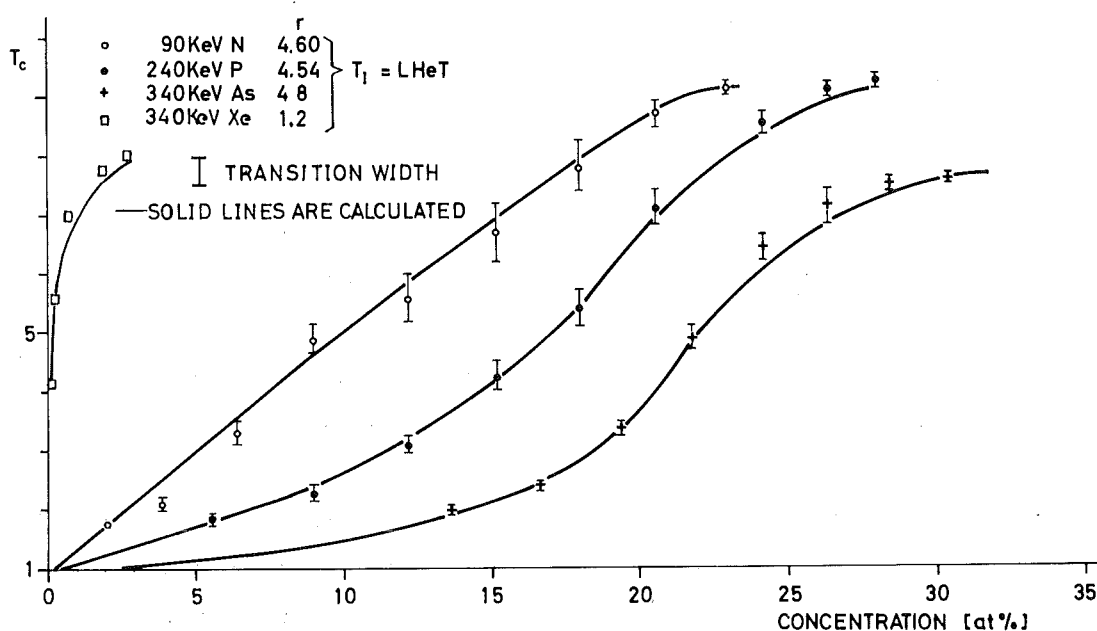


Fig. 1 T_c as function of ion concentration for a Mo-layer with high oxygen content ($\text{Kr}^+ \rightarrow \text{Mo} + 12 \text{ at. \% O}$) and pure Mo layers ($C_o < 1 \text{ at. \%}$). Solid lines are calculated using the proximity effect.

disordered regions touch each other e.g. for $F = N_d V_d = 0.64$ ($V_d =$ volume of a disordered region) or $F = K_1 \phi t V_d = 0.64$. With the values for $N_S V_S$ and $N_N V_N$ as obtained from the BCS formula for $T_c = 0.92 \text{ K}$, $T_c = 8 \text{ K}$ and $\theta_D = 460 \text{ K}$, the solid line as shown in Fig. 1 has been calculated. With N_d^{max} equal to N_o , V_d is found to be about $62 \text{ to } 78 \cdot 10^{-24} \text{ cm}^3$. About 4 to 5 Mo atoms have been displaced from their lattice site and are stabilized by one oxygen atom thus forming metastable Mo_4O , Mo_5O molecules.

ii) Mo films with impurity concentrations below 1 at. %:

If we assume a first order reaction for the formation of the disordered Mo-phase the increase of T_c should be proportional to the impurity concentration C_I present at any time during implantation: (dN_d/dt is equal to ϕ and C_I) $N_d = (\phi t) C_I \cdot K_1 = K_2 C_I^2$. The measured T_c -values for N implanted in Mo (Fig. 1) however cannot be described by a first order reaction. In order to fit the measured T_c -values (solid line in Fig. 1) we have to assume that the formation probability of Mo_xN_y -clusters during irradiation is proportional to C_N^2 e.g. F is equal to $K_3 C_N^3$. The formation probability K_3 is small ($K_3 = 5 \cdot 10^{-5}$) and the reaction is of second order. Two N atoms must be present at the same time in order to form an impurity stabilized Mo

atom cluster. With decreasing electronegativity values using P, As and Sb ions the formation probability of Mo-cluster decreases and for Sb ions implanted in Mo an increase of T_c is no longer observed. The measured T_c -values for P and As ions in Mo-layers can be described (solid lines in Fig. 1) by assuming reactions of higher order ($F_p = 3 \cdot 10^{-8} C_p^5$, $F_{As} = 1 \cdot 10^{-11} C_{As}^7$).

Using the proximity effect the results as shown in Fig. 1 and for the systems Mo-B and Mo-C can be well described by the reaction kinetics of metastable molecules formed under irradiation with compositions of about Mo_8N_3 , $Mo_{16}P_4$, $Mo_{24}As_6$, $Mo_{24}B_6$ and $Mo_{24}C_6$. For complicated interstitial carbide phases, most thoroughly studied, it is known that sub-cells with the composition $M_{23}C_6$ do indeed exist /7/. Among those $Mo_{23}C_6$ has also been observed. Therefore it is believed that the formation process of defect clusters activated by irradiation offers a reasonable explanation for the observed implantation effects.

REFERENCES

- /1/ O. Meyer, H. Mann, and E. Phrilingos, in Appl. of Ion Beams to Metals (S.T. Picraux, et al., eds., Plenum Press, New York, (1974)) p. 15
- /2/ O. Meyer, Inst. Phys. Conf. Ser. No. 28, 168 (1976)
- /3/ G. Linker and O. Meyer, Sol. State Comm. 20, 695 (1976)
- /4/ P.G. DeGennes, Rev. Mod. Phys. 36, 225 (1964)
- /5/ B. Schroeder, W.L. Johnson, C.C. Tsuei, P. Chaudhari, and J.F. Craczyk, AIP Conf. Proc. (USA) 31, 353 (1976)
- /6/ P.B. Bansal and A.J. Ardell, Metallography 5, 97 (1972)
- /7/ W. Hume-Rothery, R.E. Smallman, and C.W. Haworth, The Structure of Metals and Alloys, Inst. of Metals 17 Belgrave Square, London (1969)

4.5 Preparation of Superconducting Vanadium Layers

G. Linker and R. Smithey

Superconducting vanadium layers with varying oxygen contents were prepared by electron beam evaporation for irradiation experiments (see following report). The layers were deposited onto quartz, sapphire and carbon substrates. The background pressure in the evaporation chamber prior to evaporation was typically $2 \cdot 10^{-9}$ Torr and rose to $5 \cdot 10^{-9}$ Torr at evaporation rates of $10 \text{ \AA}/\text{s}$ and to $1 \cdot 10^{-7}$ torr at the maximum rate of $160 \text{ \AA}/\text{s}$. The substrates were baked before evaporation in situ, then deposition was performed either on substrates kept at room temperature or heated to $560 - 800^\circ \text{C}$. To introduce oxygen into the layers, the oxygen was admitted and the partial pressure during evaporation was varied in the range of $5 \cdot 10^{-8}$ to $5 \cdot 10^{-6}$ Torr.

Layer thickness, purity, homogeneity and the oxygen content and distribution have been analyzed by Rutherford backscattering of 2 MeV ^4He ions. Layers deposited onto the carbon substrates were used for this analysis thus allowing an oxygen concentration determination down to about 0.2 at.%. The layers had thicknesses in the range from 1500 to 2500 \AA and revealed pronounced oxide peaks on the surfaces. In some layers oxide peaks at the layer-substrate interface or oxygen diffusion tails from the surface oxide into the layer have been observed. Typical oxygen distribution profiles deduced from backscattering spectra are shown in Fig. 1.

Samples with the lowest oxygen content were produced at elevated substrate temperatures. Here concentrations in the range from 1.5 at.% to "not detectable" (~ 0.2 at.%) were found. Deposition at similar evaporation conditions onto substrates kept at room temperature led to higher oxygen contents up to 4 at.% and layers prepared under oxygen atmosphere had concentrations in the range of 4 to 40 at.%.

The residual resistivity ratio r (defined as the ratio of resistances at room temperature and before transition into the superconducting state) was determined as a measure of layer quality. This value however showed no close correlation with oxygen content and values of 4.5 to 6 were determined in layers with a few at.% oxygen. Best values however were found in

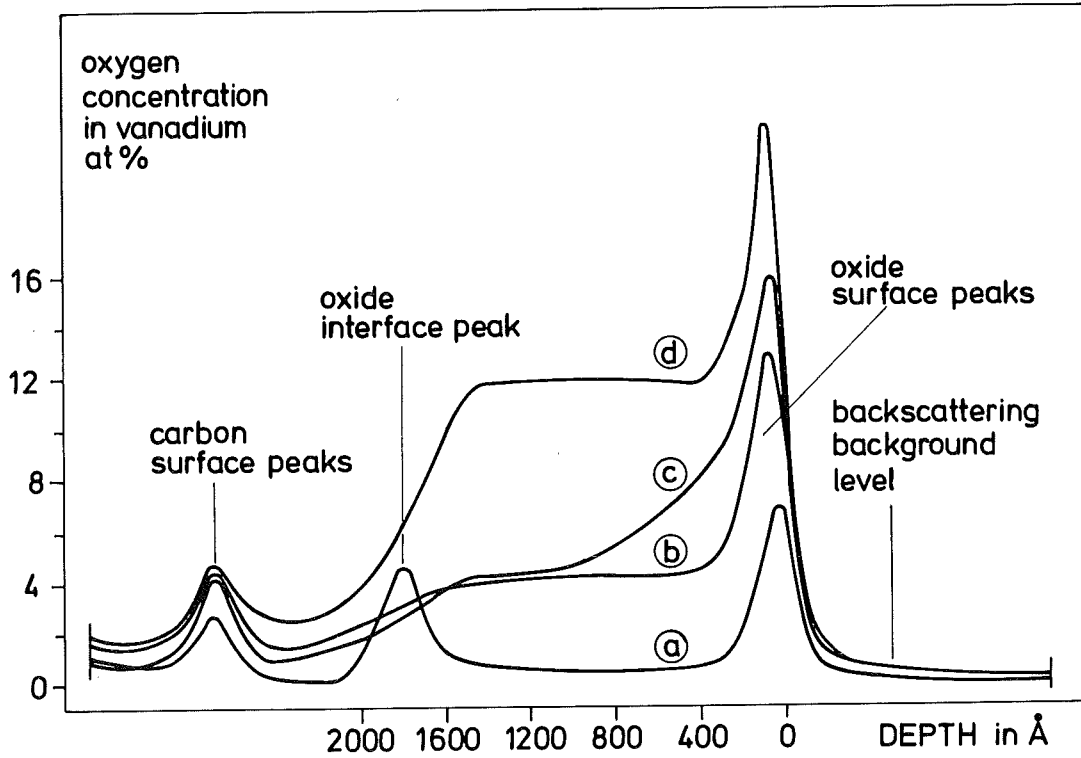


Fig. 1 Oxygen distribution profiles in evaporated V-layers
a) layer with a low homogeneous oxygen content exhibiting an oxide peak at the layer-substrate interface
b) + d) layers with medium and high oxygen content with reasonable homogeneity
c) sample with inhomogeneous oxygen concentration.

layers with least oxygen content and the maximum r of 11 was measured in a layer where no oxygen could be detected with the backscattering technique. Beyond an oxygen content of about 5 at.% r decreased and had a value < 1 for the layer with 40 at.% oxygen. X-ray analysis of the layers with high oxygen content (> 10 at.%) showed the strongest vanadium bcc lines however considerably broadened as compared to lines from a pure sample, this broadening increasing with oxygen content. In addition a line shift to lower angles, from which a lattice parameter increase of about 0.5 % has been estimated, was observed. The layer with 40 at.% oxygen revealed an amorphous-like structure.

4.6 Influence of Impurities on the Superconducting Transition Temperature of Ion Bombarded Vanadium Layers

G. Linker and M. Kräatz

Strong depressions of the superconducting transition temperature T_c in group Vb transition metal elements under ion irradiation have been observed in earlier studies /1/. The influence of impurities on the T_c depressions could not be excluded in those experiments however was not explicitly studied. Here, in an extension of our previous work, the influence of irradiation activated impurities present in a layer and of implanted impurity atoms on T_c of evaporated vanadium layers is investigated.

The V-layers were prepared by electron beam evaporation (see preceding report). T_c of the as-evaporated layers was in the range of 4.9 - 5.25 K and did not depend on oxygen concentration up to a few at. % thus indicating that oxygen was not dissolved in the vanadium but must have been incorporated in another form like e.g. in oxide precipitates.

Irradiation of the layers with $2.9 \cdot 10^{16} \text{ Ne}^+/\text{cm}^2$ at 320 keV, such that the Ne^+ ions penetrated the layers creating disorder on their paths, led to T_c depressions which were depending on the oxygen content in the layers. For layers with the lowest oxygen content small decreases in the range of 0.1 - 0.2 K were observed, then with increasing oxygen content relative depressions $\Delta T_c/T_c$ up to 0.4 occurred. It is thought that in the irradiation procedure oxygen is moved from an inactive (oxide precipitates) to an active position, here interacting with displaced lattice atoms and stabilizing a disordered structure.

In addition nitrogen and neon ions have homogeneously been implanted into vanadium layers with the lowest oxygen content. The relative T_c changes as a function of nitrogen concentration are illustrated in Fig. 1, and an almost linear relationship between $\Delta T_c/T_c$ versus nitrogen concentration is observed down to the T_c detection limit (1.2 K). For the neon implantations much smaller effects than for nitrogen were observed.

From these results it is concluded that the T_c depressions in the irradiated or implanted V layers are not due to oxygen being dissolved

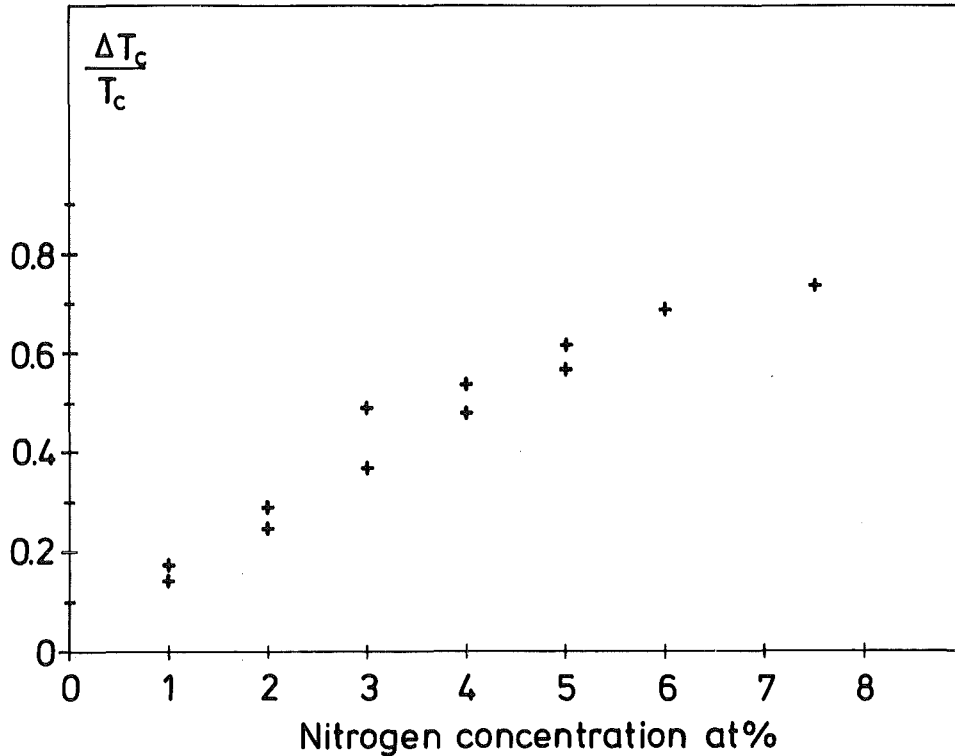


Fig. 1 Relative T_c decreases in vanadium layers implanted with nitrogen as a function of nitrogen concentration.

through the irradiation procedure (alloying effect), but that disorder generated during irradiation must be stabilized by the chemically active either implanted (nitrogen) or activated impurity (oxygen) atoms which are interacting with displaced lattice atoms. Preliminary X-ray analysis still revealed the vanadium bcc-structure in the disordered layers. However a line broadening and a considerable increase of the lattice parameter ($\sim 1\%$) was observed. The results will be published in greater detail elsewhere /2/.

REFERENCES

- /1/ G. Linker and O. Meyer, Ion Implantation in Semiconductors (ed. S. Namba, Plenum Press, New York 1975), p. 309
- /2/ G. Linker, Proc. Int. Disc. Meet., Rad. Effects Supercond., ANL, June 1977

4.7 Energy Dependent Channelling Analysis of Disorder in Ion Bombarded Metal Crystals

G. Linker

Channelling effect and backscattering measurements with energetic light ions have been widely employed for defect analysis in ion implanted semiconductors. Here a well resolved disorder peak is usually observed at the range of the implanted impurities originating from direct backscattering from displaced lattice atoms. Aligned backscattering spectra from ion bombarded metals, however, generally reveal a monotonous increase of the dechannelling yield and no damage peak is observed thus complicating the disorder analysis. Then usually complementary analysis such as transmission electron microscopy must be performed. However, also by channelling analysis itself different types of defects may be separated in metals when energy dependent measurements are performed, as has been suggested by Quéré /1/. This method relies on the different dependences of dechannelling cross sections on the energy of the analysing particles.

In this contribution results from the energy dependent channelling analysis of vanadium and molybdenum single crystals implanted either with N or C ions or bombarded with Ne ions are reported. Channelling has been performed along the [100] direction with $^4\text{He}^+$ particles and energies in the range of 1.0 - 2.8 MeV have been used. Typical spectra from a Mo crystal implanted with C^+ ions are shown in Fig. 1 with the energy of the analyzing particles as a parameter. Here a well resolved disorder peak appears at the range of the implanted impurities with increasing energy. For neon ion implantations however only a continuous increase of the dechannelling yield versus depth has been observed and no change of this behaviour occurred with increasing energy of the analyzing particles.

Plots of the dechannelling yields versus energy have shown the presence of different types of defects depending on the implanted impurities, implantation energy and depth. For the Ne^+ implantations beyond the ions projected range dechannelling was found to be energy independent thus showing the presence of stacking faults or voids. Within the ions projected range a \sqrt{E} dependence indicated the presence of dislocations or slightly misoriented regions. For the samples implanted with chemically active impurities in addition to a high

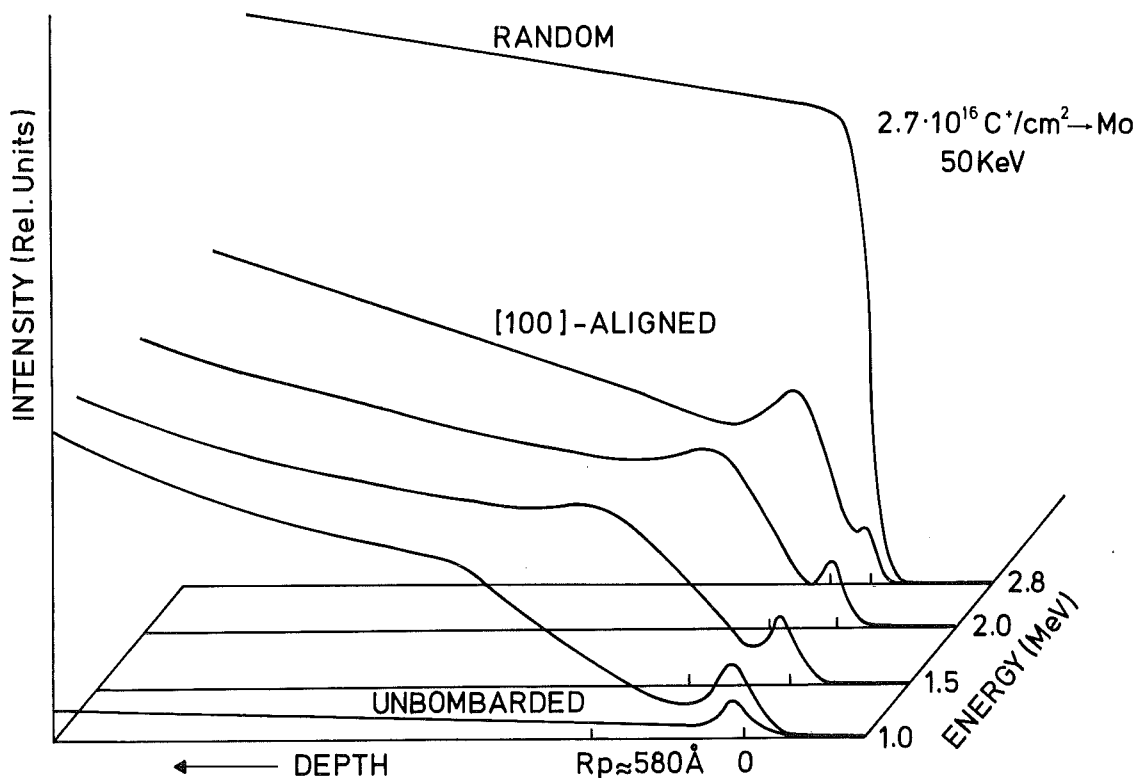


Fig. 1 Backscattering spectra of a [100] aligned Mo crystal implanted with $2.7 \cdot 10^{16} \text{ C}^+ / \text{cm}^2$ at 50 KeV with the analyzing beam energy as a parameter.

energy independent dechannelling component a second component with a slight decrease of the dechannelling yield versus energy was observed. This decrease is in agreement with the energy dependence of the dechannelling from randomly distributed lattice atoms present e.g. in impurity-defect clusters or precipitates.

Though in this kind of analysis a quantitative separation of different types of defects is difficult to perform, qualitatively however different types of defects were detected in Ne^+ or N^+ and C^+ implanted V and Mo crystals, and the use of a high analysing beam energy has proved favourable in the extraction of disorder peaks. Neon gave mainly rise to extended defects like dislocations or stacking faults whereas with chemical active impurities additional defects consisting of locally displaced lattice atoms were detected. It is thought that these local defects are stabilized by the impurities in impurity-defect clusters.

REFERENCES

/1/ Y. Quéré, J. Nucl. Mat. 53, 262 (1974)

4.8 The Dynamic Conductivity of Nb-I-Ag and Ta-I-Ag Tunneling Diodes at Low Energies

J. Geerk and K. Gärtner^a

^a*Institut für Werkstoffe der Elektrotechnik, Universität Bochum*

Tunneling measurements on the transition metals Ta and Nb have so far been carried out by Shen /1/, Gärtner /2/, Bostock et al. /3/ and Robinson et al. /4/. The results for Ta have been in good agreement with the present theory of superconductivity. The Coulomb-pseudopotential μ^+ obtained for Nb however was always too low compared to the expected value of 0.13. Robinson obtained a value of 0.04, whereas the other experimentalists obtained negative values of μ^+ ranging from -0.05 to -0.02. As the μ^+ value calculated from the inversion of the Eliashberg gap equations is sensitive to the shape of the phonon structure at low energies above the gap-edge, we performed tunneling measurements on Ta and Nb in this low energy region.

For the measurements of the first derivative dI/dV the apparatus described in /5/ was used in connection with the automatic data collection facility described in /6/. The phonon structure has been extracted by normalizing the measured density of states to a temperature smeared BCS-density of states, which was computed to 1 part in 10^5 . The technique of the junction-preparation is described in /2/.

The Ta-junctions showed a phonon structure with a nearly constant behaviour at energies below 8 meV, as it is expected for energies somewhat below the first big peak of the phonon spectrum. The gap-inversion yielded for μ^+ a value of 0.13.

Fig. 1 shows the phonon induced structures of two Nb-I-Ag junctions. At energies below the region where the transverse phonons of Nb which are peaked at 15 meV appear, the behaviour in contrast to Ta is not flat for both junctions. Junction 1 shows a drop of the curve at about 5 meV and at a somewhat lower energy the structure takes even negative values. Junction 2 shows a similar effect more pronounced and at slightly higher energies such that the whole phonon structure appears deformed up to the energy of the longitudinal resonance at 25 meV. Such an unusual drop of the phonon structure

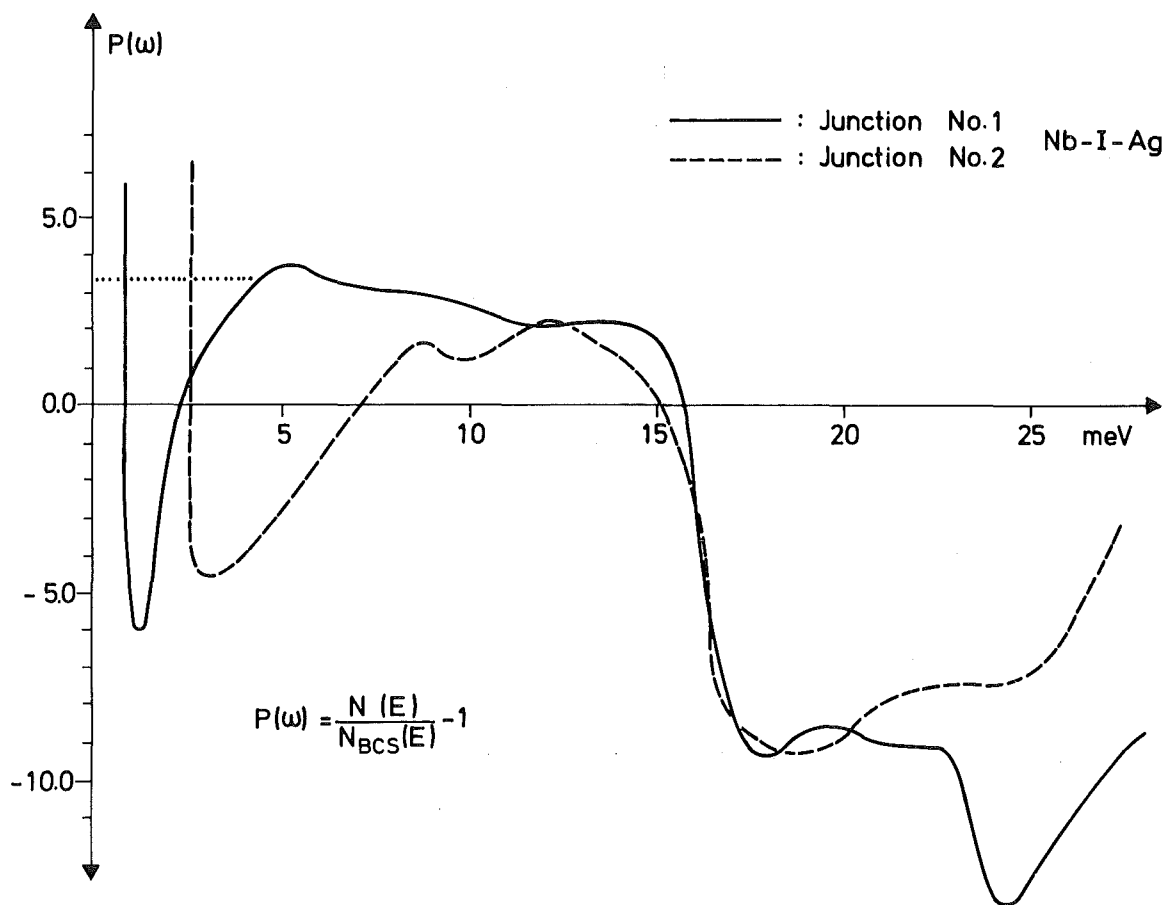


Fig. 1 The phonon induced structures in the density of states of two Nb-I-Ag tunnel junctions.

at low energy has been interpreted by Rowell and Dynes /7/ in terms of a superconductor-normal metal sandwich structure below the oxide of the tunneling barrier. Geometric resonance effects of the elementary excitations of the superconductor cause then additional oscillatory terms in the superconducting density of states as measured in a tunneling experiment. The observed drops in junction 1 and junction 2 at low energies represent the first minimum of this oscillation. Theoretical estimates using the approximate formula of Rowell /8/ show, that a coverage of 3 to 5 % of the tunneling surface by some hundred Å of normal metal - for example oxygen contaminated Nb-metal - can explain the behaviour of junctions 1 and 2.

Junction 1 was evaluated by the gap-inversion technique. The phonon structure below 5 meV was taken to be constant as indicated by the dotted line in Fig. 1. The oscillatory term in the density of states is

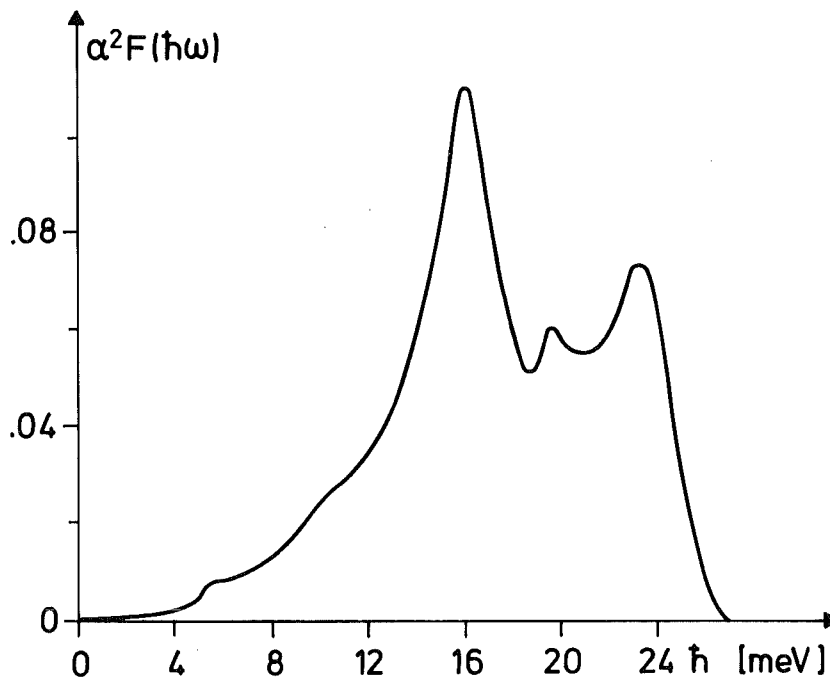


Fig. 2 The Eliashbergfunction $\alpha^2(\omega) \cdot F(\omega)$ of niobium calculated from junction 1.

exponentially damped with increasing energy. Thus it should not disturb the phonon structure at the energies of the main phonon peaks.

Fig. 2 shows $\alpha^2(\omega)F(\omega)$ from junction 1 extracted through gap inversion. The bulk value of 1.54 meV has been inserted for Δ_0 . For μ^+ a value of - 0.021 was obtained. The peak of the longitudinal phonons at 25 meV is a little more pronounced compared to the measurements of Bostock et al. and Robinson et al., despite the fact, that Robinson et al. got a far higher value for μ^+ . The low μ^+ -value of our junction will be subject of further investigations.

REFERENCES

- /1/ L.Y.L. Shen, Phys. Rev. Lett. 24, 1104 (1970)
- /2/ K. Gärtner, Dissertation 1974 Universität Bochum
- /3/ J. Bostock, V. Diadiuk, W.N. Cheung, K.H. L, † R.M. Rose, and M.L.A. MacVicar, Phys. Rev. Lett. 36, 603 (1976)
- /4/ B. Robinson, T.H. Geballe, and J.M. Rowell, Superconductivity in d- and f-Band Metals, p. 381 (1976), edited by D.H. Douglass
- /5/ J. Geerk, Progress Report of the Teilinstitut Nukleare Festkörperphysik, Ges. f. Kernforschung (KFK 2357), p. 105 (1976)
- /6/ J. Geerk, this report p. 140
- /7/ J.M. Rowell, Superconductivity in d- and f-Band Metals (1976), p. 406 edited by D.H. Douglass
- /8/ W.L. McMillan and J.M. Rowell, in Superconductivity in d- and f-Band Metals (1976), p. 381, edited by D.H. Douglass

4.9 Superconducting Partial Isotope Effect for $\text{VN}^{14/15}$

B. Hofmann-Kraeft and H. Rietschel

First measurements of the partial isotope effect on VN have already been reported /1/. In the meantime about 200 additional T_c measurements were performed together with X-ray diffraction and Rutherford backscattering analysis.

It turned out that the onset T_c of superconductivity depends on the size of the substrate as well as on its position on the Mo-plate during sputtering, the highest T_c 's being found in the middle of the large quartz discs ($\phi : 25 \text{ mm}$). Fig. 1 gives an example. The substrate material is of minor importance and the films on graphite differ from those on quartz mainly in the transition width (0.10 K on quartz, 0.25 K on graphite). This effect may be due to the rougher graphite surface which complicates the crystal growth. Taking account of these findings we used only the T_c 's in the middle of the large quartz discs to determine the isotope shift.

The uncertainties in the determination of stoichiometry and lattice constants were too large in order to guarantee the comparability of different samples. Therefore, we compared those five VN^{14} - and VN^{15} -samples, which had the highest T_c 's respectively, arguing that maximum T_c 's should be achieved under optimal and therefore comparable conditions. These ten

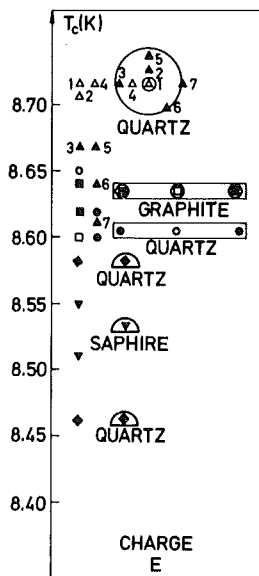


Fig. 1 Dependence of T_c on the position and size of the substrate

selected charges showed a similar distribution of lattice constants ($4.125 \pm 0.005 \text{ \AA}$), preferred orientations ([110] - and [111] - direction perpendicular to the surface) and oxygen contents of 2 ± 1 at. %.

Fig. 2 shows the measured isotope shift between these ten charges. The mean shift $\Delta T_c = T_c(\text{VN}^{15}) - T_c(\text{VN}^{14})$ is 0.06 K, whereas the difference between the two highest T_c 's is 0.08 K. A theoretical interpretation of these findings is still under progress.

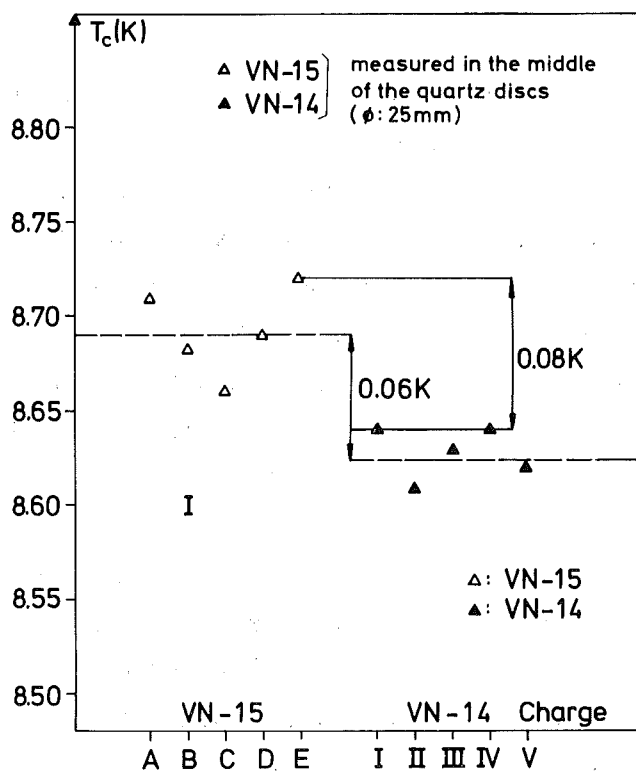


Fig. 2 Isotope shift for the ten selected samples

REFERENCES

- /1/ B. Hofmann-Kraeft and F. Ratzel, Progress Report of the Teilinstitut Nukleare Festkörperphysik, Ges. f. Kernforschung (KFK 2357), 102 (1976)

4.10 Structural and Superconducting Properties of Sputtered Vanadium-Nitride Layers

H.J. Klein

In the course of the investigation of refractory materials the study of sputtered VN layers was continued. The layers were prepared by reactive sputtering in an argon-nitrogen plasma on quartz and carbon substrates. The nitrogen pressure and the substrate temperature were varied in the range of 10^{-4} to 10^{-1} Torr and 100°C - 1000°C , respectively. The stoichiometry of the layers, their thickness, homogeneity and purity were determined by back-scattering of 2.3 MeV alpha particles from layers deposited onto carbon substrates. The superconducting transition temperature T_c was measured resistively using a standard four point probe arrangement. The microstructure of the layers was investigated using scanning electron microscopy (SEM). Lattice parameters were determined from X-ray diffraction patterns obtained with a thin film camera with a Seemann-Bohlin focussing system.

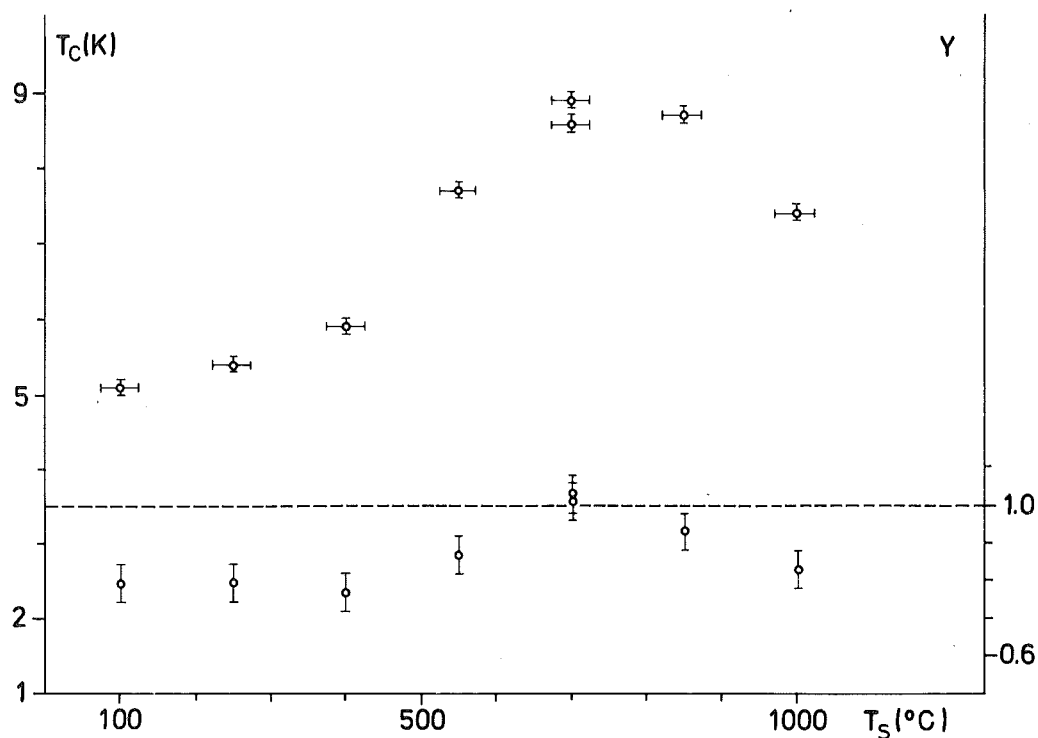


Fig. 1 T_c versus substrate temperature (upper part) and T_c versus composition Y (lower part)

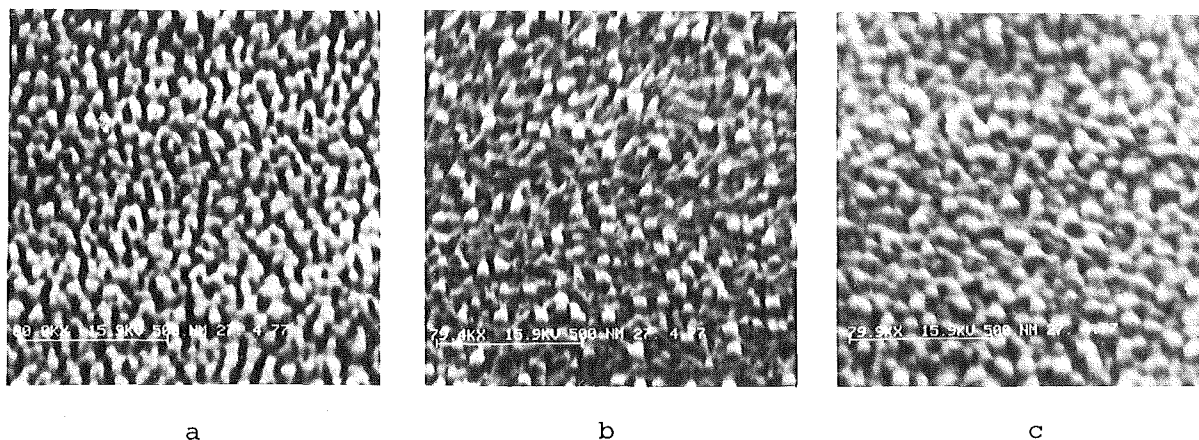


Fig. 2 SEM micrographs of layers sputtered at a) 100°C, b) 700°C, and c) 1000°C.

Results: Layers with NaCl-structure were formed for nitrogen pressures above 10^{-3} torr and had thicknesses of typically 2000 Å. The stoichiometry of the layers in this pressure range was almost independent of the nitrogen partial pressure except for the high pressures around 10^{-1} Torr. However it was sensitive to the substrate temperature. Optimum values were obtained at 700°C. Similarly, T_c depended on the substrate temperature. This dependence is shown in Fig. 1, with a maximum T_c of 8.9 K (onset value) coinciding with the optimum composition, in agreement with previous measurements [1]. T_c also was found to depend markedly on Y (Y being the ratio of the number of nitrogen atoms to the number of vanadium atoms in the layers). Only for layers with $Y > 0.85$ was T_c above 8 K, increasing to $T_c = 8.9$ K for $Y = 1$. Different substrate materials had practically no influence on T_c .

In addition the microstructure of the layers was investigated as a function of nitrogen pressure and substrate temperature. A columnar void type structure was observed in the films, consisting of columnar-like crystallites growing nearly perpendicular to the substrate surface, with the void density depending on nitrogen partial pressure and substrate temperature. At nitrogen partial pressures above 10^{-3} Torr and temperatures below 400°C pronounced voids between the columns appeared. With increasing temperature the number and size of the channels and voids decreased. Above 700°C an almost dense packing of columns was observed. As an example typical SEM micrographs of VN layers sputtered at 100°C, 700°C, 1000°C are shown in Fig. 2.

The X-ray diffraction patterns indicate that all samples with high T_c and having $Y > 0.75$, prepared at nitrogen pressures above 10^{-3} Torr, had the pure NaCl structure.

Lattice constants increased rapidly from 4.087 for $Y = 0.77$ to 4.145 for $Y = 0.95$ with increasing nitrogen content in agreement with data reported by Brauer /2/.

REFERENCES

- /1/ B. Hofmann-Kraeft, Progress Report of the Teilinstitut Nukleare Festkörperphysik, Ges. f. Kernforschung (KFK 2183), 81 (1975)
- /2/ G. Brauer and J. Schnell, J. Less-Common Metals 6, 326 (1964)

4.11 Channeling Studies in C-Implanted $NbC_{0.89}$ Single Crystals

J.M. Lombaard^a and O. Meyer

^a*Physics Department, University of Pretoria, Pretoria 0002, South Africa*

The channeling studies described in this chapter are closely related to results /1, 2/ from similar C-implanted single crystals, where T_c has been measured as a function of implantation and annealing temperature. From these previous studies it is known that T_c increases from 4 to 11 K after C-implantation at 830°C , a further increase to 11.5 K is observed after additional annealing at 1070°C and is not affected during further annealing up to 1190°C .

The purpose of the following work is to determine the radiation induced disorder in the C-sublattice for these various implantation and annealing temperatures. Implantation of $5 \cdot 10^{16}$ C/cm² at 80 keV and $1.5 \cdot 10^{17}$ C/cm² at 200 keV, corresponding to an amount of about 12 % over a depth of 3000 \AA , have been performed at 825°C . Backscattering and reaction spectra for the random oriented and [110] aligned crystal have been taken after implantation

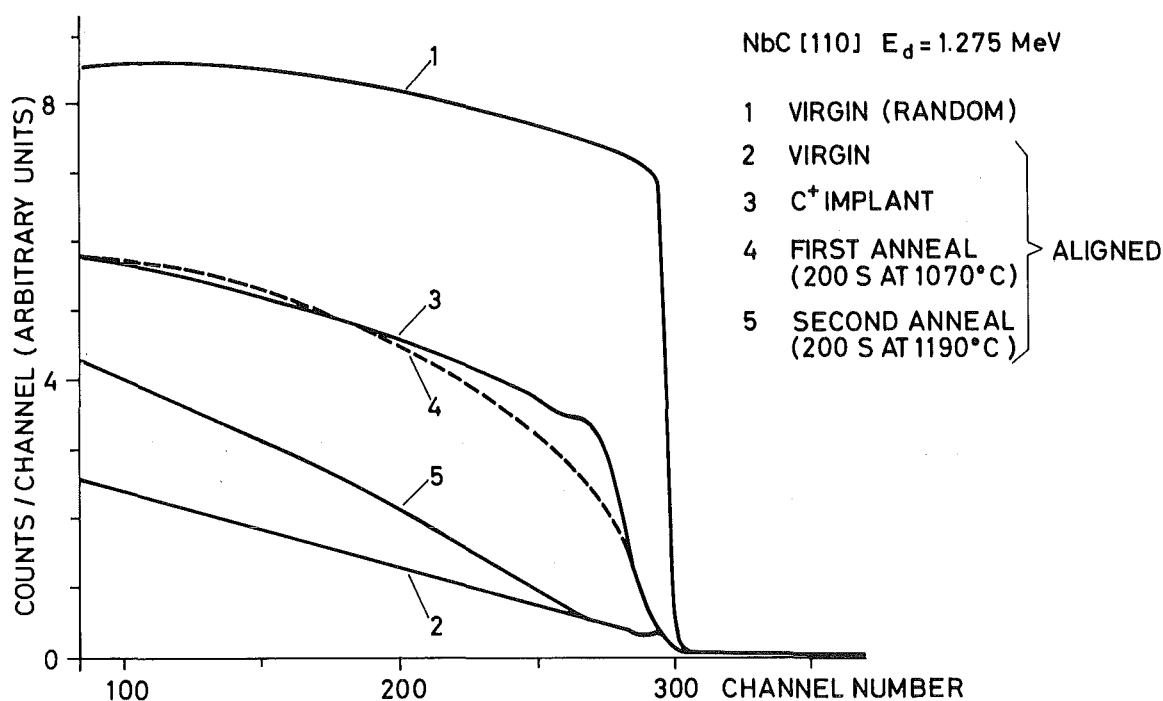


Fig. 1 Random and [110] aligned energy spectra of 1.275 MeV deuterons elastically scattered from a NbC single crystal before and after C⁺-implant and after two annealing stages ($\theta = 165^\circ$).

and after annealing at 1070°C and at 1190°C for 200 s. The spectra taken at the different annealing stages are presented in Fig. 1 for the Nb (d,d) elastic part and in Fig. 2 for the $^{12}\text{C}(d,p)^{13}\text{C}$ reaction part. The shape of the spectra in Fig. 2 resembles the reaction cross section as a function of energy; the depth corresponding to the width of the peak at high energies is about 8000 Å. The amount of implanted C can be estimated from the difference in yield of the random spectrum prior and after C-implantation (spectrum 1 and 3 in Fig. 2).

A remarkable difference can be seen in comparing the dechanneling yield defined as the ratio of the yield in the aligned spectra minus the yield in the aligned spectra of the virgin crystal to the yield of the random spectra in the Nb- and in the C-sublattice. The dechanneling yield for the Nb-sublattice increases steeply with depth and is about 0.25 at half height and saturates at 0.39, whereas for the C-sublattice the dechanneling yield is about 0.75 in the implanted region. As the dechanneling yield is proportional to the amount of damage present it is concluded that there is more damage in the C-sublattice than in the Nb-sublattice. It has been shown previously /1/ that annealing of

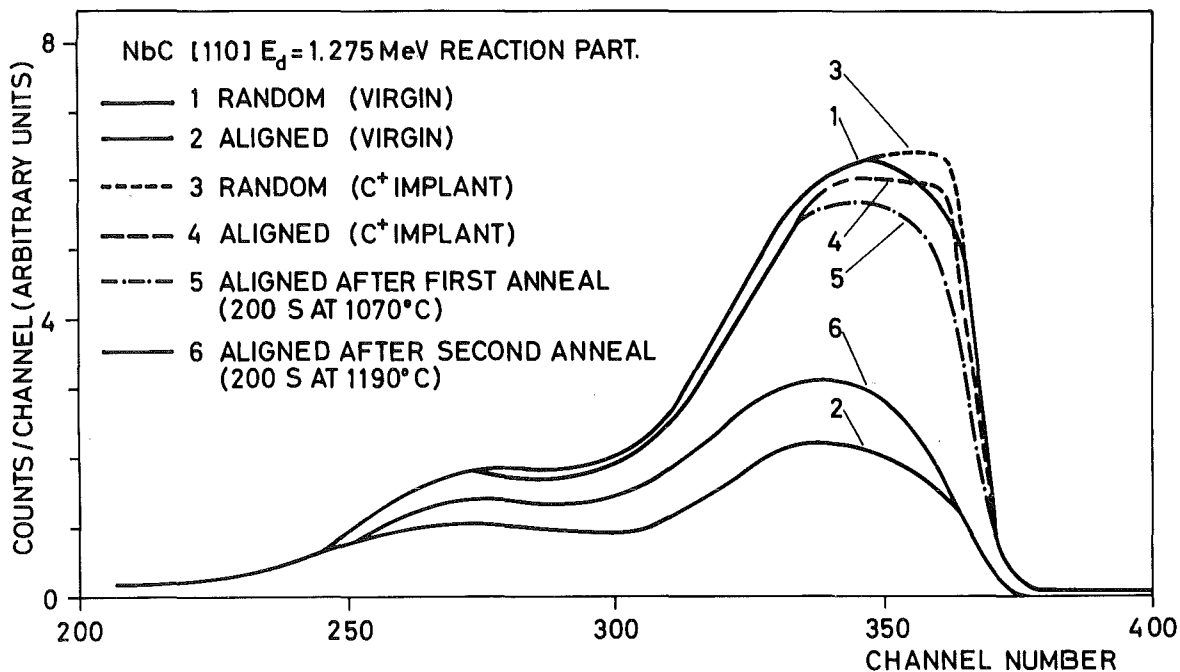


Fig. 2 Random and [110] aligned energy spectra of protons emitted at 165° during the bombardment of a NbC single crystal with 1.275 MeV deuterons.

Nb atoms in NbC displaced by implantation at room temperature, has already occurred for implants at 830°C . The shape of the dechanneling curve for the Nb sublattice after C implantation at 830°C indicates that the damage is not due to single defects but rather to extended defects such as stacking faults and dislocations for example.

In order to get more information on the kind of damage that prevails in the Nb sublattice after C implantation at 830°C the energy of the He beam has been varied between 1 and 2.8 MeV. It is known /3/ that from the energy dependence of the dechanneling yield some conclusions can be drawn on the type of defects. The dechanneling yield as a function of depth has been measured at 1.0, 2.0 and 2.8 MeV. No energy dependence could be observed and this excludes simple one-dimensional defects such as point defects or dislocations but can be explained by stacking faults. These spatially extended damage components will contribute to the dechanneling yield of the Nb as well as of the C sublattice.

For the annealing at 1070°C and 1190°C the recovery of the Nb-sublattice and the C sublattice occurs at the same time. The dechanneling yield after annealing at 1070°C is about 0.55 for the C sublattice and 0.20 for the Nb sublattice, at 1190°C the recovery is nearly completed with about 0.09 dechanneling yield in the C-sublattice and 0.04 in the Nb-sublattice near the surface.

The enhanced dechanneling yield observed for the C-sublattice may be due to C-precipitations. As T_C increases from 4 to about 10.5 K during C-implantation at 825°C , it is concluded that T_C of NbC is rather insensitive to the presence of these extended defects. The insensitivity of this material to radiation damage has been shown previously for Ar-bombarded NbC thin films /4/.

REFERENCES

- /1/ J. Geerk and K.G. Langguth, Solid State Comm. 23, 83 (1977)
- /2/ J. Geerk, K.G. Langguth, G. Linker, and O. Meyer, IEEE Transactions on Magnetics, Vol. MAG-13, 662 (1977)
- /3/ Y. Quéré, Radiation Effects 28, 253 (1976)
- /4/ O. Meyer, H. Mann, and E. Phrilingos, Application of Ion Beams to Materials, Eds. S.T. Picraux, E.R. EerNisse and F.L. Vook, Plenum Press, N.Y. (1974)

4.12 Computer Simulation of Channeling in V_3Si with a Modified Binary Collision Model

R. Kaufmann

It is well known that channeling is a sensitive method for studying not only properties of a "perfect" crystal, like e.g. the temperature dependence of the mean vibrational amplitudes, but also changes of the "perfect" crystal due to, e.g. lattice defects introduced by ion bombardment /1/. It is very difficult however to introduce all the parameters into the continuum model, which are necessary to extract quantitative results, as damage distribution for instance, from experimental data. Such parameters are electronic stopping power, angular dispersion due to electrons and amorphous surface layers, and the mean

vibrational amplitude. Therefore a Monte-Carlo-program has been developed using a modified binary collision-model to simulate the channeling process /2/. The program is now running for V_3Si with A15-structure but can easily be changed to other crystallographic structures.

For the simulation the unit cell is divided into several slices perpendicular to the desired channeling direction corresponding to the different atomic planes (Fig. 1). The incident particles are distributed uniformly over the first plane and the trajectories are then evaluated by calculating the deflection in this plane and by averaging the energy loss over the slice thickness. Assuming that the deflection takes place immediately in the planes and that the ions move linearly between two scattering events, the entrance coordinates for the next atomic plane are determined. The scattering angle is calculated in the momentum approximation /3/ by summing up the contributions of the binary collisions between an ion and each atom in the plane. This procedure is correct within the approximation used, which itself can be applied up to scattering angles of about 20° . The electronic energy loss (the nuclear part can be neglected, because the ion energies considered are in the MeV-region) is divided into an impact-parameter-dependent term due to collisions with closed-shell electrons and into a

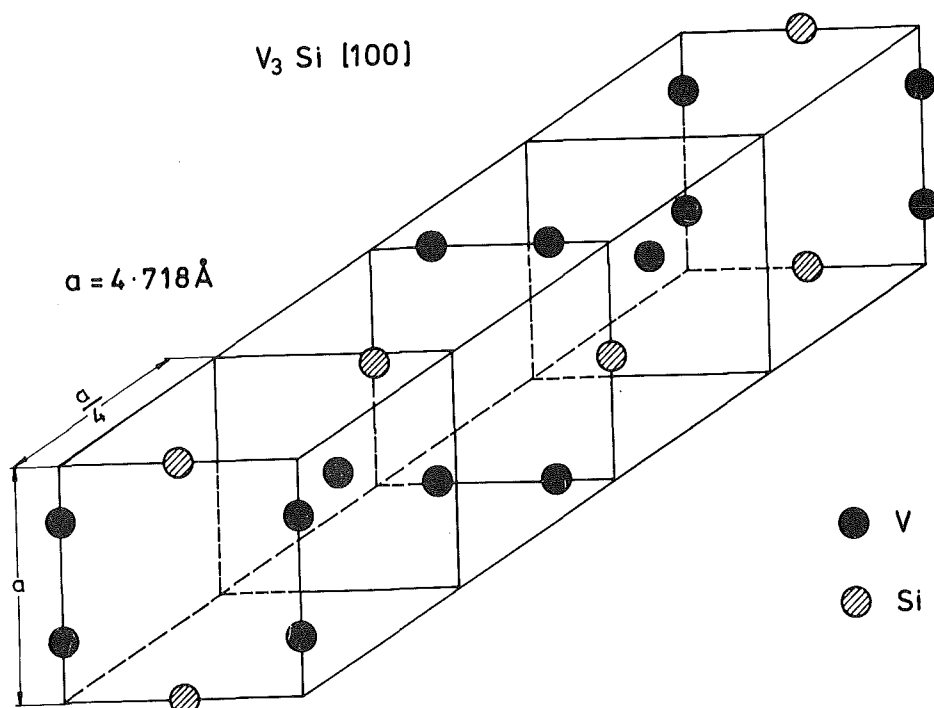


Fig. 1 Unit cell of V_3Si ; the lattice spacing in $[100]$ -direction is expanded to show the different scattering planes.

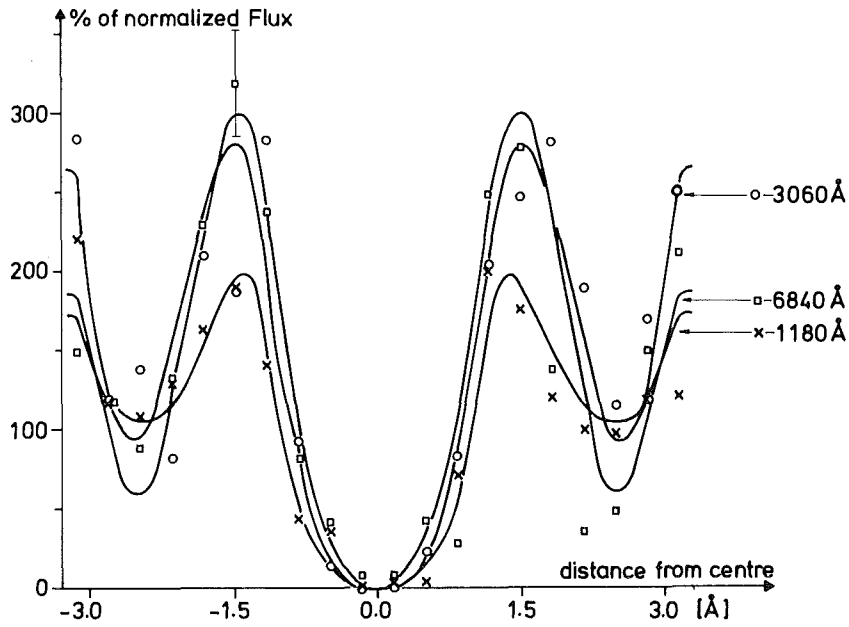


Fig. 2 Flux distributions recorded at various depths, each profile is averaged over 100 lattice spacings and taken along the plane diagonales; the error bar is calculated according to the statistics of 400 incident particles. It is clearly seen that the flux profile is developed to its full height at a depth of 3000 Å.

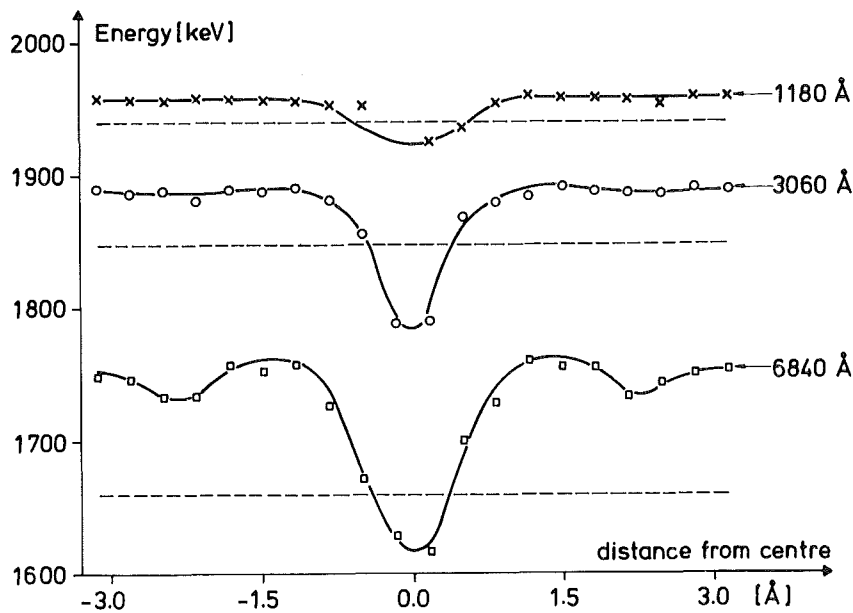


Fig. 3 Energy distributions recorded at various depths, each profile is averaged over 100 lattice spacings and taken along the plane diagonales; the dashed lines represent the energy of random incident particles at the same depths. It is seen that in spite of the flux peaks which are already developed at 3000 Å the energy profile is uniform over a large area.

constant part. This last contribution is attributed to collisions with valence electrons, which are treated to be equally spread over the lattice, and to plasma excitations/4/. The first part is averaged in the same procedure as the scattering angle. The angular dispersion of the ion beam by single collisions with electrons and thermal vibrations are both included in a Monte-Carlo treatment /3/.

The spatial distribution of the channeling ions is expected to be quite different from the uniform distribution of random incident particles and a change of these flux profiles as a function of depth should appear /5/. Fig. 2 shows the flux distribution along the plane diagonales in Fig. 1 at various depths. It is clearly seen, that the flux profile has sharp minima at the sites of the strong V-rows, where the flux vanishes and two quite well distinguishable attenuations which correspond to the saddle points of the potential. At the corner of the unit cell the flux has a relative maximum according to the potential minimum here, which however is not as deep as that in the proper channels.

Another result, the energy peaking effect which is always combined with the flux peaking effect, is shown in Fig. 3. It is seen that the energy profile has a sharp minimum at the site of the strong V-rows and two minima which are only developed at greater depths.

This phenomenon can easily be understood if one takes into account the trajectory-dependent term of the electronic energy loss which means that ions moving very close to the lattice atoms are slowed down also by collisions with closed shell electrons, whereas for particles moving in the centre of a channel this contribution can be neglected. Thus the latter have a higher kinetic energy compared to those moving near atomic strings.

As a further application it is planned to include the calculation of back-scattering probabilities and the implementation of defect profiles to simulate radiation damage. The described Monte-Carlo-program will then be a powerful instrument for the analysis of experimental backscattering data.

REFERENCES

- /1/ D.S. Gemmell, Rev. Mod. Phys. 46, 129 (1974)
- /2/ D.V. Morgan, *Channeling*; (John Wiley & Sons), (1973)
- /3/ H.D. Carstanjen, Ph.D. Thesis, University of Munich, 1973
- /4/ D. van Vliet, AERE-Report R 6395 (1976)
- /5/ D. van Vliet, Rad. Eff. 10, 137 (1971)

4.13 Channeling Effect Studies in V_3Si Single Crystals

O. Meyer and R. Kaufmann

From X-ray diffraction measurements /1/ it is known that in V_3Si the mean vibrational amplitude of the V-atoms perpendicular to the V-chain is larger than parallel to the chain. Further the phonon frequency distribution for the Si-atoms is found to be Einstein-like /2/. Thus using a Debye approximation in calculating the mean vibrational amplitude of the Si-atoms is no longer valid. Both features offer interesting test cases for the channeling technique.

Angular scans through [100] and [110] channeling directions in V_3Si have been performed using elastically scattered He ions for the V-rows and $Si^{28}(d,p_8)Si^{29}$ reaction for the Si-rows (Fig. 1).

The measured $\psi_{1/2}$ - and χ_{min} - values were compared to values calculated with empirical formulas derived from Monte-Carlo computer calculations /3/.

In complicated crystal structures such as V_3Si , rows with high scattering potentials (e.g. V-rows having small distances between the atoms) may affect the scattering potential of neighbored weak rows. This influence can be estimated by following a procedure described in /4/. Potential-energy contour diagrams in planes perpendicular to the [100] and [110] directions have been determined using the continuum potential with Molière's screening function and considering the potential contribution from a matrix with a total of 79 atoms for the (100) and of 157 atoms for the (110) plane (Fig. 2). From this calculation the multi-row potential $\Sigma V(1.2 u_1)$ and V_o , the minimum potential in the open channels between the rows have been determined and the $\psi_{1/2}$ -values have been calculated by inserting $\Sigma V(1.2 u_1) - V_o$ into the equations from ref./3/. u_1 is the rms one dimensional thermal vibrational amplitude perpendicular to the row as evaluated from neutron scattering experiments /2/, assuming isotropic vibration.

The measured $\psi_{1/2}$ -values are summarized in table 1 and compared to calculated values using single-row potentials (column 3) and multi-row potentials (column 4).

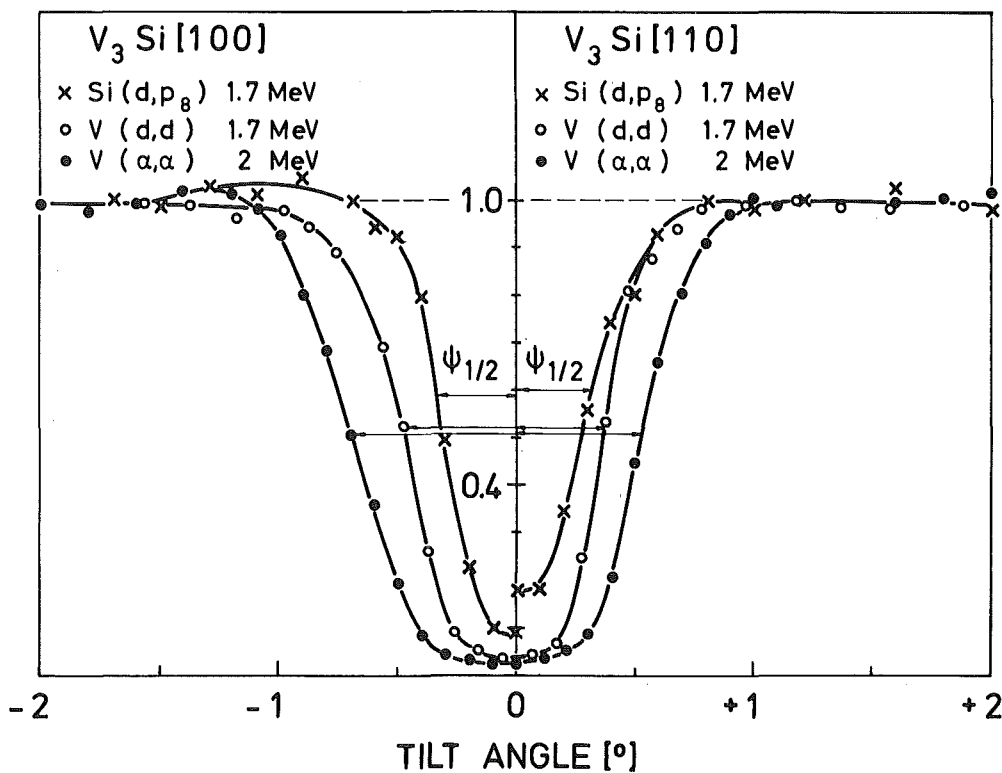


Fig. 1 Angular scans at depth of 500 Å through the [100] and [110] channeling directions.

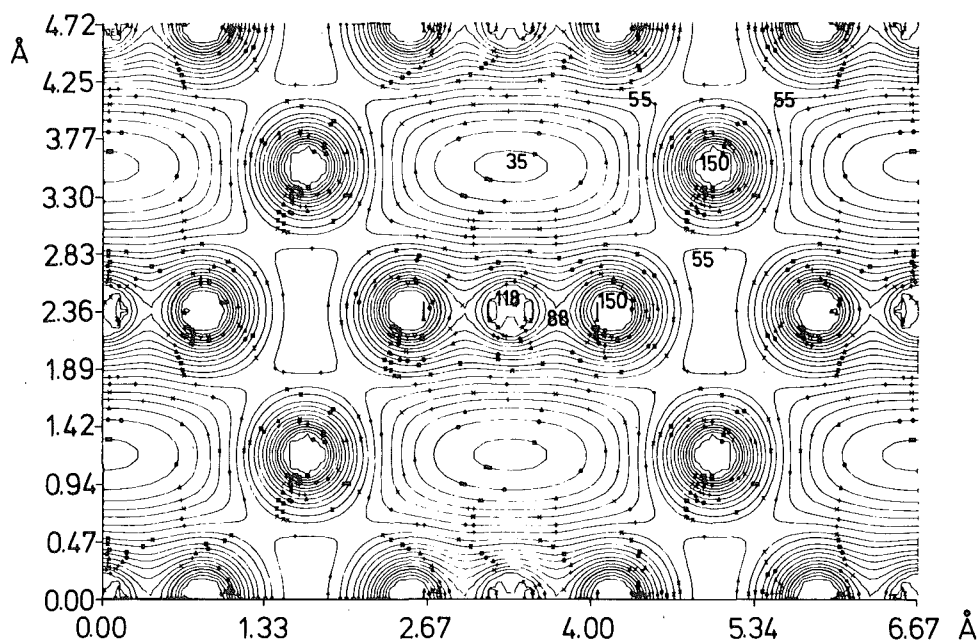


Fig. 2 Continuum potential contour plot for the unit cell, projected on the plane. (Molière screening function has been used; potential values are given in eV)

The experimental $\psi_{1/2}$ -values for the [100] directions are somewhat smaller than the theoretical values whereas the experimental values for the [110] direction are found to be larger. It is concluded that this effect is due to the anisotropic vibration of the V-atoms. The vibrational amplitude perpendicular to the V-rows in the [100] directions is larger than the vibrational amplitude under 45° to it. This anisotropic vibration was not considered in the calculation. Using the multi-row potentials and the measured $\psi_{1/2}$ -values the partial vibrational amplitudes were calculated to be $\langle u_{22}^2 \rangle^V = 0.0064 \text{ \AA}^2$ and $\langle u_{11}^2 \rangle^V = 0.0015 \text{ \AA}^2$. From $\langle u^2 \rangle^V = (\langle u_{11}^2 \rangle^V + 2\langle u_{22}^2 \rangle^V)/3$ a value of 0.0047 \AA^2 is obtained in close agreement with the $\langle u_V^2 \rangle^V$ -value of 0.0053 \AA^2 , obtained from the isotropic Debye temperature for the V-sublattice evaluated from neutron experiments (u_{22} is perpendicular to [100], u_{11} parallel to [100]). The ratio of $\langle u_{11}^2 \rangle^V / \langle u_{22}^2 \rangle^V$ is found to be 0.23, with a relative error of 40%. This value should be compared to the value of 0.8 found from X-ray analysis/1/.

The calculated $\psi_{1/2}$ -values for the Si-rows are about 0.04° larger than the experimental values. As the measured values are not extrapolated to zero target thickness but are values averaged over a deep layer it is believed that the larger theoretical values are more reasonable. Work is in progress to obtain precise data for $u_1(\text{Si})$ from the phonon density distribution and to study the influence on the channeling model. As the experimental values in [100] and [110] channeling directions are smaller than the calculated $\psi_{1/2}$ -values by the same amount, it is concluded that the Si-atoms vibrate isotropically.

The second parameter used for comparison between theory and experiment is the minimum yield. In table 2 the measured and calculated values have been summarized. The disagreement between χ_{\min}^{cal} (Si [110]) and χ_{\min}^{exp} (Si [110]) is caused by experimental difficulties in the reaction analysis. For the elastically scattered He-ions the agreement between the experimental and theoretical χ_{\min} -values is good for the [110] channeling direction where the contribution of the Si-rows to χ_{\min} of the V-rows is only 10%. In the [100] channeling direction rather large contributions from the strong V-rows guiding He-particles into the weak rows and vice versa are calculated.

Assuming that such contributions exist the calculated values for the [100] channeling direction are larger than the measured values. This indicates that the theory has to be modified for complex crystal structures.

Table 1 Experimental $\psi_{1/2}$ -values and values $\psi_{1/2}^{\text{calc}}$, calculated for single-row and multi-row potential

Experiment	$\psi_{1/2}^{\text{exp}} [^\circ]$	$\psi_{1/2}^{\text{calc}} [^\circ]$ (Barrett)	$\psi_{1/2}^{\text{calc}}$ multi-row pot. (Molière)
V (α, α) [100] 2 MeV	0.75 ± 0.02	0.81	0.78
V (α, α) [110] 2 MeV	0.52 ± 0.02	0.49	0.47
Si (d, p _g) [100] 1.7 MeV	0.35	0.39	0.39
Si (d, p _g) [100] 1.7 MeV	0.29	0.33	0.34

Table 2 Experimental and calculated χ_{min} - values

Experiment	$\chi_{\text{min}}^{\text{exp}}$	$\chi_{\text{min}}^{\text{calc}}$
V (α, α) [100] 2 MeV	0.018 ± 0.003	0.034
V (α, α) [110] 2 MeV	0.020 ± 0.003	0.020
Si (d, p _g) [100] 1.7 MeV	0.09	0.06
Si (d, p _g) [110] 1.7 MeV	0.18	0.05

REFERENCES

- /1/ J.L. Staudenmann, P. Coppens, and J. Müller, *Solid State Comm.* 19, 29 (1976)
- /2/ B. P. Schweiß, B. Renker, E. Schneider, and W. Reichardt, *Superconductivity in d- and f-Band Metals*, Ed. D.H. Douglass, Plenum Press, N.Y. (1976), p. 189
- /3/ J.H. Barret, *Phys. Rev.* B3, 1527 (1971)
- /4/ D.S. Gemmell and R.L. Mikkelson, *Phys. Rev.* B6, 1613 (1972)

4.14 Heavy Ion Radiation Damage in V_3Si -Single Crystals

O. Meyer, J. Geerk, and G. Linker

The channeling and backscattering techniques have been successfully used for investigating damage distributions in semiconductors and metals. As point defect agglomerates are the most stable defect structures after irradiation in metals, a direct backscattering component from interstitials or atoms, displaced more than 0.2 \AA from their lattice site plays a minor role /1/. These extended defects will increase the transverse energy of the incident particle beam and thus deflect particles from channeled to random trajectories /2/. The purpose of this study is to use channeling and backscattering of He ions in damaged V_3Si single crystals in order to get some insight on the structure of damage present. The results will show that the damage structures in V_3Si are completely different from those usually observed in metals.

In Fig. 1 the damage profiles produced by implanting He-ions with a fluence of $1.5 \cdot 10^{16}/\text{cm}^2$ at 50 keV and Kr-ions with a fluence of $2 \cdot 10^{14}/\text{cm}^2$ at 50 keV are shown. From the damage peak areas, which are nearly equal, it is found that about the same number of displaced V-atoms/ cm^2 have been produced although the number of implanted He-ions/ cm^2 is a factor of 75 larger than the implanted number of Kr-ions/ cm^2 . After correcting for the amount of energy transferred by nuclear collisions the damage produced by the Kr-ions is about a factor of 15 larger than for He-ions. This disagreement between retained damage after light and heavy ion irradiation has also been observed

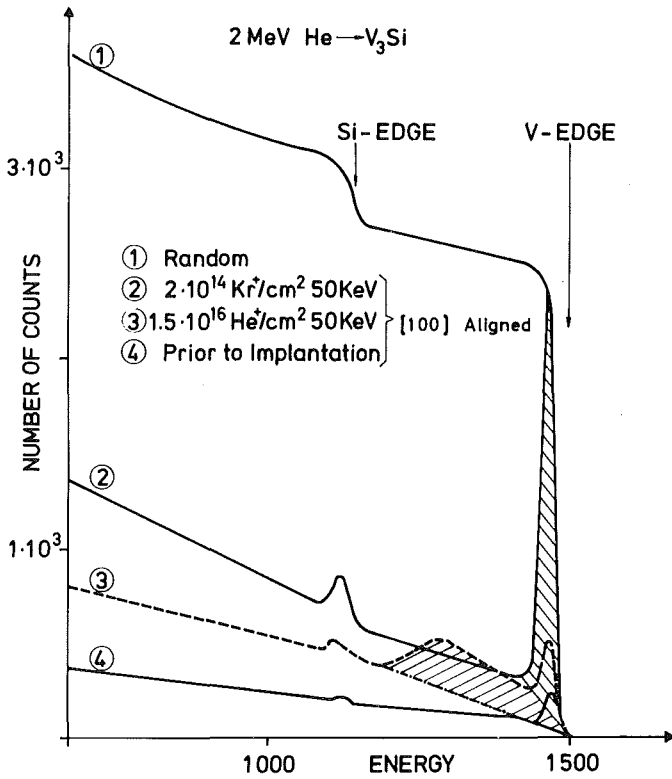


Fig. 1 Backscattering spectra for single crystal V₃Si implanted with $2 \cdot 10^{14}$ Kr⁺/cm² at 50 KeV and $1.5 \cdot 10^{16}$ He⁺/cm² at 50 KeV showing significant disorder peaks in both cases (dashed areas).

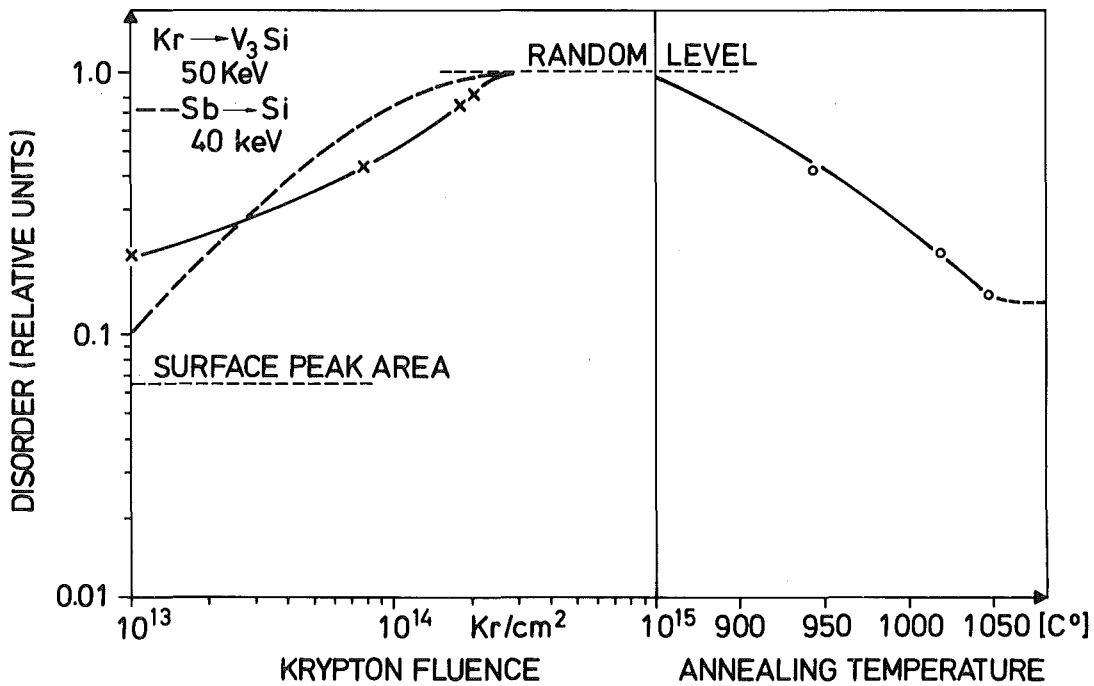


Fig. 2 Normalized damage peak area as function of the Kr-ion fluence and of the annealing temperature. For comparison the damage dependence on heavy ion fluence in Si is included (dashed line) (9).

for Si where the retained damage could be further enhanced by using poly-atomic ion implantation /3/. It is believed that the deposited energy density within each individual collision cascade will determine how much damage is created and retained.

From the damage peak areas measured as function of Kr-fluence the number of displacements per incident ion can be obtained. The result of these measurements are presented in Fig. 2. For Kr fluences equal or above $3 \cdot 10^{14}/\text{cm}^2$, corresponding to a concentration of 0.3 at. % the damage peak reaches the random level and saturates. The damage contribution to well resolved damage peaks consists of V- and Si-atoms, displaced more than about 0.2 \AA from their lattice sites. If the damage peak touches the random level, the structure has been rendered amorphous. It is found that about 720 V-atoms and 260 Si-atoms have been displaced by one Kr-ion at 50 keV. The number of displaced Si-atoms is about 1/3 of the displaced V-atoms. From theory /4/ it is estimated that about 45 keV of the total Kr ion energy is transferred into nuclear collisions. Together with the number of displaced V-atoms an effective displacement threshold energy of 23 eV is estimated. The fluence of $3 \cdot 10^{14} \text{ Kr}/\text{cm}^2$ for saturation correspond to about 2.4 dpa (displacements per atom), indicating that annealing or recombination effects are small.

The results presented in Fig. 2 are compared to those which were obtained for 50 keV Sb ions implanted in Si (dashed line in Fig. 2) /5/. A remarkable agreement exists for the damage production in the semiconductor Si and in the metal V_3Si . As current models for displacement processes in metals and semiconductors are substantially different from each other, one may conclude that the type of bonding in V_3Si is different from other metals and that a large component of covalent bonding may exist. Strong covalent bonding between adjacent V-atoms in V_3Si has indeed been observed by X-ray diffraction /6/. The disorder peaks anneal at temperatures above 900°C as shown in Fig. 2. At temperatures above 1000°C an enhanced surface peak remains, possibly caused by an oxide layer of increased thickness.

REFERENCES

- /1/ M. Gettings, O. Meyer, and G. Linker, Rad. Eff. 21, 51 (1974)
- /2/ K.L. Merkle, P.P. Pronko, D.S. Gemmell, R.C. Mikkelson, and J.R. Wrobel, Phys. Rev. B8, 1002 (1973)
- /3/ P. Baeri, S.K. Campisano, G. Foti, E. Rimini, and J.A. Davies, Appl. Phys. Lett. 26, 424 (1975)

/4/ P. Sigmund, Rev. Roumaine Physique 17, 823 (1973)

/5/ J.W. Mayer, L. Eriksson, and J.A. Davies

Ion Implantation in Semiconductors, Academic Press, N.Y. (1970)

/6/ J.L. Staudenmann, P. Coppens, and J. Mueller, Solid State Comm. 19, 29 (1976)

4.15 Proximity Effect in Irradiated V_3Si Single Crystals

O. Meyer

The superconducting transition temperature T_c in A-15 materials is strongly depressed after irradiation with neutrons, heavy ions and light ions and the mechanism responsible for the observed reduction of T_c appears to be similar. In the following we would like to show that the lowering of T_c by the proximity effect due to the presence of disordered regions having low or no T_c -values /1/ does not hold for irradiated V_3Si .

Large depressions of the superconducting transition temperature from 16.5 to 2.5 K were observed for V_3Si thin films with thicknesses of about 2000 Å after irradiation with He ions at 2 MeV /2/. We have produced the same amount of damage in V_3Si single crystals by using He ions at 300 KeV and scaling the corresponding fluence with E^{-1} . From the [100] aligned channeling and back-scattering spectra as shown in Fig. 1 for irradiated V_3Si single crystals only a small enhanced dechanneling component is visible in the region of 2000 Å from the surface. This increase in the minimum yield $\chi(t)_{\min}$ may be caused by different defect structures. Here we assume the existence of disordered regions which will cause a similar dechanneling component in metals /3/. Dechanneling and TEM results on visible clusters have been combined and a dechanneling cross section σ_d equal to $2.3 \cdot 10^{-14} \text{ cm}^2$ was obtained /3/. From the dechanneled fractions χ_{\min} and $\chi(z)$, before and after damage respectively, the density of visible clusters N_c may then be estimated from:

$$N_c = \Delta(\chi) / \left[(1 - \chi_{\min}) \cdot \sigma_d \right] \quad \text{to be about } 10^{17} / \text{cm}^3.$$

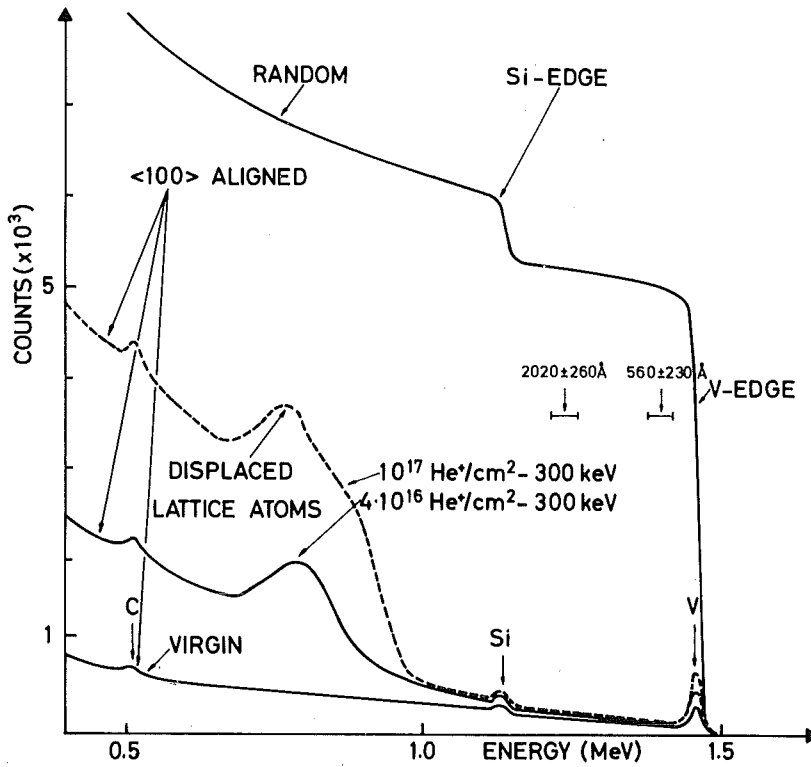


Fig. 1 Backscattering spectra for single crystal V_3Si implanted with large He fluences ($4 \cdot 10^{16} \text{ He}^+/\text{cm}^2$ and $10^{17} \text{ He}^+/\text{cm}^2$) at 300 KeV. The disorder peak is shifted to a depth of approximately 6000 \AA . A small enhanced dechanneling yield is observed in the surface region where the angular scan measurements were performed (window settings are indicated).

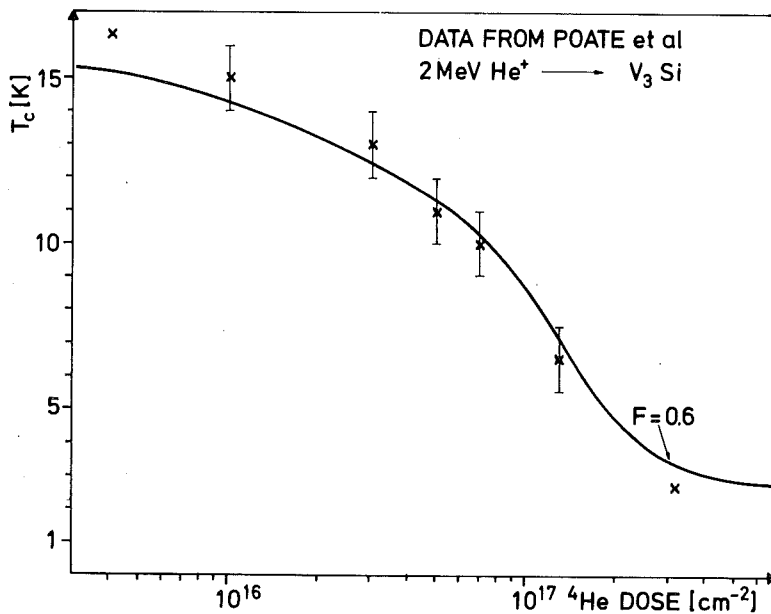


Fig. 2 Decrease of T_c with implanted He fluences as measured on irradiated V_3Si thin films (2) and compared to calculations using the proximity effects.

In Nb₃Sn irradiated with neutrons extended defects with an average size of 40 Å diameter have been observed /1/. Assuming the same average diameter for clusters in irradiated V₃Si, F is then calculated to be 0.017. Following the procedure of Pande /1/ the T_c depression due to the proximity effect has been calculated. The calculation is based on the BCS theory, on an effective N(o)V-value derived by DeGennes /4/ for layered structures and on F = 1-exp-(Vn) where V is the volume of a disordered region and n the density of primary knock-on particles (n_p ~ fluence).

In order to describe the measured data by the calculated values (solid line in Fig. 2) for V₃Si thin films /2/ as shown in Fig. 2 the following parameters were used:

N_s V_s and N_n V_n have been obtained from the BCS-formula using T_c = 16.5 K and T_c = 2.5, respectively and θ_D = 450° K (S for high T_c material, n for low T_c material). At the He-fluence of 3.3 · 10¹⁷/cm² where T_c reaches the lower saturation level, F was assumed to be 0.6. A close fit to the experiment is reached if the ratio N_s/N_n is assumed to be equal to 5. Although the measured data are described rather well, there are mainly three objections:

- i) The assumption of 2 fit parameters F and N_s/N_n is problematic.
- ii) The large decrease of N_s should be accompanied by a simultaneous yet somewhat smaller increase in V_s, in contradiction to the findings in /5/.
- iii) An upper limit in the number of extended defects as estimated from dechanneling yield for a fluence corresponding to 3.3 · 10¹⁷ He/cm² of 2 MeV is 5 · 10¹⁷ cm³ resulting in F = 0.017 which is small compared to the value of F = 0.6 used as a fit parameter at this fluence.

As conclusion follows that the T_c depression as observed after He irradiation of V₃Si thin films is probably not due to the proximity effect. In the following contribution a more reliable explanation for the increase in χ(t)_{min} and the decrease in T_c is presented.

REFERENCES

- /1/ C.S. Pande, BNL Report 22248
- /2/ J.M. Poate, R.C. Dynes, L.R. Testardi, and R.H. Hammond, Superconductivity in d- and f-Band Metals, D.H. Douglass Ed., Plenum Press, N.Y. (1976), 489
- /3/ K.L. Merkle, P.P. Pronko, D.S. Gemmell, R.C. Mikkelson, and J.R. Wrobel, Phys. Rev. B8, 1002 (1973)
- /4/ P.G. DeGennes, Rev. Mod. Phys. 36, 225 (1964)
- /5/ C.M. Varma and R.C. Dynes (see Ref. 2), p. 507

4.16 Channeling Effect Measurements of ^4He -Induced Damage in V_3Si Single Crystals

O. Meyer

As a possible defect structure in A-15 material being responsible for the large T_c -depressions observed after irradiation, a "zig-zag" atomic arrangement of the transition metals has been discussed previously /1/. The channeling technique has been used to study atom displacements in the order of 0.1 \AA .

In order to detect displaced atoms with displacement amplitudes smaller than about the Thomas-Fermi screening parameter, the transverse energy of the analysing beam has to be increased and angular scan curves have to be measured. These curves were measured at depths of 2000 \AA and 500 \AA . As an example the results obtained prior to and after implantation of $6 \cdot 10^{16} \text{ He/cm}^2$

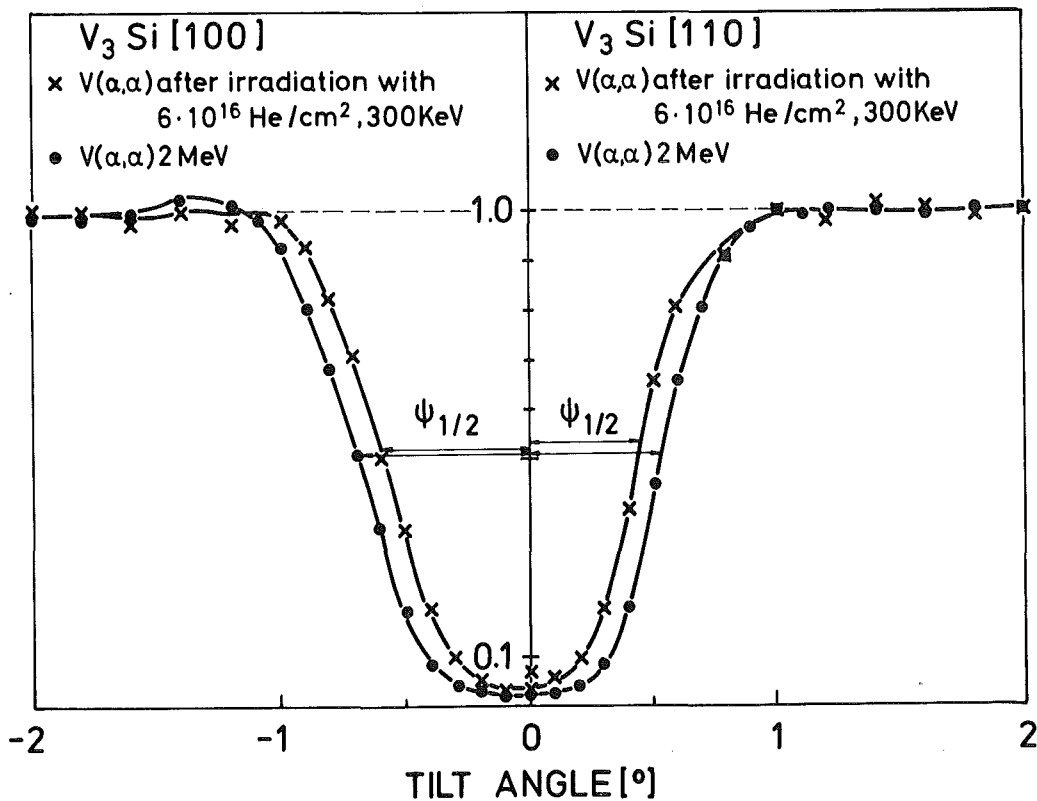


Fig. 1 Angular scan curves from 2 MeV He ions scattered from V in V_3Si single crystal for the [100] and the [110] directions prior to and after implantation of $6 \cdot 10^{16} \text{ He/cm}^2$ at 300 KeV.

are shown in Fig. 1 for the [100] as well as for the [110] channeling direction. An appreciable narrowing of the $\psi_{1/2}$ -values and a slight increase in χ_{\min} was observed. This narrowing has been measured as a function of fluence (table 2) and for different V_3Si single crystals cut perpendicular to the [110] channeling direction.

Table 1 Measured $\psi_{1/2}$ - and χ_{\min} - values after irradiation with $6 \cdot 10^{16}$ He/cm². Values prior to irradiation are given in brackets.

Experiment	$\psi_{1/2}^{\text{exp}}$ [°]	$\langle u \rangle$ [Å]	χ_{\min}^{exp}	χ_{\min}^{cal}
V (α, α) [100] 2 MeV	0.68 (0.75)	0.104 (0.084)	0.034 (0.018)	0.07 (0.034)
V (α, α) [110] 2 MeV	0.44 (0.52)	0.086 (0.05)	0.065 (0.02)	0.08 (0.020)

The decrease of the $\psi_{1/2}$ -values and the increase of the χ_{\min} -values after He ion irradiation are summarized in table 1 and can be described by an increase of the rms displacement u_1 of the V-atoms from the row. Assuming the increase to be a static displacement with a gaussian distribution and subtracting the square of the rms one dimensional thermal vibrational amplitude we obtain the

Table 2 Values of $\psi_{1/2}$ - and χ_{\min} at zero target thickness as a function of He fluence (300 keV), lowering of T_c as a function of He fluence (2 MeV) as determined by Poate et al. /2/.

Fluence at 2 MeV /4/	Corresponding fluence at 300 keV	Average T_c [°K]/4/	$\psi_{1/2}$	χ_{\min}
-	-	1.64	0.75 ± 0.01	0.020
$6 \cdot 10^{16}$	$9 \cdot 10^{15}$	12	0.75	0.022
$1.3 \cdot 10^{17}$	$2 \cdot 10^{16}$	7	0.72	0.028
$2.6 \cdot 10^{17}$	$4 \cdot 10^{16}$	3.5	0.70	0.03
$4 \cdot 10^{17}$	$6 \cdot 10^{16}$	2.5	0.67	0.032
$6.6 \cdot 10^{17}$	10^{17}	2.5	0.68	0.04
$8 \cdot 10^{17}$	$1.2 \cdot 10^{17}$	-	0.67	0.032

values for the one-dimensional rms static displacements to be 0.06 \AA perpendicular to the [100]- and 0.07 \AA perpendicular to the [110] direction.

As a severe consequence, the symmetry of the system is disturbed. Weger /2/ has shown that the matrix elements of interchain coupling are large, however because of symmetry considerations their influence on the sharp peaks of the electronic state density cancels. If the symmetry is perturbed this coupling will destroy the sharp peaks in the density of electronic states and thus depress T_c /3/.

REFERENCES

- /1/ C.M. Varma and R.C. Dynes, Superconductivity in d- and f-Band Metals, D.H. Douglass, ed., Plenum Press, New York (1976), p. 507
- /2/ M. Weger, Solid State Physics 28, 145 (1973)
- /3/ H. Rietschel, private communication

4.17 Determination of Oxygen Profiles in Layers and Bulk Material

E.L. Haase and M. Conrad

A simple nondestructive method for the determination of very low oxygen contents has not been worked out so far. In the course of investigations of the role of a controlled oxygen partial pressure during the preparation of Nb_3Ge films, the sensitivity of known methods had to be improved /1/. The backscattering technique is usually too insensitive. Use of the 3.05 MeV resonance in the $^{16}\text{O}(\alpha,\alpha)$ scattering is cumbersome, as it requires a number of measurements with varying incident energies to scan a layer of a few hundreds nm /2/. For good depth resolution one needs high specific energy loss. In this respect the $^{16}\text{O}(d,\alpha_o)$ exothermic nuclear reaction is better than the $^{16}\text{O}(d;p_x)$ reactions. What has so far seriously restricted the use of the $^{16}\text{O}(d,\alpha_o)$ reaction are interfering (d,p)-reactions from ^{16}O , ^{12}C , ^{28}Si and most of the low Z substrates.

There is a simple way to avoid such interferences. Protons have a lower specific energy loss than α -particles. So if one chooses the detector

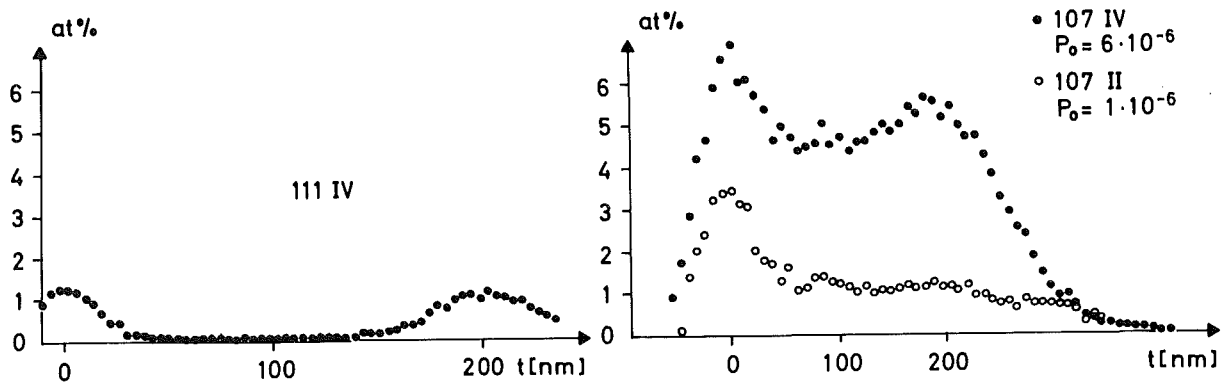


Fig. 1 Oxygen profiles of Nb_3Ge layers. Left: A film with essentially no oxygen inside and the surface and substrate surface oxide peaks. Right: Profiles of films prepared with the stated oxygen partial pressure.

thickness such that the α -particles are stopped, but the protons pass through, their resulting pulse heights will be much lower.

The substrate should meet a number of requirements. It should contain no extra oxygen or other light elements resulting in interfering nuclear reactions. Medium Z elements are best, as the Coulomb barrier prevents nuclear reactions. High Z materials can cause electronic pile-up on account of the Z^2 dependence of the Rutherford cross section for deuteron elastic scattering. For our purpose monocrystalline Si has turned out to be a fairly good substrate material. For bulk material the requirements are less severe.

To obtain a high yield, one should work near a broad resonance /3/. For our purposes the rising part of the resonance at 1.08 MeV has turned out to be optimal. Here the cross section rises approximately linearly with depth and so a small uncertainty in the incident deuteron energy causes only a negligible error in the absolute amount of oxygen, as a thin SiO_2 layer on Si is used as a calibration standard. In the Fig. 1 the pulse height spectra have been converted to depth scales using the known energy losses for deuterons and α -particles. The left figure shows the oxygen depth profile of a Nb_3Ge film which contains essentially no oxygen inside. The few counts from inside the film stem from electronic pile-up and from $^{29}Si(d, \alpha)_X$ reactions and limit the sensitivity to 0.05 at. % oxygen. The left peak stems from the surface oxide layer. Its width of 35 nm is determined by the in-

strumental resolution and the tilt angle of 78.5° . The right peak stems from the substrate surface oxide layer and is broadened by substrate roughness and energy straggling. On the right the oxygen profiles for two layers of Nb_3Ge are shown, which were grown during the presence of the stated oxygen partial pressure. The left peak is caused by the surface oxide layer.

This method has been refined for the determination of oxygen profiles in Nb_3Ge films. However its major applications will lie in the measurement of oxygen profiles generally. It has successfully been applied to measure the oxygen profile in a corroded sample of reactor stainless steel and the oxygen content of a Nb-surface for superconducting rf-cavities.

REFERENCES

- /1/ A. Tuross, L. Wielufksi, and A. Barcz, Nucl. Instr. Meth. 111, 605 (1973)
- /2/ J.R. Gavaler, J.W. Miller, and B.R. Appleton, Appl. Phys. Lett 28, 237 (1976)
- /3/ R.F. Seiler, C.H. Jones, W.J. Anzick, D.F. Herring, and K.W. Jones, Nucl. Phys. 45, 647 (1963)

4.18 The Influence of Oxygen Content on the Superconducting Properties of Nb_3Ge Films

M. Conrad and E.L. Haase

The effect of a controlled admission of oxygen during evaporation of Nb_3Ge thin films on the superconducting transition temperature T_c , the resistance ratio ($r = \text{resistance at room temperature} / \text{resistance at 25 K}$) and the lattice parameter a_0 has been investigated. In this report the results of layers evaporated onto heated Si single crystals are discussed, the films having thicknesses in the range of 1800 - 2000 Å and a Nb/Ge ratio of about 2.8. Both parameters were determined by analysis of Rutherford backscattering spectra which were measured using 2.3 MeV ^4He ions /1/. The oxygen content was determined using the nuclear reaction $^{16}\text{O}(d,\alpha)^{14}\text{N}$ with 1.08 MeV deuterons /2/. T_c and the resistance ratio r were determined by a standard four-point probe resistive measurement. T_c was taken at the temperature with a 5 % decrease of resistance. The lattice parameters a_0 were obtained by X-ray diffraction using a wide film Debye camera in Seemann-Bohlin

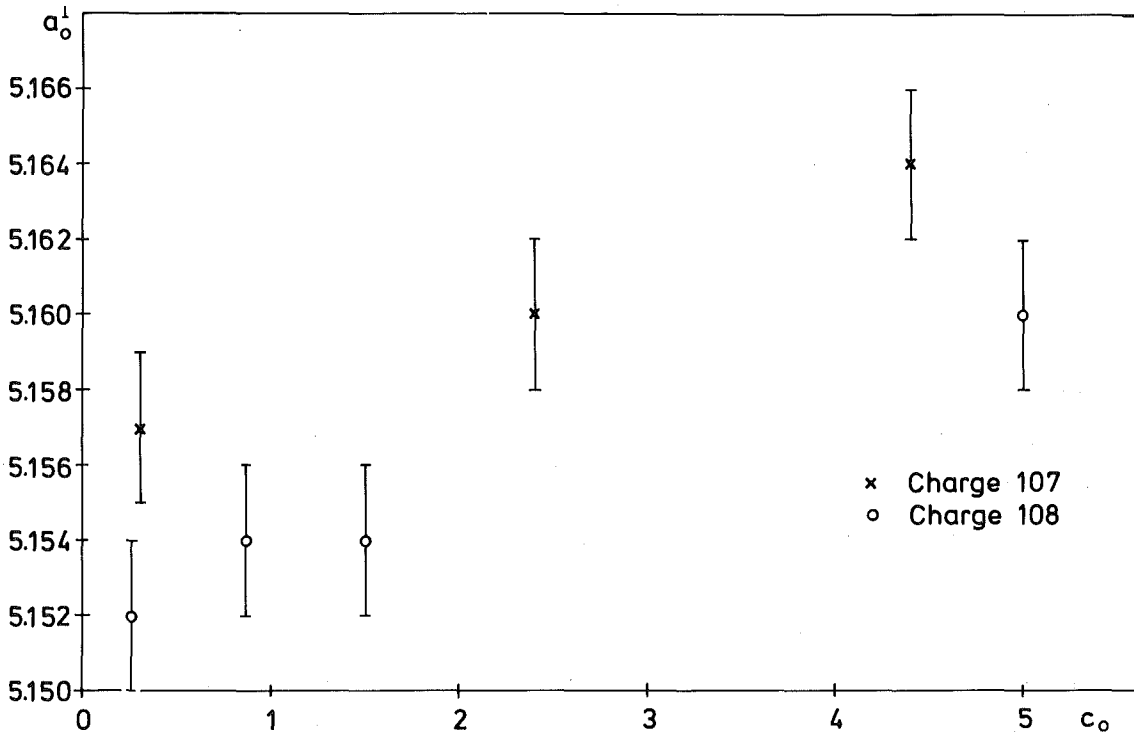


Fig. 1 Lattice parameter a_0 as a function of oxygen content in Nb_3Ge films. Nb/Ge evaporation power ratio and substrate temperature were the same for these samples.

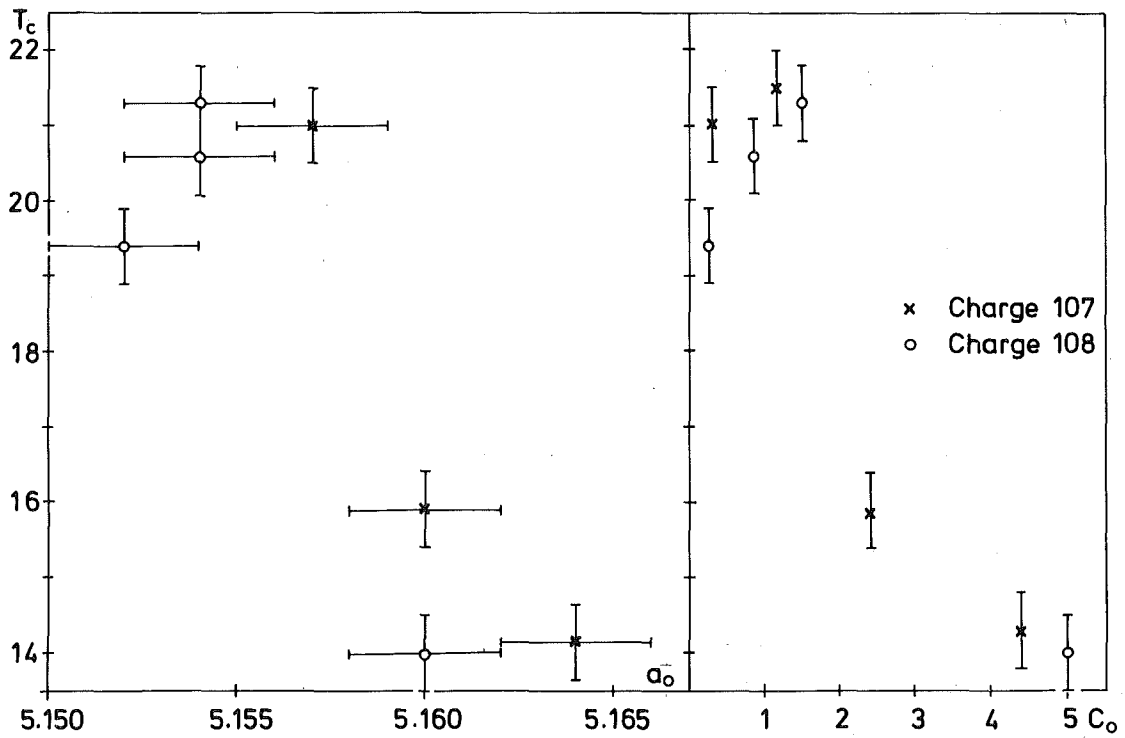


Fig. 2 T_c as a function of lattice parameter (left side) and oxygen content in Nb_3Ge films.

arrangement and also using a diffractometer in the Bragg-Brentano arrangement.

Table I summarizes the important data for the samples. The oxygen partial pressure p_{O} and the oxygen content c_{O} show an approximately linear correlation in the range $p_{\text{O}} = 5 \cdot 10^{-7}$ to $6 \cdot 10^{-6}$ Torr.

The lattice parameter values as determined by the two methods differ consistently /3/. In the Seemann-Bohlin arrangement the X-rays strike the sample with fixed glancing incidence, whereas in the Bragg-Brentano arrangement only diffracting planes parallel to the surface are effective, allowing the determination of a lattice parameter a_{O}'' . The difference is interpreted to be due to strain in the Nb_3Ge layers caused by a smaller contraction of the films as compared to the substrate when cooling down from about 850°C . The diffractometer values give the lattice parameter a_{O}'' whose dilatation is estimated to be $1^\circ/\text{oo}$, using different thermal expansion coefficients for Nb_3Ge and Si. For the film measurements an angular dependent correction was applied to obtain the lattice parameter a_{O}^\perp from diffracting planes perpendicular to the surface. Although the variations of the a_{O}'' and the a_{O}^\perp values with oxygen content are consistent, only a_{O}^\perp values are used in the following, as their errors are smaller.

Fig. 1 shows the lattice parameter a_{O}^\perp plotted vs. oxygen content c_{O} . It is clearly seen that two lines can be drawn through the points. As the crosses and the circles stem from different evaporation runs, we interpret this to be an effect due to slightly different conditions during evaporation. At 5 at. % oxygen the lattice parameter is increased by $0.005 \pm 0.002 \text{ \AA}$ (mean of $\Delta a_{\text{O}}''$ and $\Delta a_{\text{O}}^\perp$). In comparison, the same amount of oxygen dissolved in Nb would lead to an increase of 0.030 \AA . So it appears that only little oxygen is incorporated in the A15-phase.

Fig. 2 shows plots of T_{C} vs. lattice parameter at the left side and T_{C} vs. oxygen content at the right side. The fall of T_{C} for an oxygen content of more than about 1.5 at. % may be interpreted as a lattice disorder effect produced by the oxygen in the samples. Both figures show an increase of T_{C} for an oxygen content less 1.5 at. % resp. the corresponding lattice parameter. This allows the conclusion that a small content of oxygen in the sample actually helps in forming the A15-phase with high T_{C} .

It is argued by Testardi et al. /4/ that defects in the Nb₃Ge films introduced during the growth process may lead to a physical behaviour similar to that introduced by ⁴He bombardment. They also find a lattice parameter expansion by ⁴He damage. The results we obtained indicate two effects for oxygen content in Nb₃Ge films. One is the lattice swelling due to a disorder effect, the other is the improved growth condition for the A15-phase for low oxygen content, enhancing T_c in the films.

Table I

Sample No.	T _c (K)	Resistance Ratio r	Oxygen Partial Pressure P _o	Oxygen Content (at. %) c _o	Lattice Parameter a _o [±] ±0.002	a _o ^{''}
107 I	21.0	1.51	5 · 10 ⁻⁷	0.3	5.157	5.132 ± 0.002
107 II	21.5	1.66	1 · 10 ⁻⁶	1.15	5.145	5.129 ± 0.005
107 III	15.9	-	3 · 10 ⁻⁶	2.4	5.160	5.133 ± 0.004
107 IV	14.3	1.39	6 · 10 ⁻⁶	4.4	5.164	5.140 ± 0.005
108 I	19.4	1.43	<5 · 10 ⁻⁸	0.26	5.152	5.136 ± 0.003
108 II	20.6	1.55	1 · 10 ⁻⁶	0.85	5.154	5.126 ± 0.003
108 III	21.3	1.53	3 · 10 ⁻⁶	1.5	5.154	5.131 ± 0.003
108 IV	14.0	1.47	6 · 10 ⁻⁶	5	5.160	5.133 ± 0.003

REFERENCES

- /1/ E.L. Haase, Progress Report of the Teilinstitut Nukleare Festkörperphysik, Ges. f. Kernforschung (KFK 2357), 92 (1976)
- /2/ E.L. Haase and M. Conrad, preceding contribution, this report
- /3/ R. Feder, B.S. Berry, J. Appl. Cryst. 3, 372 (1970)
- /4/ J.M. Poate, L.R. Testardi, A.R. Storm, and W.M. Augustyniak Phys. Rev. Lett. 35, 1290 (1975)
- /5/ L.R. Testardi, R.L. Meek, J.M. Poate, W.A. Royer, A.R. Storm, and J.H. Wernick, Phys. Rev. B11, 4304 (1975)

4.19 Determination of Inert Gas Concentrations in Metals with Rutherford Backscattering and X-Ray Photoelectron-spectroscopy

H.J. Schmidt^a, E. Henrich^a, and G. Linker

^a*Institut für Heiße Chemie, GfK*

There are several possibilities for the final storage of radioactive ⁸⁵Kr separated from the dissolver in the nuclear fuel reprocessing procedure. An alternative to the storage in high pressure bottles is for security reasons the deposition of fission krypton into metal matrices. This can be performed by burying the noble gas atoms in evaporated or sputtered metal layers. Concentrations of Ne, Ar, and Kr from a few up to 30 at. % in bias-sputtered metal films have been already reported /1/. In this work sputtering and ion implantation were used to introduce Kr into different metals. Concentration determinations were performed using Rutherford backscattering (RBS) and X-ray photoelectronspectroscopy (XPS) to optimize the deposition or implantation parameters and test the properties of the metal-Kr samples.

In a first step however the capabilities of the analyzing methods have been compared. RBS is known to be absolute but for sufficient sensitivity is restricted to systems with high Z impurities in lower Z host matrices. For other systems a complementary analysis like XPS must be performed. This method, though not absolute, does not suffer from Z-restrictions (besides He and H detection) and a relative concentration determination for a homogeneous sample can be obtained from the following formula /2/:

$$\frac{N_1}{N_2} = \frac{\sigma_1}{\sigma_2} \cdot \frac{S_1}{S_2} \cdot \frac{\lambda_1}{\lambda_2} \cdot \frac{C_1}{C_2}$$

with σ = ionisation cross section for an electron, S = spectrometer constant depending on electron energy, λ = mean free escape depth, C = concentration of an element, N = peak intensity from XPS spectra. The indices 1 and 2 are used for target and impurity atoms, respectively. For inhomogeneous samples concentration profiles can also be obtained by taking spectra at different photoelectron escape angles.

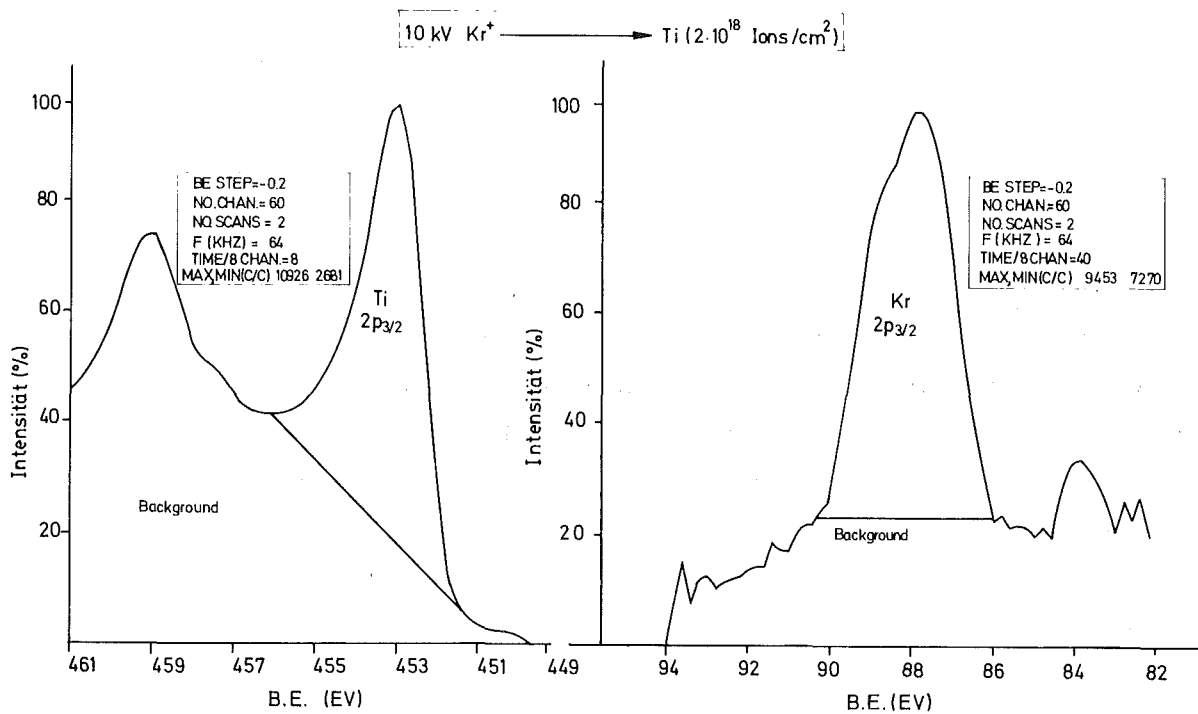


Fig. 1 Sections of a XPS spectrum from a Ti foil implanted with Kr ions showing the signals from Ti and Kr.

In Fig. 1 as an example a XPS spectrum from a Ti-foil implanted with Kr⁺ ions at 10 keV until saturation is shown. With the integrated peak intensities from this spectrum an inert gas content in the sample of 13 ± 1 at. % was determined. RBS analysis from the same foil yielded a concentration of 12 ± 0.5 at. %. This agreement within the error of the methods has also been found for other systems and different implantation conditions showing that reasonable complementary analysis can be performed using XPS and RBS.

Gas release studies at temperatures up to 1000°C showed that in most of the investigated metals diffusion of the buried gas atoms started at about 0.5 T_m with T_m being the melting point in degree K.

REFERENCES

- /1/ J.J. Cuomo, R.J. Gambino, J. Vac. Sci. Techn. 14, 152 (1977)
- /2/ H.-J. Schmidt, Diplomarbeit, Universität Heidelberg

4.20 Single Crystal Growth

B. Scheerer

Niobium-Carbo-Nitride

A $\text{NbN}_{.36}\text{C}_{.34}$ single crystal was grown by vertical float zone melting. The starting material was hot pressed NbNC-powder.

We obtained our crystal after a single pass under a N_2 -atmosphere of 20 bar. The velocity was 11 mm/h. The zoned part of the rod was 10 mm in diameter and had a total length of about 50 mm. Out of this rod we cut a single crystal of about 1.5 cm^3 .

By chemical analysis of the single crystal we obtained the following values: N = 21.4 at. %, C = 19.9 at. %.

PdFe

We started to grow PdFe-single crystals with varying Fe constant for measurements of internal magnetic fields in PdFe alloys by μ^+ spin rotations.

We prepared these samples by melting the material in a "cold crucible". By extremely slow cooling of the material it is possible to get a directed heat loss via the bottom of the cold crucible. This leads to the formation and upward growth of a single crystal throughout the entire sample. In this way a PdFe-single crystal with 0.3 at. % Fe was produced.

HoAl₂

A HoAl₂-single crystal was grown employing the method described by M. Godet et al. /1/. The material was melted in a tungsten-crucible by high frequency induction. The crystal was pulled out of the melt with a tungsten wire without any seed crystal.

REFERENCE

- /1/ M. Godet, E. Walker, and H.-G. Purwins, Journal of the Less-Common Metals 30, 301 (1973)

5. DATA PROCESSING

5.1 The Improvement of our Structure Calculation Programs Adaption of the XRAY76 to an IBM Computer

R. Kuhn

The University of Maryland has developed a new version of the XRAY-library the "XRAY76", which carries out the calculations required to solve the structure of crystals by diffraction techniques /1/.

The XRAY76 has a new, more sophisticated data management causing a faster run, and many new programs, e.g. plot routines. It has been implemented on an UNIVAC 1108 computer. We received about 90 000 cards highly blocked on a magnetic tape and had to adapt it to our 370/168 IBM computer.

The higher speed has been achieved by a set of input-output programs written in assembler language. But this assembler deck we got, did not fit either the possibilities at our installation or even the conventions of the FORTRAN programs of the XRAY76. The assembler programs have been adapted and now we have a working version of the XRAY76 on our installation.

Until now we have tested successfully the phases working with the old XRAY release: BONDLA, CRYLSQ, DATRDN, FC, FOURR, LOADAT. Furthermore some new phases are available:

1. DATCO5 is a set of data preprocessing routines. It treats the output of a diffractometer and carries out the calculations required to produce a scaled, merged, sorted and checked set of reflection data ready for the XRAY system.
2. CONTRS is a program to draw contour maps from FOURR on our STATOS plotter or the line printer.
3. PROJCT produces a projection or a perspective view of structural units on our STATOS plotter or the line printer.
4. LISTFC lists structure factors suitable for publication.
5. PEKPIK scans a Fourier or a Patterson map and detects the coordinates and densities of the maxima (peaks).
6. RLIST explores special R-factors (agreement factors between calculated and observed structure factors) for various zones and reflection groups.

In the version XRAY76 the memory space now needed is reduced from 310 K Bytes to 240 K in comparison to our former XRAY version.

REFERENCE

/1/ J.M. Stewart, Technical Report TR-446, The X-RAY SYSTEM, version of 1976, University of Maryland

5.2 Zeichnungserstellung von Printed-Card-Layouts

R. Moser

I. Graphische Ausgabe des Belegungsplanes

Es wurde ein Programm entwickelt, das eine Printed Cards (PC) entsprechende, maßstabgetreue Ausgabe des Belegungsplans liefert.

Die Eingabe wird von NOVA-Magnetbändern gelesen und in einem Vorspann (II) aufbereitet.

Die Zeichnung wird eröffnet, indem die Stromschienen geplottet werden. Um eine gute Orientierungsmöglichkeit auf der weißen Papierausgabe des STATOS-Plotters zu bieten, wird ein Rasternetz gezeichnet, das in 10er Schritten Markierungen setzt.

Die Lochlagen werden vom Programm entsprechend der Eingabe für IC-Gruppen und diskrete Bauteile definiert.

Die Daten werden folgendermaßen gelesen:

alphanumerische Bezeichnung der IC-Gruppe (A4), X, Y-Koordinaten des 1. Beines, Anzahl der Beine einer Beinreihe, Abstand der Beinreihen voneinander (4I5).

Das Programm arbeitet mit einer Matrix des Typs Integer * 2 und der Größe 280 * 290. Der Zustand der Rasterpunkte wird mit 0 = frei und 3 = belegt gekennzeichnet.

Zunächst wird die Matrix = 0 gesetzt.

Nach dem Einlesen der Daten werden die X,Y-Koordinaten für alle Beine der IC-Gruppe berechnet und es wird in der Matrix geprüft, ob alle vorgesehenen Positionen für die Lochlagen der gewünschten IC-Gruppe frei

sind. Ist dies der Fall, so werden die entsprechenden Rasterpunkte als besetzt deklariert, die Bohrlöcher geplottet und die X,Y-Koordinaten ausgedruckt.

Die geplotteten IC-Gruppen werden beschriftet. Die Beschriftung wird jedoch unterdrückt, wenn nur ein Bein pro Reihe angegeben wurde.

Konnte eine IC-Gruppe nicht gesetzt werden, so wird eine Fehlermeldung ausgedruckt. Anschließend werden die nächsten Daten eingelesen.

Wurde das Ende der Daten gefunden, so wird die Zeichnung abgeschlossen und das Programm stoppt.

Das Programm wurde für die IBM 370/168-158 unter OS/MVT entwickelt. Es benötigt 228 K Speicherplätze und 12,5 sec zum Setzen von 640 IC-Gruppen.

II. Aufbereitung der Eingabedaten

Die Eingabedaten werden von NOVA-Magnetbändern gelesen. Da hier im ASCII-Code, an der IBM jedoch im EBCDIC-Code gearbeitet wird, muß der Code konvertiert werden.

Dies geschieht mit Hilfe des PL/1-Programms ASCITSO /1/, welches mit einer Blocklänge von maximal 504 Byte arbeitet. Es verlangt als erste Information die Anzahl der folgenden Daten und dann das Datenfeld.

Da auf der NOVA die Magnetbänder unter FORTRAN und BASIC i.a. ohne Rücksicht auf die Länge der WRITE-Liste, gegebenenfalls stückweise, in einen 514 Byte-Puffer geschrieben werden (510 Byte Daten und 4 Byte Systeminformation), wird ein teilgefüllter Puffer mit Nullen aufgefüllt. Das Ende des logischen und des physikalischen Records muß also nicht identisch sein. Diese im ASCII-Code geschriebenen Nullen sind für ASCITSO nicht interpretierbare Zeichen.

Um das Programm SCITSO verwenden zu können, wurde ein Fortran-Programm zum Aufbereiten der Daten entwickelt.

Dieses Programm liest jeweils einen Block der Länge 514 Bytes als Charaktere in einen Puffer und teilt diesen in 2 Blöcke mit 255 Bytes. Dann wird in jedem dieser Blöcke das logische Ende gesucht und mit dem physikalischen Ende des Blockes verglichen. Sind beide identisch, so werden diese zwei Blöcke mit der jeweils vorangehenden Anzahl der Daten nacheinander ausgegeben und der nächste Block wird vom Band gelesen, geteilt und geprüft.

War der logische Record kleiner als der physikalische Record, so wird noch der logische Record ausgegeben und das Programm gestoppt, da dies gleichzeitig das Ende der gesamten Eingabe bedeutet.

Die Ausgabe dieses Programms wird zwischengespeichert und dient als Eingabe für ASCITSO, welches die endgültige Eingabe für das Programm zur Erstellung des Bohrplanes liefert und protokolliert.

REFERENCES

/1/ F. Kronenberger, ASCITSO, Programmbeschreibung Nr. 342 (unveröffentlicht)

5.3 Mega - Channel - Kicksorter ASSTRO

G. Ehret and H. Hanak

ASSTRO (Automatisches Summieren von Spektren auf einem TROMmelspeicher ↔ automatic cumulation of spectra on a drum) is working since several years as a part of the MIDAS - system /1/. This kicksorter for one million channels and 4.5, 7, or 11 kHz counting rate consists of

- a) a fixed head magnetic drum with 512 tracks,
- b) any NOVA - computer with 800 ns cycle time and 8 K or 16 K memory,
- c) a special drum controller,
- d) a special computer-computer adapter to the old MIDAS I (CDC 160A)
- e) a commercial computer-computer adapter to new MIDAS II (NOVA 2)
- f) a special kicksorter/input (RING)

The operating system is adaptable to 8 K of the 16 K size of memory by software switches at assembly time.

In the period reported, enhancements on item c) and f) have been carried out to meet expected problems in further reliability of the system in the near future.

The old special drum controller was built on a Data General 4040 General Interface Board. This resulted in space and noise problems for such a complex electronic device.

We therefore completely redesigned the drum controller. We used the well proved preparation techniques for four-level multiwire cards /2, 3/. These multiwire cards allow the highest packing density of integrated circuits. To allow more flexibility during the prototype test, a stage with a wire-wrapped "multiwire" card has been introduced into the preparation sequence. This wrapped drum controller is under test.

The software device handler for the RING - input has been adapted to the new list/increment unit. The unit is a standard equipment for all NOVA computers and allows more than the 64 K channel input of the RING part, which is the limit of the older unit still in use.

REFERENCES

- /1/ G. Ehret, in Progress Report of the Teilinstitut Nukleare Festkörperphysik, Ges. f. Kernforschung Karlsruhe (KFK 2183), p. 101 (1975)
- /2/ R. Moser, in Progress Report of the Teilinstitut Nukleare Festkörperphysik, Ges. f. Kernforschung Karlsruhe (KFK 2183), p. 98 (1975)
- /3/ R. Moser, in Progress Report of the Teilinstitut Nukleare Festkörperphysik, Ges. f. Kernforschung Karlsruhe (KFK 2357), p. 121 (1976)

5.4 A Lightpen for the TV-Display of the NOVA-Computer

G. Ehret, H. Hanak, and H. Sobiesiak

On-line control of experiments by computers including interrupt activity programmed in BASIC or FORTRAN do not allow the keyboard to be used as the standard device for data input. The reason for this limitation is that all interrupt activity is suspended (BASIC) or partly suspended (FORTRAN) as long as the computer is waiting for completion of the input-line. Interactive graphic evaluation of spectra would be impossible in such a multitask environment. Alternative equipment like special keyboards or switches connected via interfaces are needed, requiring complex experimenters manipulation and programming.

We therefore equipped the TV display with a lightpen, which is a simple non - mechanical device. A lightpen surrenders to the program the X,Y - coordinates of a bright spot of the 256 x 256 matrix pointed to by a light sensitive pen. The lightpen activity is under program control, permitting data input and interrupts.

6. DEVELOPMENT OF MEASURING DEVICES AND TECHNIQUES

6.1 Automatic Data Collection in Tunneling Experiments

J. Geerk

In the experimental technique of superconducting tunneling, the measurements to be made are of the energy gap and of the first and second derivatives of the tunneling characteristics of the junction in both superconducting and normal states as a function of voltage. For digital computer analysis the information which the recorder traces contain, has to be available as a set of numbers punched onto paper tape or onto cards. This digitalisation is tedious and time consuming so that a device which enables the direct recording of the derivative data onto paper tape has been built up.

Fig. 1 shows a block diagram of the whole data collection system. The junction voltage is detected by a digital voltmeter and the first derivative is measured by a potentiometric conductance bridge described in /1/. The BCD-information representing the junction voltage passes a buffer stage followed by an opto-coupler which serves to break up the big ground loop which the whole system contains. The following logic unit produces a pulse if a decimal "9" changes into a decimal "0" on the digital reading of the voltmeter. Thus, if the junction bias is swept, pulses are produced at voltage steps of fixed width.

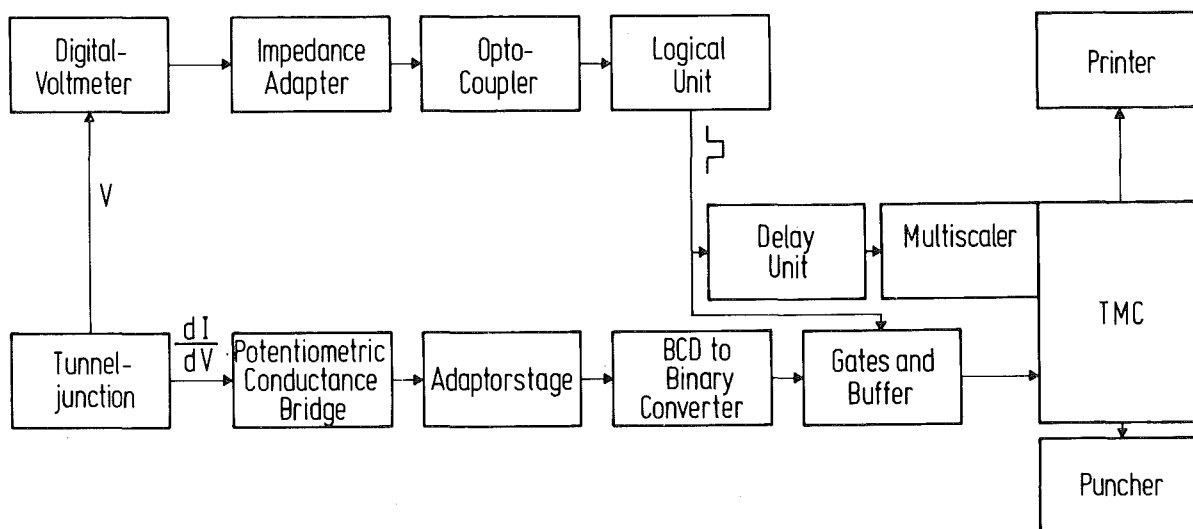


Fig. 1 Block diagram of the data collection system

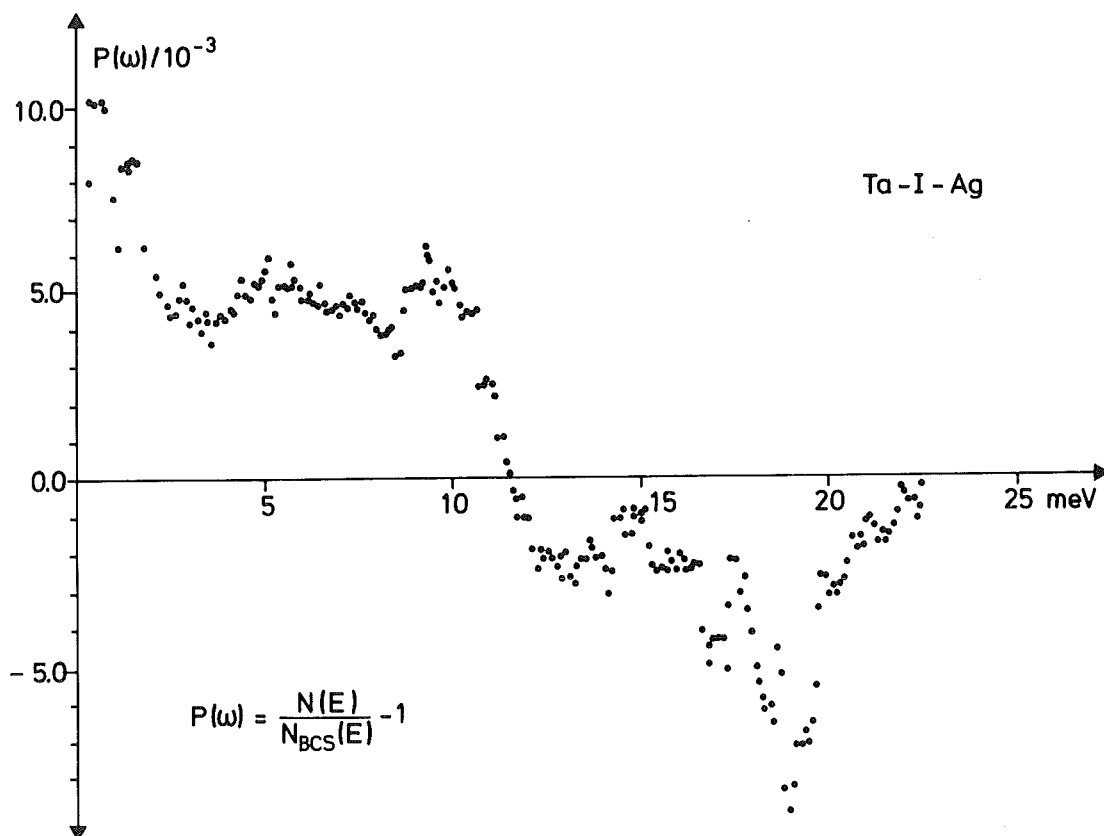


Fig. 2 Phonon structure of a Ta-I-Ag junction

The BCD-information of the potentiometric conductance bridge is, after passing an adapter stage, converted into the corresponding binary information. With the pulses from the logical unit this binary information is converted into pulses by a series of gates. After buffering, these pulses are fed into the binary arithmetic register of a multichannel analyzer TMC CN-1024. The pulse from the logical unit is delayed and given into the external trigger input of a multiscaler unit TMC-214. Thus, after taking up the information, the multichannel analyzer switches to the next channel, taking up the information of the next voltage step and so on.

After the dI/dV -characteristic is stored within the interesting voltage range the curve can be displayed and punched onto paper tape for computer analysis. As a result Fig. 2 shows the phonon induced structure of a Ta-I-Ag junction. The measurement was taken with a voltage grid of 0.1 meV and a time constant of 1 second. The scattering of the points may be reduced by the application of higher time constants.

If second derivative data have to be stored, the potentiometric conductance bridge is replaced by a digital voltmeter with BCD-output. This digital

voltmeter is connected to the output of a lock-in amplifier, which detects the second harmonic signal /2/ created by the tunneling diode.

REFERENCES

/1/ J. Geerk, Progress Report of the Teilinstitut Nukleare Festkörperphysik, Ges. f. Kernforschung Karlsruhe (KFK-2357), p. 105 (1976)

/2/ J. Geerk, Ges. f. Kernforschung Karlsruhe, KFK-2140 (1975)

6.2 Some Experiences with the "Cold Crucible"

B. Scheerer

The cold crucible is a water-cooled crucible for melting conducting materials. The material is heated by high frequency induction. The HF induces currents in the material which heat and melt the sample and create a magnetic field which holds the sample in a floated state. This procedure guarantees that there is no contact between the water-cooled crucible and the melt. It minimizes contamination by impurities and is therefore essential for melting very pure or very reactive materials such as the rare earths.

Our two cold crucibles (for sample volumes of 5 cm³ and 25 cm³) have each 16 segments. They are operated by a 40 KW, 250 KHz high frequency generator.

It was easily possible to melt 5 g niobium (m.p. = 2400°C) or 20 g nickel (m.p. = 1455°C) in the small crucible. We often produced alloys in these crucibles which due to the rapid solidification had the great advantage of a homogeneous distribution of the alloyed constituents.

6.3 The Time-of-Flight Spectrometer TOF3

N. Nücker

In the last years time-of-flight (TOF) spectrometers were used more and more in the investigation of the dynamics of solids and liquids. We therefore extended our TOF3-spectrometer (Fig. 1) at the FR2.

Thermal neutrons from the beam tube are monochromatized by a single crystal and are reflected at an angle of $2\theta = 49^\circ$. Different energies can be selected using appropriate crystals and reflecting planes. The last experiments were performed at an energy of 100 meV using copper crystals. The monochromatic neutrons are pulsed by a succeeding Fermi-chopper. The sample and analyzers are shielded by a housing formed of bricks of boron-paraffine. The sample may be fixed in a scattering box of 80 cm diameter. This box can be evacuated to better than 10^{-4} mb to avoid neutron scattering by air and for thermal isolation for low and high temperature experiments.

$^{120}\text{He}^3$ detectors are mounted in boxes at a distance of 300 cm from the sample. The boxes are fixed to a 60 degree segment filled with argon gas. The range of scattering angles may be chosen between 0° and 140° by turning this segment around its axis centered at the sample position. The counter boxes contain 6 detectors with preamplifiers, main amplifiers and discriminators with one-shot exit, sum output of TTL signals for the six counters and a high voltage supply. The boxes are supplied by + 6V, - 6V and + 24V.

A 32-input TOF-unit /1/ encodes the data which are stored in a Nova 2 computer. Data evaluation can also be performed by this computer. The TOF-data enter via an increment unit /2/ to a 32 K memory reserved for data. Programs are run in an additional 32 K memory. Data acquisition is independent of running programs, thus data evaluation may be done during the experiments.

The computer is equipped with a disk, a magnetic tape unit, a "Silent" typewriter and a TV screen. Programs written in Basic and in Fortran IV languages are supported by a common subroutine package written in assembler to access the special IO-devices. A lightpen /4/ is a very helpful tool in the data handling using a TV screen.

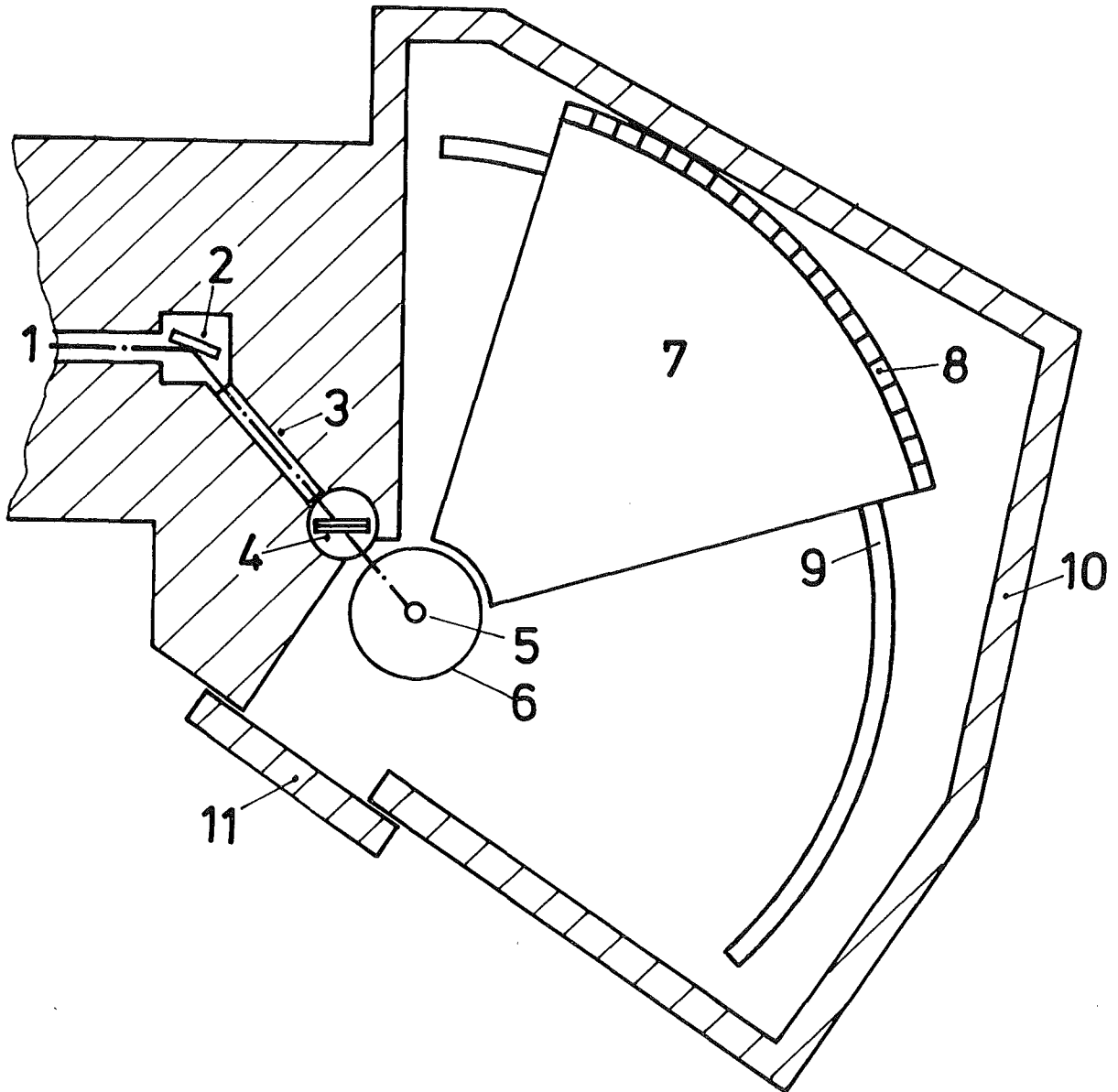


Fig. 1 TOF3 spectrometer

(1 R7 beam tube, 2 single crystal monochromator, 3 collimator, 4 fermichopper, 5 sample, 6 scattering box, 7 argon filled segment, 8 counter boxes, 9 rails for turning the segment, 10 shielding house, 11 door).

At present the following programs are available:

1. "TOF" : Program in Basic for the following purposes
 - a start und stop of data acquisition
 - b display of TOF-spectra on TV
 - c writing results on disk
 - d clear data memory
 - e counting rate control
 - f print and plot of data on the console
2. "Unt" : Program in Basic for background correction
3. "Einpho" : Program in Basic for the calculation of the phonon density of states neglecting multiphonon processes
4. "Mu" : Fortran program Muphacor /5/ for calculation of the phonon density of states with correction for instrumental resolution and multiphonons.

REFERENCES

- /1/ H. Hanak and G. Ehret, in Progress Report of the Teilinstitut Nukleare Festkörperphysik, Ges. f. Kernforschung Karlsruhe, (KFK 2054), 81 (1974)
- /2/ G. Ehret and H. Hanak, in Progress Report of the Teilinstitut Nukleare Festkörperphysik, Ges. f. Kernforschung Karlsruhe, (KFK 2183), 99 (1975)
- /3/ G. Ehret et al. to be published
- /4/ G. Ehret and H. Hanak, this report, p. 139
- /5/ J.-B. Suck and W. Reichardt, in Progress Report of the Teilinstitut Nukleare Festkörperphysik, Ges. f. Kernforschung Karlsruhe (KFK 2183), 94 (1975)

6.4 Wechsel- und Justiereinheit für Monochromatoreinkristalle

K. Weber

Beim Multidetektorflugzeitspektrometer TOF1 kann die Energie des monochromatischen Strahls durch vier in einer Abschirmwalze befindliche Monochromatorkristalle gewählt werden. Wurde für ein bestimmtes Meßproblem die günstigste

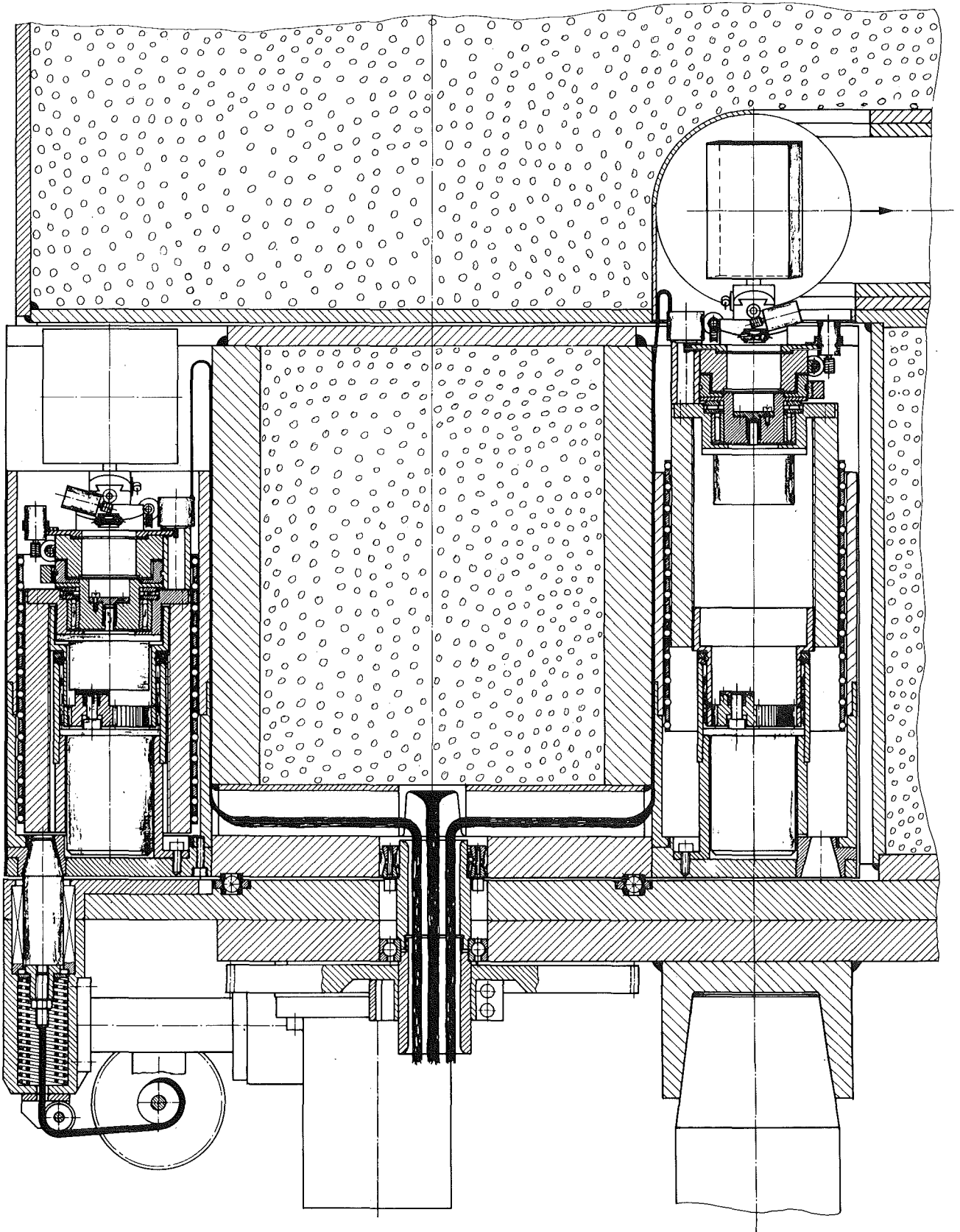


Fig. 1 Vertikalschnitt der Monochromatorwechseleinrichtung

der 4 Energien ausgewählt, wird der dafür zuständige Einkristall auf die Position unter den weißen Neutronenstrahl gedreht (nach Verriegelung der Walze), in den Strahl hochgefahren und optimal justiert. Diese vier Bewegungsabläufe werden mit der neu entwickelten, fernsteuerbaren Wechsel- und Justiereinheit realisiert.

Die gesamten Bewegungsaufgaben werden von Schritt- und Gleichstrommotoren übernommen, die von der elektronischen Folgesteuerung angesteuert werden.

Eine Energieänderung wird in folgenden Stufen durchgeführt.

1. Absenken des noch im Strahl befindlichen Monochromatorkristalls.
2. Entriegeln der Walze.
3. Drehen der Walze zur Positionierung des für die gewünschte Energie zuständigen Einkristalls unter den weißen Neutronenstrahl.
4. Heben des Kristalls in den Strahl.
5. Drehen des Kristalls in die Reflexebene.
6. Kippen des Kristalls in zwei um 90° versetzte Ebenen zur optimalen Ausrichtung des monoenergetischen Strahls.

Die technische Lösung der einzelnen Bewegungsstufen wurde wie folgt durchgeführt.

1. Heben und Senken des Monochromatorkristalls.

Eine mittels eines Getriebemotors angetriebene Gewindespindel bewirkt je nach Drehrichtung des Motors eine Auf- oder Abwärtsbewegung der in einer Kugelhülse spielfrei gelagerten Mutter. Auf dieser sind die weiteren Justieraggregate aufmontiert.

2. Ent- und Verriegeln der Walze.

Ein unter Federspannung stehender konischer Bolzen wird durch eine Motortriebeeinheit je nach Drehrichtung des Motors in die konische Bohrung der Walze eingedrückt oder herausgezogen.

Dieses Aggregat bewirkt eine genaue Positionierung der Walze und verhindert eine Verdrehung durch Vibration.

3. Drehen der Walze.

Die drehbar gelagerte Abschirmwalze besitzt vier um 90° versetzte Ausparungen für die Aufnahme der Hub- und Justierarbeiten. Ihr Antrieb erfolgt über die an die Walze angeflanschte Hohlwelle und den Stirnradantrieb durch einen Schrittmotor.

Durch Schaltnocken in Verbindung mit dem Schalter läßt sich jeder der vier Monochromatorkristalle in Position bringen.

4. Wie 1.

5. Drehen des Kristalls in die Reflexebene.

Der auf der Mutter angebrachte Drehtisch besitzt zwei Antriebe. Der erste Antrieb erfolgt direkt durch einen 5 Phasen Schrittmotor in $0,36^\circ$ Schritten über einen Bereich von 190° .

Ein zweiter Feintrieb erlaubt Verdrehungen von $< \frac{1}{10}^\circ$ in einem Bereich von $\pm 2^\circ$.

Ein über einen Stirnradantrieb verbundener Winkelschrittgeber erzeugt die Signale für die digitale Winkelanzeige mit einer Auflösung von $0,1^\circ$.

Nach Erreichen der optimalen Stellung wird der Rundtisch durch eine Backenbremse arretiert.

6. Kippen des Monochromatorkristalls in zwei um 90° versetzte Ebenen. Den Abschluß der Justiereinheit bildet das Goniometer mit dem aufgesetzten Monochromatorkristall. Die beiden um 90° gegeneinander versetzten Kipp-ebenen werden über einen Schneckenantrieb mittels eines Gleichstrom-getriebemotors angetrieben. Der Kippbereich beträgt $\pm 10^\circ$ je Ebene mit einer Einstellgenauigkeit von $< \frac{1}{10}^\circ$. Ein an jeder Kippebene angebrachter Neigungsfühler liefert die Signale für die digitale Winkelanzeige im Kippbereich des Goniometers mit einer Auflösung von $\pm 0,1^\circ$.

7. PUBLICATIONS, CONFERENCE CONTRIBUTIONS, AND SEMINARS

7.1 PUBLICATIONS

Abel, W.; Block, R.; Schommers, W.

Extended Born-Green Equation: A New Approach for Determining Pair Potentials in Disordered Systems

Phys. Letters 58 A, 367 (1976)

Bader, S.D.; Knapp, G.S.; Sinha, S.K.; Schweiß, P.; Renker, B.

Phonon Spectra of Chevrel-Phase Lead and Tin Molybdenum Sulfides: A Molecular-Crystal Model and Its Implications for Superconductivity

Phys. Rev. Lett. 37, 344 (1976)

Bassalleck, B.; Engelhardt, H.D.; Haase, E.L.; Klotz, W.D.; Lewis, C.W.; Takeutchi, F.; Ullrich, H.; Furić, M.

Neutron Pair Emission Following the Capture of π^- in ^{14}N

Phys. Lett. 65B, 128 (1976)

Block, R.; Suck, J.-B.; Freyland, W.; Hensel, F.; Gläser, W.

Structure Factor of Expanded Liquid Rubidium up to 1400 K and 200 bar

Inst. Phys. Conf. Ser. 30, Chapter 1, Part 1 (1977), p. 126

Block, R.

Struktur und Wechselwirkung in flüssigem Rubidium

Dissertation, Universität Karlsruhe 1977

KFK-2488

Crececius, G.; Maletta, H.; Hauck, J.; Fink, J.; Czjzek, G.; Schmidt, H.;

Influence of Lattice Structure and Substituent on the Magnetic Interactions in Alloy Systems

JMMM 4, 40 (1977)

Dietrich, M.; Reichardt, W.; Rietschel, H.

Phonon Densities of States of the Thorium Hydrides

Solid State Communications 21, 603 (1977)

Geerk, J.; Langguth, K.-G.; Linker, G.; Meyer, O.

The Influence of Implanted Ions on the Superconducting Transition Temperature of Transition Metals and Transition Metal Carbides

IEEE Transactions on Magnetics MAG-13, 662 (1977)

Geerk, J.; Langguth, K.-G.

Implantation and Diffusion of Carbon into Niobium Carbide Single Crystals

Solid State Communications 23, 83 (1977)

Geick, R.; Lehner, N.; Strobel, K.

Interlayer and Intralayer Forces in Halide Perovskite-Type Layer Structures

Il Nuovo Cimento 38B, 309 (1977)

Geserich, H.P.; Möller, W.; Scheiber, G.; Pintschovius, L.
Optical Investigations of the Electrical Anisotropy of $(\text{SN})_x$ Single Crystals
phys. stat. sol. (b) 80, 119 (1977)

Gompf, F.; Pintschovius, L.; Reichardt, W.; Scheerer, B.
Investigations on the Lattice Dynamics of the Carbides and Nitrides of
Niobium and Titanium
Proc.Conf. Neutron Scattering, R.M. Moon, ed., Gatlinburg, (1976), p. 129

Happel, H.; Blanckenhagen, P. von; Knorr, K.; Murani, A.
Crystal Electric Fields in Rare-Earth Al_2 Compounds
Crystal Field Effects in Metals and Alloys, A. Furrer, ed.
Plenum Publ. Corp. New York, (1977), p. 273

Heger, G.; Mullen, D.
Hydrogen Bonding and Structural Phase Transitions in $(\text{CH}_3\text{NH}_3)_2 \text{MnCl}_4$
Proc.Conf. Neutron Scattering, R.M. Moon, ed., Gatlinburg, (1976), p. 439

Hellner, E.; Heger, G.; Mullen, D.; Treutmann, W.
Combined X-ray and Neutron Diffraction Studies of the Intermetallic System
 $(\text{Cr}_{1-x}\text{Fe}_x)_{1+\delta}\text{Sb}$
Proc.Conf. Neutron Scattering, R.M. Moon, ed., Gatlinburg, (1976), p. 71

Helmbold, R.; Mullen, D.; Ahsbahr, A.; Klopsch, A.; Hellner, E.; Heger, G.
Morphologische, Neutronenbeugungs- und IR-spektroskopische Untersuchungen
an Jahn-Teller verzerrten Strukturen von $\text{A}_2\text{PbCu}(\text{NO}_2)_6$. mit $\text{A} = \text{K}, \text{Rb}, \text{Cs}$
Z. Krist. 143, 220 (1976)

Hoenig, H.E.; Blanckenhagen, P. von
Short Range Van Vleck Antiferromagnetism in Superconducting $\text{La}_{1-y}\text{Tb}_y\text{Sn}_3$
Detected by Neutron Scattering
Crystal Field Effects in Metals and Alloys, A. Furrer, ed.
Plenum Publ. Corp. New York, (1977), p. 128

Hofmann-Kraeft, B.
Messung des Partiellen Isotopeneffekts an Vanadiumnitrid
Dissertation, Universität Karlsruhe 1977
KFK-2524

Hofmann, B.
Einfluß hoher Massendefektkonzentrationen auf die Gitterdynamik von $\text{Bi}_{1-x}\text{Sb}_x$ -
Legierungen
Dissertation, Universität Karlsruhe 1977
KFK- 2398

Horsch, P.; Rietschel, H.
A New Aspect of Superconductivity in A-15 Compounds
Zeitschrift f. Physik B27, 153 (1977)

Krill, G.; Panissod, P.; Lapierre, M.F.; Gautier, F.; Robert, C.; Czjzek, G.; Fink, J.; Schmidt, H.; Kuentzler, R.

Physical Properties of Compounds $\text{NiS}_{2-x}\text{Se}_x$ with Pyrite Structure: Metal-Nonmetal Transition, Evidence for the Existence of an Antiferromagnetic Metallic Phase

J. Phys. Coll. 37, C4 - 23 (1976)

Langguth, K.-G.

Herstellung von supraleitendem Vanadiumkarbid durch Ionenimplantation

Dissertation, Universität Karlsruhe (1977)

KFK 2476 (Juni 1977)

Langguth, K.-G.; Linker, G.; Geerk, J.

Determination of Implanted Carbon Profiles in NbC-Single Crystals from Random Backscattering Spectra

Ion Beam Surface Layer Analysis, O. Meyer, G. Linker, F. Käppeler, eds., Plenum Press, New York, (1976) p. 273

Linker, G.; Meyer, O.

Superconducting Properties and Structural Transformations of Nitrogen Implanted Molybdenum Layers

Sol. State Comm. 20, 695 (1976)

Mätzke, Hj.; Linker, G.

Study of the Diffusion of Cesium in Stainless Steel Using Ion Beams

J. Nucl. Mat. 64, 130 (1977)

Meyer, O.; Linker, G.; Käppeler, F., eds.

Ion Beam Surface Layer Analysis

Plenum Press, New York, (1976)

Meyer, O.

Enhancement of the Superconducting Transition Temperature by Ion Implantation in Molybdenum Thin Films

Inst. Phys. Conf. Ser. 28, 168 (1976)

Meyer, O.

Implantieren statt Legieren

Bild der Wissenschaft 7, 82 (1976)

Meyer, O.; Seeber, B.

Channelling Effect Measurements of the ^4He -induced Damage in V_3Si Single Crystals

Solid State Comm. 22, 603 (1977)

Pintschovius, L.; Renker, B.; Comès, R.

Investigation of the Dynamical Structure Factor of $\text{K}_2\text{Pt}(\text{CN})_4\text{Br}_3 \cdot 3.2\text{D}_2\text{O}$ (KCP)

Proc. Conf. Neutron Scattering, R.M. Moon, ed., Gatlinburg, (1976), p. 432

Reichardt, W.; Rieder, K.H.
Lattice Dynamics of α -Arsenic
Proc. Conf. Neutron Scattering, R.M. Moon, ed., Gatlinburg, (1976), p. 181

Schneider, E.; Schweiß, P.; Reichardt, W.
Temperature Dependence of the Phonon Density of States for Some A15 Compounds
Proc. Conf. Neutron Scattering, R.M. Moon, ed., Gatlinburg, (1976), p. 223

Schommers, W.
Theoretical Investigation of the Liquid-Solid Transition. A Study for Gallium
Solid State Comm. 21, 65 (1977)

Schommers, W.; Geszti, T.
Comment on "Fokker-Planck Equations for Simple Non-Markovian Systems"
J. Chem. Phys. 66, 2767 (1977)

Schommers, W.
The Effect of van der Waals-Type Interactions in Metals: A Pseudopotential Model
Zeitschrift f. Physik B24, 171 (1976)

Schweiß, P.; Renker, B.; Schneider, E.; Reichardt, W.
Phonon Spectra of A-15 Compounds and Ternary Molybdenum Chalcogenides
Superconductivity in d- and f-Band Metals, D.H. Douglass, ed.,
Plenum Press, New York, (1976), p. 189

Schweiß, P.
Untersuchungen zur Gitterdynamik von A-15 Verbindungen auf Vanadiumbasis
Dissertation, Universität Karlsruhe (1976)
KFK-2528 (1977)

Stolz, H.J.; Wendel, H.; Otto, A.; Pintschovius, L.; Kahlert, H.
Acoustic and Optical Phonons in (SN)_x
phys. stat. sol. (b) 78, 277 (1976)

Wagner, W.; Reichardt, W.; Kress, W.
Lattice Dynamics of MnO
Proc. Conf. Neutron Scattering, R.M. Moon, ed., Gatlinburg, (1976), p. 175

7.2 CONFERENCE CONTRIBUTIONS AND SEMINARS

Blanckenhagen, P. von; Happel, H.; Knorr, K.
Linienbreiten der quasielastischen magnetischen Neutronenstreuung an (SE)Al₂-
Verbindungen
Verhandl. DPG (VI) 12, 201 (1977)

Czjzek, G.; Fink, J.; Schmidt, H.; Blanckenhagen, P. von; Krill, G.;
Lapierre, M.F.; Panissod, P.; Robert, C.; Gautier, F.
Covalency Effects and the Metal- Insulator Transition in NiS_{2-x}Se_x
International Conference on the Application of the Mössbauer Effect,
Corfu (Greece), Sept. 13 - 17, 1976

Daubert, J.; Jex, H.; Knorr, K.; Müllner, M.; Nücker, N.; Suck, J.-B.
Die Frequenzverteilungen von KCN und NaCN für ihre drei stabilen kristallinen
Phasen
Verhandl. DPG (VI) 12, 87 (1977)

Deiseroth, H.J.; Heger, G.; Renker, B.; Schulz, H.
Untersuchungen der Kristallstruktur des eindimensionalen elektronischen
leiters "KCP" mit Röntgen- und Neutronenbeugung im Temperaturbereich 35 K
bis 290 K
16. Diskussionstagung der AG Kristallographie, Braunschweig, 14. - 17. Sept. 1976

Fink, J.; Czjzek, G.; Schmidt, H.; Tomala, K.; Obenshain, F.E.
Messungen von lokalen Suszeptibilitäten und Momenten in verdünnten Pd-Ni-
Legierungen mit ⁶¹Ni-Mössbauerspektroskopie
Verhandl. DPG (VI) 12, 220 (1977)

Gärtner, K.; Geerk, J.
Messung der dynamischen Leitfähigkeit von Nb-I-Ag Tunnelnioden bei Energien
nahe der Energielücke
Verhandl. DPG (VI), 422 (1977)

Geserich, H.P.; Möller, W.; Scheiber, G.; Pintschovius, L.
Optische Untersuchung der elektrischen Anisotropie von (SN)_x-Einkristallen.
Verhandl. DPG (VI) 12, 52 (1977)

Haase, E.L.; Conrad, M.; Meyer, O.
Sauerstofftiefenprofile in Nb₃Ge Schichten
Verhandl. DPG (VI) 12, 435 (1977)

Heger, G.; Klein, S.; Pintschovius, L.
Untersuchungen der Kristallstruktur des polymeren Metalls (SN)_x mit Hilfe
von Neutronenbeugung
Verhandl. DPG (VI) 12, 188 (1977)

Horsch, P.; Rietschel, H.

Elektronische Zustandsdichte und Supraleitung in A15-Verbindungen
Verhandl. DPG (VI) 12, 434 (1977)

Käfer, K.

Streugesetz eines 1-D-Peierls Systems
Verhandl. DPG (VI) 12, 433 (1977)

*Krill, G.; Panissod, P.; Lapierre, M.F.; Czjzek, G.; Fink, J.;
Schmidt, H.; Kuentzler, R.*

Physical Properties of the $\text{NiS}_{2-x}\text{Se}_x$ Compounds with Pyrite Structure:
Occurrence of an Antiferromagnetic Metallic Phase
V. International Conference on Solid Compounds of Transition Elements,
Uppsala (Sweden), June 21 - 25, 1976

Lehner, N.; Wagner, V.; Heger, G.; Geick, R.

Magnonendispersion in quasi zweidimensionalen Heisenberg Antiferromagneten
Verhandl. DPG (VI) 12, 212 (1977)

Linker, G.; Meyer, O.

Nitrogen Implantation into Molybdenum: Superconducting Properties and
Compound Formation
Int. Conf. Ion Impl. Semicond. Other Mat., Bolder, Colorado, August 1976

Linker, G.; Meyer, O.

Defektanalyse in ionenimplantierten Metall-Einkristallen mit Hilfe von
Channelingmessungen
Verhandl. DPG (VI) 12, 312 (1977)

Linker, G.

Channeling Analysis of Radiation Disorder in Ion Implanted Vanadium and
Molybdenum Single Crystals
3. Internat. Conf. on Ion Beam Analysis, Washington, D.C., June 27 - July 1,
1977

Linker, G.; Meyer, O.

Influence of Ion Bombardment on the Superconducting Transition Temperature
of Evaporated Transition Metal Layers
Internat. Discussion Meeting on Radiation Effects in Superconductivity, Argonne,
Ill., June 13 - 16, 1977

Meyer, O. Seeber, B.

Untersuchungen an ^4He -bestrahlten V_3Si -Einkristallen mit Hilfe des Channeling
Effektes
Verhandl. DPG (VI) 12, 435 (1977)

Meyer, O.; Lombaard, J.M.

Channeling Studies in Carbon Implanted NbC and VC Single Crystals
Internat. Discussion Meeting on Radiation Effects in Superconductivity, Argonne,
Ill., June 13 - 16, 1977

Meyer, O.

Channeling Effect Measurements of ^4He -Induced Damage in V_3Si Single Crystals
3. Internat. Conf. on Ion Beam Analysis, Washington, D.C., June 27 - July 1, 1977

Müller, W.H.G.; Baumann, F.; Dammer, G.; Pintschovius, L.

Zur Druckabhängigkeit der Übergangstemperatur T_C von $(\text{SN})_x$
Verhandl. DPG (VI) 12, 432 (1977)

Nücker, N.

Vergleich der Phononenzustandsdichten von fcc- und dhcp-Lanthan
Verhandl. DPG (VI) 12, 396 (1977)

Nücker, N.

Untersuchungen zur Temperaturabhängigkeit der Phononenzustandsdichte von KCN und NaCN mit Hilfe der unelastischen Neutronenstreuung an polykristallinen Proben

Vortrag auf der Sommerschule in Riezlern/Universität Frankfurt, September 1976

Pintschovius, L.

Phononenanomalie in Polyschwefelnitrid $(\text{SN})_x$
Verhandl. DPG (VI) 12, 432 (1977)

Pintschovius, L.; Wendel, H.; Kahlert, H.

Acoustic Phonons of Polymeric Sulfur Nitride, $(\text{SN})_x$
in Lecture Notes in Physics, Proc. of the Int. Conf. on Organic Conductors and Semiconductors, Siófok (Hungary), September 1976

Ploog, K.; Heger, G.

Zur Struktur des Siliziumtellurids Si_2Te_3
Verhandl. DPG (VI) 12, 188 (1977)

Reichardt, W.

Phononenspektren von Übergangsmetall-Verbindungen
Verhandl. DPG (VI) 12, 394 (1977)

Renker, B.; Pintschovius, L.; Comès, R.

Inelastic Neutron Scattering Study of the $2k_F$ Instability in $\text{K}_2\text{Pt}(\text{CN})_4\text{Br}_{0.3}\cdot 3\text{D}_2\text{O}$, (KCP)

Vortrag auf der NATO-ASI, Bozen, August 1976

Rietschel, H.

Die Rolle von Kristallsymmetrie und Kristalldynamik in der Supraleitung
Verhandl. DPG (VI) 12, 166 (1977)

Rietschel, H.

Zur Energieabhängigkeit der Kopplungsfunktion $\alpha^2(\omega)$ für Supraleiter.
Verhandl. DPG (VI) 12, 397 (1977)

Rietschel, H.

Optische Phononen und Supraleitung

Kolloquiumsvortrag an der Universität Köln, November 1976

Ruebenbauer, K.; Fink, J.; Schmidt, H.; Czjzek, G.

An Investigation of Magnetic Ordering in $Gd_xCe_{1-x}Ru_2$ by ^{155}Gd Mössbauer Spectroscopy

International Conference on the Applications of the Mössbauer Effect, Corfu (Greece), September 13 - 17, 1976

Schommers, W.

Theoretical Investigations of the Liquid-Solid Transition. A Study for Gallium

3. Internat. Conf. on the Properties of Liquid Metals, Bristol, UK, July 12 - 16, 1976

Schommers, W.

Der Einfluß von Dreikörperkräften auf die Korrelationen in einem Argon-Vielteilchensystem

Verhandl. DPG (VI) 12, 361 (1977)

Tomala, K.; Fink, J.; Schmidt, H.; Czjzek, G.

Hyperfeinwechselwirkungen in intermetallischen Verbindungen von Gd mit 3d-Übergangsmetallen

Verhandl. DPG (VI) 12, 201 (1977)

Ziemann, P.

Korrelation zwischen Sauerstoffgehalt und Sprungtemperatur in Al-Filmen

Verhandl. DPG (VI) 12, 429 (1977)

8. LIST OF THE NEUTRON SPECTROMETERS AT
THE FR2 AT KARLSRUHE OPERATED BY THE IAK I

- DIF 1 : Four circle diffractometer, $\lambda = 1.035 \text{ \AA}$
- DIF 2 : Two circle diffractometer, $0.7 \text{ \AA} \leq \lambda < 2.6 \text{ \AA}$
- DIF 3 : Powder diffractometer, $\lambda = 1.28 \text{ \AA}$ or 1.09 \AA
- DIF 4 : Four circle diffractometer, $\lambda = 0.924 \text{ \AA}$ or 2.4 \AA
- TAS 1 : Three-axis spectrometer, $13 \text{ meV} \leq E_0 < 120 \text{ meV}$
- TAS 2 : Three-axis spectrometer, $8 \text{ meV} \leq E_0 < 64 \text{ meV}$
- TOF 1 : Time-of-flight spectrometer with Fermi-chopper,
140 detectors, thermal neutrons
- TOF 2 : Time-of-flight spectrometer with rotating crystal,
60 detectors, cold neutrons
- TOF 3 : Time-of-flight spectrometer with Fermi-chopper,
120 detectors, thermal neutrons
- TOF 4 : Time-of-flight spectrometer with rotating crystal,
6 detectors, cold neutrons
- MAG 1 : Spectrometer for diffuse scattering, 40 detectors,
thermal neutrons
- MAG 2 : Multipurpose spectrometer, 40 detectors, cold neutrons.

9. STAFF MEMBERS (1.6.1977)

Professional Staff

<i>Blanckenhagen, P. von</i>	<i>Heger, G.</i>	<i>Renker, B.</i>
<i>Czjzek, G.</i>	<i>Linker, G.</i>	<i>Rietschel, H.</i>
<i>Fink, J.</i>	<i>Meyer, O.</i>	<i>Schmidt, H.</i>
<i>Geerk, J.</i>	<i>Nücker, N.</i>	<i>Schommers, W.</i>
<i>Gompf, F.</i>	<i>Pintschovius, L.</i>	<i>Schweiß, P.</i>
<i>Haase, E.L.</i>	<i>Reichardt, W.</i>	

Technical Staff

<i>Abel, W.⁺</i>	<i>Kuhn, R.⁺</i>	<i>Smithey, R.</i>
<i>Ehret, G.⁺</i>	<i>Ratzel, F.</i>	<i>Sobiesiak, H.⁺</i>
<i>Hanak, H.⁺</i>	<i>Richelsen, H.⁺</i>	<i>Weber, K.</i>
<i>Kraatz, M.</i>	<i>Scheerer, B.</i>	

Visiting Scientists

Balabanov, A.; Guest from Israel
Klein, S.; Guest from SFB 127, Universität Marburg

Research Students

Block, R.; Universität Karlsruhe
Conrad, M.; Universität Karlsruhe
Gauß, C.; Universität Karlsruhe
Geibel, C.; Universität Karlsruhe
Guth, H.; Universität Karlsruhe
Götz, F.; Universität Heidelberg
Kaufmann, R.; Universität Karlsruhe
Klein, H.-J.; Universität Karlsruhe
Käfer, K.; Universität Karlsruhe
Lehner, N.; Universität Würzburg
Ziemann, P.; Universität Karlsruhe

⁺ Member of infrastructure